FCT Fundação para a Ciência e a Tecnologia
MINISTÉRIO DA CIÊNCIA, TECNOLOGIA E ENSINO SUPERIOR Portugal

Manuel da Silva Pinheiro
Development of Procedures for the Design, Optimization and Manufacturing of Customized Orthopaedic and Trauma Implants: Geometrical/Anatomical Modelling from 3D Medical Imaging
UMinho | 2015

Universidade do Minho
Escola de Engenharia

Manuel da Silva Pinheiro

Development of Procedures for the Design, Optimization and Manufacturing of Customized Orthopaedic and Trauma Implants: Geometrical/Anatomical Modelling from 3D Medical Imaging

Junho de 2015

Universidade do Minho
Escola de Engenharia

Manuel da Silva Pinheiro

Development of Procedures for the Design, Optimization and Manufacturing of Customized Orthopaedic and Trauma Implants: Geometrical/Anatomical Modelling from 3D Medical Imaging

Tese de Doutoramento
Programa Doutoral em Engenharia Biomédica

Trabalho efectuado sob a orientação do
Professor Doutor José Luís C. M. Alves

Junho de 2015

STATEMENT OF INTEGRITY

I hereby declare having conducted my thesis with integrity. I confirm that I have not used plagiarism or any form of falsification of results in the process of the thesis elaboration.

I further declare that I have fully acknowledged the Code of Ethical Conduct of the University of Minho.

University of Minho, 15th of June 2015

Full name: Manuel da Silva Pinheiro

Signature: _____

"Dream no small dreams for they have no power to move the hearts of men"

Johann Wolfgang Von Goethe

This page was intentionally left blank

Acknowledgments

Foremost, I would like to acknowledge my supervisor, Professor José Luís Alves, for the scientific guidance and continuous support of my PhD thesis. I would like to thank all the advices and suggestions, which were fundamental to finish this work successfully. I also want to acknowledge all the motivation and confidence demonstrated during the development of this thesis.

To my parents, Maria do Céu and António Pinheiro, and brothers and sisters, Sandrina Pinheiro, David Pinheiro, Maria da Luz Pinheiro and Daniel Pinheiro, for all the care, advices and unconditional support. I also would like to thank Filipa Marcos, who has been unconditionally by my side over the last two and a half years.

To my colleagues of the Mechanical Engineering Department, I appreciate all the support and companionship. To my Biomedical Engineering friends, particularly those who followed my work more closely, namely, Ana Cristina Ferreira, André Castro, Carla Pereira, Rita Rebelo, Susana Catarino and Sara Cortez. I want to express my gratitude to the colleagues of the Robotics Group, and to my friends, Bruno Danilson, David Martins, Marta Araújo, Bruno Andrade and Carina Almeida, thank you for your friendship.

I would like to acknowledge to the Portuguese Fundação para a Ciência e Tecnologia (FCT), for the financial support under the PhD scholarship SFRH/BDE/51143/2010.

I would like to acknowledge MCM for supporting this Doctoral thesis, especially Mr. Francisco Martins. I want to show my gratitude, in a very particular way, to Pedro Fernandes, who has followed closely the work done in the company and always shown his support to me, and that sadly passed away recently.

Finally, I would like to acknowledge to the Clínica Dr. Campos Costa and to the Instituto CUF, in particular to Dr. Maria do Carmo Baptista for all the help, and to the Instituto de Soldadura e Qualidade (ISQ).

This page was intentionally left blank

Abstract

The introduction of imaging techniques in 1970 is one of the most relevant historical milestones in modern medicine. Medical imaging techniques have dramatically changed our understanding of the Human anatomy and physiology. The ability to non-invasively extract visual information allowed, not only the three-dimensional representation of the internal organs and musculo-skeletal system, but also the simulation of surgical procedures, the execution of computer aided surgeries, the development of more accurate biomechanical models, the development of custom-made implants, among others.

The combination of the most advanced medical imaging systems with the most advanced CAD and CAM techniques, may allow the development of custom-made implants that meet patient-specific traits. The geometrical and functional optimization of these devices may increase implant life-expectancy, especially in patients with marked deviations from the anatomical standards. In the implant customization protocol from medical image data, there are several steps that need to be followed in a sequential way, namely: Medical Image Processing and Recovering; Accurate Image Segmentation and 3D Surface Model Generation; Geometrical Customization based on CAD and CAE techniques; FEA Optimization of the Implant Geometry; and Manufacturing using CAD-CAM Technologies.

This work aims to develop the necessary procedures for custom implant development from medical image data. This includes the extraction of highly accurate three-dimensional representation of the musculo-skeletal system from the Computed Tomography imaging, and the development of customized implants, given the specific requirements of the target anatomy, and the applicable best practices found in the literature.

A two-step segmentation protocol is proposed. In the first step the region of interest is pre-segmented in order to obtain a good approximation to the desired geometry.

Next, a fully automatic segmentation refinement is applied to obtain a more accurate representation of the target domain. The refinement step is composed by several sub-steps, more precisely, the recovery of the original image, considering the limiting resolution of the imaging system; image cropping; image interpolation; and segmentation refinement over the up-sampled domain. Highly accurate segmentations of the target domain were obtained with the proposed pipeline. The limiting factor to the accurate description of the domain accuracy is the image acquisition process, rather the following image processing, segmentation and surface meshing steps.

The new segmentation pipeline was used in the development of three tailor-made implants, namely, a tibial nailing system, a mandibular implant, and a Total Hip Replacement system. Implants optimization is carried with Finite Element Analysis, considering the critical loading conditions that may be applied to each implant in working conditions. The new tibial nailing system is able of sustaining critical loads without implant failure; the new mandibular endoprosthesis that allows the recovery of the natural stress and strain fields observed in intact mandibles; and the Total Hip Replacement system that showed comparable strain shielding levels as commercially available stems.

In summary, in the present thesis the necessary procedures for custom implant design are investigated, and new algorithms proposed. The guidelines for the characterization of the image acquisition, image processing, image segmentation and 3D reconstruction are presented and discussed. This new image processing pipeline is applied and validated in the development of the three abovementioned customized implants, for different medical applications and that satisfy specific anatomical needs.

Resumo

Um dos principais marcos da história moderna da medicina é a introdução da imagem médica, em meados da década de 1970. As tecnologias de imagem permitiram aumentar e potenciar o nosso conhecimento acerca da anatomia e fisiologia do corpo Humano. A capacidade de obter informação imagiológica de forma não invasiva permitiu, não só a representação tridimensional de órgãos e do sistema músculo-esquelético, mas também a simulação de procedimentos cirúrgicos, a realização de cirurgias assistidas por computador, a criação de modelos biomecânicos mais realistas, a criação de implantes personalizados, entre outros.

A conjugação dos sistemas mais avançados de imagem médica com as técnicas mais avançadas de modelação e maquinagem, pode permitir o desenvolvimento de implantes personalizados mais otimizados, que vão de encontro às especificidades de cada paciente. Por sua vez, a otimização geométrica e biomecânica destes dispositivos pode permitir, quer o aumento da sua longevidade, quer o tratamento de pessoas com estruturas anatómicas que se afastam dos padrões normais. O processo de modelação de implantes a partir da imagem médica passa por um conjunto de procedimentos a adotar, sequencialmente, até ao produto final, a saber: Processamento e Recuperação de Imagem; Segmentação de Imagem e Reconstrução tridimensional da Região de Interesse; Modelação Geométrica do Implante; Simulação Numérica para a Otimização da Geometria; a Maquinagem do Implante.

Este trabalho visa o desenvolvimento dos procedimentos necessários para a criação de implantes personalizados a partir da imagem médica, englobando a extração de modelos ósseos geométricos rigorosos a partir de imagens de Tomografia Computorizada e, a partir desses modelos, desenvolver implantes personalizados baseados nas melhores práticas existentes na literatura e que satisfaçam as especificidades da anatomia do paciente.

Assim, apresenta-se e discute-se um novo procedimento de segmentação em dois passos. No primeiro é feita uma pré-segmentação que visa obter uma aproximação inicial à região de interesse. De seguida, um procedimento de refinamento da segmentação totalmente automático é aplicado à segmentação inicial para obter uma descrição mais precisa do domínio de interesse. O processo de refinamento da segmentação é constituído por vários procedimentos, designadamente: recuperação da imagem original, tendo em consideração a resolução limitante do sistema de imagem; o recorte da imagem na vizinhança da região pré-segmentada; a interpolação da região de interesse; e o refinamento da segmentação aplicando a técnica de segmentação *Level-Sets* sobre o domínio interpolado. O procedimento de segmentação permitiu extrair modelos extremamente precisos a partir da informação imagiológica. Os resultados revelam que o fator limitante à descrição do domínio é o processo de aquisição de imagem, em detrimento dos diversos passos de processamento subsequentes.

O novo protocolo de segmentação foi utilizado no desenvolvimento de três implantes personalizados, a saber: um sistema de fixação interna para a tíbia; um implante mandibular; e um sistema para a Reconstrução Total da articulação da Anca. A otimização do comportamento mecânico dos implantes foi feita utilizado o Método dos Elementos Finitos, tendo em conta os carregamentos críticos a que estes podem estar sujeitos durante a sua vida útil. O sistema de fixação interna para a tíbia é capaz de suportar os carregamentos críticos, sem que a sua integridade mecânica seja comprometida; o implante mandibular permite recuperar os campos de tensão e deformação observados em mandíbulas intactas; e a Prótese Total da Anca apresenta níveis de *strain shielding* ao longo do fémur proximal comparáveis com os níveis observados em dispositivos comercialmente disponíveis.

Em suma, nesta tese de Doutoramento são investigados e propostos novos procedimentos para o projeto de implantes feitos por medida. São apresentadas e discutidas as linhas orientadoras para a caracterização precisa do sistema de aquisição de imagem, para o processamento de imagem, para a segmentação, e para a reconstrução 3D das estruturas anatómicas a partir da imagem médica. Este conjunto de linhas orientadoras é aplicado e validado no desenvolvimento de três implantes personalizados, citados anteriormente, para aplicações médicas distintas e que satisfazem as necessidades anatómicas específicas de cada paciente.

Contents

This page was intentionally left blank

List of Figures

This page was intentionally left blank

List of Tables

This page was intentionally left blank

List of Symbols and Physical Constants

Symbol	Description	Units
β^3	Cubic B-spline Basis Function	--
Γ	Velocity Field	--
$\gamma_{B,F}$	Background/Foreground Scaling Parameter	--
δ	Dirac Delta Function	--
ϵ	Linear Attenuation Coefficient	m^{-1}
ζ	CT Detector Coordinate	--
θ	CT Detector Angular Position	rad
λ	Wavelength	m
μ	Greyscale Average Intensity	HU
$\mu_{B,F}$	Average Background/Foreground Greyscale Intensity	HU
ν	Poisson Ratio	--
σ	Standard Deviation	--
ϕ	Level-set Embedding Function	--
∇	Spatial Image Gradient	--
$B_{in,out}$	Mean Incoming/Outgoing Beam Intensity	JKg^{-1}
$\tilde{c}$	Speed of Light in the Vacuum	ms^{-1}
C_{fit}	Non-linear Least-squares Cylinder Fit	--
c_t	2D Closed Curve	--

Symbol	Description	Units
c_i	Positive Real Valued Constant	--
d	Thickness of the Absorber Structure	m
d_{ij}	Distance Between Neighbouring Pixels	--
$\tilde{E}$	Energy	J
E	Elastic Modulus	MPa
f	Frequency	Hz
$F(x, y)$	Original Image/Function Data	--
g	Edge Indicator Function	--
G	Image Graph	--
h	(Current) Greyscale Value	HU
$h_{min,max}$	Greyscale Minimum/Maximum	HU
$\hbar$	Planck's Constant	Js
$H(S)$	Homogeneity Criterion	--
I	Two-dimensional Image Data	HU
I_i	Intensity of Image Pixel i	HU
K	Number of Clusters	--
L	Set of Graph Edges	--
$\mathbb{N}_0$	Natural Numbers Including Zero	--
n	Number of Segmentation Regions	--
n(x,y)	Image Noise	HU
N	Total Number of Pixel	--
N_c	Normalized Cut	--
O	Point Spread Function	--
$\mathbb{R}^+$	Positive Real Numbers	--
$R_d(\zeta, \theta)$	Radon Transform	--
S	Segmentation	--
S_E	Segmentation Energy Functional	--
S_{fit}	Non-linear Least-squares Sphere Fit	--

Symbol	Description	Units
S_{HU}	Hounsfield Scale	HU
t	Time	s
T	Threshold	--
u	Membership Function	--
V	Set of Image Vertices	--
w_{ij}	Pixel Similarity Measure	--

This page was intentionally left blank

List of Abbreviations

Abbreviation	Meaning
A	Subspinale Point (Cephalometry)
ACWE	Active Contours Without Edges
ANS	Anterior Nasal Spine (Cephalometry)
AO	Association for Osteosynthesis
AP	Antero-Posterior
Ar	Articulare Point (Cephalometry)
ASIF	Association for the Study of Internal Fixation
ASTM	American Society for Testing and Materials
AWGN	Additive White Gaussian Noise
Ba	Basion Point (Cephalometry)
BW	Body Weight
CAD	Computer Aided Design
CAE	Computer Aided Engineering
CAM	Computer Aided Manufacturing
CBCT	Cone-Beam Computed Tomography
CCD	Caput-Collum-Diaphyseal angle
CM	Confusion Matrix
CT	Computed Tomography
DAS	Data Acquisition System
DICOM	Digital Imaging and Communications in Medicine
DS	Dataset

Abbreviation	Meaning
EDT	Euclidean Distance Transform
ESF	Edge Spread Function
FCM	Fuzzy C-means Clustering
FE	Finite Element
FEA	Finite Element Analysis
FH	Frankfort Horizontal Plane
FN	False Negative
FOV	Field Of View
FP	False Positive
FWHM	Full Width at Half Maximum
GAC	Geodesic Active Contours
Gn	Gnathion Point (Cephalometry)
Go	Gonion Point (Cephalometry)
HD	Hausdorff Distance
HU	Hounsfield Units
IAPMEI	*Instituto de Apoio às Pequenas e Médias Empresas e à Inovação*
IC	Intercondylar Point
IM	Inter-malleolar Point
ISO	International Standards Organization
ISQ	*Instituto Superior da Qualidade*
KMC	K-means Clustering
LC	Lateral Tibial Condyle
LM	Lateral Malleolus
LSF	Line Spread Function
MC	Medial Tibial Condyle
Me	Menton Point (Cephalometry)
ML	Medio-Lateral

Abbreviation	Meaning
MM	Medial Malleolus
MRI	Magnetic Resonance Imaging
MSCT	Multi-slice Computed Tomography
MSD	Mean Symmetric Distance
MST	Minimum Spanning Tree
MTF	Modulation Transfer Function
N	Nasion Point (Cephalometry)
NHP	Natural Head Position
NPV	Negative Predictive Value
OA	Osteoarthritis
Or	Orbitale Point (Cephalometry)
OsiriX	Medical Image Processing Software
P	Prevalence
PC	Point Cloud
PCA	Principal Component Analysis
PET	Positron Emission Tomography
Po	Porion Point (Cephalometry)
Pog	Pogonion Point (Cephalometry)
PPV	Positive Predictive Values
PSF	Point Spread Function
RG	Region Growing
ROI	Region of Interest
ROM	Range Of Motion
S	Sella Point (Cephalometry)
SBA	Shape-based Averaging
ScanIP^{TM}	Image Processing and Model Generation Software
SE	Segmentation Sensitivity
SM	ScanIP^{TM} Mesh

Abbreviation	Meaning
SN-plane	Sella-Nasion Plane
SP	Segmentation Specificity
SPECT	Single Photon Emission Tomography
SSCT	Single-Slice Computed Tomography
SSP	Slice Sensitivity Profile
STAPLE	Simultaneous truth and Performance Level Estimation
THR	Total Hip Replacement
TN	True Negative
TP	True Positive
TT	Tibial Tuberosity
UHMWPE	Ultra High Molecular Weight Polyethylene
WT	Watershed Transform

Chapter 1

Introduction

In this chapter the industrial framework, the main objectives, and contributions of this thesis are presented. At the end, the structure of this document is briefly described.

This page was intentionally left blank

1.1 Industrial and Theoretical Framework

MCM - Mário da Costa Martins & Filho Lda. is a Portuguese company founded in 1897, and in 2009 was awarded by their industrial Success and Excellency with the *PME Excelência* prize granted by the *Instituto de Apoio às Pequenas e Médias Empresas e à Inovação* (IAPMEI). MCM's pioneering activity was focused on the development and manufacturing of orthoses. Meanwhile, most of their industrial activity has been centred in the manufacturing of metallic parts, mainly for the automotive industry.

In 2010, MCM has strategically decided to diversify their industrial activities and develop a new area of activity. They (re-)started the area of development and manufacturing of medical products, such as orthopaedic and trauma implants, and other dental and medical devices. An investment of around 800 000 € has been made, both in new facilities and in the modernization and technological re-equipment of the new business unit. Among others, it can be highlighted the acquisition of several very advanced CNC machines, some of them unique in Iberian Peninsula, as well as hardware and software for aiding the geometrical modelling of medical prosthesis and devices.

Following the MCM's strategy to be the leading manufacturer of medical products in a customer-oriented approach in the Portuguese market, in order to establish a research activity centred in the design, optimization and manufacturing of customized orthopaedic and trauma implants, a partnership was established with the Department of Mechanical Engineering of the University of Minho. Taking into account the goals of the Company, two areas of knowledge were identified as being of paramount importance and for which MCM was scarce, namely:

- The 3D geometrical reconstruction, modelling and finite element meshing from medical imaging, taking into account both the limitations of medical imaging techniques and the specificities of the target anatomical structures;

- The geometrical and functional optimization of the implants by finite element analysis, in order to customize and improve the implant's life-expectancy.

Therefore, the present work aims to establish a bridge between the industrial requirements of the company MCM and the existing scientific knowledge in the University of Minho. The creation of such operational competences is considered fundamental for fulfilling

the company's long term objective of being the leading manufacturer of customized orthopaedic and trauma implants in Portugal.

One of the major technological breakthroughs in modern medicine is the development and introduction of medical imaging devices, which have revolutionized our understanding of the Human body (Gunderman, 2006). Medical imaging techniques, such as X-Ray Computer Tomography (CT) or Magnetic Resonance Imaging (MRI), allow the creation of a virtual 3D medical modelling of internal organs and/or musculo-skeletal systems. The development of such 3D models makes possible the virtual representation of the internal structures of the human body (Suetens, 2009; Preim and Bartz, 2007; Young et al., 2008). The association of medical image-based techniques and the most advanced computer-aided-engineering (CAE) design techniques, offer the means for designing, optimize and manufacture customized orthopaedic and/or trauma implants (Heissler et al., 1998; Lin et al., 2005; Shuxian et al., 2005; He et al., 2006; Jiankang et al., 2006; Jun and Choi, 2010).

An implant is a medical device manufactured to replace a missing biological hard-structure, support a damaged biological structure, or enhance an existing biological structure. To ensure the life-success of these implantable devices, several extremely important features need to be taken into account, namely: implant surface finishing that might be coated by a bioactive material such as hydroxyapatite and roughness to improve implant biocompatibility (International and Davis, 2003); and the patient's anatomical structure and the geometrical adaptation of the implant to the patient particularities and specificities (Singare et al., 2004a, 2005; Schmutz et al., 2011). For instance, in a review carried by Carr and Goswami (2009) on knee implants, it was found that, today, there are 150 different knee implants. These authors concluded that this number is expected to grow as Total Knee Replacement evolves towards the complete customization of each prosthesis, in order to improve and increase the implant's life expectancy.

Individual custom-made prosthesis can, undeniably, improve the success of an orthopaedic replacement when compared with standard prostheses. Nowadays, it is well accepted that the use of customized or personalized prostheses can be very beneficial for patients, namely by: decreasing the post-operative pains and suffering (Flecher et al., 2010); reducing the risk of infections and rejection (Chang et al., 1999); provide better aesthetic results (Singare et al., 2005); reducing the time of surgery and speed-up

the recovery after surgery (Slover et al., 2012). However, a deep understand and collaboration between medical requirements, data treatment, designing and optimization and manufacturing is mandatory. Our knowledge on bio-structures, such as soft-tissues and musculo-skeletal systems and bone remodelling, plays a paramount role in all the process of designing and optimization of customized orthopaedic and trauma implants (He et al., 2006; Jun, 2011).

The image data acquired using CT or MRI is a set of transverse 2D image slices. The information is acquired indiscriminately from the patient and, depending on the quality of the image data, several numerical techniques such as image processing, segmentation, smoothing and sampling may be needed to identify the Regions of Interest (ROI). Once the object(s) of interest have been identified, the 3D voxel/pixel data can be re-worked to allow their geometrical reconstruction (to be used in the design and optimization of the customized implants), or to produce a finite element model for further biomechanical analysis. Therefore, in the implant development pipeline, several aspects shall be taken into account, namely: the medical imaging techniques used to acquire the image data; the geometrical reconstruction from 3D voxelized data; the identification of anatomical features; the numerical simulation and numerical optimization of the implant's geometry; determination of the strain and stress fields in the vicinity of the implant and its relation with bone remodelling process in order to decrease the probability of prosthesis loosening phenomena; material selection; and, finally, the manufacturing process by using an adequate set of manufacturing techniques (Lorensen and Cline, 1987; Chang et al., 1999; Singare et al., 2004b, 2005; Schmutz et al., 2011). In summary, in implant customization from medical image data, there are several major steps that need to be followed in a sequential way, namely:

- Medical Image Processing and Artifact Removal;
- Accurate Image Segmentation and 3D Surface Model Generation;
- Geometrical Customization based on CAD and CAE techniques;
- FEA Optimization of the Implant Geometry;
- Manufacturing using CAD-CAM Technologies.

The first fundamental step towards a customized implant is the creation of an accurate and reliable 3D geometrical model of the target biological geometry. The image reconstruction process from CT image data is known to have a very high accuracy, and almost no geometrical magnification (Hildebolt et al., 1990). However, and despite the numerous advantages, all imaging techniques are both physical and technically limited (Prokop and Galanski, 2011). Their spatial limitations restrict the accuracy and the reliability of the 3D geometrical models generated from the image data. All imaging systems act as low-pass filters and are unable to preserve sharp transitions between different anatomical structures. Therefore, object boundaries become blurred on the reconstructed image, which originates uncertainties on the accurate definition of the domain boundary. In addition, during the acquisition phase, image artifacts may also be produced. Image actifacts may difficult the interpretation of the image data, and additional image processing steps may be needed to eliminate them.

Other possible sources of domain inaccuracies are the image processing and segmentation operations applied to the image data. Therefore, the techniques employed must be chosen carefully to avoid the deterioration of the underlying information. For instance, image de-noising with linear filter in known to produce edge bias, and therefore to change the geometrical information contained in the image (Bouma et al., 2005). In addition, image segmentation is known to be highly user-dependent, especially on the degree of expertise of the Human user (Adams and Bischof, 1994). In the presence of ambiguous pixels, an inter and inter-observer variability ranging from 5 to 10% is very likely to occur, even when the segmentations are performed by experts (Landman et al., 2010).

Image segmentation is fundamental to define the voxels that belong to the ROI, from which a 3D representation of the object can recovered. 3D surface meshing from volumetric image data is a very valuable tool, not only for the visualization of the anatomy of complex anatomical structures, but also to create biomechanical models of living structures (Lorensen and Cline, 1987; Sullivan et al., 2000). In surface meshing, geometrically simpler primitives, such as triangles and rectangles, are used to approximate the original surface of the target object. Techniques such as the Marching Cubes are often used to generate surface meshes from the segmented data (Lorensen and Cline, 1987). However, surface meshing from voxelized data is commonly affected by staircase artifacts that do not

represent the natural anatomy of the structures (Sullivan et al., 2000; Drapikowski, 2008), and are often associated with the production of large meshes with very low quality. The surface meshes need further post-processing to regularize (smoothing) the triangulation, and reduces the number of geometrical primitives used (Owen, 1998). For medical applications, requirements such as accuracy, volume preservation, and conservation of distances between different anatomical structures are mandatory to obtain reliable clinical data (Bade et al., 2006).

The inadequate image processing, image segmentation and surface meshing are thought to be responsible for the great majority of the domain inaccuracies in the 3D model generation pipeline (Wang et al., 2009). The understanding of the geometrical limitations imposed by the image acquisition process, the image processing, and segmentation processes, is important to quantify the geometrical inaccuracies and their practical implications during the implant modelling phase.

The process of custom implant modelling depends on the type of implant, and the target geometry. Nevertheless, there are some modelling steps that are common to all custom implants. The first step is the definition of a suitable global anatomical reference frame, which may be independent from the global frame used to acquire the image data. The global anatomical frame may be defined through the identification of specific anatomical features, such as axes and anatomical landmarks, of the target ROI. The global frame is important to guarantee reliability and accuracy on the subsequent steps. Next, other anatomical features may be needed depending on the type of implant. The definition of auxiliary frames, measurements, and extraction of profiles along the three anatomical planes are often used during custom implant modelling. The minimization of geometrical inaccuracies is paramount to guarantee the adaptation of the implant to the individual needs of each patient during the modelling phase, because it allows the accurate definition of all anatomical features during the modelling phase. Surface mesh generation also plays a major role in the Finite Element (FE) mesh generation process. Surface meshes can be used as structural shell elements, or as an input to a volumetric FE mesh generator (Owen, 1998), and there are many FE mesh generation software's that make use of the Marching Cubes or the Delaunay criterion to define the surface mesh nodes to initiate the volume meshing process. Surface meshes are extremely important in FE simulations, since the quality of the geometrical approximation may affect the accuracy of the numerical

solutions (Frey and George, 2013).

The ability to extract high-accurate 3D models from the medical image data acquired with the most recent medical imaging machines, together with some of the most advanced CAD-CAM-CAE technologies available, may allow the development of customized implant optimized to the target anatomy and function, especially in cases of patients' abnormal anatomical geometries (Lorensen and Cline, 1987; Levoy, 1988; Sathasivam et al., 1999; Starly et al., 2005; Harrysson et al., 2007; Bhatt, 2008; Botser et al., 2009; Schmutz et al., 2010). In this context, the development and mastering of the necessary procedures for the design, optimization and manufacturing of customized orthopaedic and trauma implants, considering all steps and data flow from medical information to the mechanical manufacturing, will make the company one of the leading orthopaedic manufacturers in Portugal, and would be a differentiating factor regarding other companies worldwide.

1.2 Motivation and Objectives

The main objectives of this thesis are the development of procedures for an accurate musculo-skeletal model extraction from medical image data, and the development of implants in a customizable and patient-oriented approach.

To achieve these goals, two main steps are mandatory: (i) developing protocols and expertise on computer assisted design of prostheses and orthodontics accessories and implantable devices; (ii) mastering the manipulation and enhancement of relevant medical information, provided by the different imaging techniques in order to extract the patient's specific anatomical features/diseases. The conjunction between appropriate image manipulation and enhancement, and a well-defined designing procedure it is fundamental to ensure that the designed implants will fit optimally to the individual patient.

This thesis will address the problematic of the creation of the necessary procedures for the accurate and reliable reconstruction of 3D anatomical patient-oriented models, and of the geometrical optimization of the implant to the patient model. The finite element meshing from 2D medical imaging techniques and further geometrical optimization will be stated as a complementary objective. The desired outcomes of this work are: to acquire the necessary knowledge for mastering the customization process, namely: image processing

and enhancement techniques, medical image segmentation techniques, Computer Aided Design and Finite Element Analysis and optimization.

1.3 Contributions

The main contributions of this thesis are:

- The development of a new pipeline for highly accurate bone segmentation from CT image data;
- The development of a new tibial nailing customization protocol, as well as a new tibial nailing system. The new tibial nailing system is designed to fit the specific needs of the target bone, taking into account the most relevant concepts regarding fracture management;
- The development of a new mandibular pre-operative planning protocol based on 3D medical imaging. From the analysis of the cranio-facial anatomy, a new mandibular endoprosthesis that accurately reconstructs the missing mandible and optimizes the aesthetic outcome is proposed;
- The development of a new Total Hip Replacement customization protocol and a new Total Hip Replacement system, which optimizes the medio-lateral fit of the implant along the proximal femur.

1.4 Structure of the Thesis

The thesis is organized in 8 chapters that cover concepts related with image acquisition, image segmentation, and implant customization. Three case studies are presented to validate the proposed customization pipeline, and the Finite Element Method is used to validate the geometry of each independent implant. The chapter organization is as follows:

In **Chapter 1**, the industrial and theoretical framework, the main objectives, and contributions are described.

In **Chapter 2**, the main technological aspects related with Computed Tomography imaging are reviewed. The main features affecting image quality obtained with this imaging technique are also addressed.

A survey of the main medical image segmentation techniques is presented in **Chapter 3**. In this survey the main advantages and disadvantages are also presented. In medical image segmentation accuracy is particularly important, therefore the main aspects related with segmentation validation are also review.

In **Chapter 4**, a new two-step image segmentation pipeline for accurate bone segmentation from CT imaging is proposed. The proposed segmentation protocol aims to handle segmentation variability and segmentation accuracy in different steps. In the first step image pre-segmentation provides an approximation to the target region of interest, whereas in a second step a segmentation pipeline is applied to obtain a sub-pixel accuracy model from the target geometry. The appropriate means for image de-noise, image restoration and image segmentation are described in this chapter.

In **Chapter 5**, a custom-made tibial nailing system is proposed. The segmentation pipeline is applied to extract an accurate 3D representation of the target tibia. Based on the 3D model a tibial nailing system is designed to optimize fracture treatment. The nailing system is validated for three types of fractures along the tibial shaft, namely a proximal, a medial and a distal fracture.

In **Chapter 6**, a protocol for custom mandibular reconstruction is addressed. In addition the protocol, two solutions for mandibular reconstruction are proposed: one based on the optimized harvesting of fibular segments; the other based on a custom-made mandibular endoprosthesis. The mandibular endoprosthesis is validated for three different chewing tasks.

In **Chapter 7**, the development of a tailor-made Total Hip Replacement is described. The acetabular and femoral components are designed considering the anatomical specificities of the patient. The hip stem is further validated considering the ISO 7206-6 and ASTM F 2996-13 standards, and a simplified muscular model of the hip.

Finally, in **Chapter 8**, the main conclusions and future developments for this work are presented.

Chapter 2

Computed Tomography Imaging

Computed Tomography is the gold-standard imaging procedure for three-dimensional orthopaedic assessment. In this chapter one presents a brief overview of the fundamental technological and physical principles related with Computed Tomography imaging, as well as the main aspects often linked with image quality.

This page was intentionally left blank

2.1 Introduction to Medical Imaging

One of the major breakthroughs in the history of modern medicine was the introduction of imaging devices in clinical practice. Medical Imaging systems have led to an unprecedented improvement on medical care and have revolutionized our understanding of Human anatomy and physiology (Gunderman, 2006). The usefulness and importance of imaging in medical practice is indubitable, and imaging tools have widespread across all medical fields. Today, medical images may range from simple planar projections that can be obtained by an X-ray intensifier to more advanced and recent technologies such as virtual reality (Birkfellner, 2011). Physicians make use of medical images not only as standard visualization and inspection procedures, but also as routine tools for complementary diagnosis, for advanced surgical planning and simulation, for intraoperative monitoring and guidance during surgical procedures, for radio-therapy, among other applications (Bushberg, 2002).

Radiology as a medical research field emerged over the course of the 20^{th} century, and is probably the speciality that has experienced the greatest progresses during this period (Gunderman, 2006). The potential to non-invasively visualize the Human body, alongside with the collection of valuable spatial information, explains the success of imaging in the medical field, and the efforts made to development new imaging modalities. The main features that differentiate the medical imaging techniques found today are the radiation used during the image acquisition process (such as high-energy electromagnetic radiation or radio-frequency pulses), and the field-of-view (FOV) that can be imaged. There are more standard imaging modalities that work at a macroscopic level (such as, Magnetic Resonance Imaging and Computed Tomography), and others that acquire images at a micro-structural or even at a cellular level (for instance, Magnetic Resonance Microscopy) (Mudry et al., 2003). In addition to the radiation type and FOV, imaging modalities also differ in the principles used to produce such visual information. Medical imaging systems may be classified as transmission imaging techniques, reflection imaging techniques, and emission imaging techniques. Magnetic Resonance Imaging (MRI), Positron Emission Tomography (PET), and Single Photon Emission Tomography (SPECT) are emission imaging techniques, because image formation is based on the emission of radio waves or gamma radiation to produce the image. Ultrasound imaging is an example of

reflection-based techniques, and it basically measures the time elapsed between ultrasound emission and the echoes triggered by the interfaces between tissues with different acoustic impedances. Transmission imaging techniques such as Computed Tomography (CT) and Conventional X-ray measure the attenuation of radiation as it passes through the body (Gunderman, 2006). Techniques such as CT, MRI, PET, SPECT, and Ultrasounds can be also classified as tomographic imaging techniques. In tomographic image acquisition, two-dimensional (2D) maps of thin sections (or slices) of the Human body are produced. Unlike Conventional X-ray where all structures are superimposed in a screen-film, these tomographic sections not only produce more accurate representations of tissues, but also allow for the 3D reconstruction of any imaged structure.

Medical images are 2D or 3D intensity maps that encode the physical properties or physiological behaviour of different biological structures, when subjected to certain types of electromagnetic radiation or mechanical excitation. The information encoded in these intensity images is highly dependent on the interactions that occur between biological tissues and the radiation used. The intensities recorded are only an indirect measurements of tissue properties. Hence, medical images provide only an approximation for both geometry and biological constitution. Different tissues possess different responses to certain types of radiation, and some imaging modalities are more suitable for imaging different anatomical structures than others. For instance, Computed Tomography and Magnetic Resonance Imaging are probably the most important and routinely used image-based diagnostic tools in actual medicine (Birkfellner, 2011). The first is based on the production of high-energy electromagnetic radiation that is heavily attenuated when it passes through dense structures, while remaining almost unchanged when interacting with soft tissues. The later relies on the net magnetization of tissue, and thus is very sensitive to tissue water content (Bushberg, 2002). CT is the primary choice for 3D characterization of hard anatomical structures, and thus more appropriate for both orthopaedic and dental purposes. The fast and continuous evolution of CT machines regarding to spatial resolution and acquisition times, have made this technique a very popular examination tool (Hsieh, 2009). Nevertheless, CT images are still affected by several shortcomings, such as noise, low contrast, motion artefacts, and partial volume effect. These artifacts may significantly impair the overall resolution of the CT scan, and consequently the reconstruction accuracy of any clinically relevant structure.

Computed Tomography is the gold-standard imaging modality for 3D assessment and reconstruction of the skeletal structures. In this chapter the main aspects related with the image acquisition principles, as well as the shortcomings related with this imaging technique, are reviewed. The remainder of this chapter is organized as follows: in section 2.2 a brief historical overview and current trends of CT imaging are presented; in section 2.3 the process of X-ray production is reviewed; in section 2.4 an overview of the main interaction processes between X-ray radiation and matter is presented; Image acquisition and reconstruction from the raw data are presented in section 2.5; the main features of Multi-slice CT are reviewed in section 2.6; in section 2.7 CT image quality aspects and the most clinically relevant image artifacts are described. Ultimately, in section 2.8 are presented some concluding remarks.

2.2 The Evolution of Computed Tomography Imaging

Computed Tomography was developed in the early 1970's and has completely revolutionized medical radiology. It was the first imaging modality that enabled physicians to obtain high-quality cross-sectional images of the internal structures of the Human body, and is currently the standard choice for imaging hard structures (Mudry et al., 2003).

The first CT machine was developed by *Sir Godfrey N. Hounsfield* in 1971 (Hounsfield, 1973). The work of *Hounsfield* was based on the mathematical and experimental methods developed a decade earlier by *A. M. Cormack*, and for this invention both scientists were awarded with the *Noble Prize for Physiology and Medicine* in 1979 (Suetens, 2009). The first CT scanner took approximately 5 minutes of scanning time and approximately 20 minutes of reconstruction time to produced images with 80×80 pixels of resolution (with 3.0 mm of in-plane resolution and 13.0 mm of slice thickness) of the Human brain (Fig. 2.1 (a)) (Mudry et al., 2003; Hsieh, 2009). Since the seminal work of Hounsfield tremendous advancements have been made in CT technology. CT scanners not only have experienced remarkable improvements in both spatial resolution and contrast resolution, but also in image acquisition times which greatly expanded the applicability of this technology. Fig. 2.1 depicts a comparison between the head scan performed with the first CT scanner (a) and an up-to-date scanner (b), where resolution and contrast improvements are clearly evident. The reduction on image acquisition times had a great impact in volume coverage,

and in some sense in the overall resolution of the exam (Hsieh, 2009).

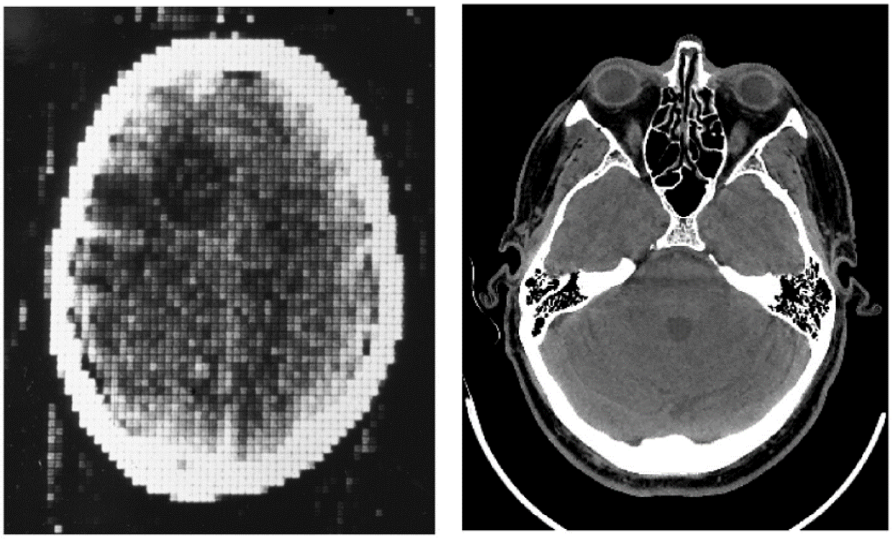

(a) (b)

Figure 2.1: Comparison between (a) an image obtained with the first CT scanner and (b) an image obtained with an up-to-date CT scanner (adapted from (Hsieh, 2009))

The technological improvements in both hardware and software have lead the way for the development of faster and more efficient CT scanners. One of the major breakthroughs was the introduction of the Multi-slice CT in the early 1990's. More recently, new applications such as the dual-energy CT for better tissue characterization, and Cardiac CT for dynamic 3D (or 4D) imaging of the heart have renewed the interest over this technology. For instance, $4D$ data acquisition in Cardiac CT is possible though the step-and-shoot approach, and a precise synchronization with the Electrocardiogram signal (Suetens, 2009). Other examples are the Cone-beam CT that is gradually expanding into the oral and maxillofacial areas, for both oral implant surgery planning and orthodontic treatment planning; and the Micro-CT for non-destructively image structures at the microscopic level, which has been used, for example, to obtain new insights into the trabecular organization of bone (Buzug, 2008).

2.3 X-ray Radiation Production

Images in CT are constructed from a large number of high-energy radiation transmission measurements through the patient, commonly referred as projection data. In order to

obtain meaningful representations of the imaged structures CT scanners must be capable of producing controlled X-ray radiation (Mudry et al., 2003). X-rays are electromagnetic waves consisting of high energy photons, whose energy $\tilde{E}$ (J) is expressed by:

$$\tilde{E} = \hbar f = \frac{\hbar \tilde{c}}{\lambda} \tag{2.1}$$

where f (Hz) is the frequency (or equivalently, the wavelength λ (m)), $\hbar = 6.626 \times 10^{-34}\ Js$ is the Planck's constant, and $\tilde{c} = 3.0 \times 10^{8}\ m/s$ is the speed of light in the vacuum (Mudry et al., 2003; Birkfellner, 2011). The X-ray frequency spectrum lies within the frequency range of 10^{18} to 10^{20} Hz, and consequently, the corresponding photon energies are on the order of the keV ($1\ eV = 1.602 \times 10^{19}\ J$) (Suetens, 2009). For medical applications, the X-ray energy typically lies within the range of 5 to 150 keV, with the energy being adjusted to the anatomical thickness, and the type of study being performed (Mudry et al., 2003). In the CT scanner the X-ray radiation is produced in the so-called *Bremsstrahlung* X-ray tube, which is basically constituted by a vacuum tube, a cathode for electron production and focusing, and a rotating anode (Fig. 2.2) (Iniewski, 2009).

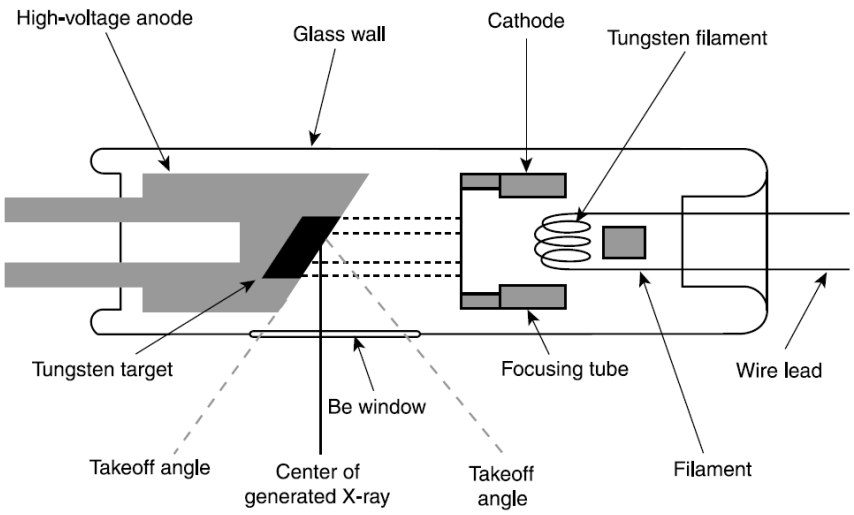

Figure 2.2: Schematic representation of the Bremsstrahlung X-ray (or simply the X-ray tube) used in the production of X-ray radiation for medical imaging purposes (Iniewski, 2009)

In the X-ray tube, radiation is produced through the thermal emission and acceleration of electrons from the cathode to the anode. If an electrical current is applied to the cathode, electrons may be released from the cathode by thermal excitation. These free

electrons are then focused and accelerated towards the anode by a high *tube potential* between the cathode and the anode. When the electrons provided with high kinetic energy come in contact with the anode material, two types of radiation may be produced: the *Bremsstrahlung* radiation and the *Characteristic* radiation. The *Bremsstrahlung* radiation is produced when the incoming electrons interact with the nucleus of a target atom. The partial loss of energy yields a continuous spectrum of low intensity X-rays photons. The electrons can also collide directly with the nucleus; in this case all electron energy is converted to Bremsstrahlung radiation and appears as the maximum energy value of the continuous radiation (Hsieh, 2009). The maximum value of the *Bremsstrahlung* radiation is bounded by the *tube potential*. For instance, for a tube potential $U = 100\ kV$ the maximum electron energy is 100 keV (Suetens, 2009). In contrast, the *Characteristic* radiation is produced when a high-speed electron interacts with inner orbital electrons of the target atom and is capable of removing it from the influence of the target atom's nucleus. The vacant electron orbital will be filled by a neighbouring electron, and an X-ray photon may be emitted. The result is the production of large numbers of X-rays at few discrete energy levels, phenomenon that is reflected in the peaks present in the X-ray spectrum (Iniewski, 2009; Birkfellner, 2011). The *Characteristic* radiation is also dependent on the anode material, which is chosen partially to produce X-rays with a desired energy (Mudry et al., 2003). Fig. 2.3 shows schematically both *Bremsstrahlung* radiation and *Characteristic radiation* and their correspondent energy spectrum.

X-ray production with X-ray tube is fairly inefficient, and most of the energy transmitted from the free electron current is loss in the form of heat (Iniewski, 2009). Generally, approximately 99% of the electrons kinetic energy is converted into heat, whereas only roughly 1% actually produces X-ray radiation. The energy of the radiation produced is dependent on the kinetic energy acquired by the emitted electrons. By increasing the tube potential, both intensity (the number of photons produced) and energy of the X-ray radiation can also be increased. The number of electrons emitted by the filament is also controlled by the current that flows through the cathode filament, and is frequently expressed in milli-Amperes per second (mAs) (Birkfellner, 2011). The voltage between the cathode and anode is expressed in kilovolts (kVp) and the current passing through the cathode (mAs), provide an estimate of the number of electrons being released from the filament by thermal excitation and the maximum energy transmitted to the

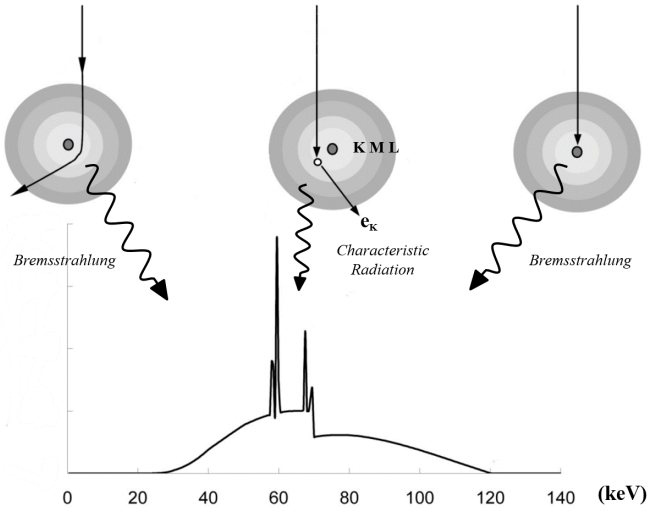

Figure 2.3: Electron interaction with the target material and x-ray tube energy spectrum (adapted from (Hsieh, 2009))

electrons by the X-ray tube. Keeping the filament current constant, an increase in the tube potential (kVp) is commonly associated with improved image quality: image noise is reduced, however patient dose is increased. Similarly, decreasing the number of electrons emitted by the filament, reduces patient dose but increases image noise (Gunderman, 2006).

The electrons emitted by the cathode are focused on a small spot of the anode in an attempt to produce an ideal point-shaped X-ray source. This focusing process causes the anode to be is constantly subjected to high thermal loads. Thermal loading also imposes a physical lower limit for the focal spot size, which limits the spatial resolution of the CT scan. The physical limit of the focal spot can be improved by using a rotating anode, where the anode material is constantly rotated and cooled, and making the anode with an angled surface (Fig. 2.2) (Mudry et al., 2003).

2.4 X-ray Interaction with Matter

Conventional X-ray radiographies are two-dimensional shadowgrams of the imaged anatomy. The brightness at each point is directly correlated with the intensity and amount of X-rays photons detected after the radiation being transmitted through the patient. Radiographic images are based on the physical principle that different parts of

the human body absorb different amounts of X-rays, and that tissue differentiation can be accomplished measuring those differences (Mudry et al., 2003). The X-ray photons may penetrate and remain unchanged, or may experience several phenomena divided into absorption or scattering effects (Iniewski, 2009). Three main types of interactions may occur, namely the *Photoelectric Effect*, the *Compton Effect*, and the *Coherent Scattering Effect*.

The *Photoelectric Effect* is the dominant interaction process when the photon energy is greater or equal to the binding energy to the atom (Bushberg, 2002). The complete absorption of the incident photons is a desirable effect for X-ray detection. This effect is important for the low contrast differentiation within the image, since most of the ionizing energy provided by the incident X-rays is dissipated locally (Iniewski, 2009; Hsieh, 2009). The *Compton scattering* effect occurs at high-energy levels and is the most important effect in radiology, as well as the predominant type of interaction between X-ray and soft tissue in the diagnostic energy range (Bushberg, 2002). Unlike the *Photoelectric Effect*, instead of being totally absorbed, the X-ray photon is deflected from its trajectory with only a partial energy loss. The Compton Effect provides little contrast information, thus almost all CT devices try to minimize its impact by either post-collimation or algorithm correction (Bushberg, 2002; Hsieh, 2009). The *Coherent Scattering* (or *Rayleigh scattering*) effect takes place mainly at low energy levels and happens when the incident photon interacts and excites the total atom. The photon is absorbed and then re-radiated with the same energy but in an arbitrary direction (Bushberg, 2002; Iniewski, 2009). This effect is quite detrimental for medical imaging because the path of the X-ray is significantly altered (Iniewski, 2009).

The net effect of these absorption and scattering interactions is that X-ray photons are attenuated when they pass through matter. The attenuation process follows an exponential law known as the *Beer-Lambert Law*, where the intensity of the outgoing beam B_{out} is correlated with the incoming beam B_{in} according to:

$$B_{out} = B_{in}e^{-\epsilon d} \tag{2.2}$$

where ϵ is the average linear attenuation coefficient, and d is the thickness of the absorber structure. This law is only applicable for homogeneous materials ($d\epsilon = 0$) and monochromatic (single energy) beams. The attenuation coefficient ϵ is the cumulative

result of these three absorption and scattering processes, $\epsilon = \epsilon_{photo} + \epsilon_{Compton} + \epsilon_{Coherent}$, and is a function of both photon energy and material properties (Suetens, 2009; Hsieh, 2009).

2.5 The CT Scanner and Image Acquisition Process

As mentioned previously, the fundamental goal of a CT scanner is to make extremely large and highly accurate X-ray transmission measurements of the patient in controlled and well-known geometry (Mudry et al., 2003). The CT scanner is built aiming the assurance of a correct relative positioning of the hardware at all times. This pre-requisite is mandatory for producing cross-sectional images that actually represent the X-ray attenuation properties of the body and guarantee the spatial relationships between different anatomical structures. The CT scanner is basically composed by a gantry, a patient table, a control console, and a computer. The main components of the gantry are the X-ray source, the X-ray beam collimator, the X-ray detector matrix, and the data acquisition system (Fig. 2.4) (Iniewski, 2009).

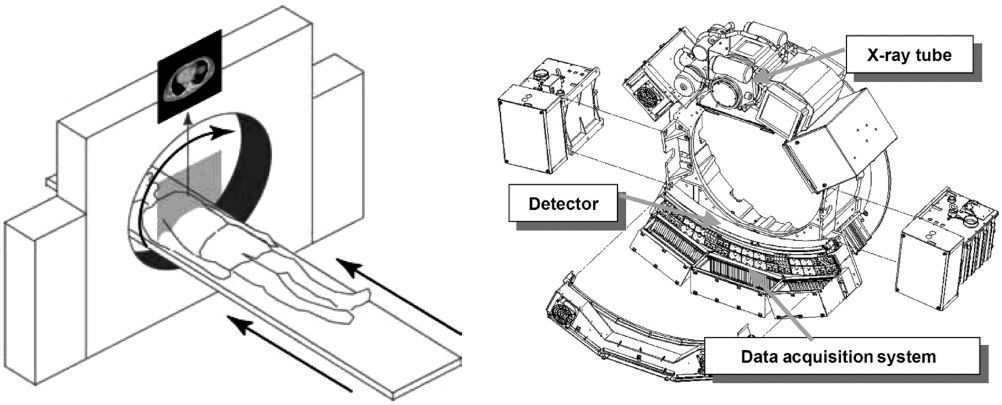

(a) (b)

Figure 2.4: In (a) the schematic representation of CT data acquisition process and in (b) the typical CT gantry (adapted from (Suetens, 2009; Iniewski, 2009))

During a CT scan a highly collimated X-ray beam is used to obtain the attenuation profile along a finite cross-section of the body (Fig. 2.4 (a)). The radiation collimation is important to shape the X-ray produced by the *Bremsstrahlung tube* into a thin fan-beam. The acquisition of the attenuation profile is then repeated at multiple discrete angular

positions (commonly each 1 degree or less), until a 180 degrees or 360 degrees rotation is completed (Iniewski, 2009; Birkfellner, 2011; Prokop and Galanski, 2011).

The acquisition of a single image may involve approximately 800 attenuation measurements taken at 1000 different projection angles, corresponding to a total of approximately 800000 transmission measurements (Bushberg, 2002). The X-ray beam attenuation is measured by a matrix of detectors located in the opposite side of the gantry. Both X-ray tube and Data Acquisition System (DAS) are mechanically coupled in order to maintain the exact spatial relationship between them at all times (Fig. 2.4 (b)). Each attenuation measurement quantifies the attenuation profile along a straight-line from the focal-spot in the X-ray tube and the detectors in DAS (Iniewski, 2009). The computation of the attenuation profile from the projection data acquired by the detectors is accomplished by relating the outgoing beam B_{out} with the incoming beam B_{in} and the distance d between the X-ray tube focal-spot and DAS according to eq. 2.2. The intensity of the un-attenuated X-ray beam (B_{in}) is commonly measured by a reference detector (Bushberg, 2002). Based on all measurements, the actual linear attenuation of each independent point within the FOV can be computed, and a 2D transversal image reconstructed along the beam projection plane (Suetens, 2009).

Currently, the most popular approach to image reconstruction from the projection data is by numerically approximating the inverse *Radon Transform*, proposed by *Johann Radon* in 1917 (Radon, 2005). The *Radon Transform* (R_d) may be expressed by:

$$R_d(\zeta,\theta) = \int_{-\infty}^{+\infty}\int_{-\infty}^{+\infty} F(x,y)\,\delta(x\cos\theta + y\sin\theta - \zeta)\,dxdy \tag{2.3}$$

where $F(x,y)$ denotes a 2D function in the x-y plane, $R(\zeta,\theta)$ denotes the projection data acquired at a given angular position θ, ζ is the detector coordinate, and δ the *Dirac* delta function (Zeng, 2010). The reconstruction approach based on the approximation to the inverse Radon Transform is commonly referred as *Backprojection*, and it is basically reversing the acquisition process. The standard *Backprojection* process leads to fairly blurred images, and to avoid this unwanted effect the sinogram is high-pass filtered prior to reconstruction. In the so-called *Filtered Backprojection*, the projection data is first convolved with a high-pass reconstruction kernel, and then projected back to 2D image matrix. Projection is accomplished by propagating each linear attenuation coefficient

ϵ along the acquisition path into the image matrix (Bushberg, 2002). The image is reconstructed by averaging the contribution of each individual ray. In Fig. 2.5 the image acquisition and reconstruction is simulated for the *Shepp-Logan phantom* (Fig. 2.5 (b)), proposed by *Larry Shepp* and *B. F. Logan* in 1974 (Shepp and Logan, 1974). Fig. 2.5 (b) shows the sinogram of the *Shepp-Logan phantom* phantom for a simulated acquisition over 360 degrees of rotation. In the subsequent images (Fig. 2.5 (*c*), (*d*), (*e*) and (*f*)) several reconstructions of the original data are depicted for different angular data, 0 degrees, 90 degrees, 180 degrees and 360 degrees, respectively. Fig. 2.5 (c) clearly illustrates the projection nature of the reconstruction process, where the projection view is stretched along the image plane.

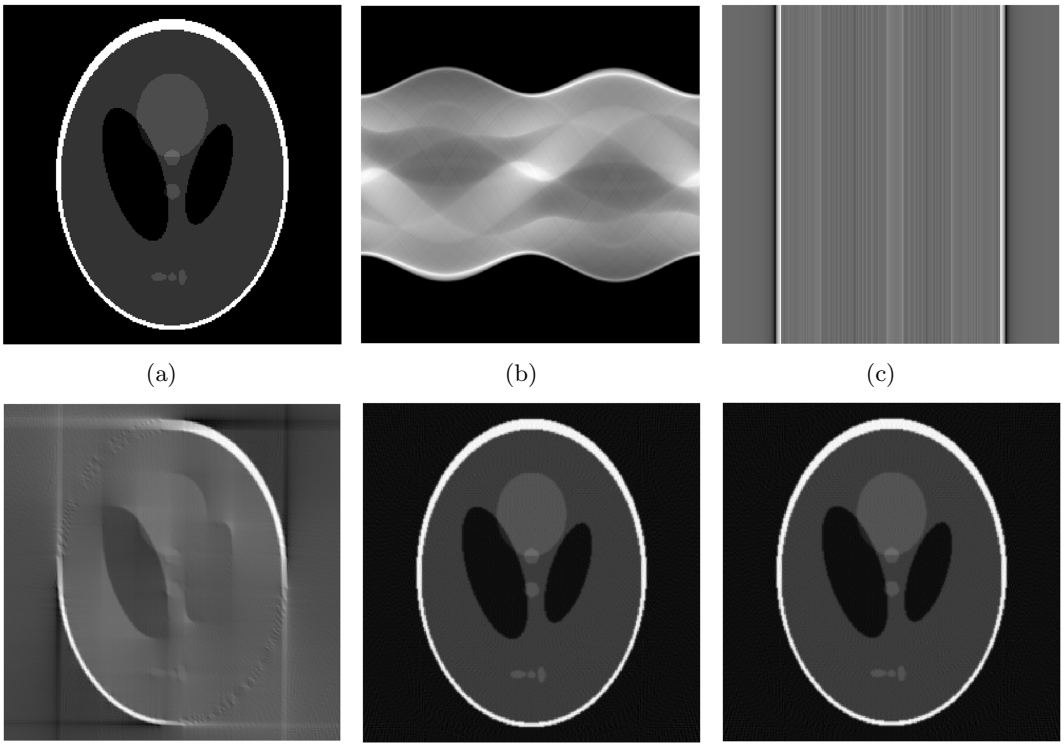

Figure 2.5: (a) the *Modified Shepp-Logan phantom*; (b) the sinogram obtained with the Radon Transform for an angular rotation of 360 degrees; (c) image reconstructed with a single projection view; (d) image reconstructed with projection views from 0 degrees to 90 degrees; (e) image reconstruction with projection views between 0 degrees and 180 degrees; and (f) image reconstruction for the full 360 degrees rotation data

Each pixel of the image represents the mean attenuation of an elementary volumetric element known as voxel, whose physical volume is defined by the in-plane resolution of

the 2D pixel matrix and the spacing between slices (Bushberg, 2002; Iniewski, 2009). In modern CT scanners, the images consist of 512×512 pixels and the grayscale represents the CT numbers expressed in *Hounsfield* units (HU). The typical CT numbers are defined by:

$$S_{CT}(HU) = \frac{\epsilon - \epsilon_{H_2O}}{\epsilon_{H_2O}} \times 1000 \tag{2.4}$$

where ϵ is once again the linear attenuation coefficient of the imaged tissue. With the HU scale as defined by eq. 2.4, air and water have a CT number of about -1000 HU and 0 HU, respectively. Bony structures do not have a unique CT number, because the ϵ of bone (as well as many other structures) depends on its composition and structure (whether if it is cortical or trabecular bone), as well as on the energy of the X-rays used in the imaging process. The HU values for different anatomical structures are shown in Fig. 2.6.

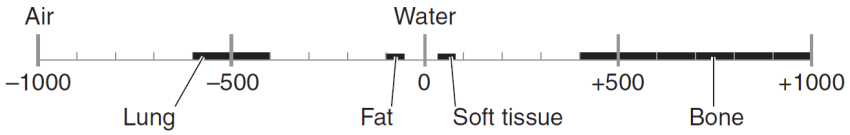

Bone	+400 → +1000
Soft tissue	+40 → +80
Water	0
Fat	−60 → −100
Lung	−400 → −600
Air	−1000

Figure 2.6: Hounsfield (HU) scale for different tissues (Lindon et al., 2010)

CT machines may acquire the projection data in different ways and depending on the scanning configuration, scanning motions, and detector arrangement. The CT machines are normally classified in terms of generations. Five generations of CT machines can be distinguished, and they reflect the evolution of the scanner over the years. The review of each generation, their advantages and disadvantages is beyond the scope of this document (the interested reader is referred to references Bushberg (2002) and Hsieh (2009)). One will only stress that the most successful configurations are the third and fourth generation configurations. Third and fourth generation have a scanning configuration similar to the one depicted in Fig. 2.4 (a), and both of them use a X-ray the fan beam geometry

for scanning purposes (Bushberg, 2002). Both types of scanners allow continuous data acquisition, simultaneously with continuous patient table movement. Hence, allowing helical and multi-slice acquisition, which was one of the major breakthroughs for obtaining faster acquisition times, better spatial resolution, shorter image reconstruction times, and true 3D imaging (Iniewski, 2009).

2.6 Helical CT and Multi-Slice CT

Initially, the acquisition process was characterized by a sequential start-stop-reversal motion, where the imaging apparatus had to be stopped and reversed for each single image acquired. The time consumed in the de-acceleration process of the gantry components was actually greater than the data acquisition time. The consequences of these inter-scan delays were poor temporal resolution and longer examination times. These limitations not only reduced the spectrum of applications of CT imaging, but also made the exams more prone to patient motion artifacts. The elimination of inter-scan delays was solved by the introduction of a low voltage slip-ring, which allowed the continuous rotation of all gantry elements. The slip-ring enables the transmission of electrical power to the rotating elements without fixed connections and thus completely eliminates inter-scan delays (Goldman, 2007a). In addition to the introduction of a continuous gantry rotation, a smooth translation movement was also added to facilitate continuous data acquisition. The association of continuous gantry rotation and the table translation gave birth to the so-called Spiral or Helical CT (Kalender et al., 1990; Toki, 1993).

Helical CT has the advantages of enabling shorter examination times. It also enables an actually continuous volume acquisition, which may avoid slice gaps and intersections (Birkfellner, 2011). Although very successful, the continuous single slice acquisition in Helical CT was extremely demanding for the X-ray source. With the Single-Slice CT (SSCT) scanners the reconstruction of long structures such as bones was literally impractical. This shortcoming led to the development of the Multi-detector spiral CT or Multi-slice CT (MSCT). The MSCT was introduced in the early 1990's and rapidly became the standard of CT imaging in medical practice (Fig. 2.7) (Goldman, 2008). MSCT systems take greater advantage of the produced X-rays, using a wider X-ray beam and using multiple rows of detectors that collect data from more than one slice at a time.

Modern scanners were introduced in 2005 and can acquire up to 64-slices simultaneously at a rotation time of approximately 0.2 seconds. MSCT scanners achieve even greater volume coverage in shorter time than Single-Slice CT scanners, and all data can be acquired in a single breath hold (Goldman, 2008; Hu, 1999). In addition, multi-slice acquisition greatly reduced the ratio between the in-plane and cross-plane resolution, allowing scans with an almost isotropic voxel size. The acquisition of thin slices have also the advantages of reducing or even eliminate partial volume effect and allow the production of high-quality off axis image reconstructions (Goldman, 2008).

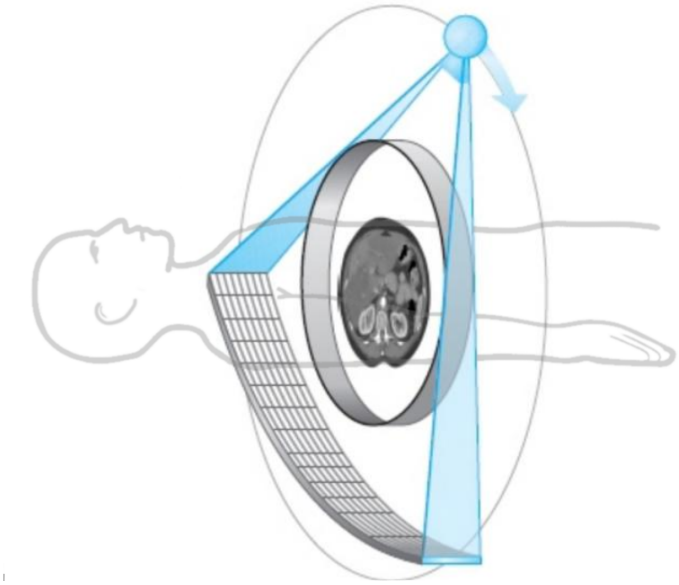

Figure 2.7: The principle of multi-slice Computed Tomography: the continuous X-ray source rotation and table translation, together with a multi-row DAS and a wider X-ray beam geometry, allow a real 3D image acquisition (adapted from (Prokop and Galanski, 2011))

The principles used in MSCT for image reconstruction are similar to the ones described in section 2.5, however the projection data is no longer in a single well-defined transverse plane. The projection data necessary for image reconstruction is obtained by interpolation from the existing raw data into user-defined transverse planes. Thus, in MSCT reconstruction images can be reconstructed at arbitrary positions, within the scanned volume (Prokop and Galanski, 2011). Image reconstruction is completely unrelated with table feed, and the spacing between the reconstructed sections is often referred as the reconstruction interval or reconstruction spacing (Mahesh, 2009).

2.7 Image Quality

The images acquired by a CT machine have low spatial resolution when compared with conventional radiographs; however they possess better contrast resolution. The fundamental measure of spatial resolution in CT imaging is the Modulation Transfer Function (MTF) of the system (Bushberg, 2002). Moreover, image quality does not resume to spatial resolution, and other aspects are importance for the overall perceivable image quality. Image quality in CT imaging, as well as in all medical imaging techniques, depends on four basic factors: spatial resolution, image contrast, image noise, and the presence of artifacts (Goldman, 2007b).

2.7.1 Spatial Resolution

Spatial resolution in CT imaging is the ability to distinguish small, closely spaced objects on the image. The spatial resolution is often measured in two orthogonal directions, namely, the in-plane resolution (in the image plane) and the cross-plane resolution (or axial resolution). The in-plane resolution is mainly affected by system's MTF, but it can also be affected by the X-ray tube focal-spot size, the detector entrance width (or aperture), and the Field-of-View (FOV) sampling. The cross-plane resolution is mainly affected by the Slice Sensitivity Profile (SSP) (Hsieh, 2009).

The in-plane resolution of a CT scanner is often measured in of line-pairs per centimetre (lp/cm) or line-pairs per millimetre (lp/mm). In practice, the scanner frequency response degrades as the number of lp/cm increases. The MTF provides an objective measure of the spatial resolution of any imaging system. It quantifies the ratio between the output and input modulation, i.e., represents the loss in image contrast as a function of spatial frequency. The spatial frequency from which the MTF approaches to zero is called the limiting frequency (Mahesh, 2009; Dougherty, 2009).

In modern scanners, the limiting resolution (limiting frequency) is commonly in the range of 0.5 to 2.0 lp/mm, which yields a spatial resolution between 0.25 to 1.0 mm. In addition to the MTF, the in-plane resolution may also be affected by the supportable spatial resolution of the image matrix. The image matrix has commonly a fixed size of 512×512 pixels, and the pixel size is defined by the FOV to be reconstructed from the raw data. Performing image reconstruction for a smaller FOV will effectively increase

the image resolution (Hsieh, 2009). When not restricted by the limiting resolution of the scanner imposed by the MTF, high-resolution reconstructions with small pixel size are limited by the physical size of the detectors in the DAS matrix (Mahesh, 2009).

The cross-plane resolution if often associated with the slice sensitivity profile (SSP). The SSP describes the system response in the axial direction, and is mainly characterized by two quantities, the Full Width at Half Maximum (FWHM) and the Full Width at Tenth Maximum (FWTM) (Hsieh, 2009). A truly parallel section X-ray beam is never obtainable in practice due to the physical limitations imposed to the focal-spot size in the *Bremsstrahlung* X-ray tube. The X-ray beam diverges as it moves away from the source, and the areas outside the primary beam also receive radiation of less intensity. The existence of a penumbra implies that adjacent portions of the scanned object also contribute to the measured attenuation in the slice (Fig. 2.8 (a)). In practice, this contribution is quantified by the SSP, and is a function of distance to the centre of the section (Fig. 2.8 (b)). The FWHM of the SSP defines the effective section thickness, and is the most common measure of the spatial resolution along the patient axis. Nevertheless, a more rigorous measure of the width of the section profile is the FWTM. The FWTM indicates the width at which objects outside the section contribute to just 10% to the CT number (Prokop and Galanski, 2011).

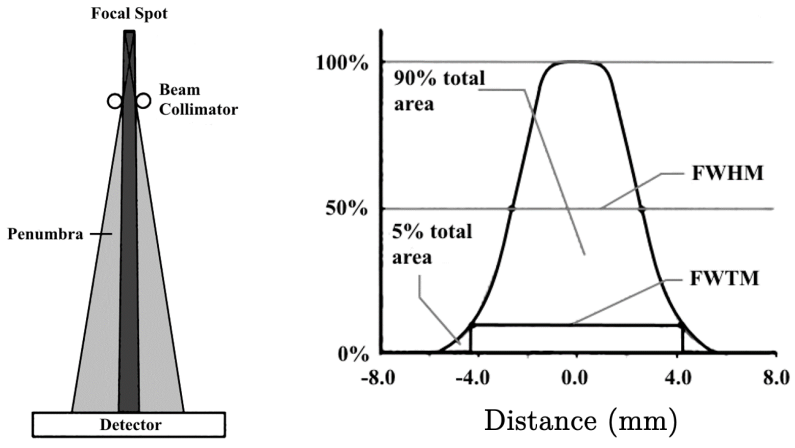

(a) (b)

Figure 2.8: The fan-beam geometry of the X-ray beam creates a penumbra area around the primary beam that influences the attenuation measured by the detector (a); this Slice Sensitivity Profile is commonly characterized by the FWHM and FWTM, and it varies with the slice thickness (adapted from (Prokop and Galanski, 2011))

Regarding the detector entrance width, the detector aperture refers to the width of each single detector in the DAS. In Single-slice CT the width of the detectors define the maximum admissible slice thickness, whereas the X-ray collimation defines the actual slice thickness. Increasing the X-ray collimator aperture will result not only in a higher dose administered to the patient but also in an increased radiation scattering (see section 2.7.4). Nevertheless, large slice thicknesses are known to achieving better contrast resolution, obtained at the cost of lower spatial resolution. On the contrary, thin slices improve cross-plane spatial resolution and reduce partial volume averaging, but are more prone to noise. The use of small detectors not only allows the acquisition of thinner slices but also increase the limiting frequency of the system (Bushberg, 2002). In MSCT the X-ray beam only defines volume coverage, and it is the detector collimation that mainly defines the cross-plane resolution (Hu, 1999).

2.7.2 Image Contrast

Contrast resolution is the ability that the imaging system has to reliably depict subtle attenuation differences between adjacent structures (Bushberg, 2002). Like in conventional radiography, contrast mainly depends on the X-ray attenuation by absorption or scattering in different types of tissues (Goldman, 2007b). It also depends on the spectrum of the X-ray tube, the X-ray detector non-linearity, and the gray level transformation after image formation (or reconstruction) (Suetens, 2009).

Image contrast is primarily influenced by the spectrum of the emitted X-rays. For instance, in breast imaging, low energy X-ray beams are used in order to enhance subtle differences between tissues, whereas in lung imaging high-energy X-ray radiation is used to suppress the difference between high density lesions and chest bones. It is also dependent on the attenuation coefficients, and the thickness of the different tissue layers along the radiation propagation plane (Suetens, 2009). The low-contrast detectability of an imaging system can be improved by increasing the slice thickness. With MSCT it is common to acquire thinner slices and then combine them into thicker slices in order to enhance the contrast resolution (Mahesh, 2009). Radiation scattering is another limiting factor to image contrast, since it produces a background intensity that reduces image contrast (Birkfellner, 2011). Another important factor that influences the contrast is the absorption efficiency of the detector. The greater the absorption efficiency, the greater the fraction of

the total radiation hitting the detector is absorbed, yielding a higher contrast in the final image (Suetens, 2009).

2.7.3 Image Noise

Image noise may arises from various sources, such as the statistical fluctuations of photon energy, the structural characteristics of the detectors, electrical noise from the hardware, and system noise from the signal processing chain. Noise is another fundamental limitation to image low-contrast resolution (Fig. 2.9 (a) and (b)). When the attenuation differences between adjacent tissues are in the order of magnitude of noise, they can no longer be distinguishable (Natali, 2003).

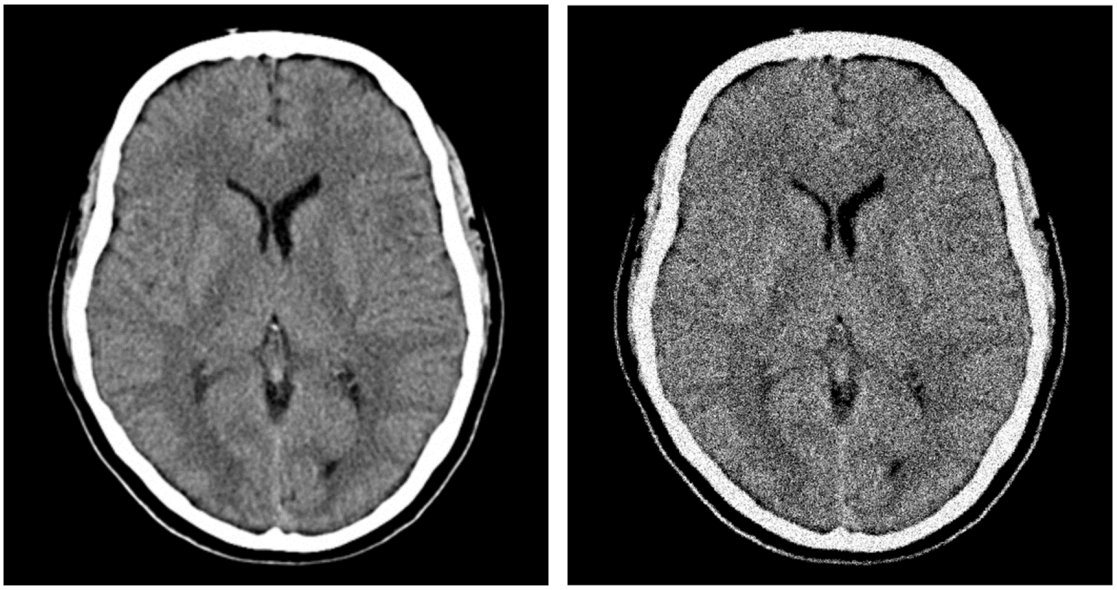

(a) (b)

Figure 2.9: In (a) the low-contrast resolution allows the differentiation between the white and grey matter in a noise-free CT image; in (b) the presence of image noise drastically reduces low-contrast resolution and the white and grey matter are barely indistinguishable

The most important source of noise is the photon fluctuation noise or quantum noise. Unlike conventional radiography, X-rays contribute to detector measurements and not to individual pixels. CT noise is thus associated with the number of X-rays contributing to each detector measurement. Quantum noise occurs due to random fluctuations on the number of photons reaching the detector (Goldman, 2007b). The number of photons striking each detector is affected by several acquisition parameters, such as the kVp, mAs,

and slice thickness (Mahesh, 2009). Image noise is also affected by the reconstruction filter in the Filtered Backprojection process. High-resolution filters enhance the visual aspect of image noise and so, normally, smooth reconstruction filters are preferred for clinical purposes (Suetens, 2009).

2.7.4 Image Artifacts

Image artifacts encountered in CT scans are dependent of the machine's architecture and design parts. Theoretically, an image artifact can be defined as any discrepancy between the reconstructed value in an image and the real attenuation value. In practice, artifacts are discrepancies that may difficult image interpretation (Hsieh, 2009).

Partial Volume Effect

The partial volume effect occurs when an object partially intrudes into the scanning plane (Hsieh, 2009; Mahesh, 2009). Partial volume effect is mainly caused by projection inter-view inconsistency and/or intra-view inconsistency. Fig. 2.10 (a) schematically illustrates these projection inconsistencies, where the partially intruded object is only detected when it is located far away from the X-ray source (Hsieh, 2009). Fig. 2.10 (b) and (c) show the difference in image reconstruction when the object is partially or fully intruded in the image plane.

Partial volume effect is also dependent on voxel anisotropy. Commonly, the voxel is larger in the z-axis than in the $x - y$ plane, and hence the section collimation contributes more to the partial volume effect than the FOV or pixel size. The evolution of the CT scanner to a multi-slice configuration enabled the collection of thinner slices and almost completely eliminated the partial volume effect (Bushberg, 2002). The partial volume effect is also different from partial volume averaging, which yields an incorrect quantification of the average linear attenuation coefficient at the interface of an object (Mahesh, 2009). Nevertheless, these two distinct phenomena are often regarded as the same partial volume effect (see for instance Prokop and Galanski (2011)).

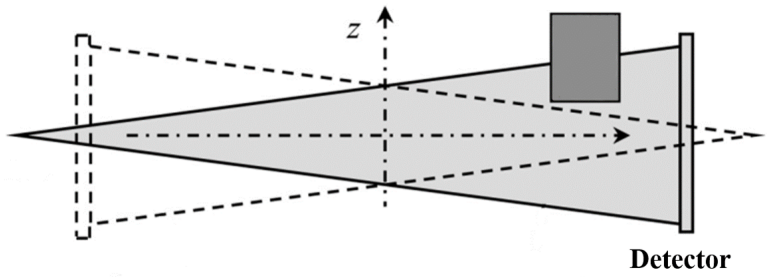

(a)

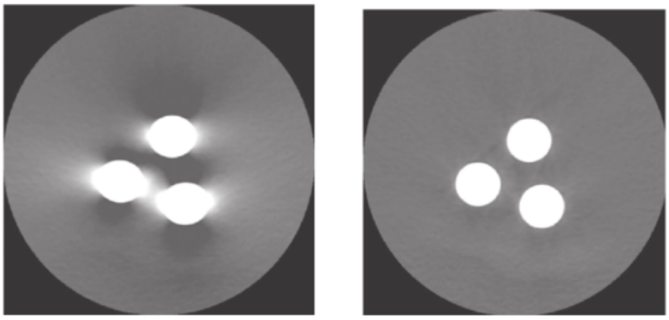

(b) (c)

Figure 2.10: In (a) the schematic representation of partial volume effect; in (b) the practical consequences of a high-density object partially intruded in the imaging plane during the acquisition process; and in (c) an image acquired without partial volume effect (adapted from (Hsieh, 2009; Mahesh, 2009))

Radiation Scattering

In section 2.4 it was stressed that the most common interaction process between X-ray photons and Human tissues is the Compton Effect. During this type of interaction the resulting low-energy photons deviate from the original path and the incident radiation is scattered in many directions. Radiation scattering causes the detected signal to deviate from the true measurement and may cause artifacts in the final image. Photons are randomly deflected from their original path, and are detected everywhere in the image (Hsieh, 2009). Radiation scattering produces a background intensity that reduces image contrast as well as its' Signal-to-Noise Ratio. This artifact can be effectively reduced by preventing scattered X-rays to reach the detector. Beam post-patient collimation has been successfully used to reduce radiation scattering by removing photons that significantly deviate from the fan-beam paths (Fig. 2.11) (Hsieh, 2009).

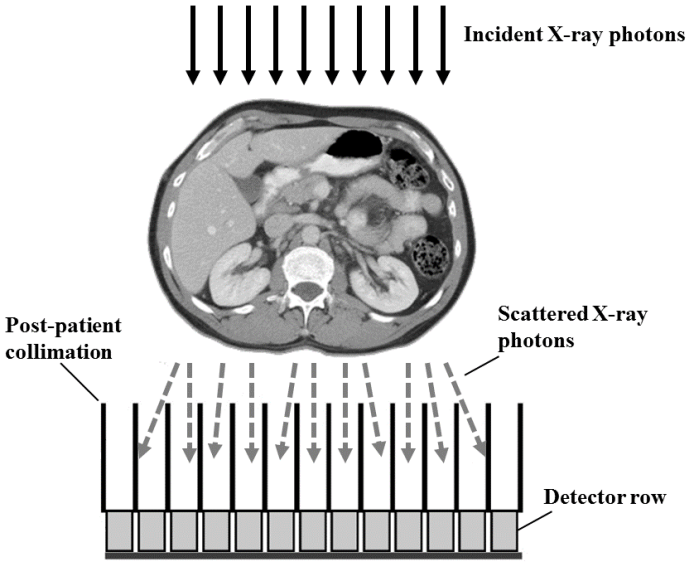

Figure 2.11: Schematic representation of radiation post-collimation for radiation scattering reduction during image acquisition

Motion Artifacts

The motion artifacts are caused by the voluntary or involuntary movement of the patient during image acquisition, and are the most common patient related artifacts in CT imaging (Mahesh, 2009). Small displacements are often related with involuntary motion and tend to cause locally inconsistent attenuation measurements, which appear as localized blurs, streaks or double contours in the reconstructed images (Suetens, 2009; Birkfellner, 2011). More gradual movement, such as cardiac motion, may also cause streak artifacts but will result primarily in a blurred representation of the moving parts (Suetens, 2009). In contrast, large displacements motion artifacts are commonly related with voluntary movements of the patient and can cause severe changes in image quality. Large displacements may cause image reconstruction inconsistencies and also the appearance of ghost images (Buzug, 2008). Stair-step artifacts along the axial direction due to respiratory motion are also very common during chest scans (Fig. 2.12) (Garcia, 2012).

Beam Hardening

The X-rays produced in the Bremsstrahlung tube possess a poly-chromatic spectrum (Fig. 2.3). As the X-ray beam passes through the FOV, low energy X-rays tend to be attenuated

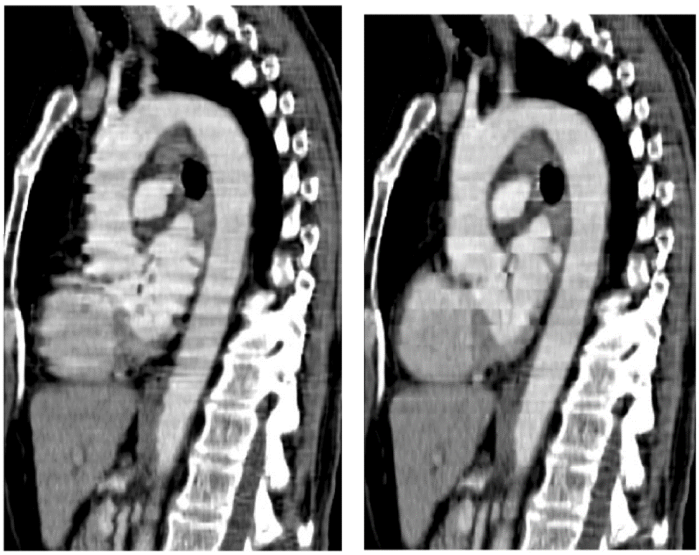

(a) (b)

Figure 2.12: In (a) motion artifacts caused by respiratory motion during image acquisition; in (b) enhanced image through motion artefact correction (Hsieh, 2009)

to a greater extent than high-energy ones, causing the energy spectrum of the beam to be distorted towards the higher energies. Beam hardening is a consequence of the increase in the average energy of the X-ray beam as it passes through tissue, and it causes tissues to appear darker than they should be ideally (Bushberg, 2002).

Projection inconsistency due to beam hardening is particularly cumbersome in the presence of high attenuation structures. The inconsistencies between individual projections may cause strikes spreading along the entire image to appear during image reconstruction. Due to the variety of materials that compose the Human body, beam hardening effect is very difficult to correct. Fig. 2.13 depicts the effect of soft tissue correction in a 35.0 cm water phantom, where the beam-hardening effect causes the centre of the phantom to appear darker than the surrounding tissue regardless of having the same attenuation coefficient as the surrounding material (Hsieh, 2009).

Metal Artifacts

Metal artifacts are caused by the presence of metallic objects inside the patient, such as metal prosthesis, pacemakers, clips, stents, dental fillings, or other metal objects outside the patient (Fig. 2.14) (Mahesh, 2009). The metallic objects can cause several artifacts at the same time, namely beam hardening, partial volume effect, under-range in the DAS,

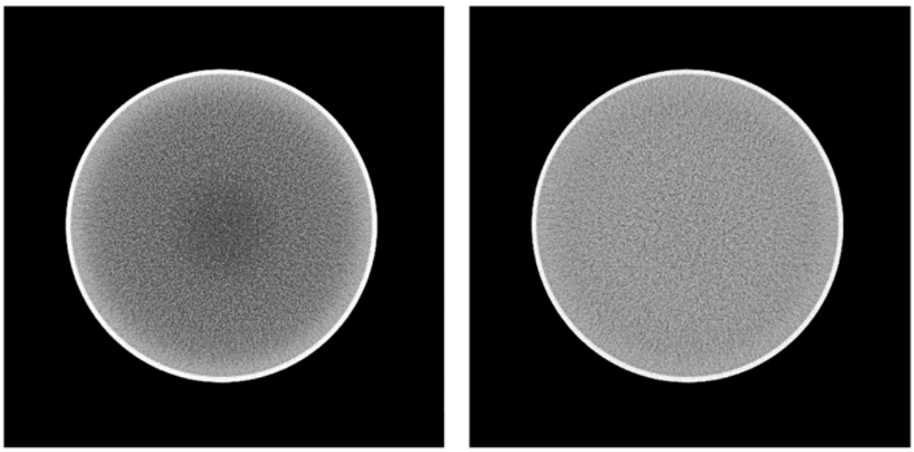

(a) (b)

Figure 2.13: Images reconstruction of a 35 cm water phantom (a) without water beam-hardening correction and (b) with water beam-hardening correction (Hsieh, 2009)

and dynamic range overflow in the reconstruction process. In the presence of a highly attenuating metal object the attenuation is so strong that the measured signal is dominated by electrical noise (photon starvation) (Hsieh, 2009). The beam hardening effect alongside with high amounts of radiation scattering induce an overall image deterioration, and dark lines radiate from sharp corners of the object due to the beam hardening effect (Birkfellner, 2011). In addition to the dark strips, bright strips are also observed in the presence of metallic objects. This is a direct consequence of the image reconstruction process that propagates high attenuation coefficient caused by these metallic objects along the image plane (Buzug, 2008).

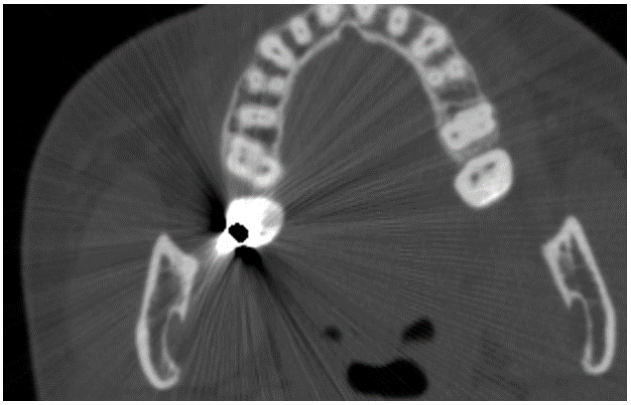

Figure 2.14: Example of metal artifacts caused by dental fillings (Birkfellner, 2011)

2.8 Summary

An overview of the most relevant aspects related with Computed Tomography imaging technology was presented in this chapter. Medical imaging has gained a paramount importance as a complementary tool for diagnosis in modern medical practice. Among all the existing modalities, Computed Tomography is probably the most successful medical imaging technique, and is particularly suitable for imaging high density structures such as the Human skeleton. Since its introduction in the early 1970's, Computed Tomography as experienced a tremendous evolution, which greatly improved the quality of the data collected and has broadened its range of applications. The most relevant breakthrough was the introduction of MSCT in the early 1990's. Alongside with real 3D data acquisition, MSCT greatly improved volume coverage, scanning times, and image quality. However, CT images are still afflicted by several image artifacts that may compromise the perceivable image quality. The major shortcoming to image quality is the system's resolution. Image resolution is affected by the whole chain from data acquisition to image reconstruction and can be quantified by the MTF. In addition, images can also be affected by low contrast, partial volume averaging, among other artifacts, which may difficult the correct interpretation of the data collected during the exam. In this sense, the image acquisition protocol should be carefully planned, in order to optimize the trade-off between image quality and patient radiation exposure.

Chapter 3

Medical Image Segmentation

This chapter covers medical image segmentation, segmentation validation and evaluation. The main algorithms for image segmentation are described, as well as their principal advantages and disadvantages. The validation of the segmentation outcomes is particularly important in medical applications. Therefore, at the end of the chapter the most relevant aspects related with segmentation evaluation are revisited.

This page was intentionally left blank

3.1 Introduction to Image Segmentation

Image segmentation aims to sub-divide the image into a set of large and meaningful regions, and is the first and probably the most important step in low-level vision. The goal of segmentation is to create a more compact and objective representation of the information contained in the image. Pixels are grouped together in order to emphasize important, interesting, or distinctive properties within the image (Forsyth and Ponce, 2012). Compactness implies a somewhat semantic representation of data, and this high-level understanding may be a key component in assisting and automating image-based radiological assessment (Preim and Bartz, 2007). Image segmentation algorithms have gain a significant role in numerous biomedical applications, such as:

- in tissue qualification and volume quantification (Shattuck et al., 2001; Lawrie and Abukmeil, 1998; Hu et al., 2001);
- a complementary tool for diagnosis (Taylor, 1995; Doi, 2007);
- in the demarcation of pathological tissues (Prastawa et al., 2004; Clark et al., 1998);
- in anatomical analysis and 3D visualization (Levine et al., 1999; Nicholson et al., 2006; Preim and Bartz, 2007);
- in treatment planning (Keall et al., 2005; Nishioka et al., 2002);
- in computer-assisted surgery (Grimson et al., 1997; Hoad and Martel, 2002; Xia et al., 2000);
- in multi-modality image registration (Yoo, 2004);
- and in image-based implant design (Harrysson et al., 2007; Singare et al., 2004b; Lee et al., 2002).

Medical image segmentation is particularly challenging due to the complexity and variability of the human anatomy and the shortcomings associated with imaging modalities (Gonzalez and Woods, 1992; Lakare and Kaufman, 2000; Ma et al., 2010). Image noise, partial volume effects, and motion artifacts may significantly influence the segmentation outcomes (Lakare and Kaufman, 2000). The prior knowledge about the imaging environment and the structures of interest may be important not only to tackle acquisition

variability, but also in the design of an efficient segmentation algorithm (Zaidi et al., 2006). The accuracy requirements of medical image segmentation are also more demanding, since segmentation must emphasise only the clinically relevant information. The segmentation must be both topologically consistent (define a closed volume) and correct, i.e., describe accurately the target geometry. The most suitable method to perform a given segmentation may vary, depending on the specific application, imaging modality, and acquisition related factors such as the presence of image artifacts (Lakare and Kaufman, 2000).

As seen in Chapter 2 during medical image acquisition, the information about all anatomical structures is indiscriminately obtained. Further image processing steps are needed to identify the regions of interest (ROI), and to separate them from the background (Lakare and Kaufman, 2000). In classical literature, image segmentation is the process of partitioning an image into several non-overlapping regions characterized by a certain homogeneity predicate, such as greyscale level or texture, and where adjacent regions have significantly different characteristics (Pal and Pal, 1993; Gonzalez and Woods, 1992; Jain et al., 1995). Formally, in image segmentation one aims to partition the entire image I in a set of n non-overlapping and maximally connected sub-regions $\{S_i\}$, such that each sub-region S_i satisfies some uniformity (homogeneity) predicate $H(S)$:

$$\bigcup_{i=1}^{n} S_i = I \tag{3.1a}$$

$$S_i \cap S_j = \emptyset, \quad \forall \ \ i,j \ \ i \neq j \tag{3.1b}$$

$$S_i, \quad i = 1,...,n \ \ are \ \ connected \tag{3.1c}$$

$$H(S_i) = TRUE, \quad \forall \ \ i \tag{3.1d}$$

$$H(S_i \cup S_j) = FALSE, \quad if \ \ i \neq j \ \ and \ \ S_i \ \ is \ \ adjacent \ \ to \ \ S_j \tag{3.1e}$$

where conditions 3.1 (a) and 3.1 (b) imply a hard partition of the image I into n regions, and where a membership function u_i can be defined for each sub-region i, where $u_i = 1$ if $(x, y) \in S_i$ and 0 otherwise, for all $i = 1, ..., n$ (Bankman, 2008; Gonzalez and Woods, 1992). In fact, this classical definition of segmentation may not be suitable to characterize all modern segmentation techniques. There are image segmentation techniques where a hard membership function may be replaced by a soft partition, where a degree of membership is attributed to each image pixel. However, this definition is still widely used to formally describe image segmentation (Bankman, 2008).

Segmentation methods are often classified as region-based and edge-based techniques. In region-based segmentation the image is divided into regions based on some $H(S)$ criteria, whereas in boundary-based techniques images are partitioned according to the detection of discontinuities (Gonzalez and Woods, 1992). They can also be classified as bottom-up and top-down approaches. Bottom-up approaches start with an over-segmented image and iteratively merge pixels that have similar properties into objects. On the contrary, top-down segmentation makes use of some prior knowledge about the object of interest to carry out image segmentation (Pawley, 2010). Despite the wide number of publications and extensive research in image segmentation, currently there is no single segmentation method that yields acceptable results for every medical image modality. Segmentation is frequently accomplished by applying several segmentation algorithms sequentially to gradually approximate the desired outcome, and methods that are designed specifically to a particular application often achieve a better performance than general purpose ones (Pham et al., 2000; Senthilkumaran and Rajesh, 2009; Luccheseyz and Mitray, 2001; Wirjadi, 2007).

The literature related with medical image segmentation is quite extensive, and it is by no means possible to succinctly cover all segmentation procedures proposed until now. Hence, in this chapter the most common and widely used image segmentation algorithms are reviewed. Some of the implementations used in this review can be found in the MATITK toolbox, a MATLAB wrapper for some Insights Toolkit (ITK) functions (Chu and Hamarneh, 2006; Ibanez et al., 2003). Alongside with the techniques description, the author also tries to present the main advantages and disadvantages for each technique. The remaining sections of this chapter are organized as follows: in section 3.2 segmentation by Thresholding is presented; in section 3.3 Region Growing techniques are described; in section 3.4 segmentation by Clustering is overviewed; in section 3.5 one reviews the main algorithms related with Graph-cut segmentation; in section 3.6 and 3.7 Level-set segmentation and Watershed Transform segmentation are described, respectively. In section 3.8 the concepts related with segmentation evaluation and validation are presented and analysed; and finally in section 3.9 the main conclusions about these topics are summarized.

3.2 Image Thresholding

Image segmentation by thresholding is probably the simplest and fastest segmentation technique available. Thresholding relies on the assumption that the different regions contained in a scene can be separated from the background solely based on their greyscale intensities. Generally, thresholding techniques can be either classified as global or local (adaptive) techniques (Pham et al., 2000). In global thresholding a single value is used to create a binary partition of the whole image data, where all pixels with intensities higher than a given value (threshold) are placed into one class, and all the other pixels into another:

$$S(x,y) = \begin{cases} 1, & \text{if I(x,y)} > \text{T} \\ 0, & \text{otherwise} \end{cases} \tag{3.2}$$

where $\min I(x,y) \leq T \leq \max I(x,y)$ (Bankman, 2008). The choice of the threshold value T is critical, and its selection is often interactively defined by the user, based on some prior knowledge about the region to be segmented. Numerous automatic threshold selection approaches have been proposed in the literature to eliminate this dependency (Sezgin et al., 2004; Wirjadi, 2007). Probably the most popular approach to optimal threshold selection is the *Otsu* Method (Otsu, 1975). The *Otsu* threshold is based on the assumption that the image's histogram is predominantly bimodal, and thus an optimal threshold can be found by minimizing the within-class variance or similarly by maximizing the between-class variance for all possible thresholds h:

$$T_{Otsu} = \max_{T} \sum_{h \leq T} p(h)(\mu_B - \mu)^2 + \sum_{h > T} p(h)(\mu_F - \mu)^2 \tag{3.3}$$

where $p(h)$ is the normalized histogram, μ is the average intensity of $I(x,y)$, μ_B is the average intensity of the background $(x,y)|I(x,y) \leq T$, and μ_F is the average intensity of the foreground $(x,y)|I(x,y) > T$. Single thresholding allows only a binary partition of the image, and the assumption of image bimodality may be insufficient or even incorrect for many practical applications. Many natural and medical images possess multiple regions with different intensity distributions; hence a single threshold may not be sufficient to segment all ROI (Demirkaya et al., 2009). Multi-modal image segmentation can be accomplished by applying multiple thresholds, where each region is characterized by an upper and lower intensity value, or applying spatially varying (or adaptive) thresholds

(Lakare and Kaufman, 2000). Adaptive thresholding takes into consideration the local characteristics of the image. Local thresholds can be determined by splitting the image into several sub-images, or by analysing the neighbourhood of each independent pixel (Bankman, 2008). In Fig. 3.1 (a) and (b) the complete CT volume partitioning into foreground and background is accomplished with a single Otsu threshold to achieve a complete image partitioning into foreground and background. Fig. 3.1 (c) and (d) a multimodal segmentation is computed by applying multiple thresholds to the foreground, in order to further divide it into hard and soft tissues.

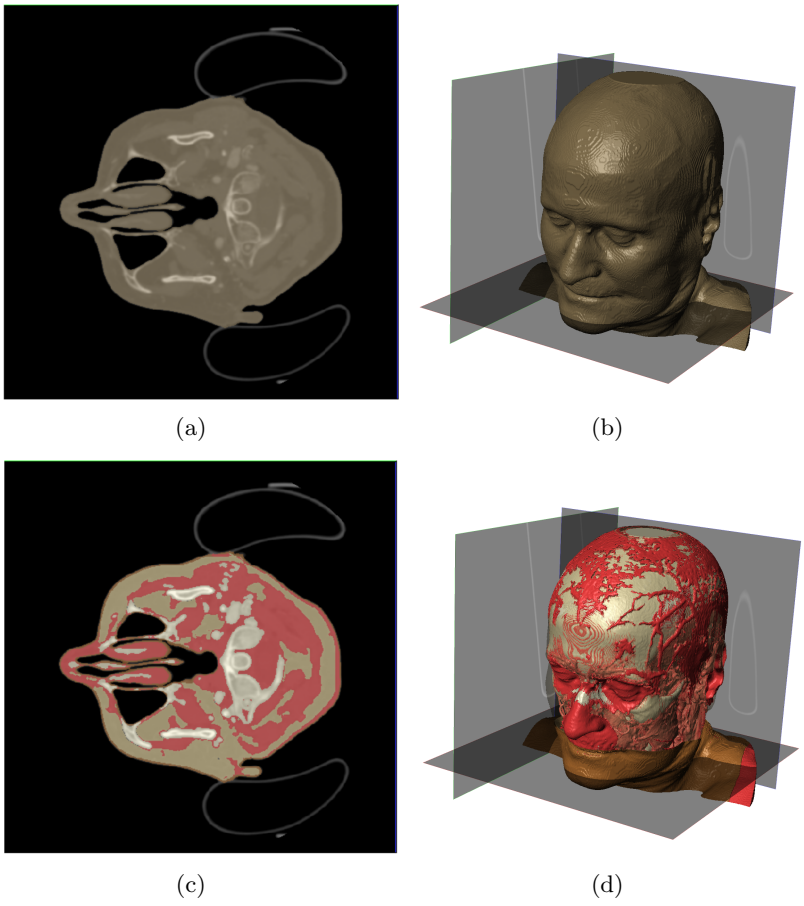

(a) (b)

(c) (d)

Figure 3.1: The panel (a) and (b) depict volume segmentation with a single threshold; (c) and (d) with multiple thresholds

In segmentation by (optimal) thresholding several shortcomings can be readily identified. The spatial context in which each grey-scale intensity value occurs is completely neglected, hence thresholding is very sensitive to noise (Pham et al., 2000). In addition, the performance of global thresholding is greatly compromised in the presence

of background in-homogeneities and poor image contrast. The segmentation results are also tightly coupled with threshold selection in global thresholding, and with threshold selection and neighbourhood size in adaptive thresholding. In many practical applications thresholding fails to produce closed contours, and additional morphological operations may be necessary to obtain a topologically consistent segmentation. Image over-segmentation and under-segmentation are also very common, with the creation of multiple disjoint regions of the same object or by merging objects that are close to each other. Although affected by a multitude of shortcomings, thresholding is still widely used in image segmentation as the initial step in an image segmentation pipeline (Dougherty, 2009).

3.3 Region Growing

Region Growing (RG) aims to segment regions of connected pixels that have similar properties, starting with some seed point(s) and then growing regions by adding neighbouring pixels that satisfy certain predefined similarity criteria (Dougherty, 2009). Seeded region growing was initially proposed by Adams and Bischof (1994), in an attempt to incorporate high-level information in the segmentation process. The starting seed points can be manually or automatically defined, and the algorithm terminates when no more neighbouring pixels satisfy the connecting criteria, and the region is no longer allowed to grow any further (Bankman, 2008).

The various approaches to RG mainly differ in the similarity criteria and the choice of the neighbourhood system. The inclusion criteria is intrinsically linked with the structure to be segmented and the type of image data available (Gonzalez and Woods, 1992). The most popular homogeneity criterion is by far the difference between candidate pixel(s) and the current average intensity value of the region:

$$H(S) = |I(x, y) - \mu_F| \leq c_1 \sigma_F \tag{3.4}$$

where μ_F defines the region average intensity, σ_F is the region standard deviation, and $c_1 \in \mathbb{R}^+$ defines the allowed deviation from the region average (Ibanez et al., 2003; Wirjadi, 2007). Eq. 3.4 states that if the difference $I(x, y) - \mu_F$ is less than a predefined value, the pixel is similar enough to be included in the region, if not it is set as an edge pixel (Bankman, 2008).

The main advantages of RG are that it is capable of correctly segment relatively homogeneous and spatially disperse regions, and it always generates connected regions (Bankman, 2008). However, the segmentation obtained by this technique is highly dependent on the correct selection of the initial seed points. Image noise and in-homogeneities can also lead to topological inconsistencies such as holes in the final segmentation. The partial volume effect and the inadequate choice of homogeneity criterion may also lead to both image over or under-segmentation (Pham et al., 2000; Pohle and Toennies, 2001; Dougherty, 2009). Edge leaking through object boundaries is also a very common problem associated with RG (Boykov and Funka-Lea, 2006).

Fig. 3.2 (a) and (d) shows the segmentation of the kidney parenchyma using standard RG algorithm with a too restrictive homogeneity criterion. Domain inconsistencies are evident. This can be alleviated by using a less restrictive $H(S)$ and constraining region growth to avoid domain leakage (Fig. 3.2 (b) and (e)). The addition of some notion of size and shape is thought to extend the applicability of RG. Modayur et al. (1997) proposed an adaptive RG protocol where $H(S)$ changes as the size of the region increases. From Fig. 3.2 (c) and (f) one can observe that the addition of the region size to the $H(S)$ avoids domain leakage, without additional spatial constraints. An automatic seed selection by thresholding was also proposed by Revol-Muller et al. (2002), whereas Rose et al. (2007) proposed a RG algorithm that uses a signed distance map to incorporate shape information and bias pixel inclusion. Nevertheless, none of these proposals completely eliminate the dependency on thresholds, and the similarity measures are still user-dependent.

3.4 Segmentation by Clustering

In segmentation by Clustering image pixels are sorted into groups, where the members show similar properties. Clustering are termed as unsupervised classification techniques, because pixel grouping is accomplished without any prior training stage or training data (Bankman, 2008). The need for training is overcome by iteratively grouping and characterizing the properties of each class, and by iteratively refining the classification with the available data (Pham et al., 2000). In this technique, image pixels are mapped

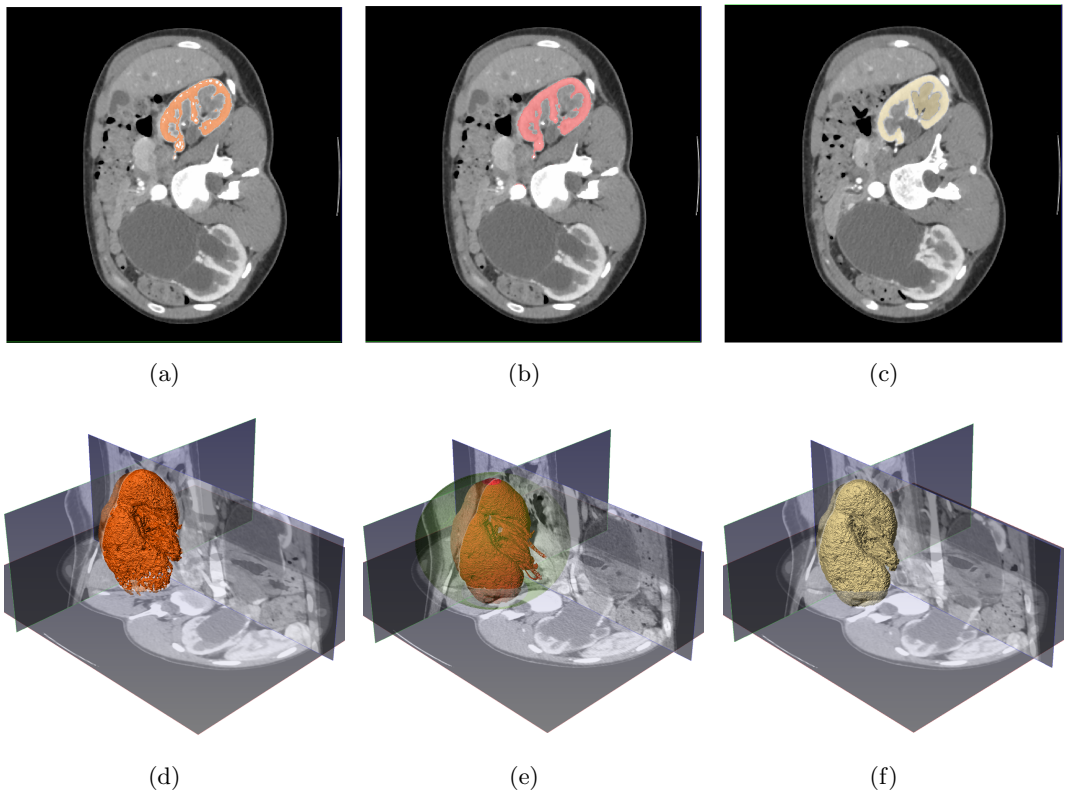

Figure 3.2: Segmentation of the kidney parenchyma through seeded region growing: in (a) and (d) standard algorithm with $c_1 = 1.95$; (b) and (e) standard procedure with $c_1 = 2.20$ and additional spatial constraint in shaded green; and (c) and (f) with size-based homogeneity change proposed by Modayur et al. (1997)

from the image space into an n-dimensional feature space, according to properties such as intensity, gradient, or any other similarity or dissimilarity measure (Demirkaya et al., 2009). Pixels are then assigned to one of the multiple predefined classes, in order to minimize the similarity measure of each individual pixel to the corresponding cluster centre. The process is iteratively repeated until no further improvements are achieved (Bankman, 2008). Next, the cluster data is mapped back onto the image space to obtain the final segmentation. Two Clustering techniques are widely used in medical imaging, namely K-means Clustering and Fuzzy C-means Clustering.

3.4.1 K-means Clustering

In K-means Clustering (KMC) the number of classes K in which the data should be partitioned is user defined (Lakare and Kaufman, 2000). Frequently, K-means Clustering

aims to minimize the within-cluster variation, i.e., the sum of the squared Euclidean distance between samples and the cluster centre (MacQueen et al., 1967). The within-class variation is often measured as:

$$S = \sum_{j=1}^{K} \sum_{i=1}^{N} \left\| v_i^j - \mu_j \right\|^2 \tag{3.5}$$

where N is the number of samples (pixels), K the number of clusters, v_i^j is the i^{th} sample of class j, with cluster centre μ_k, which is the mean intensity of $v_i^j \in \mu_j$ (Demirkaya et al., 2009). The algorithm iteratively computes the mean intensity of each cluster and segments the image by assigning each pixel to the class with the closest mean (Jain and Dubes, 1988; Pham et al., 2000). The result of K-means segmentation is always K disjoint and non-empty subsets, where each pixel only belongs to a single class (hard segmentation). In fact, and since the image is represented by a set of predefined clusters, the effect of K-means Clustering is simply the re-quantization of the whole grayscale histogram into K discrete levels (Forsyth and Ponce, 2012).

3.4.2 Fuzzy C-means Clustering

Fuzzy Clustering generalizes K-means and in contrast with the former it allows soft segmentations (Zadeh, 1965; Pham et al., 2000). The Fuzzy C-means Clustering (FCM) was first suggested by Dunn (1973) and Bezdek (1981), and instead of defining a clear (binary) classification of the data it attributes to each pixel a degree of membership for each class (Demirkaya et al., 2009). There is always a certain degree of uncertainty associated with expert's decisions. In Fuzzy C-means Clustering this uncertainty or fuzziness of the decision is modelled by the membership function, which represents similarities of objects regarding to imprecisely defined properties (Bankman, 2008). Segmentation is carried by minimizing the distance to the n-dimensional cluster centres in the feature space:

$$S = \sum_{i=1}^{N} \sum_{j=1}^{K} u_{ij}^m \left\| v_i - \mu_j \right\|^2 \tag{3.6}$$

where N is the number of samples, K the number of clusters, μ_j is the n-dimensional centre of each cluster, v_i is the i^{th} n-dimensional feature vector, and u_{ij} is the degree of membership of each pixel to each cluster. The parameter m specifies the classification fuzziness, and is usually set to 2.0 (Demirkaya et al., 2009). The membership matrix

$[u_{ij}] = U$ must satisfy the following conditions:

$$\sum_{j=1}^{K} u_{ij} = 1, \quad \forall \quad i = 1, ..., N \tag{3.7a}$$

$$0 < \sum_{i=1}^{N} u_{ij} < N, \quad \forall \quad j = 1, ..., K \tag{3.7b}$$

and quantifies the similarity between a pixel i and cluster j. The membership and cluster centres are updated according to the following relationships:

$$u_{ij}^{m} = \frac{1}{\sum_{k=1}^{K} \left(\frac{\| v_i - \mu_j \|}{\| v_i - \mu_k \|} \right)^{\frac{2}{m-1}}} \tag{3.8}$$

$$\mu_j = \frac{\sum_{i=1}^{N} u_{ij}^{m} v_i}{\sum_{i=1}^{N} u_{ij}^{m}} \tag{3.9}$$

In eq. 3.8 the degree of membership is inversely proportional to the distance to the cluster centre, whereas in eq. 3.9 the centroids are the mean of the data weighted by their membership and normalized to the total membership (Ahmed et al., 2002; Demirkaya et al., 2009).

The greatest difference between KMC and FCM (or between crisp and fuzzy sets) is that the former always produces a unique membership function, whereas the fuzzy set has an infinite number of membership functions, and other clusters (image partitions) can be generated from the initial ones (Bankman, 2008). These so-called soft segmentations model the partial volume effect, where multiple tissues contribute to a single measurement in the image matrix, and also preserve more information from the original image. In Fig. 3.3 (a), (b), (d) and (e) one can observe that FCM segments more accurately the vertebral bodies than KMC, and it also captures more information about the costal cartilage. The main disadvantages of clustering techniques are the need for an initial segmentation or a set of user-defined classes, and the inability to incorporate spatial information. The later makes clustering techniques very sensitive to image noise and to cluster initialization. In addition, the production of non-empty sets does not guarantees that the clusters are actually meaningful partitions of the image, and it is also not guaranteed that clustering converges to a global optimal solution (Pham et al., 2000; Demirkaya et al., 2009).

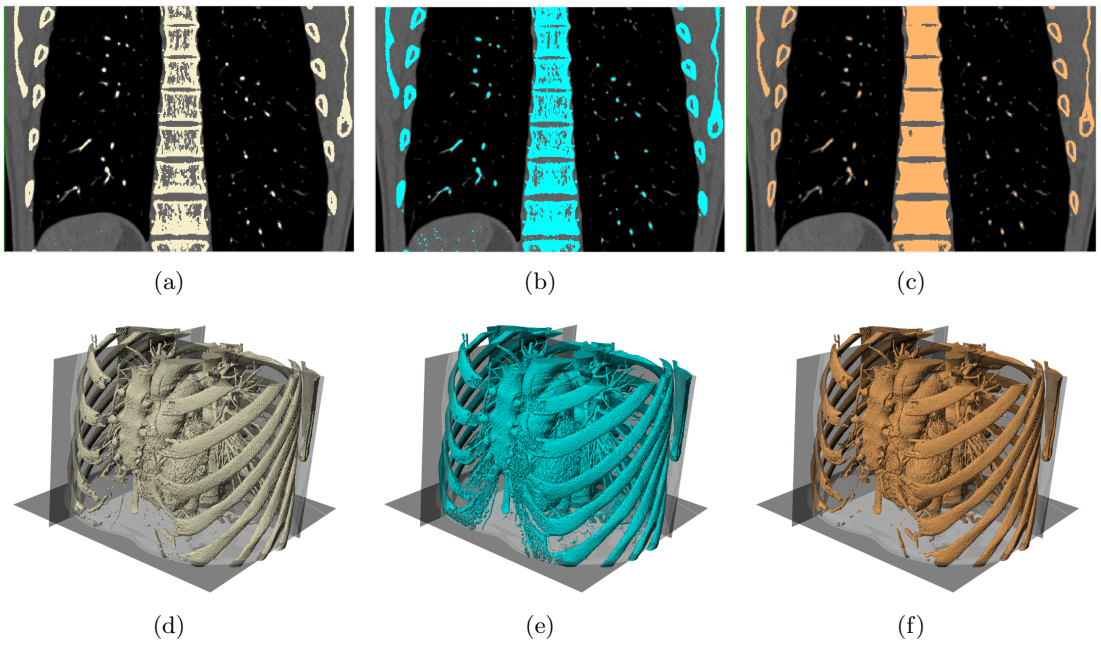

Figure 3.3: Segmentation of the thorax ribs: in (a) and (d) with K-means Clustering; in (b) and (e) with Fuzzy C-means Clustering; and (c) and (f) with Fuzzy C-means Clustering as proposed by Ahmed et al. (2002)

In an attempt to minimize these limitations, Ahmed et al. (2002) proposed a modified FCM technique to handle both noise and image inhomogeneities, where pixel labelling is affected by the distance between the pixel and its immediate neighbourhood to the cluster centres. Fig. 3.3 (c) and (f) shows that although the visible improvements in segmentation connectedness at the vertebral level, the algorithm fails to produce accurate results in the costal cartilage region. Other authors attempted to incorporate spatial information into the clustering process computing linearly-weighted sums of locally averaged images, or introducing the classification of the neighbouring pixels into the objective function (Szilagyi et al., 2003; Chuang et al., 2006).

3.5 Graph-Cut Segmentation

Clustering techniques deal with pixel similarity and how data can be summarized in a predefined set of clusters. The evaluation of intensity *per se* may lead to image over-segmentation, if the scene possesses regions with varying intensities. Graph segmentation addresses pixel similarity in a more local fashion, and segmentation is accomplished by minimizing the cost of the cut between each graph component.

Local similarity and global optimum cut between different components bias component connectedness, and thus a more high level representation of the image to be segmented (Forsyth and Ponce, 2012). Commonly, a graph $G = \{V, L\}$ is defined as a set of vertices $v_i \in V$ and edges $(v_i, v_j) \in L$ that connect adjacent vertices. In image segmentation the vertices $v_i \in V$ are defined as image pixel, and each element $(v_i, v_j) \in L$ is a weighted undirected edge connecting vertices v_i and v_j. The goal of graph segmentation is to find a set of n disjoint connected components $G = \{V_1 \cup ... \cup V_n, L_1 \cup ... \cup L_n\}$, where $L_i \cap L_j = \emptyset$ for $i \neq j$, and the similarity between vertices inside V_n is maximized and across different sets is minimized (Forsyth and Ponce, 2012; Shi and Malik, 2000). There are several proposals for Graph-Cut Segmentation in the literature, in this review one will restrict to the proposals of Shi and Malik (2000), Boykov et al. (2001), and Felzenszwalb and Huttenlocher (2004).

Standard Graph-Cut approaches favour the partitioning of the image into small groups of pixels, in order to minimize the sum of the edges that define the cut. To overcome this bias for small regions, Shi and Malik (2000)[1] suggested a normalized cut approach that computes the cut cost as a fraction of the total affinity within each group. Given two disjoint sub-sets (V_1, V_2), $V_1 \cup V_2 = V$, the normalized cut N_C can be defined by:

$$N_C = \frac{cut(V_1, V_2)}{assoc(V_1, V)} + \frac{cut(V_1, V_2)}{assoc(V_2, V)} \tag{3.10}$$

where $cut(V_1, V_2) = \sum_{i \in V_1, j \in V_2} w_{ij}$ defines the cost of the cut between V_1 and V_2, and $assoc(V_1, V) = \sum_{i \in V_1, k \in V} w_{ik}$ is the total connection from nodes in V_1 to all nodes in the graph. This score penalizes small cuts since the cut represents a great percentage of total connection between a small set to all nodes, and bias the partition of the image into smooth similar areas. For brightness images, the edge weight between connecting two nodes is defined by:

$$w_{ij} = e^{-\frac{\left\|I_i - I_j\right\|_2^2}{\sigma_I^2}} \begin{cases} e^{-\frac{\left\|\mathbf{x}_i - \mathbf{x}_j\right\|_2^2}{\sigma_{\mathrm{x}}^2}}, & if \quad \left\|\mathbf{x}_i - \mathbf{x}_j\right\|_2 < r \\ 0, & otherwise \end{cases} \tag{3.11}$$

where I_i is the image's intensity value of pixel i, $\mathbf{x}_i$ and $\mathbf{x}_j$ are the spatial location of nodes i and j in the image grid, σ_I is the intensity variance, σ_{x} is the spatial variance, and r is the neighbouring radius (Shi and Malik, 2000; Cour et al., 2004). In Fig. 3.4 (a) and (b)

[1]The source code can be found at *http://www.cis.upenn.edu/ jshi/software/*

show the segmentation of the mandible with 8 and 10 regions, respectively.

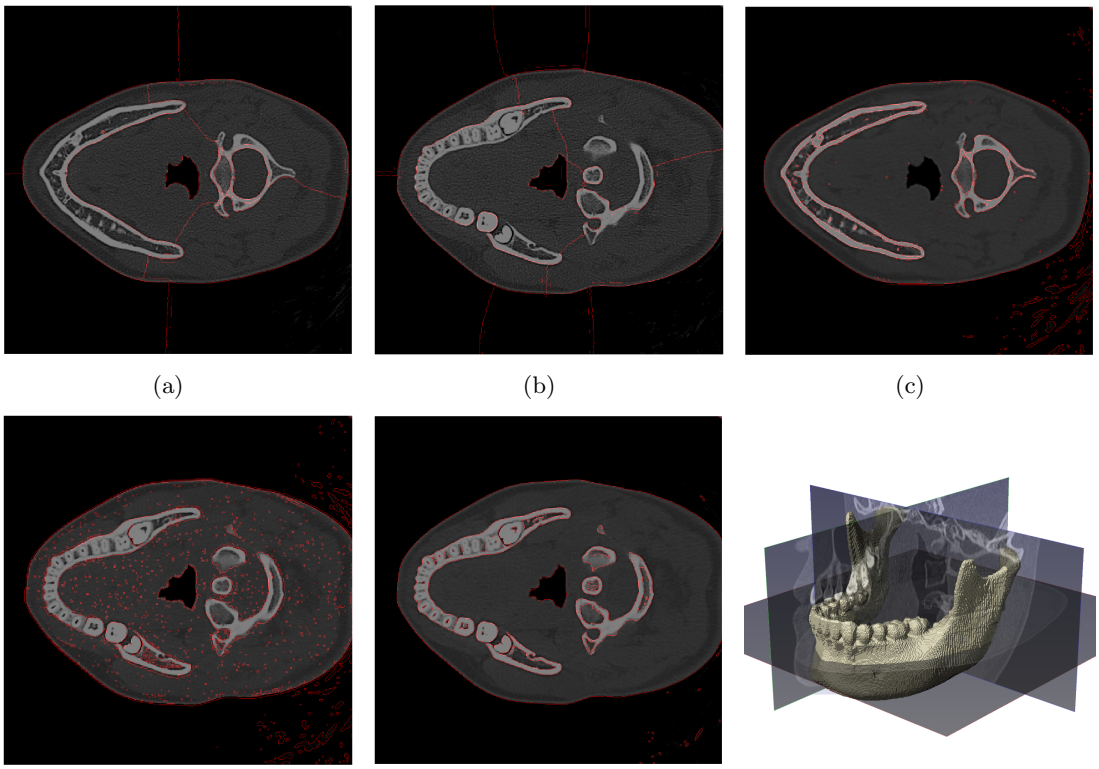

(a) (b) (c)

(d) (e) (f)

Figure 3.4: Mandible segmentation through Normalized Cuts in (a) and (b) according to (Shi and Malik, 2000); in (c) and (d) graph cut segmentation as proposed by Felzenszwalb and Huttenlocher (2004); (e) and (f) max-flow/min-cut segmentation proposed by Boykov et al. (2001)

Felzenszwalb and Huttenlocher (2004)[2] proposed an agglomerative algorithm for Graph-Cut segmentation. The algorithm starts with a number of components that is equal to the number of pixels, and then it clusters all pixels that have no clear evidence of the existence of a boundary D between them. The evidence of a boundary between adjacent components V_1 and V_2 is measured according to:

$$D(V_1, V_2) = \begin{cases} 1, & if \quad \mathrm{Dif}(V_1, V_2) > M_{\mathrm{int}}(V_1, V_2) \\ 0, & otherwise \end{cases} \tag{3.12}$$

where $M_{int}(V_1, V_2)$ is the minimum internal difference and is defined as:

$$M_{\mathrm{int}}(V_1, V_2) = \min(\mathrm{Int}(V_1) + T(V_1), \mathrm{Int}(V_2) + T(V_2)) \tag{3.13}$$

[2]The source code can be found at *http://cs.brown.edu/ pff/segment/*

where $\text{Int}(V_1) = \max_{e \in MST(V_1,E)} w_{ij}$ represents the internal difference and is defined as maximum weight of the Minimum Spanning Tree of component V_1 and $\text{Dif}(V_1, V_2) = \min_{v_i \in V_1, v_j \in V_2} w_{ij}$ is the minimum weight edge connecting two components $(V_1, V_2) \subset V$. The threshold $T(V) = \rho / |V|$ controls the evidence of a boundary between two adjacent components, where $|V|$ denotes the component size and ρ is a scaling parameter that sets the algorithm preferences for larger or smaller regions. The edge weight connecting adjacent nodes is defined as the absolute intensity difference $w_{ij} = |I_i - I_j|$ (Felzenszwalb and Huttenlocher, 2004). Fig. 3.4 (c) and (d) depict the segmentation of the mandible obtained with different values of T.

Boykov et al. (2001)[3] formulated Graph-Cut segmentation problem as the minimization of an energy functional of the form $S_E(S) = S_{E_{data}}(S) + S_{E_{smooth}}(S)$. In this functional, the data term $S_{E_{data}}(S)$ measures the agreement between image labelling and the observed intensities, whereas the smoothness term $S_{E_{smooth}}(S)$ favours a piecewise smooth labelling of adjacent pixels, and where $S \in \{1, ..., n\}$ defines the labelling assigned to each image pixel (Boykov et al., 2001). For image segmentation, the energy functional can be formalized by:

$$S_E(S) = c_2 \sum_{i \in V} H_i(S_i) + \sum_{(i,j) \in N} w_{ij} \delta_{i \neq j} \tag{3.14}$$

where $\delta_{i \neq j} = 1$ if $S_i \neq S_j$ and zero otherwise, N specifies the i^{th} pixel neighbourhood, and $c_2 \geq 0$ specifies the relative importance of the regional term (H_i) relatively to the boundary term (w_{ij}). Similarly to other graph-based segmentation approaches, w_{ij} measures pixel similarity (smoothness term) and it may be expressed by:

$$w_{ij} \propto \frac{1}{d_{ij}} e^{-\frac{(I_i - I_j)}{2\sigma_I^2}} \tag{3.15}$$

where d_{ij} is the distance between neighbouring pixels i and j (Boykov and Funka-Lea, 2006). The global optimization of the energy functional in eq. 3.14 can be addressed as finding the minimum cut on a two terminal graph, and can be efficiently computed through an optimized Max-flow/Min-cut algorithm (Boykov and Kolmogorov, 2004; Kolmogorov and Zabin, 2004). For feature extraction from a given scene an initial labelling is required, hence Max-flow/Min-cut graph image segmentation is performed over set of pre-defined

[3]The source code can be found at *http://vision.csd.uwo.ca/code/*

classes. For instance, in a foreground-background segmentation, the Max-flow/Min-cut approach starts with all pixels labelled as foreground, background, or unknown, and models for both foreground and background are computed from a set of user-defined nodes:

$$H(V_1) = -\ln P(I_i|V_1) \tag{3.16a}$$

$$H(V_2) = -\ln P(I_i|V_2) \tag{3.16b}$$

Eq. 3.16 formalizes the regional terms of the functional equation 3.14. Image partitioning is accomplished by finding the minimum capacity links between the source and the sink nodes (Fig. 3.4 (e)). The energy functional in eq. 3.14 is minimized by computing the minimum cut that bisects the source from the sink of the graph (Forsyth and Ponce, 2012).

One of the main problems associated with Normalized Cuts is that it is biased to produce segmentations where the regions have similar areas. This leads to very unnatural partitioning of the image. In Fig. 3.4 (a) and (b) the regions obtained with the graph approach proposed by Shi and Malik (2000) do not match with the underlying anatomical structures present in the image. This problem was previously evidence by Tao et al. (2007), in the segmentation of color images. Tao et al. (2007) combined Normalized Cuts and Mean Shift (Comaniciu and Meer, 2002) to produce a more computationally efficient segmentation procedure that also performs a more natural partition of the image. The Normalized cuts are also computationally expensive, and too slow to be used in practical applications. The graph-cut proposed by Felzenszwalb and Huttenlocher (2004) is more computationally efficient than the Normalized Cuts, however it produces image over-segmentation independently of the parameter ρ used (Fig. 3.4 (c) and (d)). The algorithm proposed by Boykov et al. (2001) produces good segmentations in a very efficient way (Fig. 3.4 (e) and (f)). Nevertheless, the outcomes may be heavily dependent on the foreground and background models (Forsyth and Ponce, 2012). From our experience, a good image contrast is important to obtain a good foreground-background segmentation.

3.6 Level-Set Segmentation

The Level-Set method was pioneered by Dervieux and Thomasset (1980, 1981) and further developed later on by Osher and Sethian (1988). Level-sets aim to represent image segmentation as a zero level-set of a higher dimensional implicit function ϕ, usually referred

as the level-set function (or embedding function). Curve evolution through parametric contour models rely on the explicit definition of a finite set of contour points to track curve evolution over time. Unlike parametric models, geometric models such as the level-set method add an extra dimension to the model, in order to handle implicitly curve evolution as a level curve of an higher-dimensional scalar function. In 2D, a closed curve c_t is represented as the level-set of a 3D embedding function ϕ, such that:

$$c_t = \{(x, y) | \phi(x, y, t) = k\} \tag{3.17}$$

where c_t is a geometrical deformable model at time t, and the value k is an arbitrary value commonly set to zero (Demirkaya et al., 2009). Curve evolution is governed by a time-dependent partial differential equation, known as the level-set equation:

$$\phi_t + \Gamma \left| \nabla \phi \right| = 0 \tag{3.18}$$

where ϕ_t is the temporal partial derivative of the level-set function, Γ is the velocity field that governs curve evolution, and ∇ denotes the spatial gradient operator (Ibanez et al., 2003). In the original work of Osher and Sethian (1988), the authors formalized the level-set function as a signed distance function, and focussed on motion by mean curvature flow, where the level-set velocity field Γ is expressed as the divergence of the normalized level-set, $\Gamma = div(\frac{\nabla \phi}{|\nabla \phi|})$. The evolution of level-set over time can be computed simply by applying the forward Euler method (Osher and Fedkiw, 2003).

Level-set segmentation can be performed using different image-based features, and as many other segmentation techniques several variations to the original Level-set have been proposed in the literature (Ibanez et al., 2003). In this chapter one will focus on the contributions of Caselles et al. (1997) and Chan and Vese (2001). These two techniques summarize the two general strategies used to model curve evolution, namely edge-based and region-based approaches. The Geodesic Active contours (GAC) proposed by Caselles et al. (1997) are edge-based level-sets, directly derived from the parametric Snakes model proposed by Kass et al. (1988). In the GAC framework the second order term of the Snakes model is removed, and the curve evolution is embedded into the level-set framework:

$$\frac{\partial \phi}{\partial t} = g(I) \left| \nabla \phi \right| div \left(\frac{\nabla \phi}{|\nabla \phi|} \right) + \nabla g(I) \cdot \nabla \phi \tag{3.19}$$

where $g(I)$ is an edge indicator (or stopping) function commonly given by:

$$g(I) = \frac{1}{1 + \left|\nabla \hat{I}\right|^2} \tag{3.20}$$

where $\hat{I}$ is a Gaussian filtered version of the image I (Caselles et al., 1997). Eq. 3.20 controls the propagation velocity of the level curve, and should approach zero near image edges.

Unlike the edge-based approach proposed by Caselles et al. (1997), Chan and Vese (2001) proposed a variational approach to the Level-set method derived from the Mumford and Shah (1989) model termed Active Contours Without Edges (ACWE). In this region-based approach, image segmentation is carried by searching the equilibrium between the inside and outside average intensities of the evolving curve:

$$\frac{\partial \phi}{\partial t} = \tau div\left(\frac{\nabla \phi}{|\nabla \phi|}\right) - \nu - \gamma_F \left(I - \mu_F\right)^2 + \gamma_B \left(I - \mu_B\right)^2 \tag{3.21}$$

where τ is a scaling parameter (that should be kept small to detect small or many objects), $\nu = 0$ is a correction term, μ_F and μ_B define the average intensity inside and outside the curve, and $\gamma_F = \gamma_B = 1$ are scaling parameters that control the strength of each individual average intensity on the curve evolution (Chan and Vese, 2001).

In Fig. 3.5 a foot is segmented with both GAC and ACWE. By analysing Fig. 3.5 (a), (b), (d) and (e) it is possible to observe that GAC have more difficulty to converge to the bone boundary when compared with the ACWE. In fact, the GAC are known to have some degree of dependency on the initialization and on the noise level present in the image. GAC must be initialized relatively close to the boundary (Fig. 3.5 (a)) in order to converge to the desired solution. Other problems are contour leakage through weak boundaries, and the difficulty to converge to boundary concavities. Nevertheless, since no constraints are imposed to the image, the GAC are capable of correctly segment highly heterogeneous objects (Xu et al., 2000; Lankton and Tannenbaum, 2008). The disadvantages often associated with the AWCE come from the assumption that the inside and outside region can be modelled by their average intensity. The ACWE may not be appropriate to segment highly inhomogeneous objects. However, the ACWE are less dependent than GAC on curve initialization, and are also less sensitive to image noise (Lankton and Tannenbaum, 2008). To achieve the result in Fig. 3.5 (c), (d), and (e) contour evolution was kept inside

the region of the leg, otherwise the contour would converge to the soft tissue boundary, in order to equalize the difference between inside and outside average intensities. Since the level-set model aims to equalize the inside-outside average intensities, the curve evolves towards the separation of the regions with the largest average intensity differences. The right foot was more accurately segmented with the region-based approach, particularly the metatarsal region (Fig. 3.5 (c) and (f)).

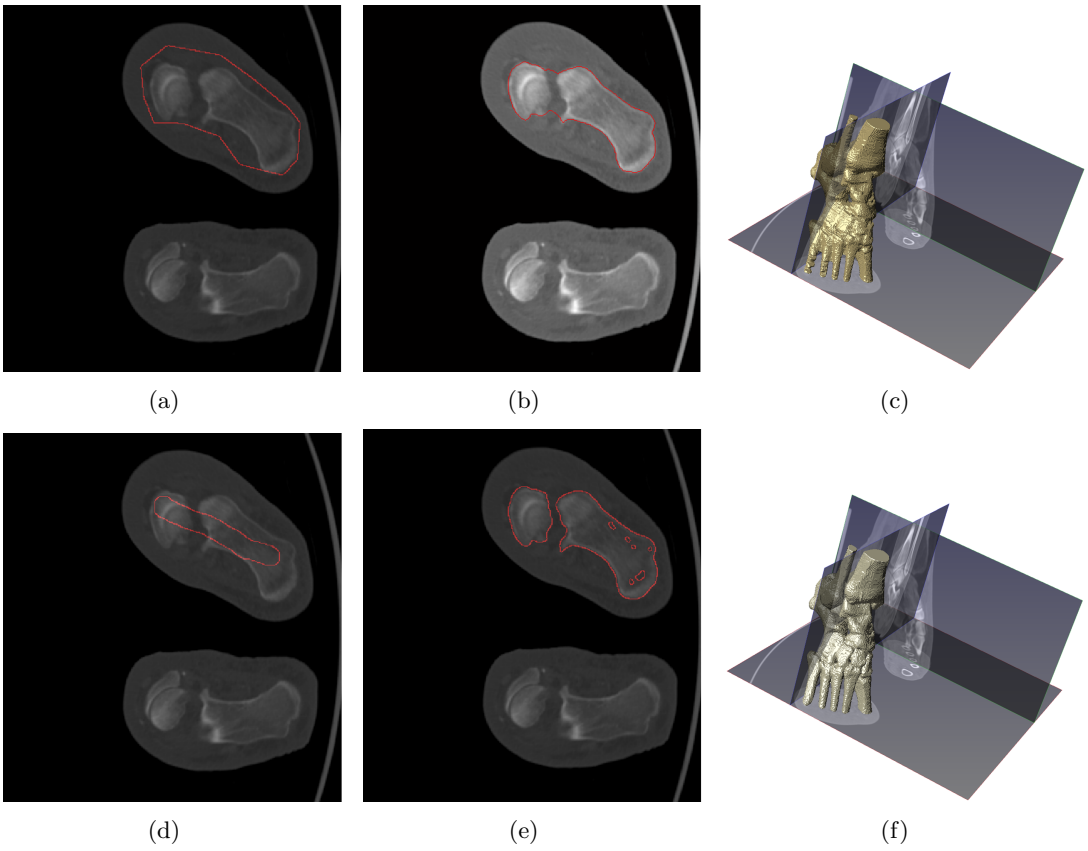

Figure 3.5: Right foot segmentation: in (a) GAC initialization and (b) the segmentation contour after 700 iterations; in (c) the volume segmentation of the whole volume; in (d), (e) ACWE initialization and final contour after 500 iterations, and in (f) the final segmentation

The Level-set method has the advantage of being extendable to an arbitrary number of dimensions, without changing the implementation and curve evolution principles (Sethian, 1999). In addition, the implicit representation of the contour by means of a higher-dimensional embedding function enables the segmentation of arbitrarily complex shapes. Topological changes such as contour breaking and merging are also straightforward (Dougherty, 2009). Level-sets may provide a continuous representation of the segmentation

contour and allow the recovery of the ROI with sub-pixel or sub-voxel resolution. Nevertheless, the precision and accuracy of this technique is still dependent on the resolution of the original image data (Pham et al., 2000). One common inconvenience associated with Level-set method is the deviation of the embedding function from a signed distance function as the curve evolves over time. This deviation may compromise curve evolution over time. The most common methodology used to avoid such problems it to re-initialize the signed distance function periodically during curve evolution (Demirkaya et al., 2009). The re-initialization is accomplished by solving:

$$\begin{cases} \varphi_t = sign(\phi_t)(1 - |\nabla\varphi|) \\ \varphi(x, y, 0) = \phi_t \end{cases} \tag{3.22}$$

where ϕ_t is the function to be re-initialized (Sussman et al., 1994; Osher and Fedkiw, 2003). The problem of curve re-initialization was addressed Li et al. (2010), which proposed a distance regularized level-set method that avoids level-set curve re-initialization during evolution. Paragios et al. (2001) addressed the initialization problem related with edge-based Level-sets by implementing the Gradient Vector Flow (Xu and Prince, 1998) into level-set framework and successfully reduced their dependency on initialization. Lankton and Tannenbaum (2008) addressed the problem of segmentation of heterogeneous objects with region-based Level-sets, by computing localized averages along the level curve. In another approach, Cremers et al. (2007) proposed a statistical formulation to the region-based Level-set method, in order to naturally incorporate image inhomogeneities, texture, and motion artifacts in the image segmentation. It is also worth noting the contribution of Bernard et al. (2009) that proposed a B-spline level-set framework that resumes curve evolution to a sequence of $1D$ convolutions. The B-spline level-set framework may be used for real-time segmentation.

3.7 Watershed Transform Segmentation

The Watershed Transform (WT) was originally proposed by Digabel and Lantuéjoul (1978), however this technique only became popular after the work of Soille and Vincent (1990). In Watershed segmentation the image is considered a topographic map (where

the height is proportional to the greyscale value), which is gradually submerged in water. As the rain falls, the droplets drain down under the action of gravity to the nearest valley (local minimum) gradually flooding the landscape. A catchment basin is defined as a group of topologically connected pixels, where any rainfall drains to the same local minima (Solomon and Breckon, 2011). During the flooding process damns are created in points where the rain drops are equally likely to fall into two or more adjacent catchment basins. These points delineate each catchment area, and are called the watershed lines or simply watersheds. The flooding process terminates when the water level reaches the height of the highest peak in the landscape (S. Jayaraman, 2011).

Soille and Vincent (1990) proposed a WT by immersion, which was simultaneously faster and more accurate than previously proposed algorithms. Given an image I defined over a squared grid V with greyscale values varying between h_{min} and h_{max} such that $I : V \rightarrow \mathbb{N}$, and where the vertices are the image pixels. The union of the set of all pixels m_k equal to the minimum threshold $T = h_{min}$ define the initial catchment basins, $S_{h_{min}}$. As the threshold is increased from h_{min} to h_{max}, the catchment basins are recursively expanded (S_h) such that:

$$\begin{cases} S_{h_{\min}} = \{(x,y) \in V | I(x,y) = h_{\min}\} = T_{h_{\min}} \\ S_{h+1} = \bigcup S_{h+1} \bigcup G_{h+1}(S_h), h \in [h_{\min}, h_{\max}] \end{cases} \tag{3.23}$$

where $\cup S_{h+1}$ denotes the union of all regional minima at threshold level $T = h + 1$ (and correspond to the creation of new previously undefined local minima), and $G_{h+1}(S_h)$ defines the geodesic influence zone of each catchment basin at threshold level $T = h$ within $T = h + 1$ (hence, define the topological closeness of each new points at $h + 1$ to each existing catchment basin). For instance, $G_{h+1}\left(S_{h_{m_i}}\right)$ defines the set of all points at $T = h + 1$ level that are topographically closer to m_i than to any other regional minimum m_j. The WT is defined as the complement of $S_{h_{max}}$ in the image domain:

$$WT(I) = V \backslash S_{h_{\max}} \tag{3.24}$$

Hence, the WT is in fact defined by the damns that partition the image domain into a set of catchment basins (Roerdink and Meijster, 2000). Fig. 3.6 depicts the segmentation of the pelvic bones with standard WT in (b), and with marker controlled WT in (c). The segmentation 3D model is depicted in Fig. 3.6 (d).

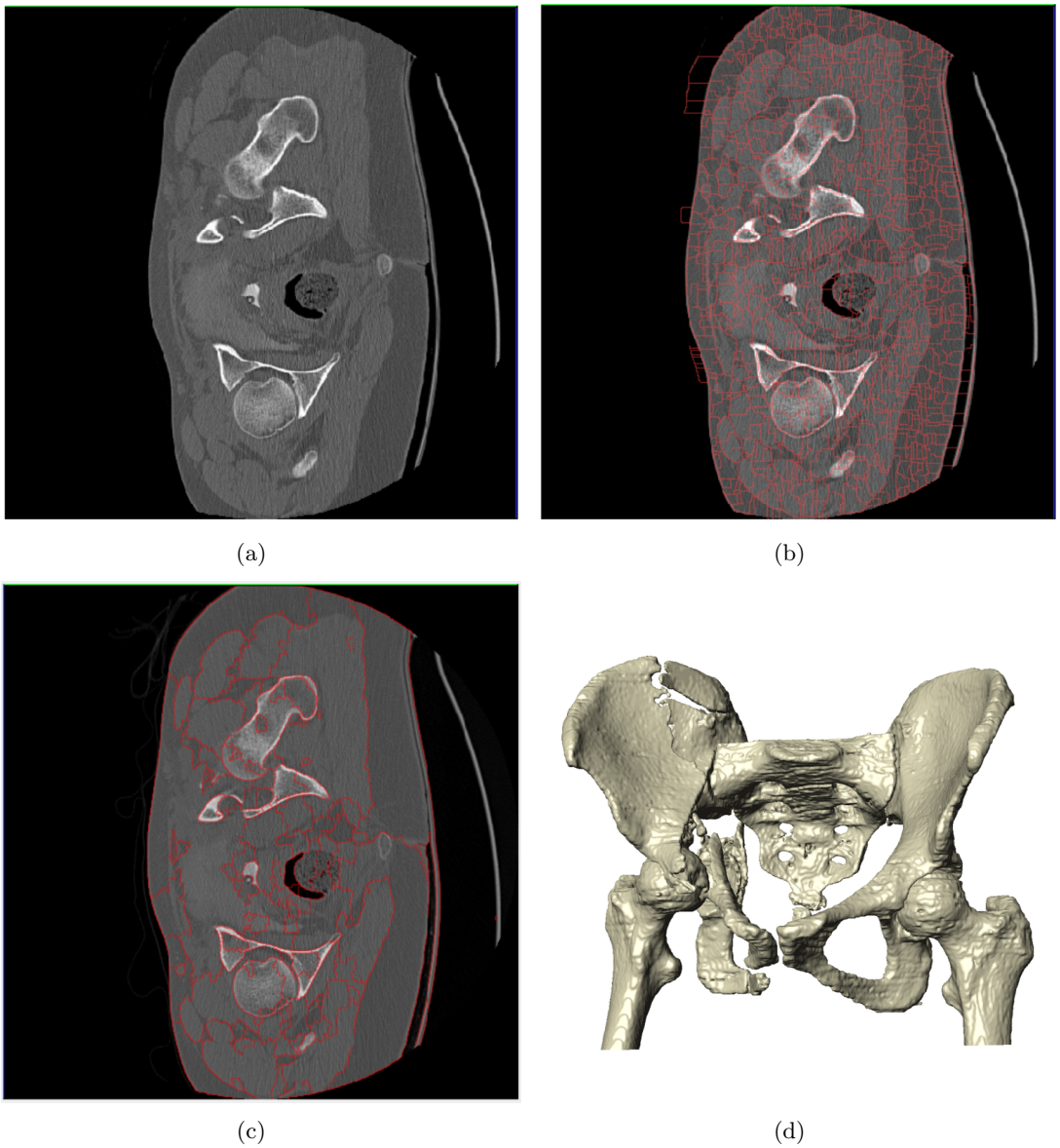

(a) (b)

(c) (d)

Figure 3.6: In (a) pelvic bone imaged acquired with CT, in (b) watershed lines obtained from the gradient of the image, in (c) marker-controlled watershed segmentation, and in (d) the final 3D model obtained with the marker-controlled watershed segmentation

In practice, the image gradient in used as the topological landscape to obtain the image partitioning (Meyer and Beucher, 1990). However, in natural scenes there are numerous local minima in the gradient image, which results in a large number of catching basins and ultimately in image over-segmentation. Over-segmentation is the most common drawback pointed to Watershed segmentation. Alternative solutions to over-segmentation are the marker-controlled segmentation, where watershed lines are only created to prevent

regions with different markers to merge (Preim and Bartz, 2007; S. Jayaraman, 2011). In addition, Hahn and Peitgen (2003) proposed the concept of merging tree, which track catching basins creation and merging events as image flooding is performed. After finishing the flooding process, the so-called pre-flooding height is used to control tree partition and basin merging, and consequently the final segmentation. In some situations image over-segmentation obtained with the WT may be advantageous. When the WT is applied over the gradient image, it always produces closed boundaries even in the presence of weak gradients.

3.8 Segmentation Evaluation and Validation

Segmentation complexity arises from the topological complexity of shapes to be segmented, from property variations across the ROI, and from the anatomical variations across individuals. Furthermore, image segmentation may also be affected by the physical limitations of the imaging systems, and the numerous artifacts that may emerge from the image acquisition process.

There are numerous image segmentation procedures proposed in the literature; however the same is not true regarding the evaluation of such algorithms. Segmentation evaluation is also a very difficult task, especially due to the difficulty to define suitable metrics for segmentation evaluation, and to define the true segmentation of a given set of images (Udupa et al., 2006). For practical purposes, segmentation without validation may be pointless, and an objective evaluation of image segmentation is fundamental to guarantee the validity and clinical applicability of any segmentation algorithm (Zhang, 1996; Zhang et al., 2008). Segmentation evaluation is not only important to ensure the overall validity of the segmentation, but also to select the most suitable segmentation procedure for a given application, to quantify segmentation accuracy, and to ensure consistency in the segmentation outcome (Bowyer and Phillips, 1998; Erdem et al., 2004).

The first fundamental notion regarding segmentation evaluation is what can be considered a good segmentation. In fact, a good segmentation may be highly user-dependent, and only rarely there is one unambiguous partition for a given scene (Adams and Bischof, 1994). Segmentation evaluation may be performed in a subjective basis, against a manually segmented reference model. Manually segmented gold-standards

intrinsically reflects the user's beliefs, understanding and degree of expertise. In addition, for certain applications manual segmentations by trained experts may be unpractical or even impossible to obtain. Ideally, a validation protocol should intrinsically define what may be considered a good segmentation. In this context Haralick and Shapiro (1985) proposed four criteria for defining a good segmentation:

- regions should be uniform and homogeneous with respect to some characteristic(s);
- adjacent regions should have significant differences with respect to the characteristic on which they are uniform;
- region interiors should be simple and without holes;
- and boundaries should be simple, smooth, and be spatially accurate.

Segmentation spatial accuracy may be defined as the degree in which the segmentation corresponds to the true ROI, and requires a reference standard that represents the true ROI. Segmentation precision measures the reproducibility of the segmentation obtained repeatedly from the same image. High spatial accuracy and high repeatability are both desirable properties for any segmentation procedure (Warfield et al., 2004).

The design of general purpose segmentation validation protocol is of enormous interest not only for the creation of a standardized framework for segmentation comparison, but also to increase segmentation reliability. Validation may be accomplished recurring to two types of data, clinical data or phantom data. On the one hand, the results obtained with clinical data (in-vivo or ex-vivo) can be readily applied to similar new data. Clinical data provide more realistic models, however the ground truth may not be available or may be very difficult to identify. On the other hand, phantom data enable a flexible parameterization to simulate different acquisition protocols, noise levels, and image resolution. The ground truth is known and may be geometrically well-defined, though phantom data may not be realistic enough to reflect the complexity of the acquisition process, and the anatomical variability observed in practice (Pham et al., 2000; Warfield et al., 2002, 2004). With phantom data the reference segmentation may be obtained through a high-resolution scan, which is subsequently degraded with noise and sampled to a lower resolution to emulate standard acquisition conditions (Preim and Bartz, 2007).

High-resolution scans allow a straightforward assessment of any segmentation obtained from a low-resolution model, against the reference gold-standard. Several validation metrics have been proposed to quantify segmentation accuracy against a high-resolution model. These metrics often quantify the distance or the degree of overlapping between the gold standard and the segmentation obtained. Distance measures quantify the greatest deviation between the segmentation and the gold standard, whereas the overlap measures quantify volumetric coherence between the gold standard and the segmentation (Preim and Bartz, 2007). The most common distance metrics are the Mean Symmetric Distance (MSD) and the Hausdorff Distance (HD). In the MSD the average distance between each pixel of the segmentation S and the closest pixel of the reference segmentation R is quantified. Since MSD is not symmetric, for each pixel of reference model R, the distance to the closest pixel of segmentation S is also calculated:

$$MSD(S,R) = \frac{1}{m+n}\left[\sum_{i=1}^{m} \min_{S_i}\left(d\left(S_i, R_j\right)\right) + \sum_{j=1}^{n} \min_{R_j}\left(d\left(R_j, S_i\right)\right)\right] \tag{3.25}$$

where m and n stand for the number of surface points in the segmentation S, and the number of surface points in the gold-standard model R, respectively. The MSD provides an estimate of the average deviation between the two segmentation contours. The Hausdorff Distance (HD) is a measure of the maximum deviation between the two segmentation contours. Similarly to the MSD, the HD is also not symmetrical and in addition to the distance between the S and the reference R, the distance between the reference R and the segmentation S must be also computed:

$$HD\left(S,R\right) = \max\left[\min_{S_i}\left(d\left(S_i, R_j\right)\right), \min_{R_j}\left(d\left(R_j, S_i\right)\right)\right] \tag{3.26}$$

where again R stands for the gold-standard model, and S stands for the segmented model. Both MSD and HD are computationally very expensive because they imply a one per all comparison between all segmentation and reference surface points. In addition, distance measures do not differentiate between over-segmentation and under-segmentation (Preim and Bartz, 2007; Gerig et al., 2001). The overlap measures quantify misclassified and correctly classified voxels. Overlap measures enable the construction of the so-called *Confusion Matrix*, which is an idea borrowed from machine learning theory. For a segmentation composed by N classes, a *Confusion Matrix* of size $N \times N$ is constructed, where each

entrance of the matrix is the number of voxels segmented with label i, while belonging to label j. Based on the *Confusion Matrix* one can define the true positive (TP), true negative (TN), false positive (FP), and false negative (FN) for each segmentation of the target object(s). Given the specified quantities several overall performance measures can be computed, such as the segmentation sensitivity (SE), specificity (SP), negative predictive values (NPV), positive predictive values (PPV), prevalence (P), among other measures, defined as:

$$SE = \frac{TN}{TN + FP} \tag{3.27a}$$

$$SP = \frac{TP}{TP + FN} \tag{3.27b}$$

$$NVP = \frac{TN}{TN + FN} \tag{3.27c}$$

$$PPV = \frac{TP}{TP + FP} \tag{3.27d}$$

$$P = \frac{TP + FN}{TP + FP + TN + FN} \tag{3.27e}$$

From the aforementioned quantities two important overlap measures can be computed, namely the Dice and Jaccard coefficients:

$$Dice = \frac{2 \times TP}{2 \times TP + FP + FN} \tag{3.28a}$$

$$Jaccard = \frac{TP}{TP + FP + FN} \tag{3.28b}$$

Both *Dice* and *Jaccard* coefficients take values between 0.0 and 1.0, where 1.0 indicates complete overlap (Dice, 1945; Jaccard, 1912; Popovic et al., 2007). The overlap measures can be all directly computed from the *Confusion Matrix*. The major drawback of the overlap measures when compared with the distance measures is that all misclassified voxels have the same effect on the quality of the segmentation regardless of their distance to the ideal segmentation (Akhondi-Asl and Warfield, 2004).

As stated previously, the validation problem is mainly dependent on the existence of a reliable ground truth, which in many practical situations may not be available. In some cases an approximation to the true segmentation can be obtained by combining multiple segmentations performed by a group of experts. The fundamental question assessed by expert segmentation fusion (or label fusion) is how the different expert segmentations can be combined in order to obtain a reliable estimate of the true segmentation. It is

worth noting that an expert may be any human expert, or automatic, or semi-automatic segmentation procedure. Label fusion has experienced a growing interest in the last couple of decades, and several algorithms have been proposed to solve this problem. The simplest form to perform multiple expert label fusion is by a so-called Voting rule (or sum rule). In a voting rule approach, each expert segmentation is considered as a vote for whether a certain image voxel may belong to the region of interest. The voxels for which the majority of the experts agree as belonging to the ROI are taken as the reference standard segmentation (Ho et al., 1994; Windridge and Kittler, 2003; Cordella et al., 1999).

Another popular approach to label fusion is the Simultaneous truth and Performance Level Estimation (STAPLE) proposed by Warfield et al. (2002). STAPLE takes a collection of expert segmentations and uses the Expectation-Maximization (EM) algorithm to compute a probabilistic estimate of the ground truth segmentation. Similarly, Rohlfing and Maurer Jr (2007) proposed a Shape-based Averaging (SBA) label fusion technique, based on a signed Euclidean Distance Transform (EDT). Instead of computing the statistical significance of each segmentation (STAPLE), SBA averages the shape of each individual segmentation given their signed EDT. More recently, and following the ideas developed in the SBA approach, Cardoso et al. (2012) proposed the Geodesic Shape-based Averaging that extends the Euclidean framework of SBA approach into a geodesic based distance.

The computation of a gold standard segmentation from multiple experts is both time consuming and may be, in some situations, impractical. In addition, expert's decisions in ambiguous voxels may vary; an inter and intra-expert segmentation variability of approximately 5 to 10% is highly expected to occur (Landman et al., 2010). The main disadvantages of Voting rules are that it does not specifies the number of experts that need to be taken in consideration to obtain a reliable ground truth segmentation, and a majority is only unique for an odd number of voters. In addition, the vote counting regards each expert equally, without considering the degree of expertise of each individual voter, and it does not incorporate any prior knowledge about the ROI. The most appropriate vote ordering or decision combining strategy remains unclear (Warfield et al., 2002).

In most of the aforementioned techniques, the classifiers performance is computed in a voxel-wise approach, that are strongly affected by the presence of spatial uncertainty or positional noise (Rohlfing and Maurer Jr, 2007). Artaechevarria et al. (2009) and Langerak

et al. (2010) demonstrated that STAPLE has a limited performed when poorly initialized. In addition, experts may not be capable of delineating the object of interest with the same accuracy along its' entire domain. Thus, accounting for spatial varying performance may be fundamental to achieve an optimized ground truth segmentation. Sabuncu et al. (2010) concluded that STAPLE performed better than Majority voting; however, it also performed worst comparatively to local and global weighted voting strategies that take into consideration local image intensity differences. To address these issues, Commowick et al. (2012) proposed an extension of the original STAPLE algorithm that locally computes, via a sliding window, the performance parameters of each classifier.

Although segmentation through label fusion techniques seems to be potentially more accurate than each individual segmentation; the accuracy is achieved essentially by reducing uncorrelated errors across various segmentations. This fact was noted by Rohlfing and Maurer Jr (2007), where the authors stated that all generic classifier combination methods (including SBA) are insensitive to the spatial relationships between classified samples, and their results are invariant to arbitrary spatial pixel permutations as long as the same permutation is applied to all inputs. Furthermore, Robitaille and Duchesne (2012) concluded that the performance of both Voting rule, STAPLE, and SBA is highly dependent on the performance dissimilarity between expert segmentations, and suggested a hybrid STAPLE-Vote-SBA technique that selects the appropriate label fusion protocol given the measured segmentation dissimilarity. The authors also concluded that, in general, SBA outperformed both STAPLE and the Voting rule. In agreement with previous findings, Wang and Yushkevich (2012) concluded that weighted-voting label fusion techniques may underestimate the volume of convex structures, and, more importantly, that multi-atlas segmentation by label fusion is biased towards repeated atlas in the dataset.

3.9 Summary

Image segmentation is a fundamental step for the high-level understanding of a given scene. Throughout the years numerous segmentation algorithms have been proposed, but there is still no single algorithm capable of solving the segmentation problem. Instead, segmentation is often accomplished using multiple segmentation algorithms to

gradually approach the desired outcome. In this chapter the main algorithms employed for image segmentation were reviewed, as well as their main advantages and disadvantages. The performance of a segmentation procedure is highly dependent on the application, the type of data available, and the degree of experience of the user. Nevertheless, from all the algorithms presented in this chapter, the Level-set method seems to be the most interesting methodology for accurate bone segmentation. The Level-sets are relatively independent on the initialization, provide continuous and smooth contours, are topologically flexible, and have the potential for sub-pixel accuracy segmentation. Another paramount aspect related with medical image segmentation is the evaluation and validation of the segmentation outcomes. Several evaluation metrics have been proposed to assess image segmentation. Evaluation through label fusion may produce more accurate results than a single segmentations, however the final image partition may be biased towards systematic errors present in different segmentations. In addition, performing multiple segmentation may be time consuming, and hence incompatible for an industrial setting. The correct approach for segmentation fusion is still an open issue, and more extensive details are beyond the scope of this work.

Chapter 4

Bone Segmentation Protocol

In this chapter a medical image segmentation pipeline for accurate bone segmentation from CT imaging is proposed. It is a two-step methodology, with a pre-segmentation step, in which the user is free to employ the necessary means for segmenting the desired region of interest, followed by second automatic segmentation refinement step. The automatic segmentation refinement is composed of several sub-steps, namely image deconvolution, image cropping, and interpolation. The user-defined pre-segmentation is then refined over the deconvolved, cropped, and up-sampled version of the image. Segmentation outcomes are validated against a gold standard model obtained using the coordinate measuring machine Nikon Metris LK V20 with a digital line scanner LC60-D.

This page was intentionally left blank

4.1 Introduction to Accurate Bone Segmentation

The first milestone towards custom implant development is the accurate extraction of the target anatomical structure from medical image data. The tremendous evolution of CT imaging led to the widespread of this technique to all medical fields. CT imaging became a fundamental tool in medical practice. From the engineering standpoint, CT imaging can be used for the development of patient-specific biomechanical and finite element models, as well as in the development of custom implants (Bargar, 1989; Garg et al., 1985; Stulberg et al., 1989). Currently, this technique is the modality of choice for imaging the Human skeletal system. For either trauma or orthopaedic purposes, the ability to enhance the radiological contrast between hard and soft-tissue facilitates image segmentation, and the production of good representations of the periosteal and endosteal surfaces of the bone. The accurate segmentation of bone is the only way to guarantee the overall fit to the patient's anatomy, which is paramount for the long-term success of the implants (Engh and Bobyn, 1985; O'Connor et al., 1987). Nevertheless, the degree of patient fit necessary to minimize the biological impact of the implant is still unknown. On the one hand, too much implant fit to the target anatomy may preclude implant insertion and may cause severe damages to the host bone (Walker and Robertson, 1988). On the other hand, the absence of implant fit may cause interfacial micromotions that prevent bone ingrowth and implant osseointegration (Walker et al., 1987; Mandell et al., 2004).

Chapter 2 addressed some of relevant aspects related with CT technology. There are aspects related with the hardware and software that may limit the degree of certainty with which an anatomical structure can be acquired from a set of images. Image acquisition causes a natural degradation in image quality due to the limited frequency response of the imaging system. The sharp transitions between adjacent structures found in reality become diffuse in the final image. Image blurring is commonly associated with the production of overestimated representations of the original domain. Hangartner and Gilsanz (1996) concluded that CT imaging produced large domain overestimations for structures with a cortical thickness below 2.0 mm.

The amount of spatial blur is often modelled in the image space by the system's Point Spread Function (PSF). Prevrhal et al. (1999) found that the inner and the outer cortical surfaces of bone could only be accurately determined for thicknesses greater than the Full

Width at Half Maximum (FWHM) of the PSF. In a phantom study, Kang et al. (2003) convolved the ideal attenuation profile according to the specifications of the European Spine Phantom with the system's PSF and obtained domain overestimations up to 40% of the original phantom thicknesses. The largest thickness overestimations were observed for structures with a width smaller than the FWHM of the PSF. In another phantom study, Ohkubo et al. (2008) observed that for small diameter spheres (< 2.0 mm) their apparent diameter was overestimated, and that for spheres with a diameter close to zero the apparent diameter was in fact the FHWM of the PSF. Therefore, the FWHM of the PSF seems to provide a measure of the maximum spatial frequency that can be accurately encoded by a given CT machine.

The reconstruction FOV may also be critical to the domain accuracy. As seen in section 2.7.1 the size of the reconstruction FOV defines the final pixel size. Image reconstruction with a small FOV effectively increases image resolution. On the contrary, a wider FOV implies image reconstruction with larger voxel sizes that can exceed the effect of the FWHM of the PSF. Therefore, in high-resolution reconstructions the PSF if often the limiting factor, however for larger FOV if the pixel size is larger than the FWHM, the PSF is spread to occupy a single pixel in the reconstructed image (Dougherty, 2009). Maloul et al. (2011) concluded that the reconstruction with large voxel sizes had a higher impact on bone thickness overestimation than smaller sizes. Authors also concluded that large voxel sizes are detrimental to the accurate representation of thinner and/or highly curved structures.

Inaccuracies directly linked with the image acquisition process are not the only sources of domain deviations found in practice. Domain inaccuracies caused by the acquisition process may be minimal when considering other error sources. Although limited by the system's frequency response and FOV, image reconstruction in CT imaging is known to have a very high accuracy, and to be almost free of geometrical magnification (Hildebolt et al., 1990). Image segmentation is probably the major source of domain deviations between the original geometry and the final reconstruction. Image segmentation is often affected by high inter and intra-expert variability, and the image processing and segmentation chain may contribute with up to 70% of the average error found in the final reconstruction (Wang et al., 2009). In the literature, a plethora of studies have addressed bone segmentation. However, few have evaluated the accuracy of the segmentation

outcome. From those addressing segmentation accuracy, two segmentation approaches arise, namely the adaptive/relative thresholding according to the local statistics or the attenuation profile normal to the bone surface, and optimized single or multiple thresholding.

In an early study, Rothuizen et al. (1987) analysed the CT attenuation profile normal to the bone's surface, and concluded that an absolute threshold was insufficient to accurately define the femur's cortical shell. The relative thresholds of 45% and 50% of the maximum HU profile value were proposed to segment properly the diaphyseal and metaphyseal regions of the femur, respectively. Aamodt et al. (1999) proposed a 600HU as the optimal threshold to segment the endosteal surface of the femur. In the eight femurs tested, the minimum average deviation between the rasped endosteal surface of the femur and the 600HU contour was 0.03 ± 0.52 mm. More recently, Kang et al. (2003) employed the 50% relative threshold to correct the boundary of the segmentation, with a maximum deviation of half-voxel from the ground truth. Rathnayaka et al. (2011) compared the outer and inner cortical surface of five cadaveric sheep hind limbs obtained with Canny-edge detection, single and multiple thresholding segmentation against a 3D contact scanner and micro-CT model. The multiple threshold approach considering three anatomical regions (proximal, diaphyseal and distal) was found to be the more accurate, with an average deviation of 0.18 mm for the outer contour, and an average deviation of 0.17 mm for the inner contour. Exploiting the concept of relative thresholding, Treece et al. (2010) proposed a Levenberg-Marquardt-based segmentation algorithm to quantify femoral cortical thickness with sub-millimetre accuracy. In this work an ideal high-resolution attenuation model was fitted to the HU attenuation profile normal to the bone's surface and then thresholded with the 50% relative threshold. A similar approach was used by Pakdel et al. (2012) to segment bones from the craniofacial skeleton. Both algorithms allow the production of sub-pixel accuracy estimates of both inner and outer surfaces of the bone.

The recovery of the cortical bone through these thresholding techniques may have, however, some limitations. As stressed in section 3.2, segmentation by single thresholding, although simple, is very sensitive to image in-homogeneities, to image noise, to threshold selection. Segmentation accuracy is tightly coupled with the image resolution, and with the surface reconstruction protocol. In multiple and adaptive thresholding, some of the aforementioned limitations are handled due to the local nature of the threshold.

The threshold is applied to sub-volumes along the bone's surface to ensure threshold optimality within each region. However, with the application of single, multiple, or adaptive thresholds there is no guarantee that a closed contour will be obtained. Prevrhal et al. (1999) stressed that applying solely an adaptive threshold to the profile produces incorrect estimates of the bone's surface, especially in regions with thin cortical shells.

The conjugation of adaptive thresholding and model fitting seems to overcome the aforementioned limitations of this technique, because the threshold is applied to an ideal attenuation profile derived from the observed HU data. In addition, model fitting allows the determination of a set of boundary points with sub-pixel accuracy, theoretically bounded by the high-resolution model. Nevertheless, from our practical experience these methodologies possess several other disadvantages. First, the application of adaptive/relative thresholds to each boundary pixel (or set of boundary pixels) is extremely time consuming and unpractical. Second, it is very difficult to accurately estimate the true normal to the surface of the cortical bone at each boundary point. The normal direction is highly affected by the discrete nature of the image, fact has also been stressed by Yao et al. (2005). Third, the surface of the bone has to be sampled and each surface point needs to be processed independently, which produces highly irregular contours. Ultimately, it also produces unreliable estimates of the bone surface if the observed attenuation profile deviates from the ideal attenuation profile. This is particularly problematic near the articular surfaces of bones. For instance at the hip joint level, both the existence of high attenuation coefficients near the geometrical centre of femoral head, and the proximity of the iliac bone are very difficult to handle with these techniques.

In this work a different approach to accurate bone segmentation is proposed. The proposed protocol allows the segmentation of bony structures with sub-pixel accuracy, and intrinsically guarantees the smoothness of the extracted contours. As many other segmentation procedures proposed in the literature, our segmentation pipeline starts with a rough segmentation of the Region of Interest (ROI) defined by the user, which is subsequently refined in a second step to obtain a final model with sub-pixel accuracy. In the previous chapters, it was stressed the impact of the imaging system's performance and the variability of segmentation in model accuracy. It was also stressed the need for segmentation validation, in order to guarantee both the accuracy and the consistency of the image segmentation process across different users and Datasets. In the present work,

the proposed segmentation protocol is validated through the comparison between the segmentation outcome and a geometrically well-defined gold standard. For segmentation validation purposes, a synthetic bone often used for mechanical testing is used as the gold standard. The remainder of this chapter is organized as follows: in section 4.2, the segmentation protocol, the definition of the segmentation gold standard, and the means for quantifying the accuracy of the CT machine are described; in section 4.3 one presents a methodology to estimate the PSF of the CT machine; in section 4.4 the impact of the domain discretization (voxel *vs.* average error) in the model accuracy is analysed; section 4.5 and section 4.6 refer to the description and discussion of the results obtained with the proposed segmentation pipeline; and, ultimately, in section 4.7 the summary and conclusions of the present chapter are drawn.

4.2 Materials and Methods

In Chapter 3 it was stressed the complexity of the image segmentation problem. Despite the huge amount of scientific efforts, currently there is still no segmentation technique that provides satisfactory results for all segmentation problems. Due to the degree of variability in the Human anatomy and image artifacts, segmentation methods designed specifically for each application often produce better results than general purpose algorithms. Nevertheless, some degree of standardization is desirable, particularly when the segmentation is part of the product development pipeline. Therefore, in this work one proposes a two-step segmentation protocol for reliably and accurately extract hard tissue structures from image data. To evaluate the accuracy of the newly proposed segmentation protocol, a phantom study was carried out: one composite replica of the Human femur (Fig. 4.1) commercially available at the Sawbones website[1] was imaged with a CT machine. The image acquisition process was carried with a fourth-generation CT scanner Toshiba *Aquilion*^{TM} 64 at the CUF Hospital, Porto (Portugal).

During image acquisition and reconstruction different scan settings were used. Three geometrically simpler phantom objects were added to the acquisition process. In practice, these geometrically simpler phantoms may be important to characterize the image acquisition process, especially the limiting resolution of the CT scanner. The tested

[1] *http://www.sawbones.com/*

(a)

(b)

(c)

(d)

Figure 4.1: (a) the gold standard composite femur, (b) the reference calibrated hollow cylinder with a diameter of approximately 9.81 mm, (c) the ceramic box, and (d) the brass alloy wire with a diameter of 0.10 mm used to estimate the system's Point Spread Function

objects were a calibrated hollow cylinder with an outer diameter of 9.81 ± 0.02 mm, a brass alloy wire with a diameter of 0.10 mm, and a ceramic box with dimensions $12.51 \times 13.81 \times 18.01 \pm 0.01$ mm (Fig. 4.1 (b), (c) and (d)). The compact nature of these phantom objects allow them to be imaged simultaneously with the patient, and may avoiding the need of a dedicated phantom to assess the spatial resolution of the CT scanner. The ability to quantify the system's limiting resolution was evaluate against the CATPHAN 528, which is a commercially available phantom widely used for quality control. The CATPHAN 528 was imaged to quantify the true in-plane resolution of the CT machine, against which the performance of each phantom could be compared. The summary of image acquisition protocols and reconstruction resolutions for the phantom femur, the CATPHAN 528, and the three other phantoms is presented in Table 4.1.

Table 4.1 also resumes the relevant settings related with image reconstruction from the raw data. Dataset #1 and the cylinder phantom were imaged simultaneously, and reconstructed with the maximum resolution of the scanner. The raw data of this scan was used to produce two additional reconstructions with 0.5 mm and 1.0 mm of slice

Table 4.1: Summary of the CT image acquisition protocol and target reconstruction resolution for each Dataset (DS): Datasets #1, #2 and #3 were obtained from the raw data, whereas in Datasets #4 and #5 the in-plane resolution was downscaled to 1/2 and 1/4 of the original (reconstructed) resolution

	Data Acquisition								
	DS#1	DS#2	DS#3	Cylinder	Box	CATPHAN 528	Wire	DS#4	DS#5
Tube Voltage (kV)	120	120	120	120	120	120	120	120	120
Tube Current (mA)	200	200	200	200	200	200	200	200	200
Scan FOV (mm)	240	400	400	240	400	400	400	240	240
Slice Thickness (mm)	0.3	0.3	3.0	0.3	0.3	0.3	0.3	0.5	1.0
Pixel Spacing (mm)	0.243	0.525	0.525	0.243	0.525	0.460	0.460	0.486	0.972
Number of Slices	1547	1671	168					929	465
Reconstruction Kernel	FC 30	FC 84	FC 84	FC 30	FC 84	FC 84	FC 84	FC 30	FC 30
Reconstruction Matrix	512x512	512x512	512x512			512x512		256x256	

thicknesses. In MSCT any additional reconstructions from the raw data can be obtained by simply changing the target slice thickness prior to the image reconstruction. The in-plane resolution of these two additional Datasets was posteriorly down-sampled to obtain almost isotropic voxels, and hereafter referred as Dataset #4 and Dataset #5. Similarly to Dataset #1, the same acquisition protocol was used for Dataset #2 and #3, the box phantom, the CATPHAN, and wire phantom. The gold-standard segmentation was obtained by digitizing the outer surface of the composite bone using a coordinate measuring machine *Nikon Metris LK V20* with a digital line scanner *LC60-D*, which guarantees 28 μm of spatial accuracy. Digitalization of the composite bone was performed at the Instituto Superior da Qualidade (ISQ) Lisbon, Portugal.

Regarding the two-step segmentation protocol, in the first step the user performs a pre-segmentation of the domain/image. In this step, the technique(s) more suitable for obtaining an initial segmentation of the bone may be applied. The output of image pre-segmentation should contain a set of ROIs of interest (for instance, the segmentation of the composite femur and the phantom object(s)), and may also have some additional spatial constraints (such as the CT table). The pre-segmentation aims to provide some high-level information about the desired domain, as well as some spatial relationships between any existing adjacent structures. This allows to handle segmentation variability prior to segmentation refinement. Fig. 4.2 exemplifies the pre-segmentation pipeline for the composite bone. In the pre-segmentation, a single global threshold is used to define the two regions of interest, namely the composite femur and the reference cylinder. In addition to the two objects, a hard spatial constraint corresponding to the patient table of the CT machine is added to the image pre-segmentation. Each ROI (composite femur, cylinder

mask, and patient table masks) acts as spatial constraint to the level-set evolution, avoiding the incorporation into any other region. For instance, during cylinder segmentation both the composite femur segmentation and the patient table become spatial constraints to the level-set evolution, avoiding the incorporation of the table pixels into the cylinder mask.

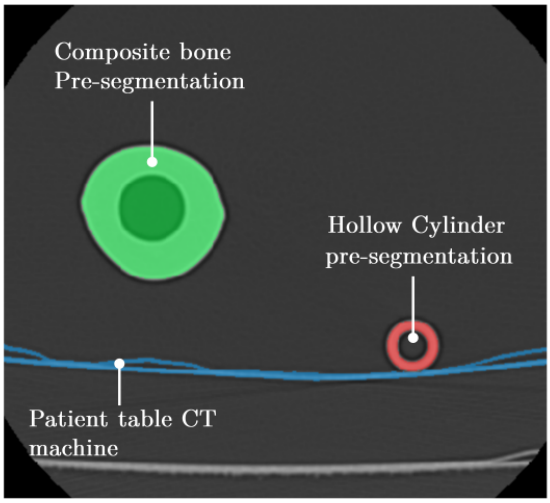

Figure 4.2: Pre-segmentation of the composite femur with the proposed segmentation pipeline, where the segmentation of the composite femur and reference cylinder are target ROIs, and the patient table acts as a hard spatial constraint to the level-set evolution during segmentation refinement

In the second step (which will be referred as refinement step), a fully user-independent and automatic segmentation refinement composed by several sub-steps is performed in order to optimize the pre-segmentation. Fig. 4.3 schematically depicts the proposed segmentation refinement protocol. First, image deconvolution is applied to the image, in order to minimize the partial volume effect caused by the PSF during image acquisition. In section 4.3 one introduces a procedure for accurately estimate the PSF of the CT machine. Next, the image is cropped around the ROI according to the pre-segmented data, and up-sampled with cubic spline interpolation:

$$\beta^3 = \begin{cases} \frac{2}{3} - \frac{1}{2}|x|^2(2-|x|), & 0 \leq |x| < 1 \\ \frac{1}{6}(2-|x|)^3, & 1 \leq |x| < 2 \\ 0, & 2 \leq |x| \end{cases} \tag{4.1}$$

where x defines the finite support of the basis function. Thévenaz et al. (2000) concluded that cubic spline interpolation provides the best interpolation strategy for image processing

applications, both in terms of computation effort and image induced artifacts. Finally, segmentation refinement is performed over the interpolated ROI. The Active Contours Without Edges (ACWE) are used to extract a high-resolution contour from the image data, considering the spatial constraints defined in the pre-segmentation step:

$$\frac{\partial \phi_i}{\partial t} = \tau div\left(\frac{\nabla \phi_i}{|\nabla \phi_i|}\right) - \gamma_F \left(I - \mu_F\right)^2 + \gamma_B \left(I - \mu_B\right)^2 + c_3 \mu_B \sum\nolimits_{k=1;k\neq i}^{n} S_k \qquad (4.2)$$

where ϕ_i is the level-set corresponding to the pre-segmented region S_i, $\gamma_F = \gamma_B = 1$, μ_F and μ_B are the average intensity inside and outside the curve as defined in Chapter 3, and the final summation assigns the average intensity of the background to all the remaining pre-segmented sub-regions S_k multiplied by a user defined cost $c_3 > 0$.

The Chan-Vese ACWE level-set method is less sensitive to curve initialization, and noise than other level-set methods. Therefore, the ACWE allow a less restrictive pre-segmentation step. During segmentation refinement, each 2D image is processed independently, as well as each ROI contained in the pre-segmentation. This reduces the computational complexity and memory requirements of the segmentation refinement, by applying image interpolation in smaller region at each iteration. Two refinement outputs are considered (Fig. 4.3). The new segmentation can be directly exported to the CAD modelling software via point cloud, or downscaled to the original image resolution for further surface or Finite Element mesh generation. In addition, to test the robustness against image noise, the segmentation refinement was tested over Datasets #1 to #5 corrupted with Additive White Gaussian Noise (AWGN), with a standard deviation of $\sigma_{Noise} = 10$ HU.

Phantom studies for segmentation evaluation have some clear limitations. A comparable image quality in terms of resolution, contrast, and the absence of noise and image artifacts may be very difficult to obtain in practice (see Fig. 4.2). However, contrarily to natural Human bones, composite bones may have less inter-specimen variability, are ready available, are easy to handle, and do not degrade over time (Cristofolini et al., 1996). In addition, these composite replicas possess mechanical properties that mimic both natural cortical and trabecular bones, and are now widely used for mechanical testing of implants (Finkemeier et al., 2000; Completo et al., 2007; Au et al., 2011). Phantom studies do not fully represent the complexity of the clinical data, however they provide a well characterized ground truth reference model when biological

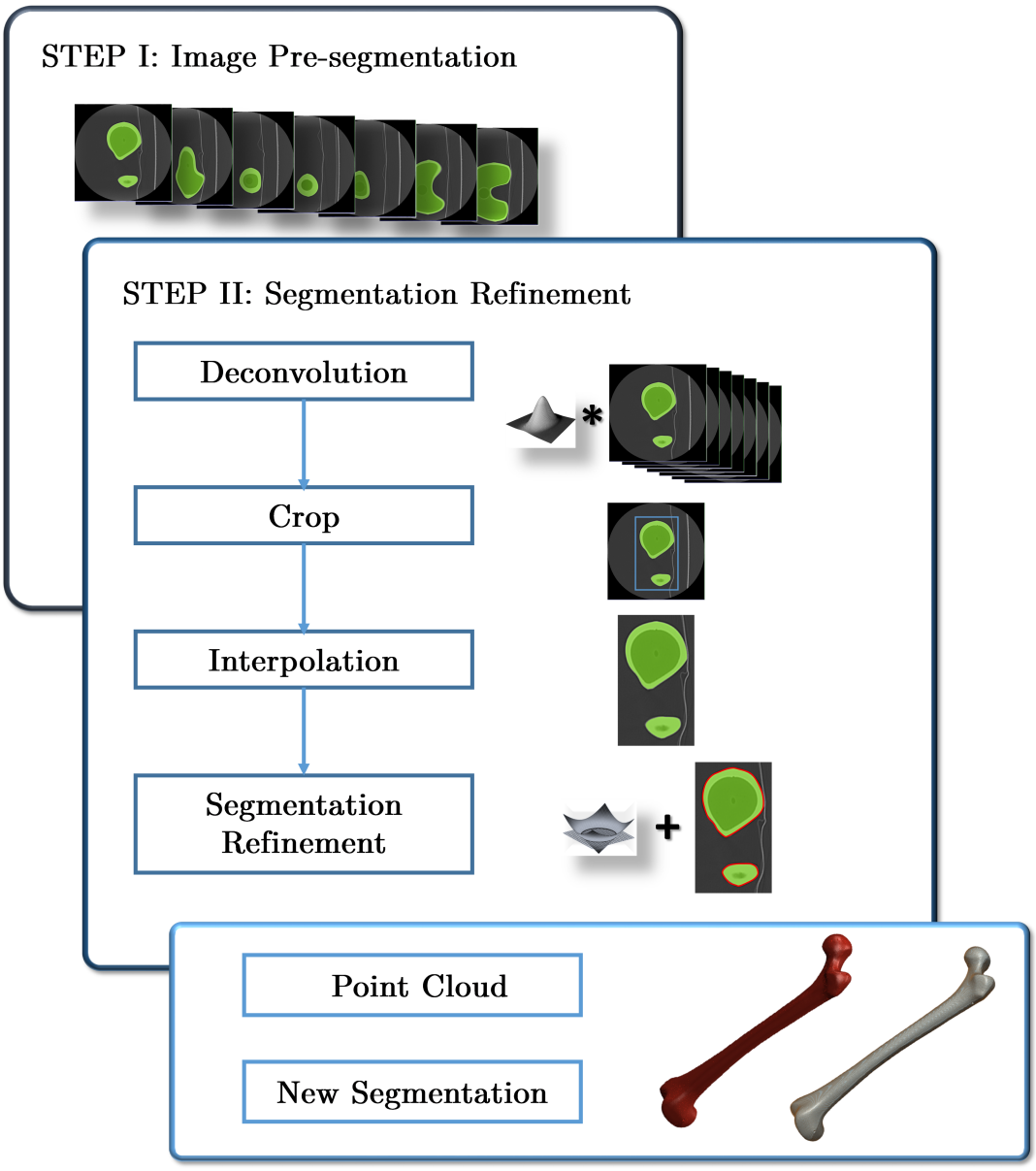

Figure 4.3: Schematic description of the image segmentation protocol proposed: in a first step the user performs a pre-segmentation of the domain aiming to provide some high level information of the desired ROI and other neighbouring structures; in a second step the pre-segmentation will be the starting point for a fully automatic segmentation refinement, which encompasses image deconvolution, image cropping, interpolation and segmentation by the level set method

tissues are not available. Another advantage is the possibility to define a high-resolution ground truth of the target geometry, with which the low-resolution segmentations can be directly compared.

4.3 Image Deconvolution and Point Spread Function Estimation

It is known from image acquisition theory that any image obtained from an imaging system is not perfect and is only an approximation to the real (ideal) scene. The real image is never available due to the intrinsic nature of the acquisition process. However, an estimate of its true distribution may be obtain by considering the output image and some prior knowledge about the system's behaviour. In 2D image acquisition theory, the imaging system is commonly considered as being linear and spatially invariant, and the output image $I(x, y)$ may be correlated with the input image $F(x, y)$ according to:

$$I\left(x,y\right) = F\left(x,y\right) \otimes O\left(x,y\right) + n\left(x,y\right) \tag{4.3}$$

where $\otimes$ denotes the 2D convolution, $O(x, y)$ denotes the system blurring effect of the system's PSF, and $n(x, y)$ is an addictive noise term (Campisi and Egiazarian, 2007). Image noise $n(x, y)$ is typically a stochastic process that may be originated by a multitude of processes that produces unwanted fluctuations in the recorded signal (Solomon and Breckon, 2011). Noise is particularly problematic when one aims to find image edges. Edge detection is very sensitive to image noise, and frequently is preceded by a low-pass filtering of the image. Image de-noising can be efficiently accomplished with both linear and non-linear filters. Nevertheless, linear filtering (such as Gaussian filtering) suffers from two major drawbacks; it smooth's indiscriminately image features and noise, and dislocates image features (Demirkaya et al., 2009). Edge bias due to Gaussian smoothing has been studied and quantified by various authors (Verbeek and Van Vliet, 1994; Mendonça et al., 2004; Bouma et al., 2005). In contrast, non-linear filtering enables efficient noise removal without the unwanted effect of edge dislocation observed with linear filtering (Demirkaya et al., 2009). Thus, it is more appropriate to perform image de-noising by non-linear filtering, because it efficiently removes noise without the problems associated with linear filtering. For instance, image non-linear filtering can be efficiently performed recurring to

algorithms such as the anisotropic diffusion proposed by (Perona and Malik, 1990).

The problem of recovering $F(x, y)$ from $I(x, y)$ is known as *Image Deconvolution*, and is intrinsically limited by the knowledge about the PSF and the noisy processes related with the acquisition itself. Image restoration in this work is accomplished by applying a standard iterative blind deconvolution algorithm. The MATLAB function *deconvblind* is used for the purpose of image restoration. The *deconvblind* uses the Lucy-Richardson algorithm to obtain the new estimate of the original scene $\hat{F}_{k+1}(x, y)$ and the new estimate of the PSF $\hat{O}_{k+1}(x, y)$ and can be defined as:

$$\hat{F}_{k+1}(x, y) = \hat{F}_k(x, y) \left[\frac{I(x, y)}{\hat{O}_k(x, y) \otimes \hat{F}_{k+1}(x, y)} \otimes \hat{O}_k^*(x, y) \right] \tag{4.4a}$$

$$\hat{O}_{k+1}(x, y) = \hat{O}_k(x, y) \left[\frac{I(x, y)}{\hat{O}_k(x, y) \otimes \hat{F}_{k+1}(x, y)} \otimes \hat{F}_k^*(x, y) \right] \tag{4.4b}$$

where $\hat{F}_k^*(x, y)$ and $\hat{O}_k^*(x, y)$ are the complex conjugates of $\hat{F}_k(x, y)$ and $\hat{O}_k(x, y)$, respectively, and where $k \in \mathbb{N}_0$, and $\hat{F}_0(x, y) = I(x, y)$ is the acquired image, and being image noise $n(x, y)$ neglected. The blind deconvolution is not dependent on the knowledge of the system's spatial blurring (Richardson, 1972; Ayers and Dainty, 1988; Solomon and Breckon, 2011; Pantin et al., 2007). However, we found that robust results may be obtained if an accurate initial guess of the system's PSF is provided.

Image resolution is inherently linked with the hardware and software used for image acquisition, therefore the MTF may be considered a fixed and deterministic quantity (Solomon and Breckon, 2011). In practice, the MTF is approximated by computing the response of the imaging system to different line-pair frequencies with specially designed phantoms. The PSF encodes equivalent information, and is defined by the magnitude of inverse Fourier Transform of the MTF. Therefore, the MTF encodes the highest recordable spatial frequency that the system can reproduce properly, whereas the PSF the smallest distance that the system can resolve (Dougherty, 2009). The PSF of the system is frequently approximated by a normalized Gaussian function as stated by the central slice theorem:

$$O(x, y, z) = \frac{1}{(2\pi)^{\frac{3}{2}} \sigma_x \sigma_y \sigma_z} e^{\left(\frac{x^2}{2\sigma_x} + \frac{y^2}{2\sigma_y} + \frac{z^2}{2\sigma_z} \right)} \tag{4.5}$$

where σ_x, σ_y, and σ_z denote the standard deviation in each orthogonal direction. Two

assumptions are commonly found in literature for the PSF, namely: (i) the PSF is assumed to be uniformly invariant in the slice plane; and (ii) the cross-plane PSF is generally also assumed to be invariant in the axial direction (Prevrhal et al., 1999; Treece et al., 2010; Easton Jr, 2010; Pakdel et al., 2012). In practice, the PSF is not completely isotropic and shift invariant, however this approximation can be safely made for most CT scanners, as well as for several other medical imaging modalities (Nickoloff and Riley, 1985; Dore and Goussard, 1997). For simplicity one will only consider the estimation of the in-plane blur, and hence eq. 4.5 will be reduced to its 2D counterpart.

Several approaches to determine the MTF of an imaging system have been proposed in the literature. In addition to the line-pair patterns, the MTF can also be estimated through the Line Spread Function (LSF), which can be determined by imaging thin wires or narrow slits. The LSF can be alternatively determined from the system's Edge Spread Function (ESF), simply by differentiating the edge response to radiopaque objects (Beutel et al., 2000; Smith, 1997). The successful characterization of the MTF through the ESF was reported by several authors (Cunningham and Fenster, 1987; Cunningham and Reid, 1992; Samei et al., 1998; Mori and Machida, 2009). Recalling Fig. 4.1, the three phantom objects proposed in this work exploit both the determination of the limiting resolution of the CT scanner through the measurement of the system's impulse response (through the wire phantom) and ESF.

The wire phantom provides a direct measure of the in-plane PSF, which can be computed directly from the recorded attenuation profile. Regarding the ESF, and similarly to other authors, it was determined by analysing the attenuation profile along the surface normal to both the calibrated cylinder and ceramic box. To do so, the reference cylinder CAD model was discretized and superimposed to the CT images. The contour of the CAD model was sampled and the normal to the surface at each pixel was determined by computing the eigenvectors of the structure tensor matrix derived from the gradient of the image, ∇I. Next, the extracted attenuation profile was smoothed and de-noised by computing the multi-scale Wavelet decomposition. In the Wavelet domain, the signal can be efficiently de-noised by simply applying a threshold to the coefficients obtained from the Wavelet Transform (Mallat, 1989; Mallat and Zhong, 1989). According to our experiments, the Sure-shrink hard-thresholding over the wavelet coefficients provides the best results for 1D signals (see references Donoho and Johnstone (1995); Donoho (1995)).

The wavelet hard-thresholding allows the extraction of the signal outline without the inconvenience of degrading or shifting signal features as observed with Gaussian smoothing, or other linear filtering techniques. It also allows the removal of unwanted high-frequency components from the signal that may compromise the analysis of the signal gradient. The 1D PSF profile estimate was computed by simply fitting a Gaussian function to the gradient of the signal envelop. The Gaussian fitting was performed over a narrow band around the gradient maximum, in order to remove the influence of adjacent structures (Smith, 1997). A similar approach was applied by Joshi et al. (2008) to completely characterize the PSF using a single image. The final estimate of the PSF was defined as the average of all PSF estimates along the sampled phantom edges. Fig. 4.4 depicts the PSF of the Toshiba *Aquilion*^{TM} 64 scanner obtained directly from the CATPHAN 528 and wire phantom, as well as the estimates obtained through the ESF.

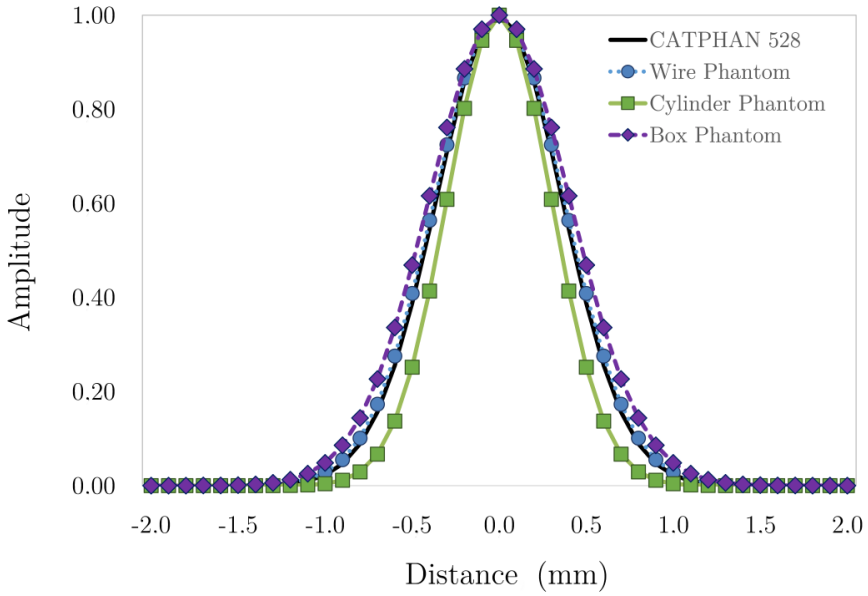

Figure 4.4: The PSF of the fourth-generation Toshiba Aquilion^{TM} 64 CT scanner with the CATPHAN 528, the 0.10 mm wire phantom, and the calibrated hollow cylinder and ceramic box phantoms

To the CATPHAN 528, the PSF has a standard deviation of $\sigma_{528} = 0.3633$ mm, and a FWHM of approximately 0.86 mm. With the wire phantom, a very similar estimate was obtained, $\sigma_{wire} = 0.3737$ mm and FWHM of 0.88 mm. The ceramic phantom provides a slightly overestimated standard deviation of the scanner PSF ($\sigma_{box} = 0.4272$ mm), whereas

the hollow cylinder provides an underestimation of the impulse response of the system, with a $\sigma_{cylinder} = 0.3145$ mm. The ceramic box is the phantom that most deviates from the standard deviation of the CATPHAN 528. For all phantom objects a single image was analysed. The determination of the PSF is both fast and accurate. The limiting resolution determined by the CATPHAN 528 and the wire phantom is approximately 0.88 mm, which, for some Datasets, is larger than the voxel size (see Table 4.1). According to Prevrhal et al. (1999) the FWHM defines the smallest spatial frequency that can be accurately described by the CT scanner. For Datasets #1, #2 and #4 both the in-plane and the cross-plane spatial resolutions are affected by the limiting resolution of the scanner. In the same way, only the in-plane resolution of Dataset #3 is affected by the limiting resolution of the system, whereas in the Dataset #5 the voxel size is the limiting factor in all three directions. Thus, an important point would be to predict the expected errors that each one of the aforementioned quantities may produce in the final reconstructed model.

4.4 Discretization Effect in the Domain Accuracy

The system's PSF may not be the only factor affecting the spatial resolution of the CT scan. Image reconstruction with large slice thicknesses is commonly associated with larger model inaccuracies (Prevrhal et al., 1999; Sato et al., 2003; Goto et al., 2007). Physical factors such as the supportable spatial resolution of the image matrix of the Data Acquisition System, and data discretization and pixel interpolation during *Filtered Backprojection* may limit image resolution.

In a recent study, Meurer et al. (2013) demonstrated that alongside with the slice thickness, the FOV also influences the spatial resolution of the scan and the amount of partial volume averaging. The size of the voxel may be more critical than other potential error sources, such as the surface meshing parameters. In Cortez et al. (2013) the impact of the voxel size and meshing parameters in the representation of a Human lumbar motion segment was analysed. It was concluded that the resolution of the CT scan (voxel size and slice thickness) was the major source of geometrical inaccuracies of the reconstructed model. Therefore, the effect of domain discretization (slice thickness and voxel size) cannot be neglected when assessing the achievable model accuracy from a given set of CT images.

To understand the effect of pixel size in domain accuracy, a fully computerized

study with the gold-standard model was conducted. Object discretization and surface meshing were performed with the software Simpleware ScanIP^{TM} v4.0, currently available at MCM. The Simpleware ScanIP^{TM} provides several tools for volumetric medical image visualization, alignment, processing, and segmentation. The software has also the Simpleware $+CAD^{TM}$ Module that enables the creation of voxelized data from standard CAD formats, and the so-called $+FE$ Module for FE volumetric or surface mesh generation. For a more detailed description of the software features the interested reader is referred to the software's Reference Guide and related bibliography (Simpleware, 2011; Young et al., 2008). The $+CAD^{TM}$ Module uses a sampling strategy that produces discrete models that have always a maximum domain deviation of half-a-voxel (Fig. 4.5).

Figure 4.5: Comparison between the reference femoral surface model obtained with Nikon Metris LK $V20$ (blue) and domain sampling with an isotropic voxel size equal to 3.0 mm (magenta)

Domain discretization was carried out with different isotropic voxel sizes. The voxel sizes considered in this analysis were $\{5.0, 3.0, 2.0, 1.5, 1.0, 0.5, 0.2\}$ (mm). The surface mesh was generated with standard settings for all voxel sizes and no surface mesh refinement was applied to the model. Surface mesh smoothing cycles were set to 20 cycles, as recommended in the user manual (Simpleware, 2011). The Mean Symmetric Distance (MSD) and the Hausdorff Distance (HD) were used to quantify the average and maximum domain deviation from the gold standard, respectively.

Fig. 4.6 (a) depicts the evolution of the average and maximum domain error as a function of the voxel size. The average error due to the domain discretization varied

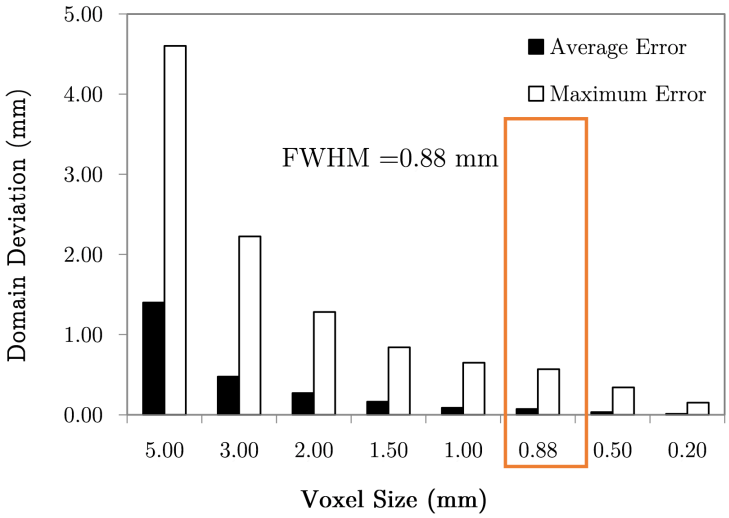

(a)

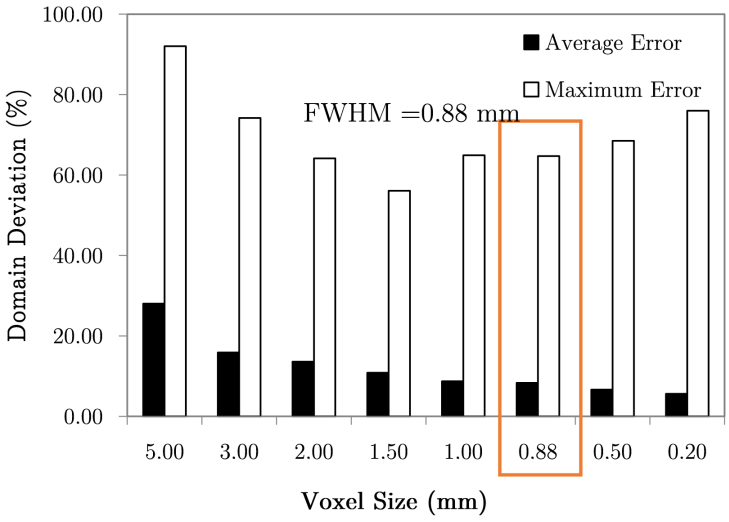

(b)

Figure 4.6: (a) the average (MSD) and maximum (HD) surface errors between the Nikon Metris $LK\ V20$ gold standard and the surface mesh obtained after domain discretization for all voxel sizes, and (b) average and maximum deviation normalized by the voxel size for all voxel sizes

between 1.401 ± 0.836 mm and 0.011 ± 0.012 mm, whereas the maximum deviation was 4.603 mm and 0.152 mm for a voxel size of 5.0 mm and 0.2 mm, respectively. The results show that when the domain sampling increases, both the absolute average and the maximum error decrease. The largest domain deviations are found in small localized sharp

features along the reference model. This is a direct effect of domain discretization that is unable to preserve geometrical features smaller than the sampling size, and becomes particularly evident for denser domain samplings. For a voxel size consistent with the size of the FWHM of the PSF, theoretically an average error of 0.073 ± 0.066 mm (8.3% of the sampling size) and a maximum deviation of 0.569 mm are expected to occur due to the domain discretization.

In Fig. 4.6 (b) the average and maximum errors are normalized against the sampling size. The normalized average error decreases from 28% to 5.6% of the sampling size, while the maximum error decreases from 92.1% to 56.1% for domain samplings between 5.0 mm and 1.5 mm. However, for edge lengths equal and below 1.0 mm, the maximum error shows a growth tendency, reaching 76.0% of the domain sampling for 0.2 mm. The normalized average error decreases and becomes almost constant for smaller sampling sizes, whereas the maximum normalized error increases initially for larger sampling sizes and increases as the sampling size becomes smaller. These observations provide an evidence that domain deviations may exist regardless of the sampling size used, and that the average deviation converges to a fixed percentage of the sampling size. For the previously determined FHWM, the sampling process introduces an average error of approximately 8.3% of the sampling size. This value can be used to limit the interpolation process, since re-sampling the data with a pixel size smaller than the 8.3% of the FWHM of the PSF may not provide more geometrical information about the target domain.

4.5 Image Segmentation and Refinement Protocol

The segmentation refinement pipeline encompasses several sub-steps, namely image deconvolution, cropping, interpolation, and level-set segmentation. The segmentation refinement protocol was tested in both noise free and noisy images corrupted with AWGN. Image de-noising is performed prior to image deconvolution, because in the Lucy-Richardson it is assumed that the image is noise-free. Fig. 4.7 illustrates each refinement sub-step. In Fig. 4.7 (a) the pre-segmentation of both noise-free (top) and noisy image (bottom) is shown. Image de-noising (applying anisotropic diffusion) eliminates most of the background fluctuations in the image, and image de-convolution enhances the

high-frequencies in the image (Fig. 4.7 (b)). Image cropping and interpolation produce a magnified version of the target structure (Fig. 4.7 (c)), reducing the computational cost of segmentation refinement process. Finally, the level-set method is applied over the high-resolution image, allowing the production of accurate representations of the target structure (Fig. 4.7 (d)). Performing the segmentation refinement over a high-resolution image allows not only the definition of a high accuracy set of points, but also to correct the pre-segmentation of the target domain (Fig. 4.8).

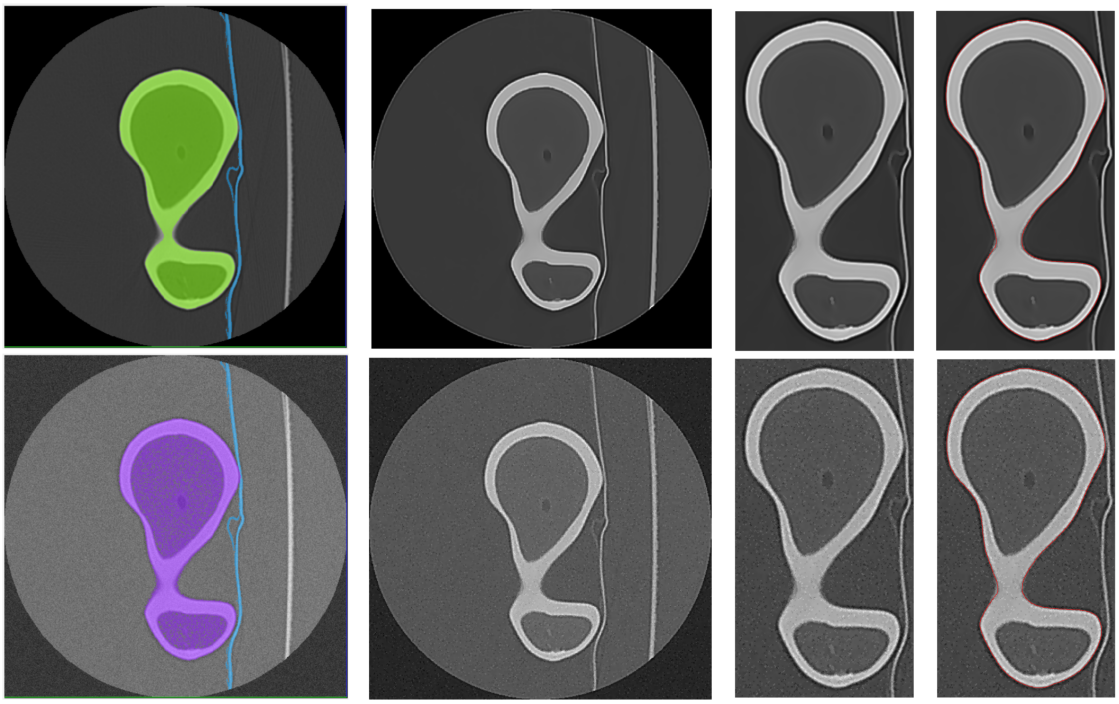

(a) (b) (c) (d)

Figure 4.7: Segmentation refinement pipeline applied to the Dataset #1: (a) image pre-segmentation of the noise-free image (top) and noisy image (down); (b) image data after de-noising with anisotropic diffusion and image deconvolution; (c) image cropping and interpolation around the pre-segmented region; and (d) the final segmentation over the interpolated image data

Two outputs may be produced after segmentation refinement (Fig. 4.3), a high-resolution point cloud model obtained directly from the interpolated image, and a down-scaled version of the high-resolution segmentation. The surface mesh model obtained from the point cloud will be referred as Point Cloud (PC) model, whereas its down-scaled version will be referred simply as ScanIP Mesh (SM) model. As mentioned previously, image refinement is performed independently in each image, therefore the PC

model is obtained tiling the cloud points contained in a set of equally spaced contours. The axial spacing between points is dependent on the slice thickness, and the final surface mesh is obtained from the triangulation of the cloud points, within the CAD software Delcam Powershape. In contrast, the down-scaled model was generated within Simpleware ScanIP^{TM} v4.0, with standard pre-smoothing and mesh refinement settings (Simpleware, 2011; Young et al., 2008).

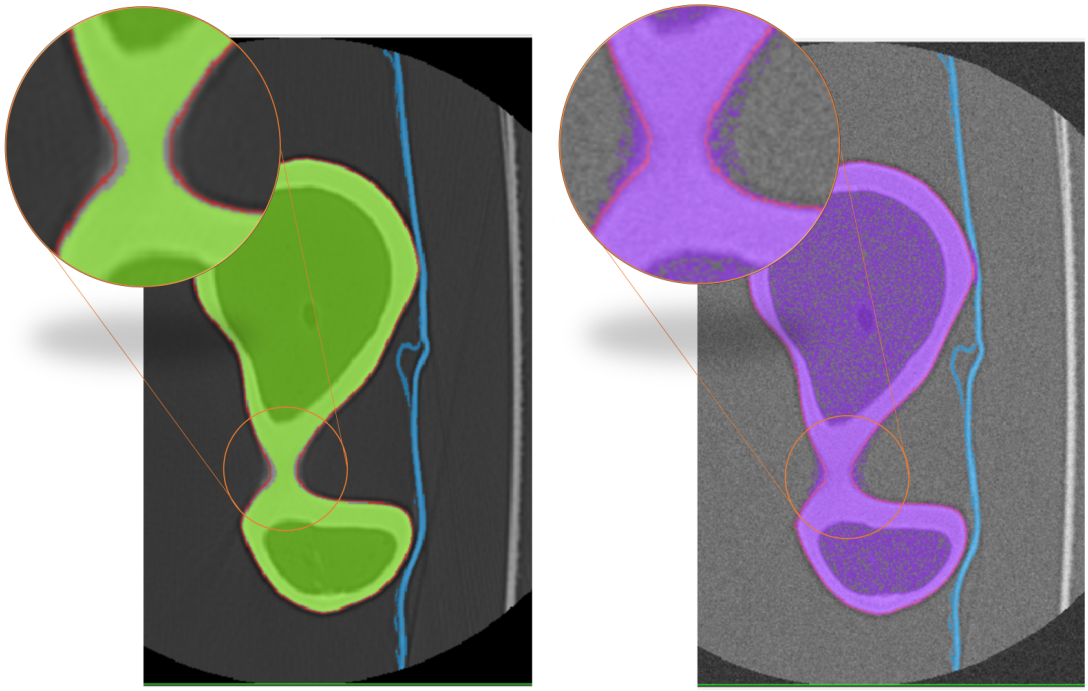

(a) (b)

Figure 4.8: Down-scaled result of the segmentation refinement pipeline applied to the segmentation of the phantom femur in Dataset #1 without image noise in (a) and with AWGN, $\sigma_{Noise} = 10$ HU, in (b)

The two surface models were produced and evaluated with distance and overlap measures. Segmentation outcomes in each independent Dataset were evaluate with the HD, MSD, and the Dice coefficient. In Fig. 4.9, the final PC model obtained from the segmentation of Dataset #1 and the comparison with the Nikon Metris LK $V20$ gold standard, whereas Fig. 4.10 depicts the down-scaled segmentation with Simpleware ScanIP^{TM} v4.0 overlapped with the reference surface. A close agreement between both PC and SM and the gold standard is observed for both cases.

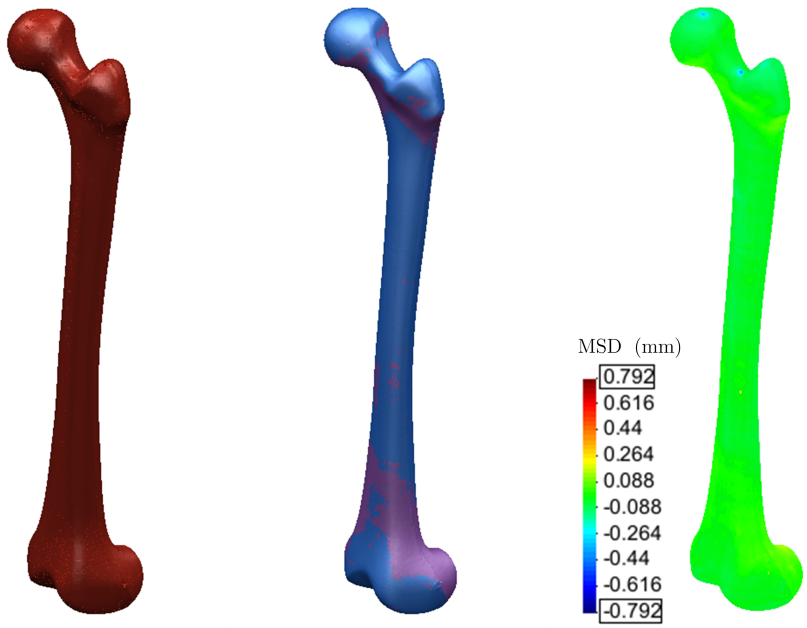

(a) (b) (c)

Figure 4.9: On the left, (a) the point cloud obtained from the segmentation of the phantom femur from Dataset #1, in the middle, (b) the surface mesh generated from the point cloud (magenta) and reference femoral surface obtained with the Nikon Metris $LK\ V20$ (blue), and on the right, (c) the comparison between the two surfaces using the MSD

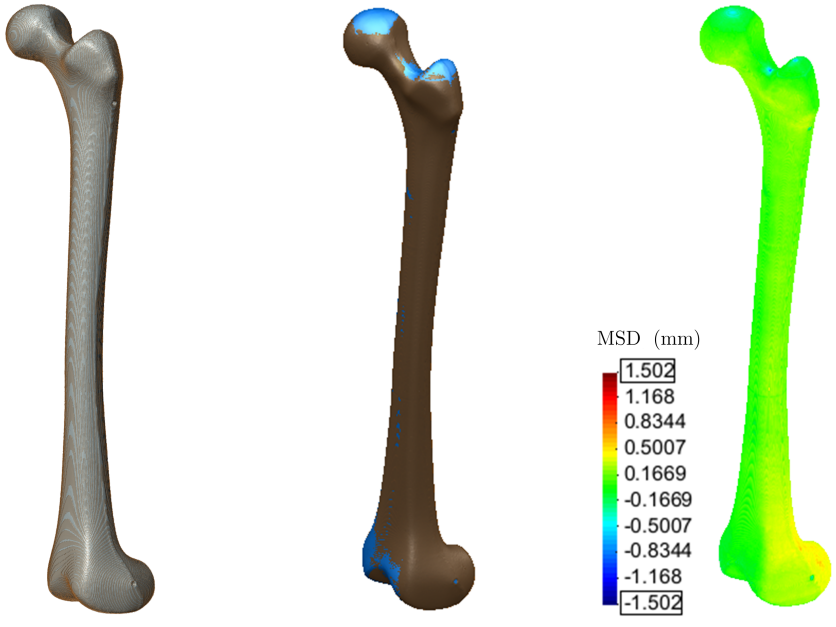

(a) (b) (c)

Figure 4.10: On the left, (a) the domain pre-segmentation and final segmentation after refinement for the Dataset #1, in the middle, (b) the surface mesh generated with Simpleware ScanIP^{TM} and the reference model, and on the right, (c) the comparison between the two models using the MSD

The agreement between the PC and SM models and the gold standard for all noise-free and noisy Datasets regarding the distance measures are summarized in Table 4.2 and Table 4.3. The average error between the gold-standard surface mesh obtained with Nikon Metris LK V20 and the PC for DS # 1 was 0.077 ± 0.075 mm (Fig. 4.9), whereas for the SM model the average error was 0.151 ± 0.125 mm (Fig. 4.10). For the Dataset #2 the average error of the SM was 0.348 ± 0.209 mm, for the Dataset #3 the average error was 0.262 ± 0.192 mm, 0.284 ± 0.115 mm for the Dataset #4, and 0.617 ± 0.501 mm for Dataset #5. Comparing the results shown in Table 4.2 and Table 4.3, the surface meshes generated directly from the high-resolution point cloud allow the production of more accurate models for all Datasets. The reduction on the average error ranges from 51% for Dataset #1 to 26% for Dataset #5 (0.159 ± 0.164 mm) for noise-free images. Similar values were observed for the noisy Datasets, and therefore the algorithm shows robustness against image noise.

Table 4.2: Segmentation accuracy for the PC model according to the HD and MSD measures for the noisy and noise-free Datasets

	Resolution (mm)			Model Deviation (mm)		
Dataset	In-plane		Cross-plane	Average (MSD)	Std.	Maximum (HD)
#1	0.243	0.243	0.30	0.077	0.075	0.792
#2	0.525	0.525	0.30	0.119	0.109	0.841
#3	0.525	0.525	3.00	0.103	0.173	1.843
#4	0.486	0.486	0.50	0.080	0.084	0.851
#5	0.972	0.972	1.00	0.159	0.164	1.073
#1 + AWGN	0.243	0.243	0.30	0.086	0.109	0.971
#2 + AWGN	0.525	0.525	0.30	0.121	0.112	0.908
#3 + AWGN	0.525	0.525	3.00	0.178	0.170	2.187
#4 + AWGN	0.486	0.486	0.50	0.103	0.083	0.907
#5 + AWGN	0.972	0.972	1.00	0.153	0.134	1.199

In the PC model, surface meshes are obtained by triangulating the 3D points, and surface smoothness is directly driven by the smoothness of the level-set contour. Contrariwise, in the SM models, the final accuracy is not only dependent on the segmentation accuracy, but also on the settings used for the surface mesh generation. The results show that surface mesh tiling allows an accurate definition of the femoral outer surface, not only in high-resolution scans, but also in scans with more *"clinical "* (or real) settings, such as the ones in Dataset #3. Surface meshing directly from the point cloud data effectively avoids the straircase artifacts commonly observed with larger slice

Table 4.3: Segmentation accuracy for the SM model according to the HD and MSD measures for the noisy and noise-free Datasets

	Resolution (mm)			Model Deviation (mm)		
Dataset	In-plane		Cross-plane	Average (MSD)	Std.	Maximum (HD)
#1	0.243	0.243	0.30	0.151	0.125	0.899
#2	0.525	0.525	0.30	0.348	0.209	1.020
#3	0.525	0.525	3.00	0.262	0.192	1.810
#4	0.486	0.486	0.50	0.284	0.115	1.022
#5	0.972	0.972	1.00	0.617	0.501	2.349
#1 + AWGN	0.243	0.243	0.30	0.172	0.130	1.164
#2 + AWGN	0.525	0.525	0.30	0.368	0.173	1.412
#3 + AWGN	0.525	0.525	3.00	0.342	0.199	1.821
#4 + AWGN	0.486	0.486	0.50	0.273	0.174	1.550
#5 + AWGN	0.972	0.972	1.00	0.572	0.275	1.776

thicknesses, and greatly improves the final model accuracy. As an illustrative example, Fig. 4.11 (a) and (b) depicts the differences between the two PC and SM models at the proximal and distal ends of the femur. The differences between the two models are evident,i.e., the staircase artifacts observed in the SM model are avoided in the PC model (Fig. 4.11 (b)).

In section 4.4, it was shown that for a domain sampling consistent with the FWHM, an average error 0.073 ± 0.066 mm was expected. As expected, image segmentation is an additional source of model errors. Nevertheless, the average error obtained for Dataset #1 is in close agreement with the theoretical discretization error. The results show that the whole chain of image deconvolution, interpolation, and segmentation only adds an average error of approximately 4.69% to the theoretical average error (for a voxel size consistent with the FWHM = 0.88 mm). The spatial limitations imposed by the PSF may superimpose to the pixels size in some Datasets, namely, DS #1 to #4. Fig. 4.12 compares graphically the theoretical average and maximum deviation from the gold standard due to domain discretization, considering the FWHM of the PSF, and the average and maximum error of all PC models. The average error added to the final model by the segmentation chain range from 4.69% for Dataset #1 to 46.54% for Dataset #5 (of the theoretical error) for images without noise. For the image data corrupted with AWGN the average error increases slightly when compared with the noise free case. Likewise, image segmentation increases the maximum deviation from the gold-standard model: there is an increase in the maximum deviation from the gold standard that ranges from 28.11%

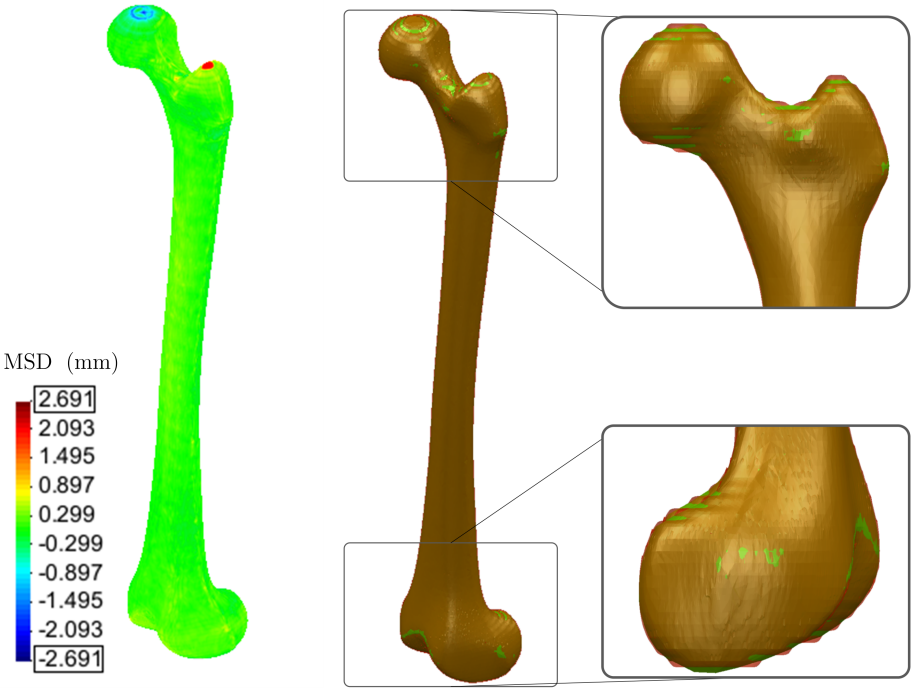

Figure 4.11: Comparison between the PC and the SM model: on the left, (a) the comparison between the gold standard and the model obtained from Dataset #3, and on the right, (b) the superposition (within *Delcam Powershape*) of the point cloud surface model (green) and ScanIP $+FE$ Surface model (brown)

for Dataset #1 to 45.42% for Dataset #5 (for images without noise). Moreover, the most important conclusion to be taken from Fig. 4.12 is that it is the domain discretization that mostly contributes to the final deviation from the ground-truth, when compared with the segmentation refinement chain.

Table 4.4 summarizes the correct and incorrectly classified pixels for Datasets #1 to #5. There is an almost perfect segmentation of the composite femur in all Datasets. A minimum Dice coefficient of 0.953 was obtained for the Dataset #5. The higher number of FP pixels comparatively to the number of FN pixels shows that the SM models overestimate the target domain, as can be seen for instance in Fig. 4.10. Contrarily to the SM models, PC models slightly underestimate the gold standard model (see for instance Fig. 4.9), with the exception of Dataset #2 and #5. Domain under or overestimation can be quantified comparing the volume of each segmented mesh with respect to the volume of the gold standard model; volume deviations for each final model are shown in Fig. 4.13.

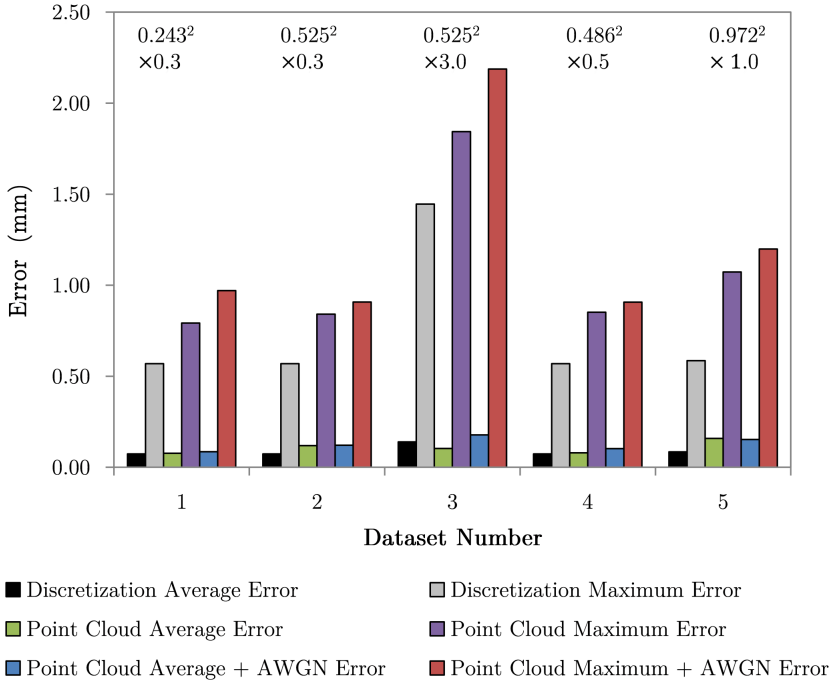

Figure 4.12: Comparison between the average (MSD) and maximum (HD) domain error caused by domain discretization with domain sampling consistent with the system's PSF and the average (MSD) and maximum (HD) error of the final models obtained from the PC procedure

Table 4.4: Evaluation of the accuracy of the Segmentation obtained by the Surface Mesh model according to the overlap measures for noise-free and noisy Datasets: True Positive (TP), True Negative (TN), False Positive (FP), and False Negative (FN)

Dataset	TP (pixels)	FP (pixels)	TN (pixels)	FN (pixels)	Dice
#1	2.5×10^7	4.6×10^5	3.8×10^8	1.2×10^5	0.989
#2	5.4×10^6	2.4×10^5	4.3×10^8	1.8×10^4	0.976
#3	5.4×10^5	2.2×10^4	4.3×10^7	5.1×10^2	0.979
#4	3.7×10^6	2.0×10^5	5.7×10^7	6.1×10^4	0.967
#5	4.7×10^5	4.5×10^4	7.1×10^6	1.2×10^3	0.953
#1 + AWGN	2.5×10^7	5.1×10^5	3.8×10^8	1.1×10^5	0.988
#2 + AWGN	5.4×10^6	2.6×10^5	4.3×10^8	7.7×10^3	0.976
#3 + AWGN	5.4×10^5	2.8×10^4	4.3×10^7	3.0×10^2	0.974
#4 + AWGN	3.7×10^6	1.9×10^5	5.7×10^7	6.3×10^4	0.968
#5 + AWGN	4.7×10^5	4.0×10^4	7.1×10^6	1.5×10^3	0.958

The maximum volume deviation was found for the noise free Dataset #5. The PC models underestimate the ROI in Datasets #1, #3 and #4, more precisely by -0.31%, -0.55% and -0.01%, respectively, and overestimate it by 0.55% in Dataset #2, and by 1.27%

in Dataset #5. For the down-scaled model volume overestimation ranges from 1.52% for Dataset #1 to 8.09% for Dataset #5, in case of noise free images, and from 1.73% to 7.70% for Dataset #1 to #5, respectively. Interestingly, for Dataset #5 the average error and volume deviation decrease with the addition of Gaussian noise. The addition of Gaussian noise and the filtering process cause an increase in the average HU intensity of the foreground pixels, while the background intensity remained almost unchanged; the net effect was an overall increases of the image's contrast. Therefore, the slightly smaller average error and volume deviation are a consequence of the sensitivity of ACWE to image contrast.

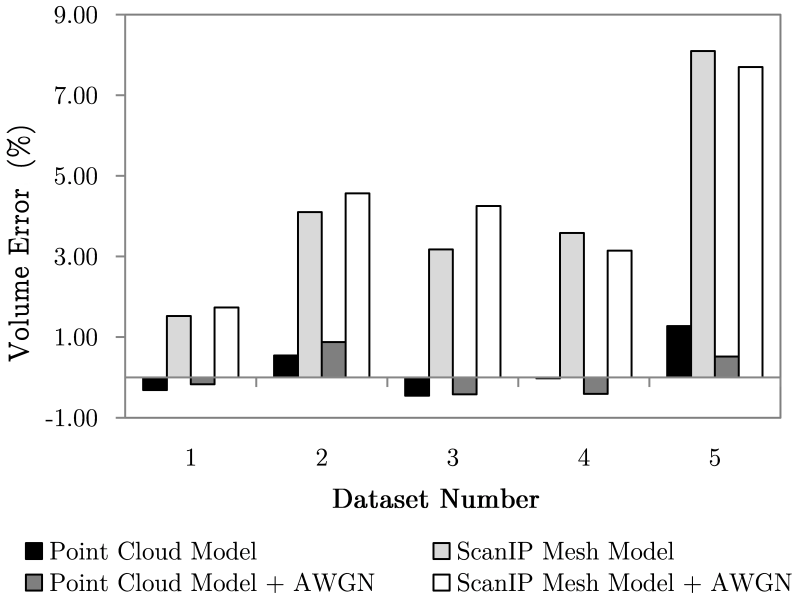

Figure 4.13: Volume error between the gold standard model obtained with the Nikon Metris $LK\ V20$, the PC-based model and SM model for noisy and noise-free images

In order to evaluate the performance of the proposed protocol, a pelvic CT was segmented. The pelvic girdle has multiple bones with complex shapes. The presence of a major fracture along the right iliac bone that passes through all three anatomical regions of this bone, namely both ilium, the ischium, and the pubis, is an additional source of segmentation complexity. Image pre-segmentation step was obtained using image thresholding and manual segmentation.

The pelvic girdle allows the evaluation of the segmentation protocol against different entries, as well as multiple anatomical regions with irregular shapes caused by the bone

fracture. Fig. 4.14 show some details about the volume pre-segmentation, with the final contours obtained with the refinement step. In Fig. 4.14 (a) and (b) is shown that the segmentation protocol preserves both user-defined spatial constraints, and smaller and thinner structures. The contours of each individual region are preserved and well defined, which indicates that the spatial constraints effectively restrain curve evolution along the image plane. This is particularly important near the sacroiliac and hip joints, where bone proximity may compromise the segmentation of each region. Object under and over-segmentation is also handled well within the refinement step, and the level-set converges to the desired contour (Fig. 4.14 (c)). In practice, under-segmentation may trap the level-set in a local minimum and compromise the final segmentation outcome. In the presence of ambiguous pixels the domain should be over-segmented rather than under-segmented. The pre-segmentation step also allows the definition of the target contours. For example, in Fig. 4.14 (d) the user can predefine the segmentation of the outer and/or inner contours of the femur. The geometrical constraints defined in the pre-segmentation can also be used to provide this type of high-level information to the refinement step. Fig. 4.15 shows the surface models obtained with both the Simpleware ScanIP meshing after segmentation refinement in (a), and the surface mesh generated within the Delcam Powershape directly from the point cloud model in (b). As shown previously and despite the geometrical complexity of each ROI, the generation of the surface models directly from the high resolution point cloud models produce smooth and potentially more accurate surface models.

4.6 Discussion

During image acquisition the CT scanner acts as a low-pass filter, eliminating all the high-spatial frequencies. The practical consequence of this is that sharp transitions between different anatomical regions become unclear, and sometimes barely recognizable. The edge blurring effect often leads to the overestimation of the ROI, and the recovery of the original scene is intrinsically limited by our knowledge about the system's PSF. The ability to accurately determine the PSF is of paramount importance if one aims to extract geometrically accurate models from medical images.

In this work we have tested three different phantom objects and their ability to estimate

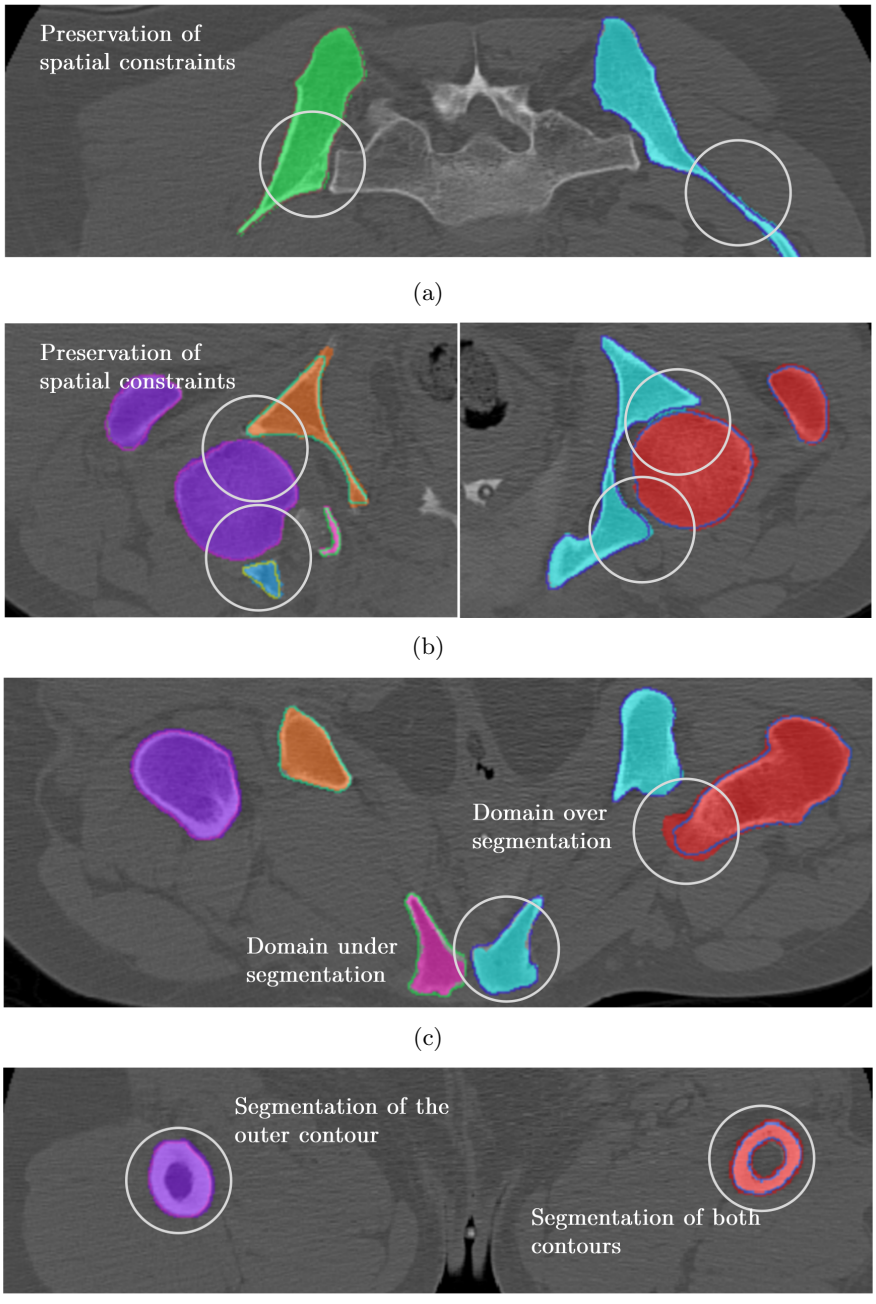

Figure 4.14: Segmentation of a pelvic CT scan with the proposed protocol: image pre-segmentation superimposed to the final contours for each ROI are obtained after segmentation refinement: in (a) preservation of the spatial relations between the sacrum, right and left iliac bones; in (b) preservation of the spatial relations between multiple regions and between the acetabular cavity and femoral head despite their proximity; in (c) the ability to handle both under or over-segmentation; and in (d) the possibility to segment the outer or both inner and outer contours of the femur

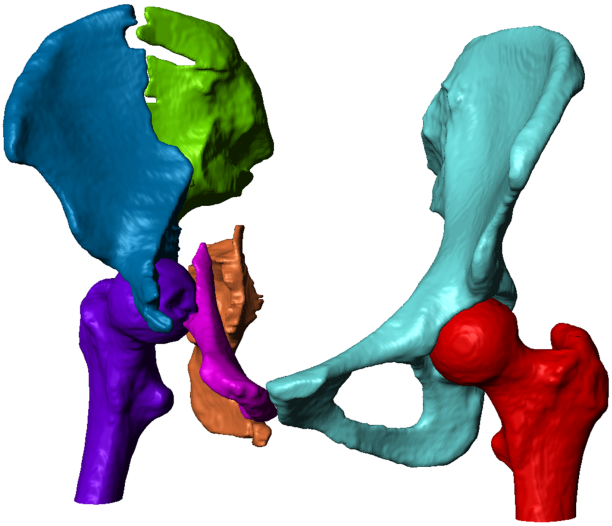

(a)

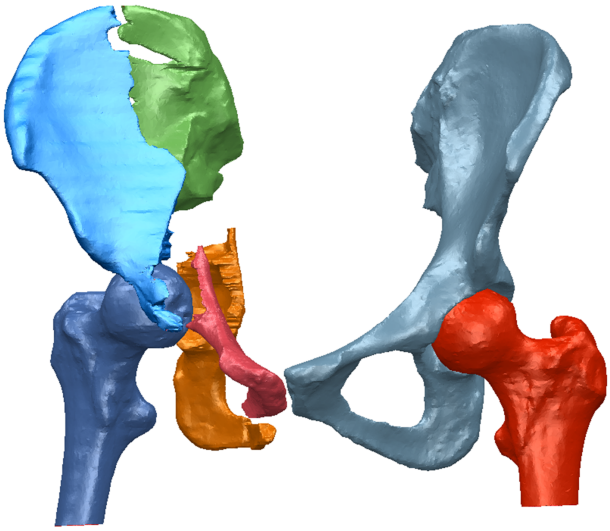

(b)

Figure 4.15: In (a) the surface model obtained with the Simpleware ScanIP after segmentation refinement and down-scaling to the original resolution of the CT scan, and in (b) the surface meshes obtained directly from the high-resolution segmentation point cloud

the system's PSF against the CATPHAN 528, which is the phantom routinely used for quality control. The phantom objects aim to estimate the PSF either directly from the system's response to an impulse signal, or indirectly through the estimation of the ESF. Relatively good estimates were obtained with all phantoms. However, the brass wire with a diameter of 0.10 mm provided the most accurate estimate of the PSF with a standard

deviation error of only 2.9% when compared with the PSF obtained with the CATPHAN 528. Similar values for the Toshiba Aquilion^{TM} 64 system were obtained by Verbist et al. (2008). Unlike direct measurements, the estimation of the PSF through the analysis of the system's response to strong edges implies additional signal processing steps. Gaussian filtering has been associated with edge bias by several authors (Verbeek and Van Vliet, 1994; Mendonça et al., 2004; Bouma et al., 2005). In addition, the ESF may be affected by the presence of image noise during the calculation of the gradient of the attenuation profile. Noise must be eliminated prior to the calculation of the gradient. In this context, Mori and Machida (2009) proposed an additional blurring correction step to eliminate the Gaussian smoothing effect from the estimate of the MTF. Instead of correcting the result, wavelet thresholding can be used to avoid linear signal filtering. Our results show that although less accurate than the wire phantom, the estimate of the PSF through the ESF and wavelet de-noising produces quite good approximations to the real CT spatial blurring function. The wavelet thresholding provides the means to accurately reduce the noise level along the attenuation profile, and to estimate the ESF without the need for any compensation procedure.

In practice, the accurate quantification of the system's PSF allows to accurately recover the original image using more standard image deconvolution algorithms. In fact, the accurate estimate of this quantity proved to be quite important to obtain accurate segmentations from image data. Krissian et al. (2000) showed that the radius estimation of tubes in CT images can be improved by modelling the PSF correctly. Similarly, Sato et al. (2003) concluded that modelling the Gaussian blurring in image post-processing is advantageous for accurate thickness determination. More recently, Pakdel et al. (2012) concluded that reversing the blurring degradation prior to segmentation is essential for the construction of accurate FE models from medical imaging.

Regarding image segmentation, a two-step segmentation pipeline was proposed. In the first step a user-defined estimate of the ROI is performed. The pre-segmentation should provide a good estimate of the desired segmentation, and may also contain additional spatial constraints to limit the following refinement step. The second step performs a segmentation refinement given the initial guess computed in step one. Segmentation refinement comprehends four sub-steps, namely image deconvolution with the PSF estimate as described in section 4.3, image cropping, image interpolation and

level-set segmentation. This procedure was applied in the segmentation of several CT volumes, obtained with different acquisition settings, and different FOV. The segmentation outcomes were validated through a phantom study, where the final models were compared against a gold standard surface mesh. The gold-standard representation of the phantom object was acquired using a coordinate measuring machine Nikon Metris $LK\ V20$ with a digital line scanner $LC60-D$, which guarantees 28 μm of spatial accuracy.

For the PC model the maximum average deviation from the gold standard was 0.159 mm for DS #5 (noise-free images) and 0.178 mm for DS #3 (noisy images), whereas the maximum deviation was 2.187 mm for Dataset #3 corrupted with AWGN (Table 4.2). These results show that the accurate estimation of the system's PSF, conjugated with image interpolation and level-set segmentation provide quite good segmentations of the target geometry. In addition, results provide clear evidences that surface meshes computed from a high-resolution 3D point cloud provide a more accurate representation of the bone than the standard surface meshing from the voxelized data. The point cloud data allows the generation of surface models that are both smooth and relatively independent from the surface meshing. Surface triangulation from adjacent contours (or surface tiling) also avoids staircase artifacts due to large section variation between consecutive slices caused by large slice thicknesses (Keppel, 1975). The advantage of using surface tiling is observable when comparing the results obtained for Datasets #2 and #3. The average errors obtained with Dataset #2 and #3 differ only by 0.016 mm. Nevertheless, the largest maximum deviation observed in the PC models may also be a consequence of surface mesh tiling, as can be observed in Fig. 4.11 (a). Enhanced information from other anatomical planes and point cloud post-processing may also be needed to obtain more accurate surface estimates especially near articular surfaces.

The results also show that is the FOV that plays a major role in segmentation accuracy rather than the slice thickness and corroborate the observation made in the phantom studies carried by Ohkubo et al. (2008) and Meurer et al. (2013). Using the high-resolution point cloud to generate the surface meshes may allow the acquisition of image data with more clinical settings, reducing the exposure of the patient to the radiation without a significant loss of model accuracy.

Image processing and segmentation are commonly seen as the main error sources in the 3D reconstruction from CT image data (Hildebolt et al., 1990; Wang et al., 2009).

From our analysis and considering the average error associated with any discretization of a continuous domain, the errors associated with the proposed segmentation pipeline varied from 4.69% to 46.54% of the final error. In section 4.4 it was analysed the average deviation from the gold standard for different sampling sizes, and an average error varying from 5.6% to 28% for finer to coarser scales was observed. For a domain sampling consistent with the system's PSF the normalized average error is approximately of 8.32% of the sampling (0.073 ± 0.066 mm).

In an ex-vivo study, Damstra et al. (2010) concluded that there were no significant differences between the linear measurements between 12 landmarks taken in 10 dry mandibles performed over CBCT surface reconstructions with 0.25 mm and 0.40 mm of voxel size. These observation show that the final resolution of the segmented model is not limited by the size of the reconstruction voxel. If the FWHM is larger than 0.40 mm, the same overall spatial resolution is expected for both the 0.40 mm to 0.25 mm scans. When determining the error related with the discretization process, the FWHM of the PSF should be consider instead of the actual reconstruction voxel size. Hence, in this study, an average error of 0.073 ± 0.066 mm is expected to occur solely due to domain discretization. This fact may also explain the average errors obtained with Dataset #1 to #4, which are very similar despite of the voxel size, and the considerable increase in the average error observed for Dataset #5. In Dataset #1 and #4, the system's PSF is the main limitation to the model spatial accuracy, whereas in Dataset #5 the main limitation is the voxel size itself. The average error obtained from Dataset #1 shows that the whole chain of image deconvolution, image up-scaling through cubic spline interpolation, and subsequent segmentation, there is almost no information degradation or distortion due to the image processing pipeline. Our observations also corroborate previous observations by Cortez et al. (2013), in which the domain discretization contributes in a larger extent to the final error of the surface mesh model.

The two-step segmentation proposed in this work is very similar to other methods proposed in the literature. For comparison purposes, the main results obtained by other authors, as well as the in-plane and cross-plane resolutions of the CT image data, are summarized in Table 4.5.

From the analysis of Table 4.5 it can be seen that only two cases have an average error smaller than the maximum average error obtained with the proposed segmentation

Table 4.5: Bone segmentation accuracy in other studies found in the literature

	Resolution (mm)			Model Deviation (mm)		
	In-plane		Cross-plane	Average	Std.	Maximum
Aamodt et al. (1999)	0.312	0.312	2.00	0.03	0.52	5.75
Kang et al. (2003)	0.200	0.200	0.50	0.20	0.09-0.13	0.26
Oka et al. (2009)	0.293	0.293	0.63	0.46	0.03	0.49
Wang et al. (2009)	0.195	0.195	1.00	0.21	0.12	0.47
Liang et al. (2010)	0.480	0.480	0.50	0.14	--	1.81
Treece et al. (2010)	0.589	0.589	1.00	0.02	0.77	--
Rathnayaka et al. (2011)	0.390	0.390	0.50	0.18	0.20	--
Pakdel et al. (2012)	0.480	0.480	1.00	0.14	0.11	--
Dataset #1	**0.243**	**0.243**	**0.30**	**0.077**	**0.075**	**0.792**
Dataset #2	**0.525**	**0.525**	**3.00**	**0.119**	**0.109**	**0.841**
Dataset #4	**0.486**	**0.486**	**0.50**	**0.080**	**0.084**	**0.851**

refinement protocol, namely the optimized 600 HU threshold proposed by Aamodt et al. (1999) and the Levenberg-Marquardt-based algorithm proposed by Treece et al. (2010). Regarding the proposal of Aamodt et al. (1999) it is worth mentioning that the same accurate results were not reproduced in all eight femurs considered in the analysis. For the eight femurs the average error varied from -0.20 mm to 0.20 mm, which is larger than the maximum average error obtained with our algorithm for all Datasets. Similarly, the algorithm proposed by Treece et al. (2010) has a standard deviation from the average value of 0.77 mm. Therefore, 68.2% of the surface points are within -0.365 mm and 0.405 mm from the surface (considering the deviation on each side of the thickness measure). Comparing with the results in Table 4.2, in the worst case scenario (Dataset #5), 68.2% are at a maximum distance of 0.322 mm from the ground truth. The algorithm proposed by Treece et al. (2010) mainly oscillate around the true surface of the cortical bone instead of recovering it. Slightly less disperse results were obtained by Pakdel et al. (2012), with 68.2% of the surface points within the distance range of 0.030 to 0.250 mm. For a comparable pixel resolution (Dataset #4), the results obtained with the proposed algorithm have a smaller average error of 0.080 mm (with 68.2% of the surface points within the interval of -0.004 to 0.164 mm) for noise free data, and with an average error of 0.103 mm (with 68.2% of the surface points within the interval of 0.020 to 0.186 mm) for noisy data.

The practical implications of an average deviation from the gold standard of 0.159 mm (0.178 mm with AWGN) in custom implant modelling are still unclear. In an early study, Carlsson et al. (1988) found that implant-bone surface gaps of 0.35 mm or more

were not bridged by cortical bone, and that this value is close to the critical gap width for which direct lamellar bone apposition occurs onto unloaded implants. In an animal study, Pazzaglia et al. (1998) found that there was no bone integration at the interface of roughened titanium rods with 0.30 mm of diametrical gaps at the bone-implant interface. In addition, Penzkofer et al. (2009) concluded that enlarging the tibial canal by 0.30 mm can easily lead to a maximum intra-fragmentary shear movement of approximately 0.65 mm. Intra-fragmentary bone movements are of paramount importance for proper bone healing or delayed fracture union. Augat et al. (2003) concluded in an animal study that an intra-fragmentary shear movements of 1.50 mm may significantly delay bone union, whereas Schell et al. (2005), in another animal study, concluded that for shear intra-fragmentary movements below 0.80 mm optimal bone healing was observed.

The inaccuracies obtained with the proposed algorithm may have minor practical implications in the performance of the custom implants developed from the 3D models for both orthopaedic and trauma applications. It also allows us to model custom implants with more restrictive tolerances than other authors. In Aamodt et al. (1999) an inward offset of 0.50 mm to the contours obtained with the 600 HU contour was proposed to avoid custom femoral stem over dimensioning. Endosteal contour shrinkage is needed due to the large standard deviation (0.52 mm) around the average error (Table 4.5). Another factor worth mentioning regarding the implant performance after implantation is the surgical technique used to position the implant within the host bone. In a comparative study, Paul et al. (1992) concluded that the femoral canal reaming of the femoral cavity by means of a robotic system is far more accurate than the traditional broaching technique used by surgeons. The linear gaps measured between the implant surface and the femoral canal after traditional broaching ranged from 1.0 to 3.0 mm, whereas with the surgical robot were 0.03 to 0.08 mm. Hence, under traditional surgical techniques, the inaccuracies due to the surgical procedure may play a more relevant role in the implant outcome than the geometrical accuracy obtained during implant modelling.

The deviation from the ideal contour in lower resolution Datasets may be related with the assumption of homogeneity implicit to the ACWE framework, and its sensitivity to image contrast. For the high-resolution Dataset #1, these assumptions seem to be met by the CT images, and a quite accurate estimate of the bone's surface is obtained. The assumption of homogeneity may not hold for low resolution Datasets, where partial

volume averaging is more pronounced. The sensitivity to image contrast was also observed comparing the results obtained in Dataset #5 and Dataset #5 + AWGN. Nevertheless, our results also show that bone segmentation through the level-set method is accurate and possesses numerous advantages against other segmentation methods.

The level-set method is robust to noise, it guarantees contour smoothness, is topologically flexible, and allows a straightforward incorporation of user-defined spatial constraints. Yao et al. (2005) concluded that Geodesic Active contours (GAC) were not suitable for accurate bone segmentation. In fact, the GAC are less topologically flexible than the ACWE used in this work. The Chan-Vese ACWE level-set method has the advantage of being topologically more flexible and also less sensitive to initialization. This fact was previously noted by Truc et al. (2010), which concluded that the ACWE level-set method have an excellent ability to accurately segment bone regions in CT imaging. The ACWE allow a more flexible pre-segmentation process.

As described in section 4.1 the information normal to the edges of the ROI was successfully used by several authors to accurately extract both inner and outer surface of the bone. The addition of edge information may help to minimize the effect of partial volume averaging and the dependency on the image contrast. The incorporation of the information normal to the bone surface in the proposed segmentation refinement protocol is also possible. The direction of the normal vector is known at all-times and can be calculated directly from the signed distance function. The incorporation of such information may constitute a possible improvement to the current methodology, and may be important to increase the accuracy of the segmentation for lower resolution Datasets.

The main limitations of the present study are directly linked with the limitations often associated with every phantom study. Phantom studies are flexible to parameterize and allow the simulation of different acquisition and reconstruction protocols, noise levels, among others. In this type of studies the ground truth may be accurately characterized, and does not change under different environmental conditions. Nevertheless, phantom studies may not be realistic enough to model the complexity of the real world. The CT images used in this analysis have good contrast and are almost noise free. Such images are very difficult or even impossible to obtain in practice. The ACWE are very robust to noise but sensitive to image contrast, therefore in real data the performance of the present algorithm may be slightly degraded. Furthermore, although the use of ACWE enables

some degree of flexibility in the pre-segmentation step (as seen in Fig. 4.14). There is still, however, some dependency on the curve initialization. Image under-segmentation seems to be more problematic than over-segmentation, hence in ambiguous pixels it is better to over-segment the domain rather than excluding the pixels. The elimination of such a dependency and the extension of the protocol to the third dimension, in order to obtain a 3D point cloud instead of the current 2D contours, are natural evolutions to the newly proposed algorithm, and will be considered in future work. These may facilitate the pre-segmentation step and may help to overcome the limitations of surface mesh tiling near bone ends, and allow the production of more accurate models near articular surfaces.

4.7 Summary

In this chapter a two-step segmentation pipeline for accurate bone segmentation from CT image data was proposed. The proposed methodology tries to handle segmentation variability by allowing a first free pre-segmentation step, where the user can employ the necessary means to obtain a good approximation to the target segmentation. The second step is standardized and fully automatic and encompasses image restoration, cropping, interpolation, and level-set segmentation. Each ROI is handled independently and the remaining ROIs are taken as spatial constraints to the level-set evolution. The proposed methodology produces accurate estimates of the target geometries with a maximum average deviation of 0.159 mm and 0.178 mm for images corrupted with AWGN. The pre-segmentation allows the definition of both spatial and geometrical constraints that successfully drive the refinement step towards the desired domain partition. The level-set framework allows the incorporation of these constrains into the refinement step in a straightforward manner. According to the results, it can be concluded that surface meshes extracted directly from the high-resolution point cloud reflect more accurately the target ROI. For these meshes, the final model accuracy is mostly affected by the image acquisition and reconstruction, rather than by the image segmentation and surface meshing processes. It can also be concluded that the CT machine PSF can be accurately determined using a brass alloy wire phantom with a diameter of 0.10 mm. The direct measures provide slightly more accurate estimates of the system's Point Spread Function, when compared with indirect measures based on the Edge Spread Function.

Chapter 5

Intramedullary Nailing System

In this chapter a Computed Tomography based tibial nailing design protocol is presented. Taking into account recent concepts related with fracture management, a new tibial nailing system is proposed. The tibial nailing system is validated for three types of acute tibial fractures and for the critical loading conditions, found along the proximal tibia during Human locomotion.

This page was intentionally left blank

5.1 Introduction to Fracture Management

A bone fracture is a disruption of the normal architecture of the bone, caused by single or multiple overloading events. Bone fractures may have different etiologies and three fracture types can be identified, namely: acute fractures, chronic fractures, and pathological fractures. Acute fractures are high-energy, sharp edged, and well-defined fractures caused by severe bone overload; chronic fractures are delayed unions or non-unions and have rounded ends; pathological fractures are bone disruptions caused by a pre-existing disease such as osteoporosis (Townsend et al., 2012).

Fractures can also be classified according to their anatomical location, pattern of disruption, degree of bone fragmentation, and relative displacement between the main fragments (Townsend et al., 2012). The most widely used fracture classification system is probably the AO Fracture Classification System, proposed by the AO-ASIF Foundation (Fig. 5.1). In the AO Fracture Classification System, an identifying number is attributed to each long bone, as well as to the pelvis, the spine, the hand, and foot (1 - Humerus; 2 - Radius-Ulna; 3 - Femur; 4 - Tibia-Fibula; 5 - Spine; 6 - Pelvis; 7 - Hand; and 8 - Foot). Each independent bone is further subdivided into three anatomical regions, the proximal segment or region 1, the diaphyseal segment (region 2), and the distal segment (region 3). The two initial numbers of the AO Classification System clearly define the location of the fracture. Next, the fracture is classified according to an increasing scale of fracture severity, where A strands for simple or multi-fragmentary fractures, and where multi-fragmentary fractures can be wedged (type B), or complex (type C) fractures. Each type of fracture can be subdivided into another three groups and subgroups, also in an increasing order of complexity and decreasing successful expected outcome. These two additional numbers provide the information about the morphology of the fracture (Müller et al., 1991). For instance, in the presence of a mid-shaft circumferential disruption (simple fracture, A) of the tibia-fibula complex, with an intact fibula, the AO Classification is $42 - A1.1$.

Bone fractures can cause the loss of the supporting function of bone, and cause severe impairments to mobility. In the presence of a bone disruption, the human body attempts to naturally stabilize the mobile fragments by promoting pain-induced movements. However, bone is commonly unable to repair itself under such unstable conditions (Kenedi, 1971). Therefore, the surgical treatment aims first to stabilize the fracture site, providing guidance

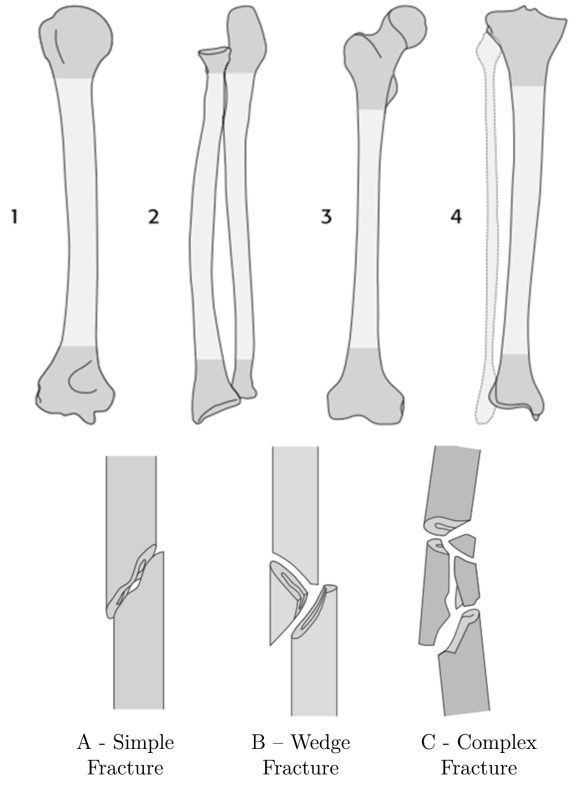

Figure 5.1: The AO-ASIF Fracture Classification system: the first and the second numbers specify the bone and the anatomical sub-region where the fracture occurred; the letter A, B and C define the type of bone fracture from simple to complex fracture, and the two additional numbers provide the morphological information about the fracture pattern (Müller et al., 1991)

and supporting the bone healing process. The degree of stability needed is heavily dependent on the type of fracture and anatomical location. Nevertheless, there is always the need for some inter-fragmentary movement for proper healing. Currently, internal fixation is the gold standard for the management of the great majority of the bone fractures, whether by applying an intramedullary nailing system or a locking compression plate. Intramedullary nailing systems are flexible fixation devices often used in the management of mid-shaft fractures, whereas compression plates are the treatment of choice for intra-articular fracture management, where complete stability is vital (Rüedi et al., 2007).

Fracture management via internal fixation devices aim the immediate stabilization and full function recovery of the injured limb (Rüedi et al., 2007). Contrarily to compression

plating, an intramedullary nailing system is a load sharing device that allows early weight-bearing across the fracture site and provides temporary support to the bone. The biomechanical principles of intramedullary nailing were introduced by Küntscher (1940) in the 1940. The initial designs of intramedullary rods provided only relative stability without inter-fragmentary compression. Later on, Küntscher and Rinne (1967) also introduced the concept of intramedullary reaming. Bone reaming allowed not only the preparation of the medullary canal to a specific nail diameter, but also allowed a more efficient fixation due to the accurate fit between the nail and the diaphyseal region of the medullary canal (Müller et al., 1991). Herzog (1958) also modified the Kuntscher tibial nail by adding a proximal 20 degrees and distal 5 degrees bend to the tibial intramedullary nail, and lateral slots at the distal end to accept anti-rotational wires. These new concepts allowed a more anatomical placement of the femoral nails within the medullary cavity, and the eccentric insertion of the tibial nail permitted the preservation of the tibial plateau (Morandi et al., 2010). Grosse et al. (1978) were responsible for the introduction of the interlocking system. The interlocking system enhanced the ability of intramedullary nails to withstand torsional movements, axial loads, and prevent limb shortening (Schandelmaier et al., 1996). It also provided a mechanism to avoid rotational and longitudinal mal-alignment in long bones, reduced the rates of infection, fracture non-union or malunion, and allowed shorter recovery times when compared with conventional non-locking nails (Kempf et al., 1985).

Due to the continuous evolution of nail design and materials, the indications for both reamed and unreamed intramedullary nailing systems have been expanded. In the last decades, the applications of intramedullary nailing systems have expanded to the treatment of very proximal and distal tibial and femoral fractures, which where commonly managed with standard compression plating or external fixation techniques (Bong et al., 2006; Konrath et al., 1997). Currently, the intramedullary nailing is considered the gold standard surgical procedure for the treatment of diaphyseal closed or open tibial fractures (Alho et al., 1992; Henley et al., 1998; Hooper et al., 1991; Schandelmaier et al., 1997; Morandi et al., 2010; Schmidt et al., 2003). The design features of modern tibial nails allow an easier insertion, provide enhanced fracture stability, and reduce the axial mal-alignment between the main fragments (Kuhn et al., 2007, 2008).

Nowadays, two types of intramedullary nails can be used for tibial fracture management, namely reamed or unreamed nails. In unreamed nailing there is no need

for medullary canal preparation during surgery, they are commonly triangular in shape, and smaller in diameter when compared with reamed intramedullary nails. There is still, however, a lot of controversy in the medical community regarding which techniques is the most suitable for fracture management. On the one hand, both open and closed tibia fractures seem to benefit from reaming. With reamed nailing faster healing times and fewer hardware failures were demonstrated in several studies (Hutson et al., 1995; Finkemeier et al., 2000; Ziran et al., 2004). On the other hand, in animal trials, unreamed solid nails showed an improved preservation of the blood supply, and a higher resistance to infection when compared with reamed nailing. However, with unreamed nailing systems longer recovery times were needed to achieve bone union (Melcher et al., 1995). Unreamed nails seem to perform satisfactorily well in mid-shaft stable fractures, but in multi-fragmentary unstable, segmental, proximal or distal fractures, they seem to increase the risk of healing disturbances, implant failure, and mal-alignment (Hutson et al., 1995; Uhlin and Hammer, 1998; Ziran et al., 2004).

Tibial fractures are the most common fractures of long bones (Praemer et al., 1999; Schmidt et al., 2003). Fractures of the tibia are frequently associated with high-energy trauma, and their complexity may vary from simple closed fractures to vascular compromised limb fractures at high risk of amputation. Contrarily to the thigh, the absence of abundant soft tissue in the leg is an additional risk factor to fracture management and to a complete functional recovery (Flint, 2008). The efficient treatment of tibial fractures is particularly important due to the long recovery period and high ratio of permanent morbidity, especially in major tibial fractures (Horne et al., 1990). The design of functionally optimized tibial nailing devices capable of enhancing the treatment outcomes may be particularly important in tibial fracture management.

In this chapter an optimized tibial nailing system for the management of tibial fractures is developed. The current chapter is organized as follows: in section 5.2 the anatomy of the Human leg is reviewed; in section 5.3 the surgical tibial nail planning is described; section 5.4 the segmentation protocol used to segment the 3D tibial model from the CT data is presented; section 5.5 is dedicated to the description of the tibial nail design, and section 5.6 to the validation of the implant geometry according to biologically plausible critical loading conditions found at the proximal tibia during full weight bearing; ultimately in section 5.7 the main conclusions are summarized.

5.2 Anatomy of the Human Tibia and Fibula

The leg skeleton is composed by two bones, the tibia and the fibula, which articulate with each other both proximally and distally. The tibia articulates with the femur in the proximal region forming the knee joint, whereas distally it articulates with the talus bone in the ankle or taloclural joint. The fibula is not involved in the knee joint, but it is an important part of the ankle joint.

The tibia or shinbone is situated in the medial side of the leg, and is the second strongest and largest bone of the human body (Fig. 5.2 (a)). It is a weight bearing bone, responsible for receiving the body weight and transmit it to the foot. The bone is prismatic in shape, wider proximally than distally. In the proximal end it possesses two concave eminences that articulate with the condyles of the femur, the medial and lateral condyles (Fig. 5.2 (b)). Separating the medial and lateral condyles there is a protrusion, the intercondylar eminence that widens the articulating surface and provides attachment for the anterior and posterior cruciate ligaments (Gray and Lewis, 1918). On the anterior surface, the tibia has a prominent process called the tibial tuberosity, which provides attachment to the patellar ligament. At the distal end, the medial surface of the tibia forms the medial malleolus, which articulates with the talus bone of the ankle, whereas the lateral side articulates with the fibula at the fibular notch (Mader and Galliart, 2005).

The fibula is a thin elongated bone with slightly expanded ends, located slightly posterior to the tibia on the lateral side of the leg (Fig 5.2 (a)). Although not responsible for any load-bearing function, it provides attachment to several muscles in the leg. In its proximal end, the fibula articulates with lateral aspect of the tibia, slightly below the tibial lateral condyle. Whereas in the distal end it possesses a projection, the lateral malleolus that articulates with the talus and gives lateral stability the tibiotarsal joint. On the medial side the fibula is attached to the tibia by the interosseous membrane (Mader and Galliart, 2005; Frank et al., 2013).

In males, the long axis of the tibia lies vertically and parallel to the axis of the contralateral tibia, whereas, in females, the anatomical axis has a slight oblique direction downward and lateralward (Gray and Lewis, 1918). In the sagittal plane, the tibial medial and lateral condyles have a posterior slope of about 10 to 20 degrees what contributes to the antero-posterior staibility of the knee joint. In the axial direction the lateral malleolus

lies approximately 15 to 20 degrees more posteriorly than the medial malleolus (Fig. 5.2 (b)) (Mader and Galliart, 2005).

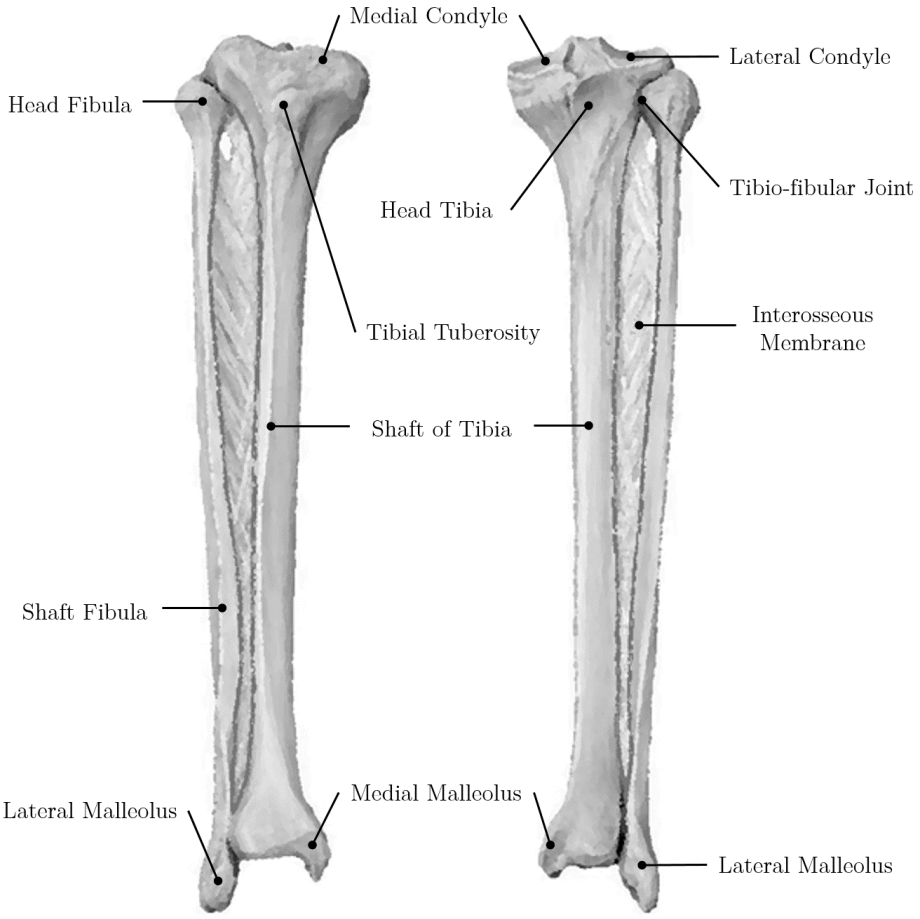

(a)

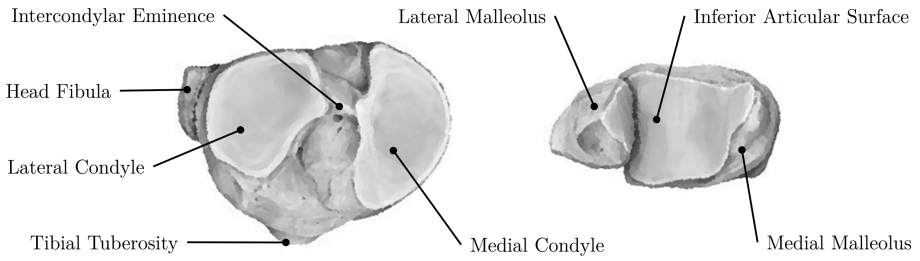

(b)

Figure 5.2: The skeleton of the Human leg composed by the tibia and fibula (a), and the proximal and distal aspects of the human tibia and fibula (b), (adapted from (Schuenke and Schulte, 2011))

In the tibial plateau several axes and landmarks can be defined as anatomical guides during surgical procedures, such as Total Knee Arthroplasty (Fig. 5.3). The tibial centre is defined as the bisection of the transverse tibial axis, and lies near the lateral insertion of the anterior cruciate ligament. The upper tibial transverse axis is defined as the line connecting the medial and lateral midpoints of the medial and lateral condyles, respectively. The antero-posterior tibial axis is often defined as the perpendicular extension of the tibial centre on the transverse tibial axis. In the axial direction the tibial tuberosity is typically externally rotated 18 degrees relative to the antero-posterior axis. Similarly to the upper tibia, the centre of the distal tibia is often determined as the midpoint of transmalleolar axis between the medial and lateral malleoli (Stiehl et al., 2007). The transverse axis of the upper tibia and the transverse axis of the lower tibia should make an angle of approximately 23 degrees when superimposed (the transmalleolar axis is externally rotated 23 degrees relative to the transverse condylar axis) (Schuenke and Schulte, 2011). Another axis that can be defined is the posterior condylar axis that passes along the most posterior aspects of both tibial condyles. The posterior condylar axis of the tibia is rotated 3 to 4 degrees relative to the transverse tibial axis (Stiehl et al., 2007).

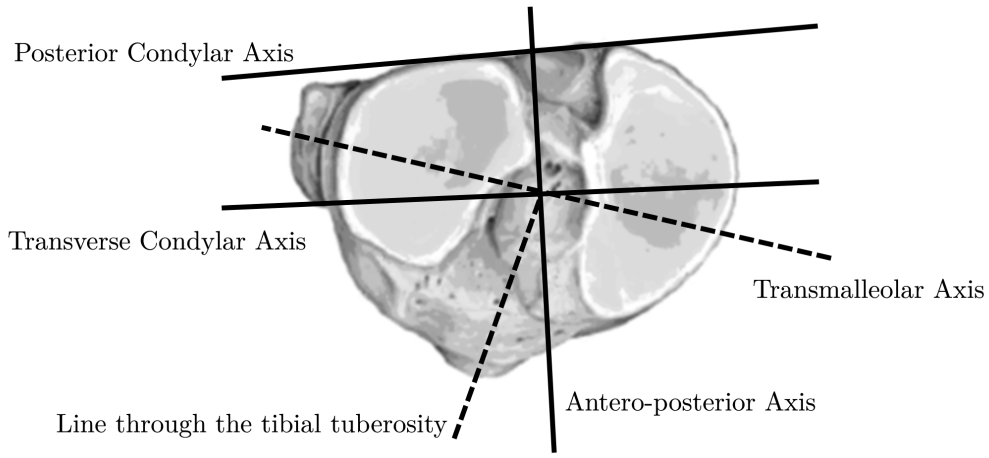

Figure 5.3: The anatomical axes of the proximal tibia (adapted from (Stiehl et al., 2007; Schuenke and Schulte, 2011))

5.3 Surgical Planning and Insertion Technique

As mention in the introduction (section 5.1), one of the major goals of tibial nailing is the preservation of the leg length. The correct implant length is determined during pre-operative planning. The nail length is determined by measuring the distance between the knee joint line and the tibiotarsal joint and subtracting 30 to 40 mm in the unaffected side. The nail diameter is defined by finding and measuring, with a radiolucent ruler, the isthmus of the medullary canal (Texhammar et al., 1994).

During nail insertion, the patient is positioned in a supine position with the knee of the affected limb bended 90 to 100 degrees (Fig. 5.4). A skin incision of 15 to 20 mm is made in line with the tibial medullary cavity and sufficiently far from the entry point on the bone (Texhammar et al., 1994). The entry point on the bone should be in line with the axis of the intra-medullary canal and the lateral tubercle of the inter-condylar eminence, whereas in the lateral view the entry point should be located over the anterior edge of the tibial plateau (Synthes, 2006). It is important to position the entry point as proximally as possible to facilitate nail insertion, however sufficiently below the intercondylar area to avoid damaging the articular cartilage. The correct definition of the nail entry point is paramount, because the mal-positioning of the entry point may lead to axial and rotational mal-alignment, what is commonly associated with stress fractures of the hardware (Rockwood et al., 2010). In case of reamed tibial nailing, the medullary canal should be over-reamed at least 1.0 mm wider than the intramedullary nail used to bridge the fracture (Bhandari et al., 2003).

5.4 Segmentation of the Human Tibia

The DICOM image data used in this chapter can be found and downloaded from the OsiriX public database website[1]. The size of the DICOM volume was cropped along the sagittal plane, in order to reduce the overall size of the image data to be processed (Fig. 5.5).

The volume segmentation was performed in a top-down fashion, starting with an initial foreground-background segmentation that was progressively refined until the final segmentation was achieved. First, the Otsu Threshold was used to discriminate the

[1] *http://www.osirix-viewer.com/datasets/*

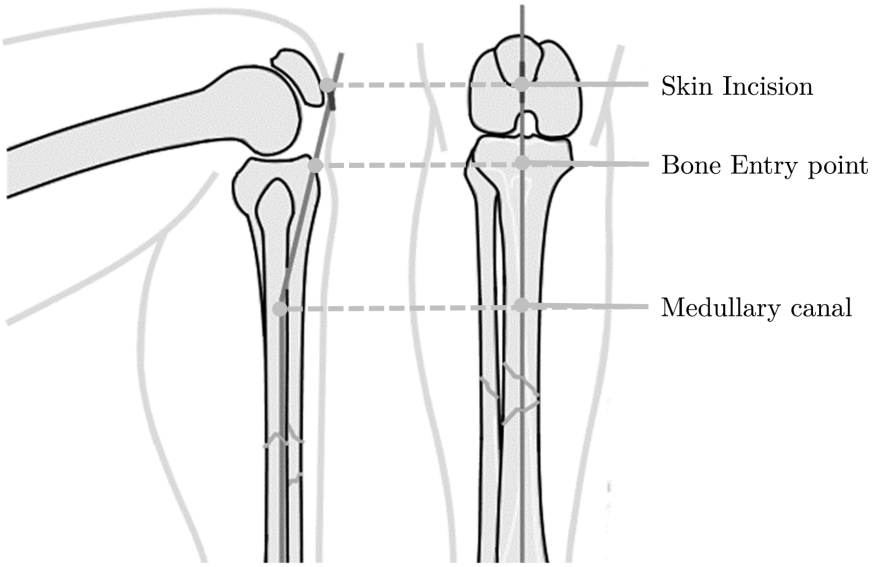

Figure 5.4: Surgical approach to tibial nailing, with the affected leg flexed 90 to 100 degrees: the skin incision is made in line with the medullary canal and far from the entry point in the bone, whereas the bone incision is placed as proximally as possible near the tibial plateau (adapted form (Rüedi et al., 2007))

foreground from the background. The thresholding indiscriminately selects all voxels above the specified value (Fig. 5.5 (a)). Both Human soft and hard tissue as well as the CT table were segmented, due to their high attenuation values comparatively to the background. The binary partition obtained by global thresholding was further sub-divided into leg and CT table, applying a Region Growing (RG) operation to the foreground mask. These two operations allowed the complete separation of the foreground (Human tissue) from the background (machine hardware) (Fig. 5.5 (b)). Next, the bony tissue was segmented from the remaining soft tissues belonging to the foreground. A Fuzzy C-means Clustering (FCM) with four clusters (soft tissue, fat, trabecular bone and cortical bone) was applied solely to the foreground pixels. Fig. 5.5 (c) depicts the clustered data, where fat is represented by the darker greyscale value, and the cortical bone corresponds to the brighter pixels (the greyscale represents the average intensity of each cluster normalized to a 256 greyscale). Since our focus is the correct definition of the medullary canal both trabecular and cortical bone were combined into the same final mask, which was then refined according to the segmentation refinement proposed in Chapter 4 (Fig. 5.5 (d)).

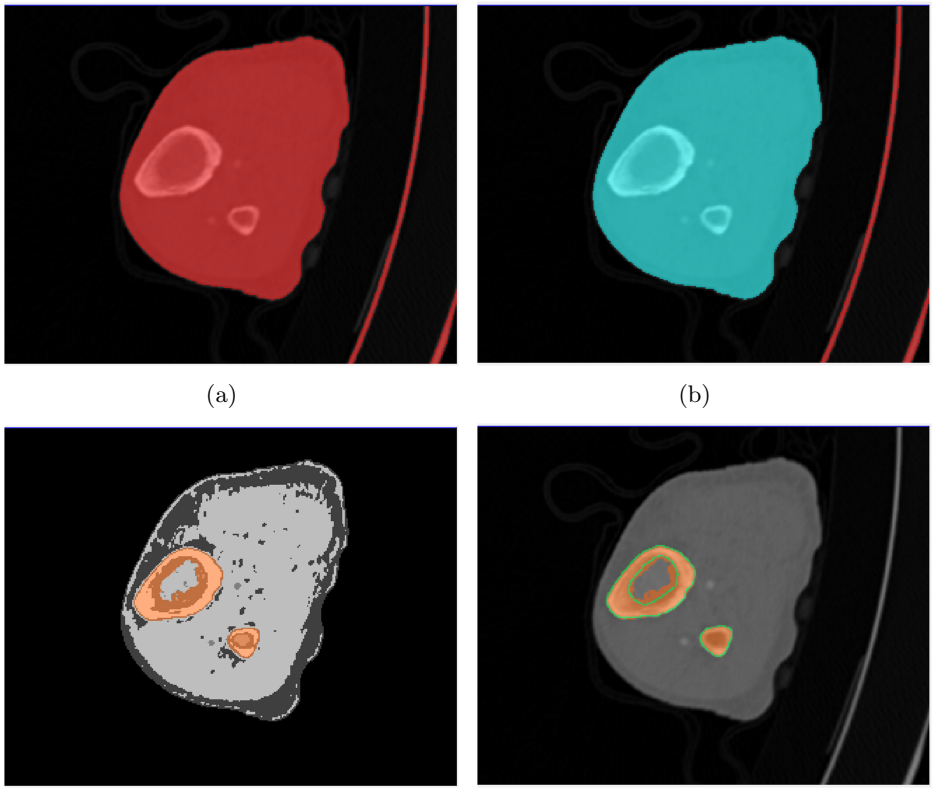

(a) (b)

(c) (d)

Figure 5.5: Segmentation protocol of the human tibia: in (a) volume segmentation by global thresholding; in (b) separation of the human body from the CT table by applying a binary RG; in (c) Fuzzy clustering is applied to discriminate the hard and soft tissues in the leg; and (d) segmentation refinement of the inner and outer surface of the bone

5.5 Design of the Tibia Intramedullary Nailing System

For correct tibial nail planning, first one needs to properly define the relevant anatomical frames and landmarks associated with the human leg. The International Society of Biomechanics (ISB) defined a standard coordinate system to describe the tibia-and-fibula complex (Fig. 5.6). In this reference frame, several external landmarks need to be identified, namely: the tip of the medial malleolus (MM), the tip of the lateral malleolus (LM), the most medial point on the border of the medial tibial condyle (MC), the most lateral point on the border of the lateral tibial condyle (LC), the tibial tuberosity (TT), the inter-malleolar point (IM) located midway between MM and LM, and the intercondylar

point (IC) located midway between the MC and LC anatomical points. With these landmarks the standard anatomical planes of the tibial-fibula complex can be defined. The frontal plane contains the IM, MC and LC points. The sagittal plane is perpendicular to the frontal plane and contains the long axis of the tibia/fibula, which is defined as the line connecting the points IC and IM. The transverse plane is perpendicular to both the frontal and sagittal planes (Wu et al., 2002).

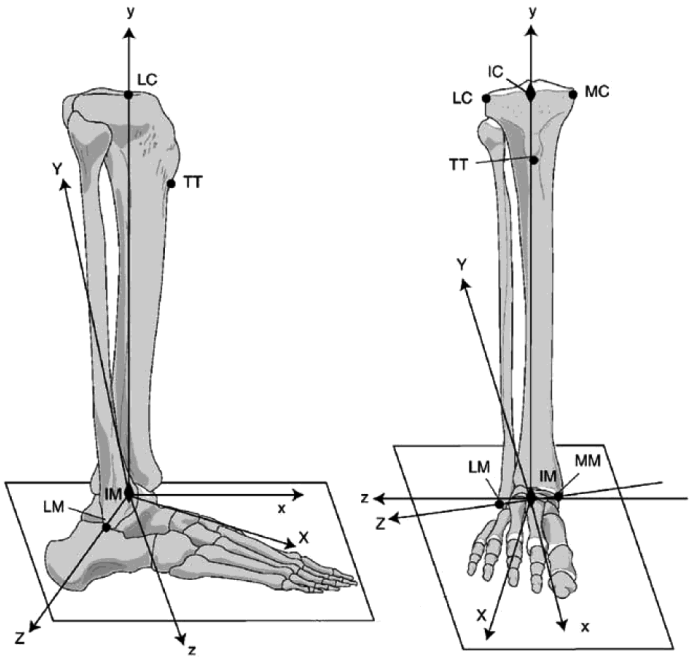

Figure 5.6: Reference frame for the Human tibia proposed by the International Society of Biomechanics (ISB) ((Wu et al., 2002))

The MC and LC anatomical points also define the upper transverse axis of the tibia. In a CT-based study, Cobb et al. (2008) analysed the rotational alignment of the proximal tibia in Total Knee Replacement surgery. The tibial upper transverse axis was defined as the line connecting the medial and lateral condyle centres, and the condylar centres were approximated by the centres of two circles best-fitted to the medial and lateral surfaces of the tibial plateau. The best-fit circles provide a direct estimate to both MC and LC anatomical points, and can be used as a guideline for the determination of other anatomically related landmarks. From section 5.2 the antero-posterior axis of the upper tibia is orthogonal to the transverse axis, and is internally rotated approximately 18 degrees relatively to the line connecting the centre of the tibial plateau and the tip of the TT. The

lower axis of the tibia can be easily defined manually by visual identification of both MM and LM. One can reduce the subjectivity in the definition of the lower tibial axis, recalling that these two axes should be rotated approximately 23 degrees relative to each other. The MC and the LC where defined as the intersections between the line connecting the medial and lateral condylar centres and the best-fit circles along the medial and lateral surfaces of the tibial plateau, respectively. Fig. 5.7 depicts the definition of the tibio-fibular frame according to the described procedure.

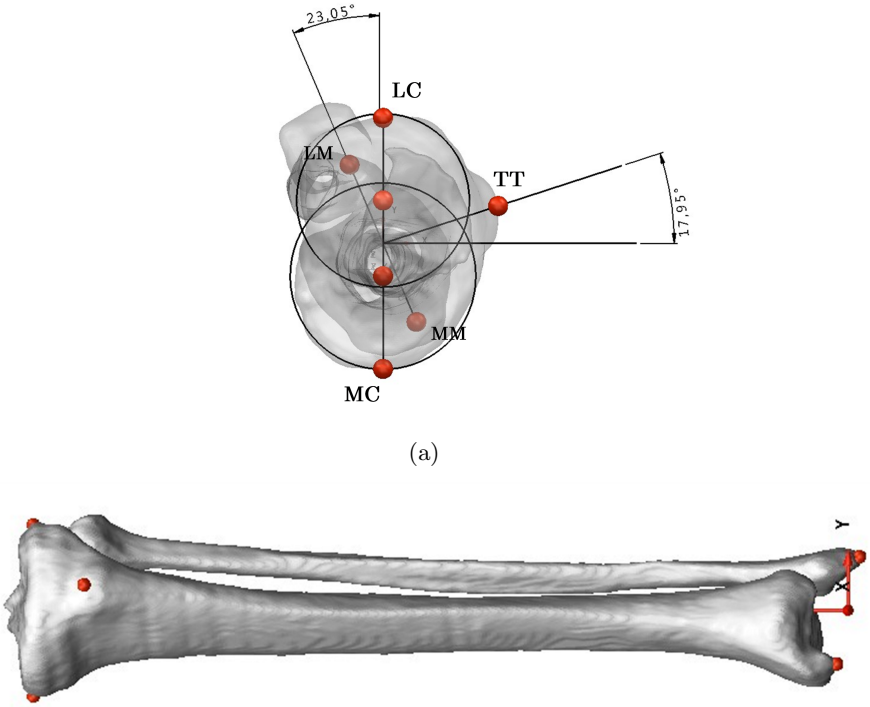

(a)

(b)

Figure 5.7: Determination of the tibio-fibular reference frame: in (a) the determination of the medial tibial condyle (MC) point and the lateral tibial condyle (LC) by defining the centre of the medial and lateral condyles according to Cobb et al. (2008), and the anatomical correlation with the lower transverse axis of the tibia; in (b) the coronal view of the alignment of the tibio-fibular complex in the newly defined frame

Considering the newly defined anatomical frame, the distance between the intercondylar eminence and the inferior articular surface in the ankle was measured to define the tibial length. A distance of approximately 350 mm was measured. Therefore, the tibial nail should have a length between 310 to 320 mm. Next, a set of equally spaced cross-sections of the medullary cavity were extracted to determine the spatial

orientation of the tibial medullary canal. The geometrical centre of each cross-section was determined by fitting 2D circle to the mesh points, using non-linear least squares. The tibial intra-medullary axis was defined as the 3D line that best-fits the centres of all cross-section circles, and was computed applying the Principal Component Analysis to the centres of all cross-sections (Jackson, 2005). In Fig. 5.8 the coronal and sagittal alignments of the tibial nail along the medullary canal are shown. The intra-medullary axis passes near the lateral tubercle of the inter-condylar eminence, which is in agreement with the surgical guidelines for tibial intramedullary nailing (Synthes, 2006). The entry point in the anterior aspect of the tibial plateau for intramedullary nail insertion is also illustrated in Fig. 5.8 (a). The axial cross-sections along the medullary canal used, for the determination of the tibial intra-medullary axis, are shown in detail in Fig. 5.8 (b) and (c). For tibial nail design, coronal and sagittal sections of the outer and inner surfaces of the tibia in the coronal and sagittal plane were also considered (Fig. 5.8 (b) and (c)). These sections provide useful anatomical information to optimize the position of the implant in these two anatomical planes, and to optimize the proximal and distal bends of the tibial nail on the sagittal plane.

The current trend in intramedullary nailing is the co-called *ream-to-fit* technique, where medullary canal reaming is reduced to the minimum. In a comparative study, Ziran et al. (2004) showed that the limited reaming techniques have better clinical outcomes in open fractures than unreamed nailing, and no differences in terms of infection were found between the two nailing techniques. Regarding the nail body, tibial nails may be solid or tubular. Tubular nails allow the use of guide wires for an easier insertion. In an animal study tubular nails showed more susceptibility to infection than solid nails (Melcher et al., 1994, 1995). Solid nailing techniques allow small diameter nails to be used, without implying a reduced fatigue strength of the implant. Small diameter nails are commonly associated with higher rates of fatigue failure, while several studies have identified the breakage of the interlocking screws rather than the nail diameter as the main cause for implant failure (Hutson et al., 1995; Uhlin and Hammer, 1998; Finkemeier et al., 2000). Gaebler et al. (1999) concluded that small diameter nails used in conjunction with larger diameter interlocking screws have an enhanced fatigue strength. In addition, the use of partially threaded screws instead of fully threaded screws may double the fatigue resistance of the locking system.

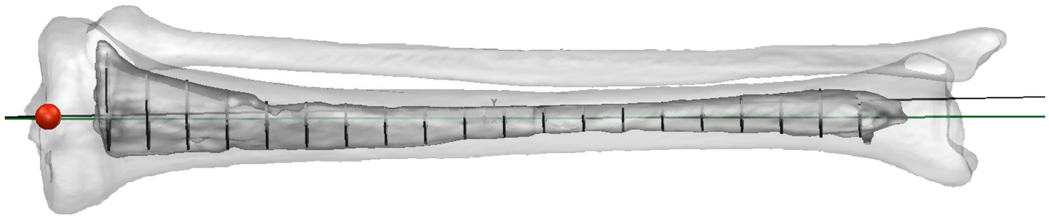

(a)

(b)

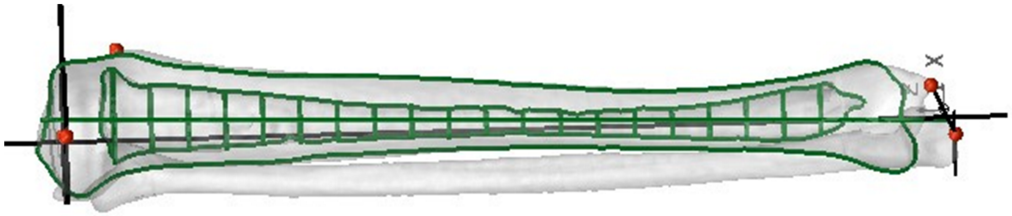

(c)

Figure 5.8: (a) the orientation of the tibial medullary canal obtained from the best-fit to the centres of equally spaced cross-section of the medullary canal (green line), the orientation of the tibial shaft axis as proposed by the ISB (black line), and the nail entry point (red sphere); (b) and (c) the coronal and sagittal views of the axial cross-sections used for intramedullary nailing design, respectively

Taking into account the aforementioned guidelines, the design of a solid, small diameter tibial nailing system was considered. The optimum diameter for the nail was determined by finding the isthmus of the segmented medullary canal. Limited reaming allows the preservation of most of the blood supply, which is important for the bone healing process. The diameter of the isthmus extracted from the segmented model was 9.95 mm, hence the diameter of the nail was set to 10.0 mm. Since at least 1.0 mm of over reaming is needed for nail insertion, a minimal of 11.0 mm of diameter reaming is needed for nail insertion

(Bhandari et al., 2003). Fig. 5.9 illustrates the 10.0 mm diameter tibial nail design within the medullary canal, as well as the proximal and distal holes for implant-bone interlocking.

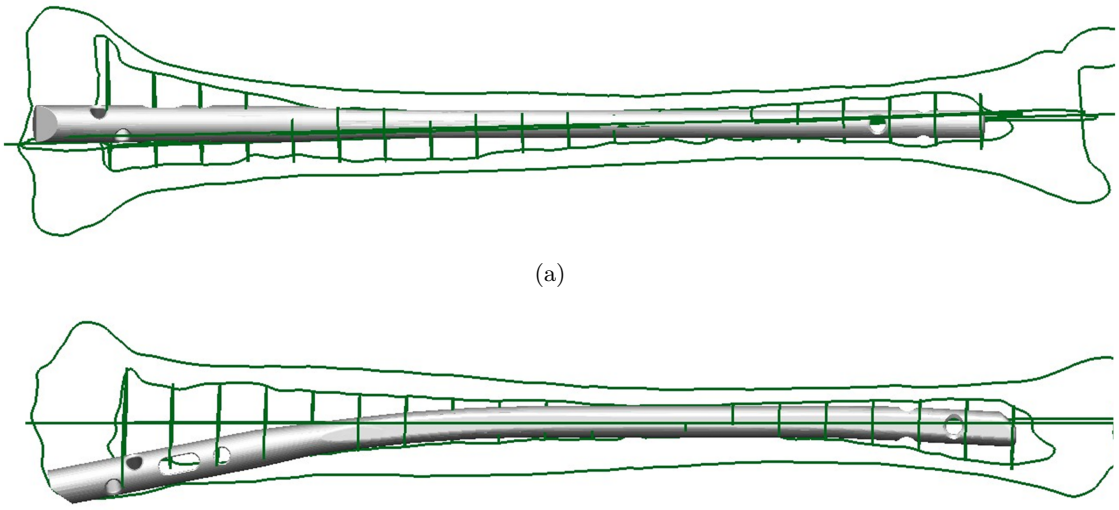

(a)

(b)

Figure 5.9: General overview of the fit of the proposed intramedullary nailing system and the underlying anatomy (a) in the coronal plane and (b) in the sagittal plane

Another relevant issue regarding tibial fracture management is fragment mal-alignment during nailing. Fragment mal-alignments are very difficult to correct post-operatively. In proximal tibial fracture, one of the major sources of proximal mal-alignment in proximal tibial fractures is the Herzog bend. The use of a more proximal Herzog bend with 10 degrees at 50 mm seems to reduce the amount of mal-alignment of the distal fragment (Hsu and Dickson, 2006; Leung et al., 2006). Diameter mismatch between the tibial nail and the medullary cavity is also an additional source of fracture instability. Laflamme et al. (2003) concluded that proximal interlocking with oblique screws improve the mechanical stability of proximal fractures when compared with parallel interlocking screws. In a more recent study, it was concluded that proximal oblique screws are a less favourable configuration to resist cyclic loading, and consequently such configuration is more prone to fatigue fracture in the long term (Weninger et al., 2009).

Distal fractures seem to suffer from the same diameter mismatch between the nail and the medullary cavity. Distal tibial nail locking is often achieved by placing multiple screws with different anatomical orientations. The existence of multiple holes in the distal end

of the nail is, however, detrimental for the fatigue strength of the nail. Intramedullary nails with three or more distal holes are more prone to fatigue failure, because, when left empty, the holes act as stress concentration areas. This is particularly hazardous if the distal screw hole is close to the fracture site, or if one is in the presence of slowly healing fractures (Franklin et al., 1988). Hajek et al. (1993) concluded that only one distal screw was needed to provide the adequate distal fixation to femoral shaft fractures treated with interlocking intramedullary nailing. The same was not observed for tibial fractures, and Kneifel and Buckley (1996) concluded that by using two distal screws instead of one, implant failure could be reduced from 59.1% to only 5%. Implants with two *very* distal locking holes avoid stress concentration near the fracture site, and are more suitable for the treatment of very distal tibia fractures (Leung et al., 2006).

From the previous considerations, oblique screws placed solely in the proximal end of the tibial nail seems to be unsuitable for fracture management of the tibia. Nevertheless, they play a paramount role in fracture stabilization, and the possible improvement in fracture stability cannot be neglected. Hence, a combination of both oblique screws and medio-lateral screws seems to be the most plausible way to overcome the limitations of both systems. More recent commercially available tibial nailing systems use a combination of both medio-lateral and oblique screws for proximal interlocking (Kuhn et al., 2008). A proximal locking system with both medio-lateral locking screws, with a dynamic slot for implant dynamization, and two oblique screws was designed (Fig. 5.9 (a) and (b)). This configuration allows the placement of two locking screws in an early weight bearing phase, and the dynamization of the nail-bone construct later on. Two oblique locking screws were introduced in the very proximal end of the nail. These screws may provide improved mechanical stability to very proximal tibial fractures, which is important to the treatment of very proximal medial fractures. The centre-to-centre distance of the proximal oblique screws was set to 8.0 mm, as well as the length of the dynamic slot (Fig. 5.9). The distance between the dynamization slot and the proximal static screw was set to 10.0 mm. An Herzog bend of 11.0 degrees was considered in the proximal end of the tibia, to follow the anatomy of the target tibia in the sagittal plane (see Fig. 5.9 (b)). At the distal end of the tibial nail, a 3.0 degrees anterior bend was added in order to facilitate the insertion of the nail. Fig. 5.10 shows a preview of the tibia-fibula complex after implantation.

The distal interlocking system was designed with only two distal locking screw holes.

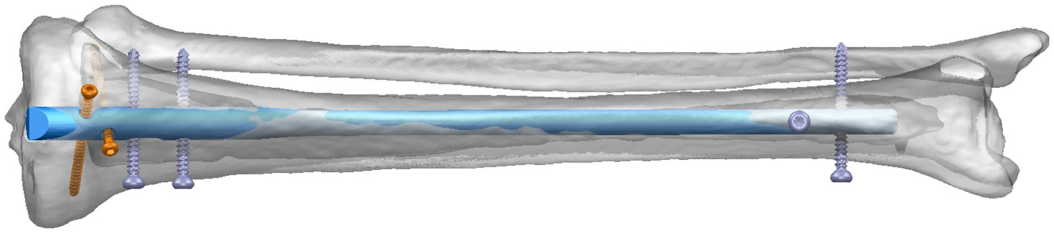

Figure 5.10: Coronal view of the tibial intramedullary nailing system, with proximal oblique and medio-lateral interlocking, and distal antero-posterior and medio-lateral locking screws

The two distal screws are oriented along different anatomical planes and are the minimum number of screws needed to minimize implant failure. Fig. 5.11 shows the intramedullary tibial nail proposed with some additional geometrical details. The two distal screws may be oriented in the medio-lateral direction and antero-posterior direction, or vice-versa. The centre-to-centre distance between the two distal screws was set to 15.0 mm, whereas the distance to the distal end of the implant was set to 20.0 mm. With such configurations the system provides a cross-plane fixation. The multi-directional insertion of locking screws reduces implant instability, and seems to reduce the incidence of nail breakage (Rüedi et al., 2007; Nork et al., 2005). Finally and following the concept of small diameter nails with larger screws, the intramedullary nail was designed to function with 5.0 mm diameter screws, which is half of the diameter of the tibial nail body. The screws were designed to function as static locking screws.

5.6 Validation of the Tibial Intramedullary Nailing System

To analyse the behaviour of the proposed nail geometry, the tibial intramedullary system was virtually placed in position within the tibia, and a Finite Element Analysis (FEA) was carried out. After positioning the implant, the implant-bone complex was discretized with an isotropic 0.50 mm voxel size. Finite Element mesh generation was performed with Simpleware ScanIP $+FE$ Module, whereas the Finite Element Numerical simulations were performed using a home-developed solver named *DD3IMP* (Oliveira et al., 2008).

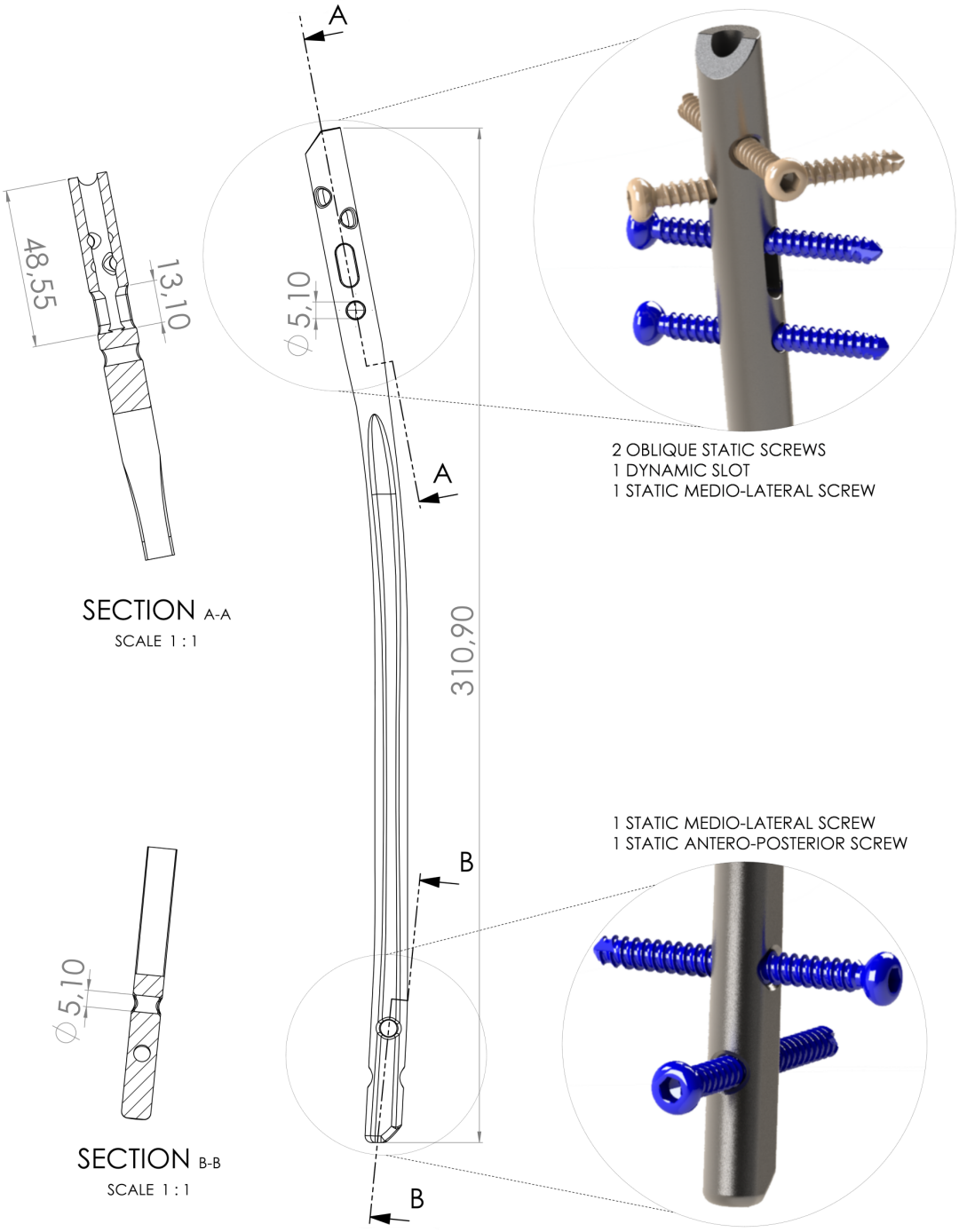

Figure 5.11: Intramedullary nailing system with the proximal and distal interlocking screws: proximal end with two oblique screws and two medio-lateral screws (one with static or dynamic positioning); and the distal end with two static screws, the most proximal screw positioned in the medio-lateral direction and the most distal in the antero-posterior direction

5.6.1 Finite Element Model and Mechanical Properties

During the FE mesh generation stage several simplifications were made to the initial model. First, the interlocking screws were modelled as simple cylinders, and all the geometrical features related with the screw's threads were removed. The trabecular bone was also excluded from the analysis. This simplification was necessary in order to facilitate the Finite Element mesh generation, to obtain a more accurate geometrical description of the surface of the intramedullary nail and, at the same time, reduce the overall size of the problem. The fibula was also not considered in the FE analysis since it is not responsible for any load-bearing function (Mader and Galliart, 2005).

The FE mesh of the implanted tibia was generated with 10-nodes quadratic tetrahedral elements directly from the voxelized data. For implant evaluation, three mid-shaft types of fractures were simulated by creating a proximal, a medial, and a distal defect along the tibial shaft. Each tibial shaft defect has 11.0 mm of length, and the most proximal and distal defects were located 10.0 mm below and above the nearest screw, as proposed by Duda et al. (2001). The simulated mid-shaft tibial fractures correspond to a $42 - C2.1$ type fracture according to the AO Classification system with one intermediate segmental fragment (Müller et al., 1991). In addition, two distal screw configurations were tested in this study. The first configuration with the most proximal screw oriented antero-posteriorly and the second screw oriented medio-laterial direction (AP-ML), and a second configuration with the first screw oriented in the medio-lateral direction and the second screw oriented antero-posteriorly (ML-AP).

Mesh convergence analysis was carried by analysing the nodal displacement and equivalent (von Mises) stress of four hundred points along the lateral, medial, anterior and posterior surface of the tibial intramedullary nail. Mesh convergence was observed for a minimum tetrahedral edge length of 1.25 mm, with more than 180000 elements and 320000 nodes. The average change in the nodal displacement and the equivalent stress over the four hundred points was $< 5\%$. The same meshing parameters were used to generate the six meshes, corresponding to each tested fracture site plus the two distal locking screw configurations. The material assigned to the intramedullary nail was a Ti-6Al-4V titanium alloy. Both the cortical bone, tibial nail and interlocking screws were modelled as linear elastic, isotropic and homogeneous. The mechanical properties of the cortical bone where:

Young's modulus $E = 17900$ MPa and Poisson's Ratio of $\nu = 0.30$ (Reilly and Burstein, 1975), whereas for the tibial nail and interlocking screws a Young's modulus $E = 113800$ MPa and a Poisson's Ratio of $\nu = 0.34$ were considered (Welsch et al., 1993).

5.6.2 Boundary Conditions

During Human locomotion the leg may be subjected to high internal loads (Novacheck, 1998). Ground reaction forces and internal joint forces may reach several times the subject's body weight (Nilsson and Thorstensson, 1989; Bergmann et al., 2001). Recently, using inverse dynamics analysis over a musculoskeletal model of the human lower body, Wehner et al. (2009) concluded that the highest internal forces acting on the tibia were always observed at the end of the stance phase; it was found that the contact forces acting of the knee may reach 3.3 times the subject's body weight (BW). In addition, an external rotation momentum of 15 BWmm acting along the long axis of the tibia was also observed.

In the analysis of the intramedullary nailing system a patient BW of 80 Kg was considered. Since the reaction force in the knee is unevenly distributed between the lateral and medial tibial plateaus, 40% of the load was applied to the lateral tibial condyle, and 60% to the medial tibial condyle (Morrison, 1970; Harrington, 1976; Duda et al., 2001). In Fig. 5.12 the loading conditions are presented schematically. The medial and lateral reaction forces were applied approximately at the centre of each tibial plateau. An additional external momentum of 12 Nm was also applied at the proximal end of the tibia, in order to resemble more accurately the critical loading conditions found during the stance phase of the gait cycle (Wehner et al., 2009). The model was restrained at the tibiotarsal joint in all three direction, and the interlocking screws were considered rigidly bounded to the cortical bone and to the intramedullary nail.

5.6.3 Results

The proposed intramedullary nailing system was numerically tested for three types of tibial fractures and two distal screw configurations under critical loading conditions found during Human gait analysis. For all fracture and distal screw configurations, the equivalent (von Mises) stress distribution along the nail and screws were analysed.

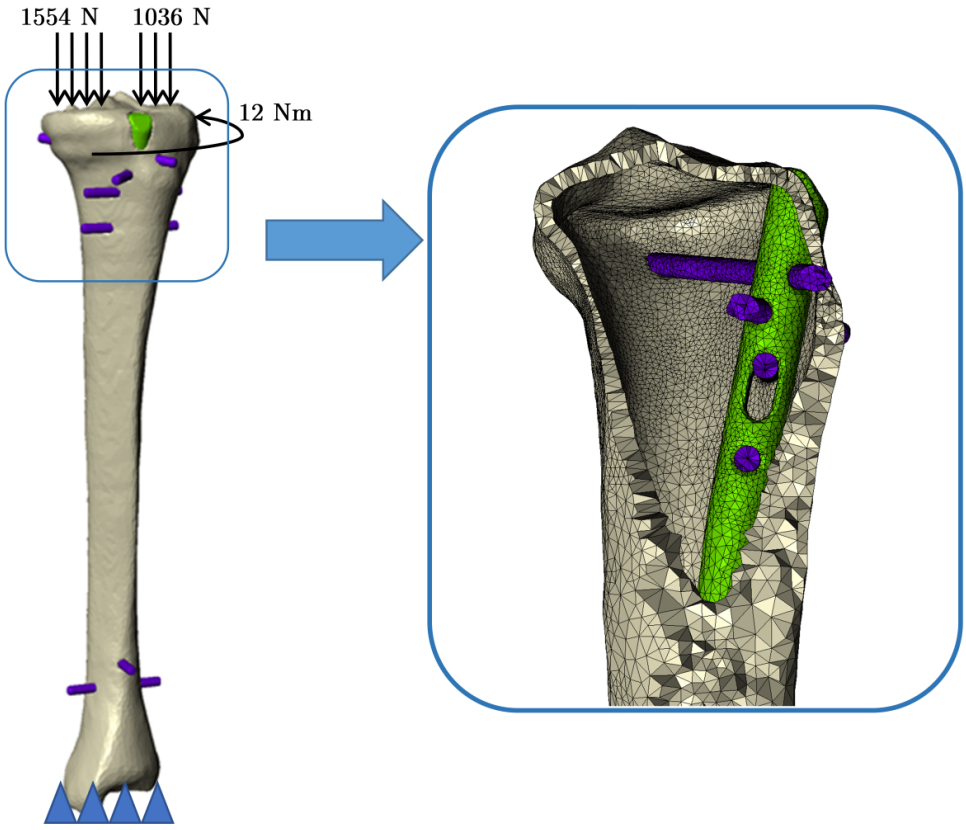

Figure 5.12: The final FE model of the tibia and intramedullary nailing complex, without trabecular bone, and the schematic representation of the loading and boundary conditions applied to the model for implant validation

An intramedullary nail is a load sharing device, which provides mechanical support and guidance during the bone healing process after bone fracture. The stress concentration along the interlocking nailing system was larger than the stress along the cortical bone. This is a well-known phenomenon termed as stress shielding, and it is a consequence of the greater Young's modulus of the Ti-6Al-4V titanium alloy comparatively to the elastic modulus of the cortical bone. Unlike other implants, stress shielding is a desirable consequence of tibial nailing, at least in an early healing stage of the bone healing process. Under the prescribed loading conditions, the intramedullary system was mainly bent along the sagittal and coronal plane, due the larger reaction force applied to the medial condyle of the tibia. The maximum equivalent (von Mises) stresses observed along the tibial nail, for all loading conditions, was below 240 MPa, the fatigue limit for the Ti-6Al-4V alloy (Welsch et al., 1993).

Fig. 5.13 and 5.14 depict the von Mises stresses along the tibial nail and interlocking screws for all fractures and distal screw configurations. Fig. 5.13 shows the iso-contours of the equivalent stress along the nail and the interlocking screws for the proximal, the medial, and the distal fractures and AP-ML distal screw configuration. The maximum equivalent stress was observed along the anterior surface of the nail near the first distal screw for all types of fractures. The maximum equivalent stress ranged from 206.0 MPa for the distal fracture to 224.0 MPa for the proximal fracture. In the ML-AP configuration the maximum equivalent stresses were observed in the AP screw (second distal screw). The maximal stresses in the AP distal screw ranged from 197.0 MPa for the distal fracture to 168.0 MPa in the medial fracture (Fig. 5.14). The maximal stresses were comparatively smaller than the stresses registered in the AP-ML distal screw configuration. Contrarily to the AP-ML configuration, where the first screw was always significantly more loaded than the second screw, in the ML-AP configuration the equivalent stresses observed in the first and second screw were very similar. The results show that, in the later configuration, the load may be distributed more equally between the two distal screws, and the ML-AP may be less prone to fatigue fracture.

Regarding the proximal screws, the equivalent stresses observed at each independent screw increased as the fracture was moved towards the proximal end of the tibia (Fig. 5.13 and Fig. 5.14). Similarly to the observations for the distal screws, the maximum equivalent stresses were found in the AP-ML configuration. Under this configuration, the maximum equivalent stresses were observed at the proximal static screw, with a maximum equivalent stress of about 183.0 MPa for the proximal fracture. In the ML-AP configuration a slightly smaller equivalent stress of 170.0 MPa was observed. The maximum stresses found along the oblique screws were always below 100.0 MPa, with a maximum of 68.0 MPa for the ML-AP configuration. Globally, for the AP-ML screw configuration and for all fracture configurations, the proximal static and the (first) antero-posterior distal screws were the more critically loaded, while for the ML-AP configuration the critical screws were the static proximal screw and the second (also AP) distal screw. Furthermore, for the intramedullary construct, the most demanding fracture configurations were the proximal fracture (for the AP-ML configuration), and the distal fracture (for the ML-AP configuration).

The differences in stress distributions along the tibial nail due to the distal screw configuration were minimal. The equivalent stresses found along the sagittal plane of

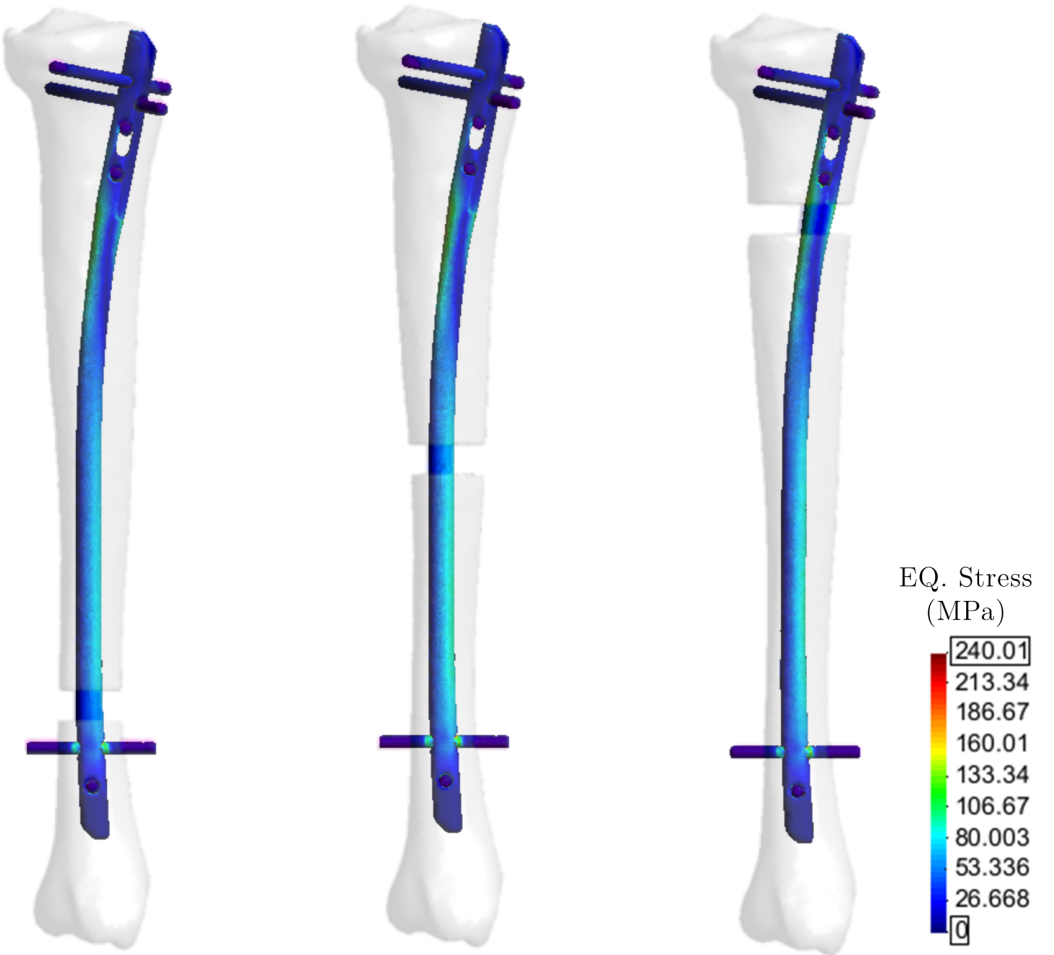

Figure 5.13: Equivalent stress distribution (MPa) along the intramedullary nail and interlocking screws, with an AP-ML distal screw configuration for both distal, medial and proximal tibial fracture

the implant for a proximal fracture are depicted in Fig. 5.15 and 5.16 (for both AP-ML and ML-AP configurations, respectively). Along the posterior surface of the tibial nail, the stress concentration was more pronounced at the proximal end of the implant with a maximum von Mises stress of approximately 150.0 MPa (Fig. 5.15). The largest stress concentrations were observed mainly around the dynamic slot, proximal static slot, and Herzog bend, decreasing from the proximal to the distal end of the implant. The tibial nail mainly bends around the fracture site and the Herzog bend. The proximal end is firmly displaced with the proximal tibial fragment and the distal end remains static. Similar stress concentrations were observed along the anterior aspect of the tibial nail. In both

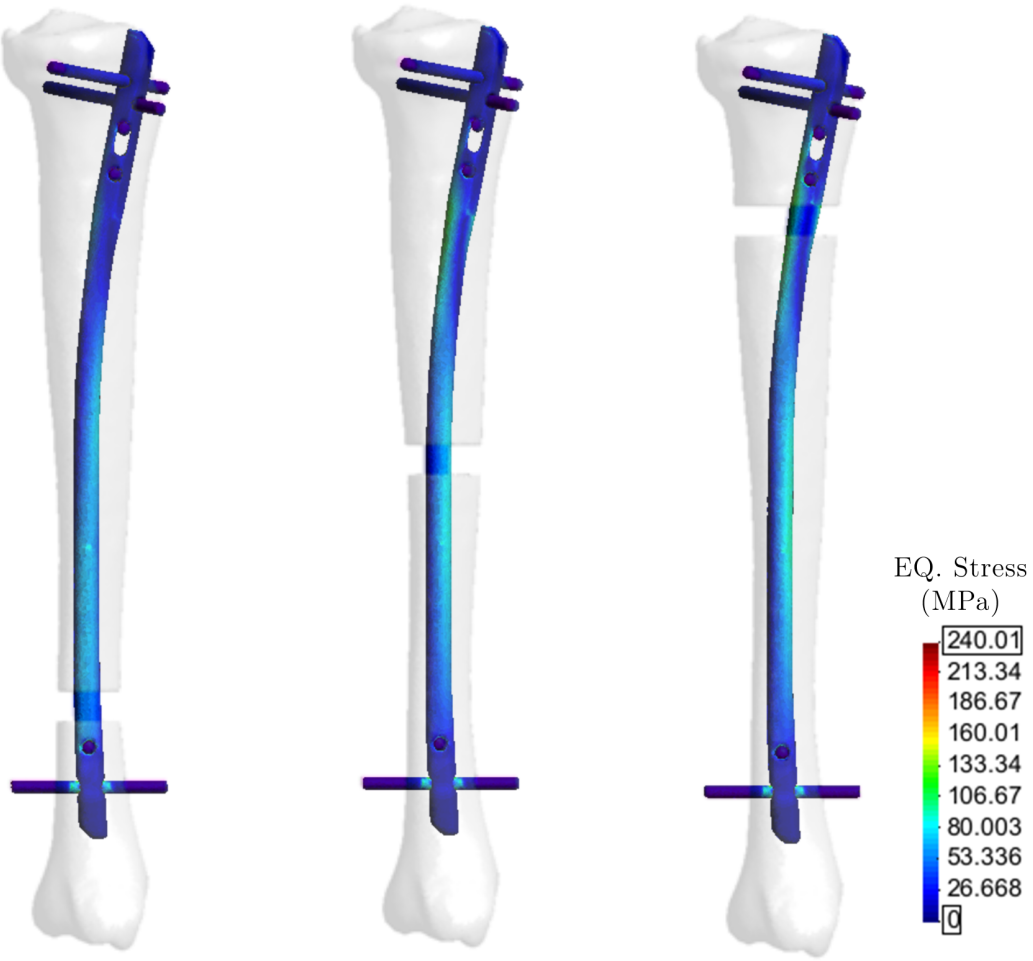

Figure 5.14: Equivalent stress distribution (MPa) along the intramedullary nail and interlocking screws with ML-AP distal screw configuration for both distal, medial and proximal tibial fracture

cases there is a gradual increase in the equivalent stress to approximately 110.0 MPa, followed by a decrease after the proximal static screw towards the Herzog bend. Below the Herzog bend the stress increases and stabilizes around 100.0 MPa along the middle section of the implant. As expected, at the distal end peak stress concentrations were found near the distal screw holes (Fig. 5.15 and Fig. 5.16). The stresses observed at the surface of the intramedullary nail are below the fatigue limit for the Ti-6Al-4V titanium alloy.

In the above analysis the boundary conditions applied to the tibial model represent a critical loading scenario, where a major tibial fracture is conjugated with full weight

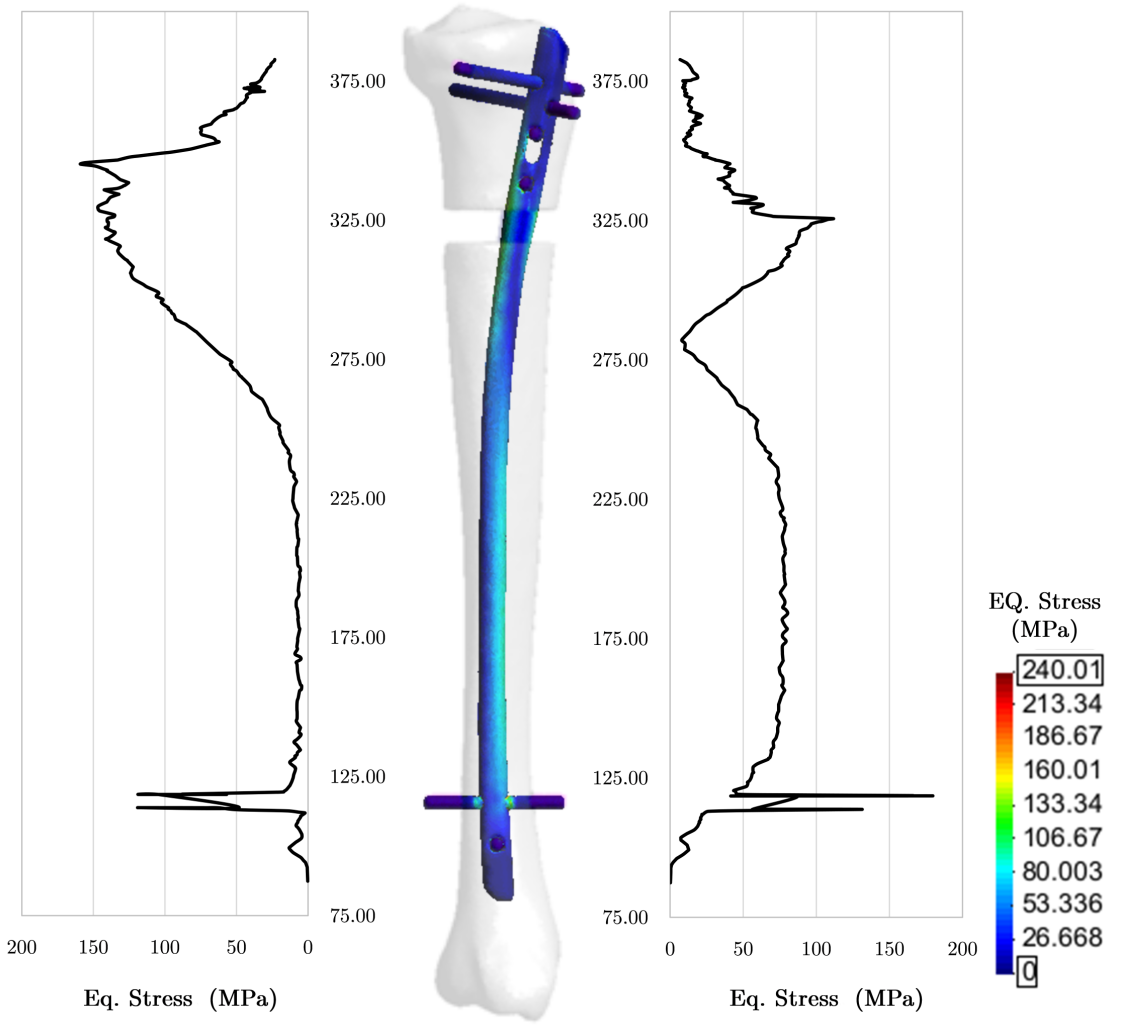

Figure 5.15: The equivalent stress (MPa) at the posterior and anterior aspects of the tibial intramedullary nail for a proximal tibial fracture and AP-ML distal screw configuration

bearing. These loading conditions are very difficult to occur in a clinical setting. Nevertheless, it allow the prediction of possible weak spots in the tibial nail design. Interestingly, it was also observed a significant difference in the relative inter-fragmentary displacements between the two distal configurations considered is this study. The maximum relative displacements between the two bone fragments observed with the AP-ML configuration at the fracture site were 1.52 mm, 1.36 mm and 1.93 mm for the distal, medial and proximal fractures, respectively, while the same fractures had a maximum relative nodal displacement was 0.30 mm, 1.07 mm, and 1.44 mm

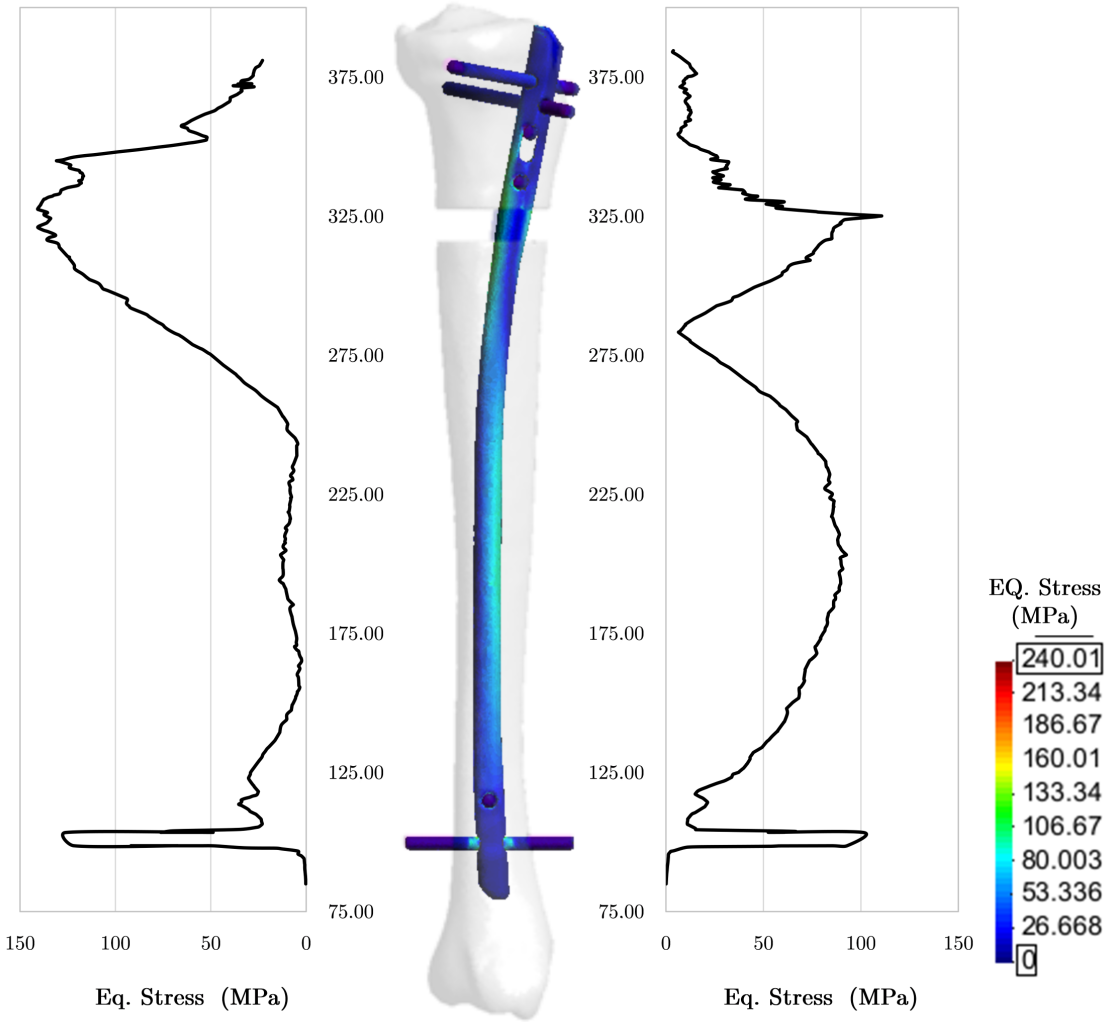

Figure 5.16: Equivalent stress (MPa) profile along the posterior and anterior aspects of the tibial intramedullary nail for a proximal tibial fracture and ML-AP distal screw configuration

for the ML-AP configuration. There is a considerable reduction in the maximum inter-fragmentary displacement at the fracture of approximately 21% for the medial fracture, 25% for the proximal fracture and 80% for the distal fracture when the ML-AP configuration is compared with the AP-ML configuration. In practice, the reduction of the inter-fragmentary may be a key aspect to promote a proper bone healing.

5.6.4 Discussion

A new intramedullary tibial nailing system, considering both historical, medical, anatomical, and recent technological concepts related with tibial fracture management was proposed. The implant geometry, the proximal, and two distal interlocking configurations were validated under critical loading conditions. In post-operative fracture management, patient mobilization and partial weight bearing is usually performed in the first 6 weeks after surgery. The progress to full weight bearing is delayed until callus formation, and pain-free weight bearing is evident, which usually occurs 6 weeks after surgery (Giannoudis and Pape, 2014). The proposed intramedullary nailing system was tested under the critical loading conditions observed during the normal Human gait cycle, as proposed by a recent biomechanical study (Wehner et al., 2009). The loading conditions considered in this work represent a full-weight bearing scenario during early bone healing process immediately after surgery. After tibial nailing, there is a post-operative period where leg mobilization and weight bearing are restrained, therefore, the aim is solely to validate the implant geometry under critical loading conditions.

One of the major breakthroughs in fracture management was the introduction of interlocking screws into the intramedullary nail construct. Interlocking screws increase the ability of intramedullary nails withstand torsional movements, axial loads, and prevent limb shortening (Schandelmaier et al., 1996). In addition, interlocking screws can be inserted though small skin incisions, adding only small wounds to a sometimes critically compromised soft tissue, reducing the blood loss due to the surgical procedure, avoiding periosteal stripping, and preserving the blood supply around the injured bone (Hajek et al., 1993; Tanna, 2010; Brinker, 2013). However, the loads transmitted to the interlocking system along the axis of the tibial nail may lead to screw failure both proximally and distally (Weninger et al., 2009).

The optimization of the interlocking screws positions and their response to loading is one of the critical aspects in intramedullary nailing, and may enhance inter-fragmentary congruence and reduce the risk of hardware failure. Under the prescribed loading conditions one can conclude that the most suitable distal configuration for the tibial nailing is the ML-AP configuration. Hsiao et al. (2003) concluded, using a FE study, that the most suitable screw configuration for the distal tibia was two screws placed in

the antero-posterior direction, and that the minimum stress concentration at the level of the most proximal screws occurred when this was placed in the antero-posterior direction. In the present study, the screws placed in the AP direction are more critically loaded than the ML screws, whether placed as the first or second distal screw. If the first distal screw is placed in the medio-lateral direction instead of the antero-posterior direction, one effectively reduces the risk of fracture of the first distal screw for all fracture configurations (proximal, medial and distal). It also allows a more homogeneous distribution of the distal stresses between the two distal screws, reducing the overall risk of fatigue fracture.

Regarding proximal interlocking screws, in a recent study carried by Weninger et al. (2009) several commercially available tibial nails were mechanical tested, simulating a full weight bearing of 6 weeks. It was observed the failure of at least one of the oblique screws in every specimen. It was observed that proximal medio-lateral screws seem to withstand better axial loadings than oblique screws, and that the usage of oblique screws proximally should be reconsidered. In the proposed nailing system the oblique screws were used in conjunction with two medio-lateral screws for proximal interlocking. A maximum equivalent stress of approximately 68.0 MPa was observed at the second oblique screw for all fracture configurations. In addition, larger equivalent stresses were observed in the proximal medio-lateral screws when compared with the oblique screws. This proximal screw configuration seems to provide efficient load bearing through the medio-lateral screws sustaining most of the load applied, and successfully unload the oblique screws. In this proximal screw configuration the oblique screws act mainly as stabilizing features to the proximal end of the tibial nail (Laflamme et al., 2003). The results also show that 5.0 mm oblique screws, together with the 5.0 mm medio-lateral screws, may prevent proximal oblique screws from fracturing. The stresses observed across the proximal screws also differed according to the fracture site. In general, it was observed an increase of the maximum stress as the fracture site was moved towards the locking screw.

In practice, the performance of the interlocking system under loading conditions is far more critical than the nail itself. Implant failure due to nail breakage is rare. The rates of failure for the tibial nails range from 0 to 6%, whereas the rates of failure of the interlocking screws range from 6 to 14% (Sanders et al., 1994; Whittle et al., 1995). The results obtained show that the proximal end of the nail is more critically loaded than the distal and medial regions. Ruiz et al. (2000) reviewed 338 fractures treated with

intramedullary tibial nailing, and concluded that fractures in the distal third of the tibia had a higher incidence of nail breakage compared to all other fractures. This shows that the two large distal screws may provide enough strength to the construct, avoiding nail breakage. The distal screws may be moved closer to the distal end of the implant to allow the management of more distal fractures. In the proximal region, the oblique static and dynamic holes in the proximal end of the tibial nail do not seem to be the weak region, where the nail may be susceptible for fatigue fracture. The centre-to-centre distances between the proximal screws do not seem to compromise the design either.

In the treatment of shaft fractures, flexible fixation systems allowing some degree of inter-fragmentary movement commonly have better outcomes than completely stable systems (Townsend et al., 2012). Uhlin and Hammer (1998) found, in a consecutive series of 55 tibial shaft fractures stabilized with unreamed nails, that the selection of the appropriate nail diameter was unreliable using pre-operative radiographs. The authors suggested CT imaging as an alternative means for tibial nail pre-operative planning. The proposed implant planning protocol may not only be useful for tibial implant design, but also as a routine tool for tibial nailing surgical planning. In addition, it may allow the development of the interlocking system to satisfy individual fracture needs, and provide a more tight fit between the tibia and the implant. In animal studies, Schell et al. (2005) have shown that optimal bone healing is observed if the shear intra-fragmentary movements are kept below 0.80 mm, and Augat et al. (2003) concluded that intra-fragmentary shear movements of the order of 1.50 mm may significantly delay bone union. Although the loading considered conditions do not reflect accurately the post-operative period, where leg mobilization and weight bearing are restrained and weight bearing is progressive. Differences in the linear inter-fragmentary displacements between the two screw configurations were observed. The ML-AP configuration showed a reduced inter-fragmentary movement for all tested fractures, when compared with the AP-ML configuration. In some cases, the maximum linear displacement was below the critical value of 1.50 mm. No direct conclusions can be drawn from the results obtained, however it can be hypothesized that a ML-AP distal screw configuration may also provide a more suitable fixation towards bone healing.

5.7 Summary

In this chapter one has proposed a tibial intramedullary nailing protocol from CT image data. It was proposed also a tibial intramedullary nail system with optimized proximal and distal interlocking systems. The proximal interlocking system is composed by two oblique screws and two medio-lateral screws. The small stress concentrations observed at the proximal end of the tibial nail suggest that the use of both medio-lateral and oblique screws for proximal interlocking seems to avoid proximal oblique breakage. In addition, it is also possible to conclude that two distal screws placed in the medio-lateral and antero-posterior direction are less prone to fatigue fracture than the antero-posterior and medio-lateral configuration. Our results also corroborate the hypothesis that smaller diameter nails in conjunction with larger diameter interlocking screws may have an enhanced fatigue strength.

Chapter 6

Custom Mandibular Reconstruction

In this chapter custom mandibular reconstruction is addressed. The natural anatomical and occlusal relation are used to accurately reconstruct a mandibular defect. Tow solutions are presented, a tailor-made surgical guide to optimize bone harvesting at the donor site, and a custom mandibular endoprosthesis that may be a useful alternative for patients in whom the traditional bone grafting cannot be performed. Both solutions aim to fully restore the facial profile and aesthetics.

This page was intentionally left blank

6.1 Introduction to Mandibular Reconstruction

Mandibular reconstruction is often needed to compensate bone loss related with trauma, inflammatory disease, and benign or malignant tumours (Goh et al., 2008). Mandibular resection caused by malignant or aggressive odontogenic tumours often originate extensive defects on the orofacial cavity, including bone, oral mucosa, muscles, and teeth (Peled et al., 2005). The primary objective of a mandibulectomy is to remove all deceased biological tissues and provide quality of life to the patient. The surgical procedure should provide both functional and cosmetic rehabilitation. Bone and soft tissue reconstruction must be chosen individually for each patient in order to maximize the functional and aesthetic outcome (Peled et al., 2005; Flint et al., 2010).

Ideally, oro-facial reconstruction should restore the oral competency, maintain occlusal relationships between the remaining teeth, allows for prosthetic dental restoration, restore bone continuity and the contour of the lower third of the human face, as well as the facial symmetry (Taylor, 1982; Goh et al., 2008). The implanted material should provide sufficient height for adequate muscle attachment, provide the possibility for dental implant insertion, and allow the restoration of the normal occlusion and articulation of the mandible. Mandibular reconstruction has experienced a great evolution in particular in the last decades; however, an ideal solution for the anatomical reconstruction of the mandible has not yet been achieved. Several techniques are used today, namely: free bone grafts; pedicle bone grafts; particulate bone cancellous marrow grafts; reconstruction plates; microvascular free flaps. Most recently, other techniques such as disc distraction osteogenesis, tissue engineering and modular endoprosthesis were tested mainly to eliminate the need for harvesting bone from a donor site (Goh et al., 2008). For a complete overview of all mandibular reconstruction techniques, the interested readers are referred to review references Goh et al. (2008) and Wong et al. (2010).

During mandibular reconstruction, considerable amounts of soft and hard tissue may be needed for the complete rehabilitation of the lower facial region. The most common donor sites are the iliac crest, the radius forearm, the scapula, and the fibula (Peled et al., 2005). Each one differs in the quality and quantity of bone and soft tissue availability, in the quality of the vascular pedicle, in the possibility of bone reshaping and placement of dental implants in a second stage surgery (Goh et al., 2008). The fibular

flaps and the iliac flaps provide the most suitable bone stock for dental implant-based mandibular rehabilitation, and are preferred against the other donor sites (Miloro et al., 2004). Currently, microvascular free flaps are seen as the gold standard for mandibular reconstruction: this technique will be hereafter briefly described.

The first microvascular free fibular bone flap transfer (Fig. 6.1) was reported by Hidalgo (1989), and was used to reconstruct a segmental defect on the mandible. This techniques has revolutionized oro-mandibular reconstruction, since it enabled a compound graft transfer with bone and soft tissue, without damaging their own vascular supply, to the head and neck regions (Bak et al., 2010). Since these bone grafts are never deprived from their own blood supply, the healing process will start immediately at the osteotomy sites, shortening the recovery time and reducing the risk of post-operative complications (Goh et al., 2008). Success rates near 100% have been reported with this technique, even in the treatment of the most adverse situations (Gurtner and Evans, 2000). Currently, free microvascular flaps are used to reconstruct large mandibular defects (Haughey et al., 1994), where there is inadequate soft tissue or the recipient site has already been subjected to radiation (Östrup and Fredrickson, 1975), to manage chronic infections, to correct previous surgeries, and in primary mandibular reconstruction due to aggressive odontogenic tumours (Disa and Cordeiro, 2000; Peled et al., 2005).

The microvascular fibular flap provides the greatest amount of bone transfer comparatively to the other donor sites, and allows the reconstruct of large mandible defects, even after a complete jaw resection (Santamaria et al., 1998; Leon et al., 1999; Peled et al., 2005). The length of bone available that can be extracted in a single microsurgical transfer is more than 200 mm, whereas the skin paddle is up to 250 mm in length and 50 mm in width (Ferri et al., 1997). The fibular flaps have well-vascularized soft tissues and allow multiple osteotomies for precise bone shaping. These two features are important to properly restore all anatomic relations and obtain an aesthetic outcome (Hidalgo, 1989; Peled et al., 2005). In addition, the fibular flap provides bicortical bone with enough thickness to support osseo-integrated implants (Frodel et al., 1993; Moscoso et al., 1994; Su and Fernandes, 2014), this characteristic is of paramount importance for the reconstruction and support of over-dentures, and consequently for complete oro-facial functional recovery (Pogrel et al., 1997; Dalkiz et al., 2001; Nagy et al., 1998),

Free microvascular fibular reconstruction has numerous advantages against other

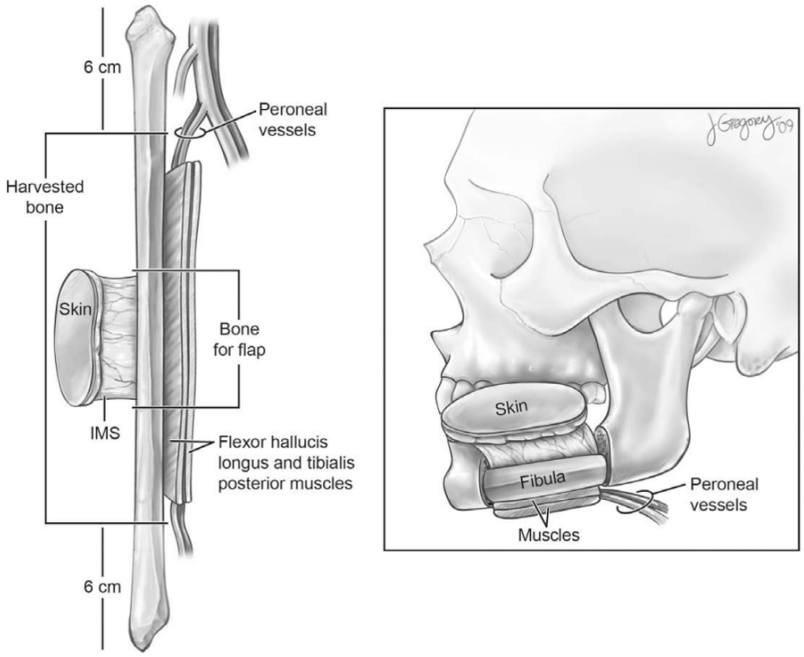

Figure 6.1: Schematic representation of the microvascular free fibula mandibular reconstruction ((Bak et al., 2010))

microvascular free flap techniques. Nevertheless, this procedure cannot be performed in patients that have deficient lower limb vascularization. For instance, patients with ischemic diseases of the lower limbs, arteriosclerosis, small length of the fibula pedicle, and limited thickness of the soft tissue are not eligible for this type of mandibular reconstruction (Ferri et al., 1997). Mandibular reconstruction also implies a long and complex operation; it commonly implies surgical morbidity on the donor site; prolonged hospitalization time; and a long recovery process with delayed function. It also may be not suitable for elderly people with multiple medical problems, which cannot be subjected to a long reconstructive surgical procedure (Wong et al., 2012a).

Several authors have addressed mandibular reconstruction through the development of custom implantable devices. Custom devices aim to reduce the time and complexity of the surgical procedure, to enhance the aesthetic outcome, and to reduce or even eliminate the need for bone harvesting. Fig. 6.2 depicts some of the implantable solutions that can be found in the literature. There are predominately two types of custom-made implants: the titanium trays that shape and provide mechanical to the bone grafts collected from one of the possible donor sites, such as, the custom-made titanium trays proposed by Samman

et al. (1999) and Singare et al. (2004a) (Fig. 6.2 (a) and (b), respectively); and replacement implants that rely on the fixation concepts often associated with reconstruction plates to substitute the missing part of the mandible. Peckitt (1999) proposed the so-called THORP system, composed by a custom-made mandibular titanium body attached to a mandibular reconstruction plate (Fig. 6.2 (c)). Although the good early functional and aesthetic outcomes, soft tissue complications and loosening around the fixation screws were observed after a two-year follow-up. Li et al. (2014) proposed a plate-like implant for the secondary reconstruction of large mandibular defect (Fig. 6.2 (d)). The implant was functioning well 3 years after implantation and no signs of screw loosening or plate fracture were observed. More recently, the company *Xilloc Medical BV* documented the development and implantation of a complete custom made mandibular implant (Fig. 6.2 (e)), obtained from the patient's CT scan (Nickels, 2012).

Tideman H. (2006) proposed an endoprosthesis composed by several modules and a screw-based locking system for the accurate mandibular reconstruction (Fig. 6.2 (f)). The successful implantation of a cemented titanium alloy (Ti-6Al-4V) modular endoprosthesis in fours pigs and four monkeys was reported by Lee et al. (2008). After 3 months of follow-up, the authors reported that in the monkeys group there were no signs of implant loosening. There was no masticatory function loss and no signs of occlusion problems. Nevertheless two of the modular endoprosthesis systems failed due to the screw connection between the different modules. The modular endoprosthesis was extended to the ascending ramus and mandibular condyle by Goh et al. (2009a) as an alternative to the traditional temporomandibular joint replacement techniques. Normal temporomandibular joint function, mouth opening and occlusion were observed post-operatively.

The main issue related with custom implants applied in mandibular reconstruction is the failure of the screwed connections between the bone-implant interface. This problem has been widely described in the literature. Several authors concluded that plates fixed in the buccal aspect of the mandible have to withstand unfavourable forces that often lead to loosening of the screws and fracturing of the plates (Kim and Donoff, 1992; Spencer et al., 1999; Shibahara et al., 2002). In a finite element study, Knoll et al. (2006) concluded that masticatory loads and high chewing forces may lead to fatigue failure of the reconstruction plates and/or to screw loosening. A wider flat plate design with square screw configuration was proposed to bridge a mandibular angle defect and to minimize the stress concentration

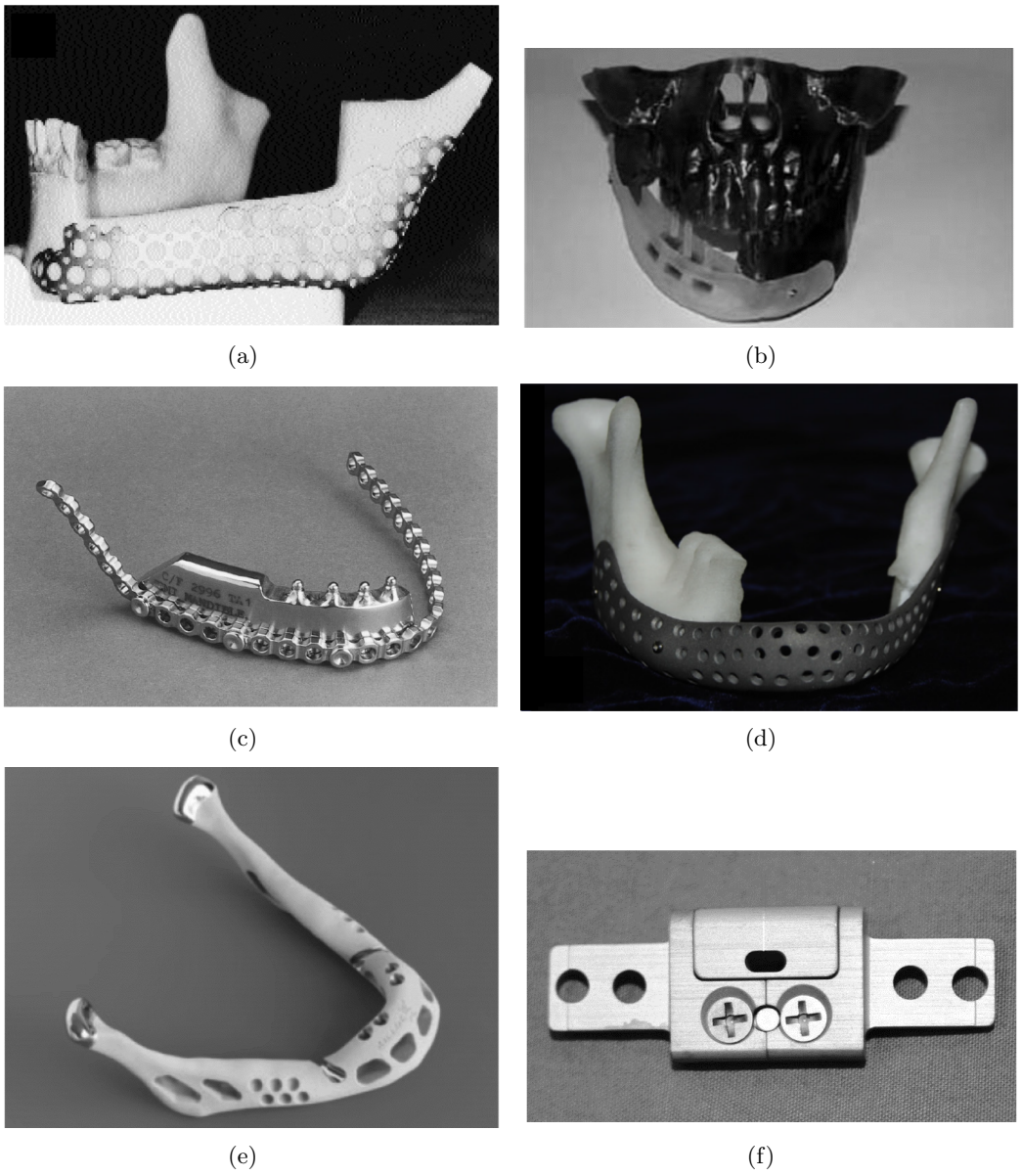

(a) (b)

(c) (d)

(e) (f)

Figure 6.2: Different custom-made mandibular replacements proposed in the literature: (a) the custom tray proposed by Samman et al. (1999); (b) the custom tray developed by Singare et al. (2004a); (c) the THORP described by Peckitt (1999); (d) the plate-like device proposed by Li et al. (2014); (e) the complete jaw implant proposed by Xilloc ((Nickels, 2012)); and (f) the modular endoprosthesis proposed by Tideman H. (2006)

across the cortical bone and plate screws. Ramos et al. (2011) analysed the stresses along custom-made temporomandibular joint implants, and observed high stresses at the level of the first screw regardless of the implant geometry used to interface the mandibular bone. Similarly, Wong et al. (2012a,b) proposed a modular endoprosthesis with a different screwed configuration. High stress concentrations around the connecting screw and the stem caused the long term failure of the implant due to fatigue. The high tendency for transverse bending of the new modular design may also lead to implant loosening when treating large mandibular defects.

Microvascular free flap reconstruction is still the most beneficial approach to mandibular rehabilitation, and possesses many advantages to the patient that may be difficultly to match with other implantable or non-implantable approaches. From the abovementioned analysis, mandibular endoprosthesis may be the most interesting alternatives to microvascular free flap reconstruction, as they may avoid screwed connections along the bone-implant interface. Nevertheless, more long term in-vivo evaluations are needed to consider this technique a reliable alternative to more standard techniques. In these type of implants, modularity seems to be an issue. This increases the need for implant customization, in order to adapt it to the specific anatomy of the patient. Both custom microvascular fibular flap reconstruction and endoprosthesis-based mandibular reconstruction are covered in this chapter. The concepts related with these two approaches are applied to a real case study, where a major mandibular defect was caused by an extensive bone necrosis. The patient under analysis underwent a mandibulectomy and the mandible was reconstructed with the microvascular free fibular technique. The proposed methodology aims to pre-plane the fibular cuts in order to optimize the size of each bone segment and mandibular shaping. This methodology can be also applied for the development of custom mandibular implants, which in some specific situations may be a viable alternative to the microvascular free fibular reconstruction. The remainder of this chapter is organized as follows: in the next section (section 6.2) the main anatomic and cephalometric concepts related with the human craniofacial anatomy are reviewed; in section 6.3 the volume segmentation protocol is described; in section 6.4 the cephalometric evaluation of the current case study is presented; in sections 6.5 and 6.6 the mandibular reconstruction planning through microvascular fibular segments and through a mandibular endoprosthesis are described; in section 6.7 mandibular endoprosthesis is mechanically

evaluated under different chewing tasks; and, ultimately, in section 6.8 one presents some of the main conclusions and achievements of this work.

6.2 Human Craniofacial Anatomy and Cephalometry

The human skull is composed by 22 bones, 8 forming the cranium, and 14 the facial skeleton (Fig. 6.3 (a) and (b)). The main function of the skull is to protect the brain, and provide attachment to the muscles responsible for the facial movement. The 8 bones that constitute the cranium are the frontal bone, the parietal bones in each side of the skull, the occipital bone, the temporal bones that lie inferiorly to both parietal and occipital areas, and the zygomatic bones that form the prominence of the cheek. Near the inferior margin of the temporal bones there is the external acoustic meatus, which lies inward to the internal auditory system, and the mandibular fossae that articulates with the mandible condyles. In the inferior surface of the occipital bone there is a large opening, the foramen magnum, from which the nerve fibres branch from the brain to the vertebral canal to become part of the spinal cord (Shier et al., 2011).

The mid-facial skeleton has 13 immovable bones and the movable jawbone. They define the shape of the face and provide attachment for muscles, which control the jaw and facial expressions. The maxilla forms the upper jaw and the anterior roof of the mouth; it contains the alveolar cavities that surround the upper teeth. The mandible (Fig. 6.4 (a)) is a horizontal bone (the body) with two flat portions projected upwards (the rami) that defines the lower jaw. Each portion has two processes, the mandibular condyle and the coronoid, which articulate with the mandibular fossae of the temporal bone, respectively (Shier et al., 2011).

The human mandible is a movable bone attached to the cranium by several muscles and ligaments, and is the largest and strongest bone of the face. The mandible can be broadly divided into 7 non-overlapping anatomical regions (Fig. 6.4 (b)). The body is curved and has a dense cortical structure on the lateral and medial surfaces, with a small core of cancellous bone containing nerves, blood vessels, and lymphatic vessels. The lower portion of the body contains heavy, thick bone that changes very little throughout life (Flint et al., 2010). It is the region of the mandible that has the greatest cortical plate thickness, and the changes in height and width throughout life in this region seems to be related with

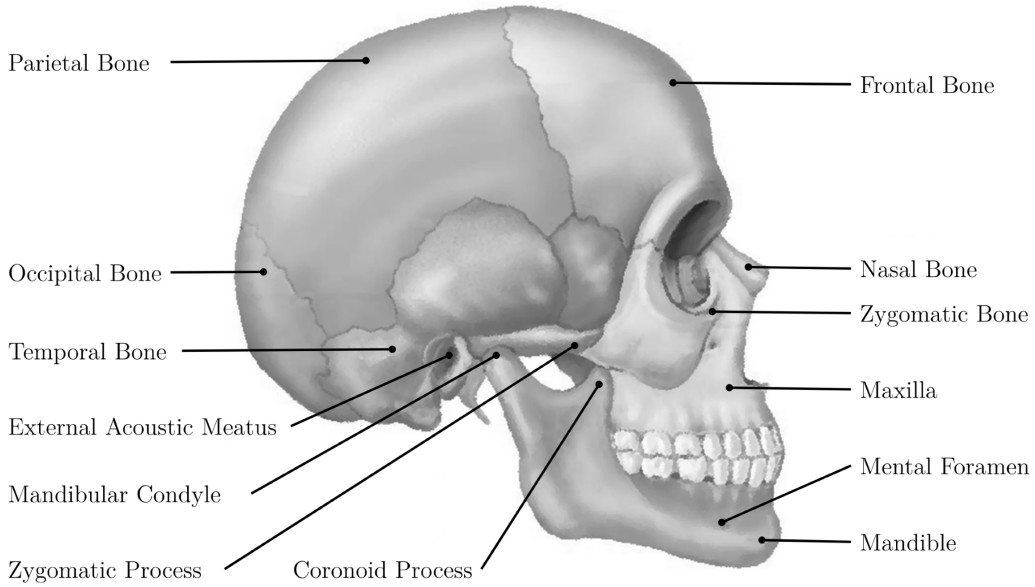

(a)

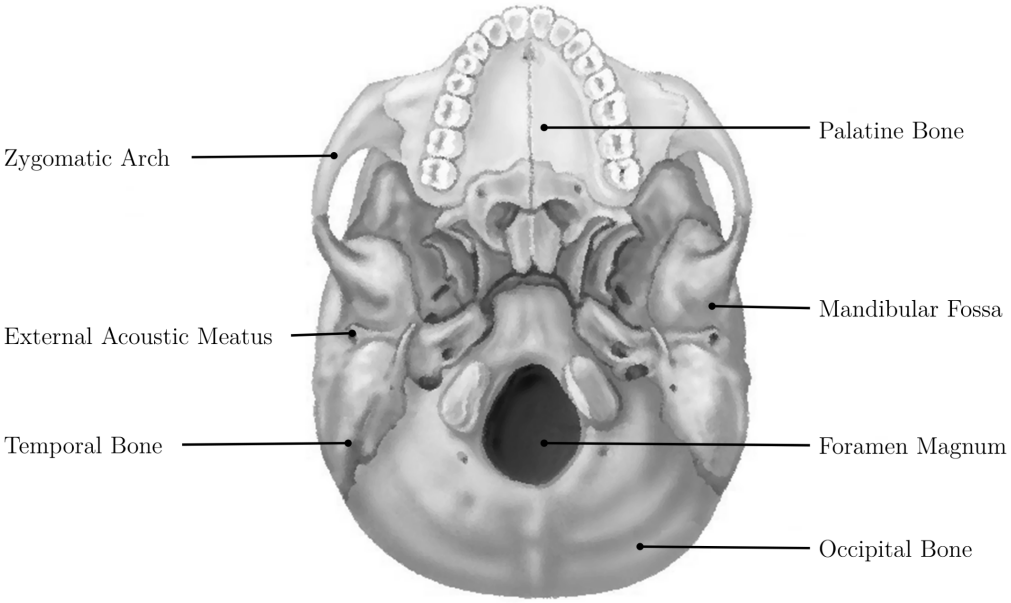

(b)

Figure 6.3: Human Craniofacial anatomy, sagittal view in (a) and inferior axial view in (b) (adapted from (Shier et al., 2011))

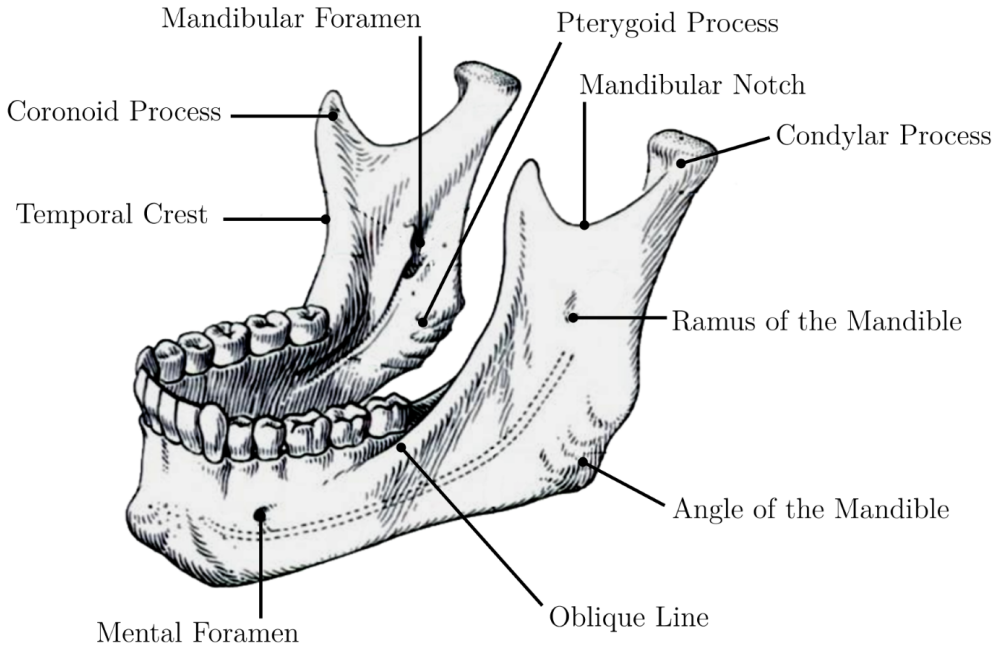

(a)

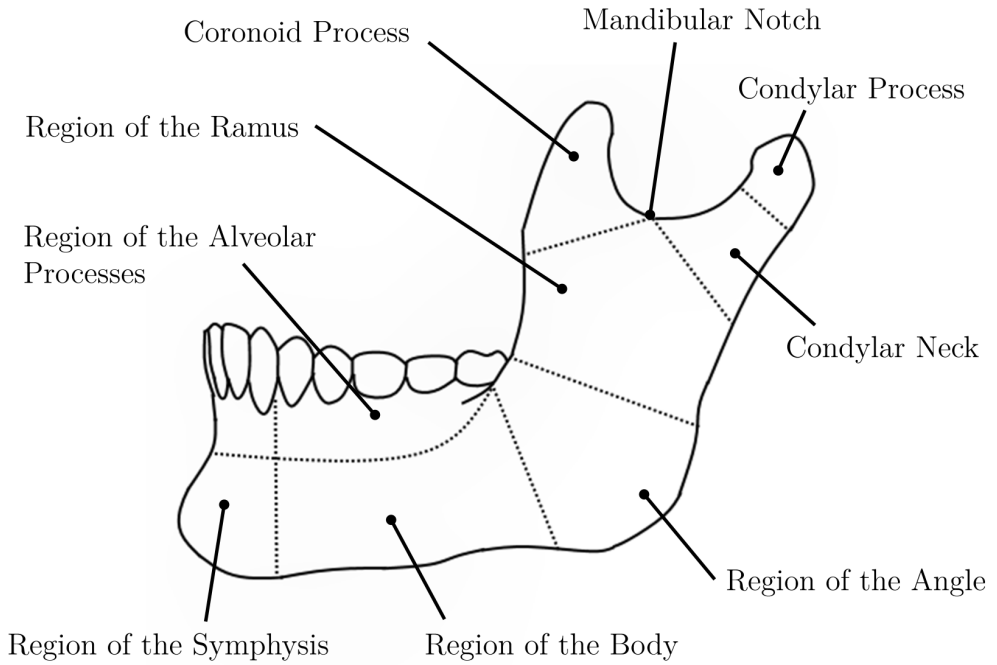

(b)

Figure 6.4: The anatomy of the Human mandible in (a) and the anatomic sub-regions in (b) (adapted from (Dauber, 2011) and (Flint et al., 2010))

mastication and function (Tracy et al., 1965). The medial portion of the mandible also has sixteen alveolar processes, which vary in size and depth, and provide attachment to the teeth (Fig. 6.4 (b)). In each side of the body, below the second premolar and approximately midways between the upper and lower border, there are mental foramens (Fig. 6.4 (a)). The mental foramen provides a passage for the mental vessels and the mental nerve. The mental nerve provides sensation to the teeth roots and to the soft tissue of the lower lip and chin. The lateral rami meet the body at nearly right angles and articulate with the skull through the temporomandibular joints (Gray and Lewis, 1918; Flint et al., 2010).

The lateral surface of the ramus is flat and gives attachment almost exclusively to the Masseter muscles (Fig. 6.4 (a) and (b)). The medial surface presents near its centre the mandibular foramen, and is the entrance point for the interior alveolar vessels and mental nerve (Fig. 6.4 (a)). Below the mandibular foramen there is a rough surface for the insertion of the medial Pterygoid muscles. The posterior border of the ramus is thick, straight, and continuous with the inferior border of the body, forming the angle of the mandible. The Coronoid process is located more anteriorly and the Condylar process more posteriorly. The two processes are separated by a deep concavity, the mandibular notch. The Coronoid process is a thin triangular eminence with a smooth lateral surface for the insertion to the Temporalis and Masseter muscles. The Condyle articulates with the temporomandibular joint, and its anterior surface has a depression for the attachment of the lateral Pterygoid muscle (Gray and Lewis, 1918).

Cephalometric analysis is the study of the dental and skeletal relationships of the Human head. It is commonly used by dentists and orthodontists to evaluate facial growth, as a tool for treatment planning in cases of abnormal development, or as an assessment method for treatment outcomes. The standard cephalometric assessment relies on the planar identification of several anatomical angles, lines and landmarks through a cephalometric radiograph, and subsequent establishment of the sagittal and vertical relations of the craniofacial skeleton, the soft tissue profile, the dentition, the pharynx, and the cervical vertebrae (Mitchell, 2013).

The cephalometric analysis is based on the determination of the so-called Natural Head Position (NHP) (Moorrees and Kean, 1958). Commonly, the NHP is determined physiologically rather than anatomically, and is the position that the head adopts when

the patient is sitting or standing, looking to the horizon or at a distant object (Proffit et al., 2006; Cobourne and DiBiase, 2010). Today, with the generalization of CT systems and the advent of Cone-Beam Computed Tomography (CBCT), 3D measurements are expected to replace traditional 2D cephalometric measurements in a forseenable future. With CT imaging, clinicians may instantly access both the lateral, frontal, and panoramic views of the head, and obtain more accurate and reproducible estimates of all cephalometric landmarks (Swennen et al., 2005). Nevertheless, 3D-based cephalometric assessment is a relatively new technique, and the great majority of the available textbooks is still focussed on conventional 2D cephalometry. Therefore, one will only refer to the standard 2D cephalometric landmarks and planes used to evaluate the craniofacial anatomy. In Fig. 6.5 the most common anatomical landmarks, lines and reference planes employed in conventional craniofacial cephalometric analysis are depicted.

Every cephalometric analysis starts with the definition of the cephalometric reference frame, which defines the true horizontal and the true vertical direction. Since the true NHP is very difficult to obtain, additional anatomical planes are used to correct this variability. One of the most common reference cephalometric plane is the Frankfort plane (FH). The FH plane is defined as the line connecting the lower margins of the bony orbit (Or) to the upper margin of the external auditory mentus (Po), and it commonly defines the true horizontal plane (Fig. 6.5). The Sella-Nasion plane (SN-plane) that connects the centre of the pituitary fossa (S) to the most anterior point of the frontonasal suture (N), defines the cranial base and is also (although less commonly) used to define the true horizontal plane. The true vertical plane is defined by the McNamara line, which is perpendicular to the FH plane and passes through the N point (Singh, 2008). These lines (in conventional cephalometry) are very useful as guidelines to guarantee the consistency on the identification of all craniofacial landmarks and planes. The need for further clinical intervention is based on the comparison between these planes and landmarks with a comparable group of individuals. Hence, the guidelines for orthodontic treatment are obtained by comparison, with other geographically related individuals or average models (Mitchell, 2013).

Cephalometric analysis aims to preserve function and aesthetics. The position and shape of the mandible plays a major role in facial aesthetics, and it is the greatest source of facial asymmetry (Yáñez-Vico et al., 2011). The ideal face can be divided into equal

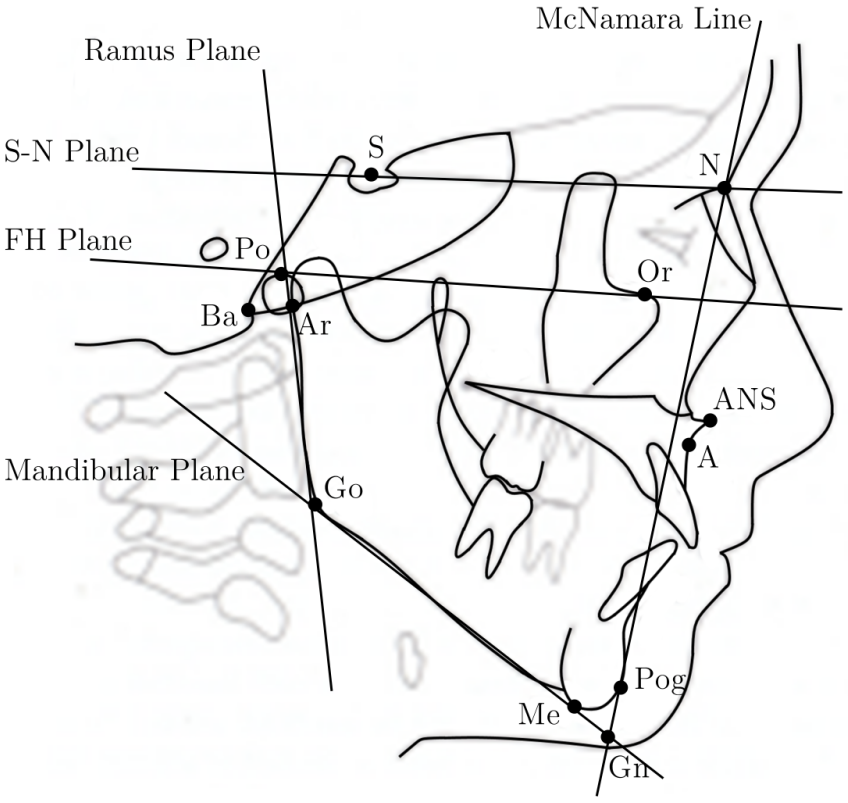

Figure 6.5: Anatomical landmarks and planes commonly used in cephalometric assessment: Nasion (N) - the most anterior point of the frontonasal suture; Sella (S) - the centre of the pituitary fossa; Orbitale (Or) - the most inferior point on the lower border of the bony orbit; Porion (Po) - The most superior point of the external and internal auditory meatus; Articulare (Ar) - the intersection point of the ramus plane and the occipital bone; Gonion (Go) - the intersection of the ramus plane and the mandibular plane; Menton (Me) - the most inferior point of the mentum section; Gnathion (Gn) - the point on the chin determined by bisecting the angle formed by the facial and the mandibular plane; Pogonion (Pog) - the most prominent point of the chin; Subspinale (A) - the deepest point on the concave outline of the upper labial alveolar process; Basion (Ba) - The most inferior posterior point of the occipital bone at the anterior margin of the occipital foramen; Anterior Nasal Spine (ANS) - The most anterior point at the sagittal plane on the bony hard palate; Frankfort horizontal plane (FH) - A line connecting the Po and Or points; $McNamara$ line - the line which passes through N and is perpendicular to FH; SN plane - A line connecting the Sella and the Nasion points; Mandibular plane a tangent line to the lower border of the mandible; Ramus plane - a tangent line on the posterior contour of the ramus (adapted from (Athanasiou, 1995; Sato et al., 2014; Kawashima et al., 2002; Cobourne and DiBiase, 2010))

thirds, namely the upper third from the frontal hairline to the glabella, the middle third from the glabella to the soft tissue of nasal base, and the lower third from the nasal base to the lowest point on the chin (Fig. 6.6). These measures can be more accurately determined considering several cephalometric landmarks. The height of the facial middle third can be determined as the distance from the Nasion point (N) to the Subspinale point (A), which is the deepest point on the concave outline of the upper labial alveolar process. Whereas the lower third is defined as the distance from the point A and the Me point, which is the most inferior point of the mandible (Athanasiou, 1995; Miloro et al., 2004; Flint et al., 2010; Sato et al., 2014). Differences in the height of each subdivision may suggest facial disharmony in the vertical plane. The facial lower third can be further divided into another thirds, being the upper lip in the upper third, and the lower lip on the remaining two thirds (Mitchell, 2013).

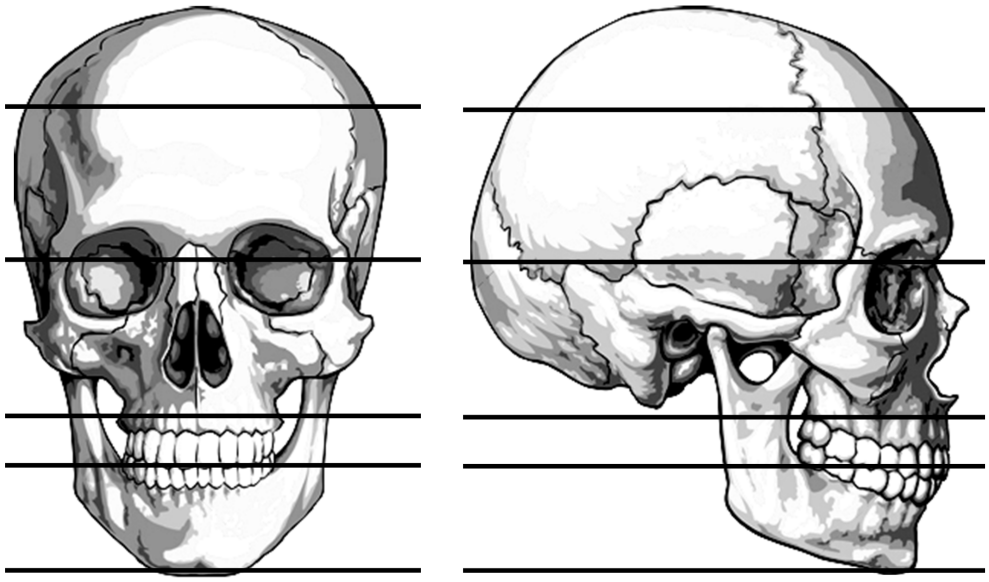

(a) (b)

Figure 6.6: Ideal facial height division: the upper third, from the frontal hairline to the glabella; the middle third, from the glabella to the soft tissue of nasal base; and lower third, from the nasal base to the lowest point on the chin (adapted from (Proffit et al., 2006))

6.3 Segmentation of the Human Mandible

The current case study aims the development of a customized solution for the reconstruction of a major mandibular defect caused by an extended osteonecrosis. Bone segmentation was carried out with image optimal thresholding as described in Chapter 3, section 3.2. Morphological operations were applied to remove isolated pixels and to achieve a complete foreground-background segmentation of the DICOM volume (Fig. 6.7 (a)). The cranium, mandible and vertebral bodies were manually segmented from the thresholded data (Fig. 6.7 (b) and (c)). Image segmentation refinement was performed with the algorithm proposed in Chapter 4. The outcome of the refinement process was down-sampled to the original resolution and imported to Simpleware ScanIP^{TM} for further surface mesh generation (Fig. 6.7 (d)). Fig. 6.7 (e) and (f) show the mask profiles obtained with the segmentation refinement, the coronal and the sagittal views of the final segmentation.

Osteonecrosis was pointed as the main cause for a major bone loss in the anterior aspect of the mandible. It is observable from Fig. 6.7 (e) and (f) the complete bone loss from the chin to the level of the second molars. It also depicts the pathological positioning of the two remaining mandibular segments. Both mandibular segments were rotated inward and upward relatively to their correct anatomical position. It is worth noting that no non-pathological information was available at the time of the study. The correct position of the mandibular segments, as well as the dimension of the lower third of the patient's face, were estimated from other facial structures and known anatomical relations.

6.4 Cephalometric Evaluation

Cephalometric evaluation starts with the definition of the anatomical reference frame of the head, which may be completely independent of the CT machine internal reference system. According to Madsen et al. (2008) an ideal cephalometric reference system should have good reliability, good intra-observer variability, and average orientation close to the true horizontal or vertical planes. Madsen et al. (2008) concluded that the NHP could be reliably reproduced with an average error of approximately 2 degrees. However, cephalometric analysis should be performed using more than one reference plane. The

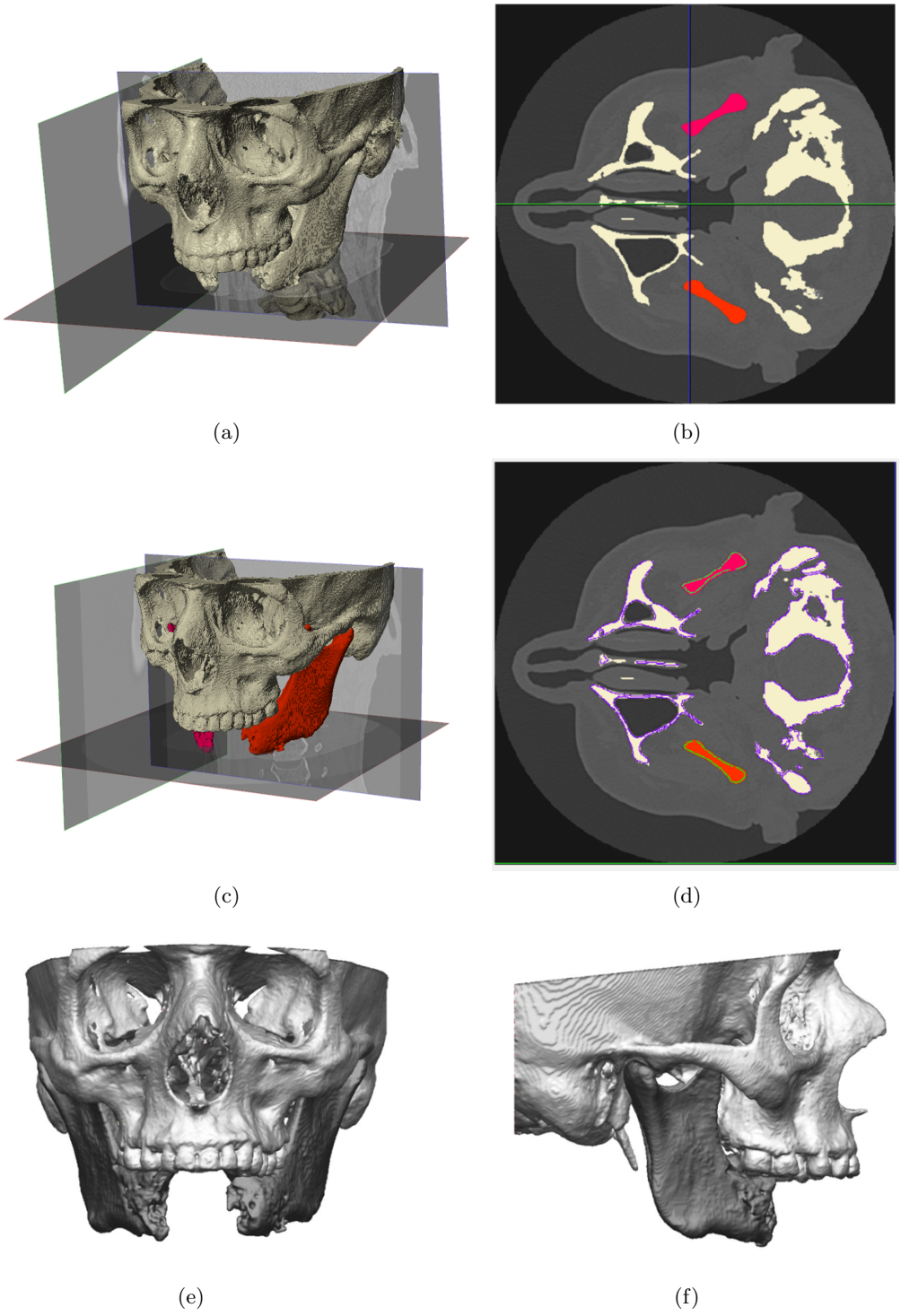

(a) (b) (c) (d) (e) (f)

Figure 6.7: Overview of the segmentation procedure used in the design of a custom mandibular implant: in (a) segmentation by thresholding; in (b) and (c) manual individualization of the different bones; in (d) mask correction and down-sampling to the exam resolution; and in (e) and (f) the coronal and sagittal view of the final model

main problem associated with the conventional cephalometric reference system is that it is very subjective, and very often, not applicable to computationally generated models.

In this work the NHP was approximated considering the cepahlometric reference frame proposed by Lagravère et al. (2006). This reference system aims to standardize 3D image orientation of the human skull. The reference frame is defined over four points derived from five anatomical landmarks, namely: the midpoint between geometric centres of foramina spinosum, left and right centre of the superior-lateral border of the external auditory meatus, and the midpoint of the foramen magnum (Fig. 6.8). The horizontal plane is defined by three of the five aforementioned anatomical landmarks: the midpoint between geometric centres of foramina spinosum, and the left and right centre of the superior-lateral border of the external auditory meatus; the sagittal plane (symmetry plane) is perpendicular to the horizontal and contains both the midpoint between geometric centres of foramina spinosum, and the centre of the foramen magnum. These reference planes were developed for 3D image-based models, and are relatively independent from the anatomical landmarks used for cephalometric assessment. In addition, they have been recently successfully applied in the assessment of craniofacial asymmetry, recurring to 3D models generated by CT images (Yáñez-Vico et al., 2011). The importance of having a reliable referencing system to ensure the correct spatial position and symmetry of the head was also stressed by Singare et al. (2004b) in the project of chin augmentation implants.

To correctly define the position of the head, the FH must be defined as the true horizontal direction or the McNamara line as the true vertical direction. However, the FH plane is very difficult to determine in practice (3D cephalometry). Both the Po and the Or landmarks are bilateral structures, and their determination is affected by the natural asymmetry of the head (Cobourne and DiBiase, 2010). In an ideal adult the McNamara line lies approximately 1.0 to 2.0 mm posterior to the A point, therefore the determination of this line is more straightforward than the FH plane (Proffit et al., 2006; Meneghini and Biondi, 2012). The McNamara line has also the advantage of belonging to the mid-sagittal plane (defined previously), which ensures consistency with the current reference frame, and allows the definition of the true vertical direction within the current reference frame. The head frame proposed by Lagravère et al. (2006) was adjusted to have the true vertical direction defined according to the McNamara line.

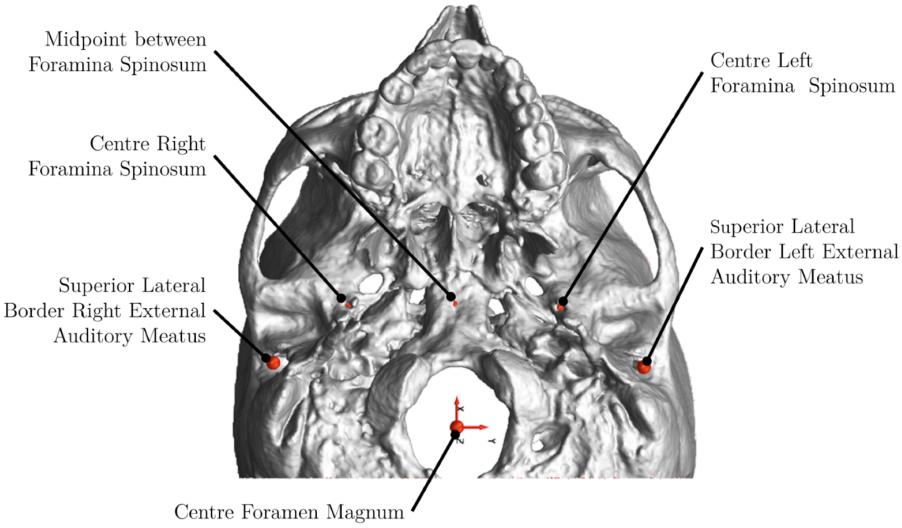

Figure 6.8: Determination of the head reference planes according to the methodology proposed by Lagravère et al. (2006)

After defining the head reference frame, the mandibular segments were rotated to their natural position. Each mandibular segment was rotated about the most superior point of each condylar process (SCo reference point), as defined by Hilgers et al. (2005). The aim of this step was to restore the correct teeth occlusion between the upper and lower first and second molars. For occlusion correction, the guidelines proposed by Angle's Classification were considered. The Angle's Classification is one of the oldest, and probably the most widely used, method to qualitatively assess teeth occlusion. The method is based on the assumption that the first permanent molars erupt in a constant position within the facial skeleton. Based on this classification system, three types of malocclusion can be discriminated:

- Class I or neutrocclusion: the mesiobuccal cusp of the upper first molar occludes with the mesiobuccal groove of the lower first molar;
- Class II or distocclusion: the mesiobuccal cusp of the lower first molar occludes distal to the Class I position;
- Class III or mesiocclusion: the mesiobuccal cusp of the lower first molar occludes mesial to the Class I position.

The three types of malocclusion proposed by Angle's are graphically shown in Fig.

6.9. From Angle's classification, it can be observed that that between the upper and lower teeth arches a tooth-to-two-teeth relationship should be observed. In addition, in the transverse (or coronal) anatomical plane a centric occlusion should be observed, i.e., the lingual upper molar cusps should occlude the lower molar fossa (Singh, 2008).

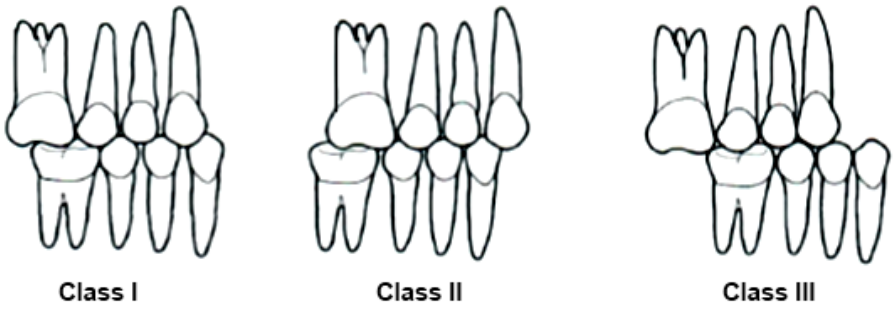

Figure 6.9: The Angle's malocclusion classification: in (a) class I or neutral occlusion, in (b) class II or distocclusion where the lower teeth are displaced posteriorly, and in (c) Class III or mesiocclusion where the lower teeth are displaced forward (adapted from (Mitchell, 2013)

The correct definition of the NHP and the restoration of the normal occlusion between the remaining lower teeth are two fundamental steps prior to the cephalometric assessment itself. Now one can determine several cephalometric landmarks and planes associated with the lower face, and estimate the position of the chin. Only then the length of each fibular segment to be removed from the donor site and the overall shape of the mandibular implant can be estimated.

First, two mandibular (anatomical) planes were defined, namely: the mandibular plane, defined as the tangent line to the lower border of the mandible; and the posterior ramus plane, defined as the tangent plane to the posterior contour of the ramus (Athanasiou, 1995). Both planes were computed applying the Principal Component Analysis (PCA) to the set of selected surface mesh points. Fig. 6.10 (a) shows the sagittal view of the lower mandibular and the posterior ramus planes. Next, the intersection between the mandibular plane and the McNamara line along the mid-sagittal plane allow the determination of the, which is by definition the intersection between the facial and the mandibular lines along the sagittal plane (Athanasiou, 1995). More importantly, and taking into account the height of each facial third (Fig. 6.6 (a) and (b)), the Me point can

be determined by finding the intersection of the mandibular line and an horizontal line, perpendicular to the McNamara line 56.88 mm below the A point (Fig. 6.10 (b)).

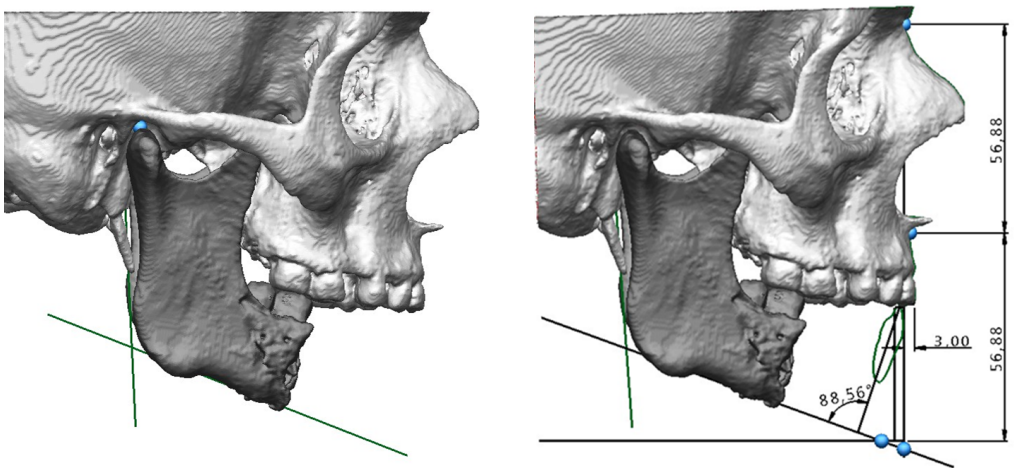

(a) (b)

Figure 6.10: (a) sagittal view of the posterior ramus plane and the mandibular plane; (b) determination of the Gn point, the Me point, and the position and orientation of the lower teeth according to the mandibular plane, the McNamara line, the facial height, and the Ballard's conversion

The McNamara line possesses three cephalometric landmarks, namely: the N point; the Gn point; and the Pog point. The Pog point is fundamental for understanding the antero-posterior positioning of the chin, and consequently the sagittal extent of the lower face. The three anatomical points (Me, Pog and Gn) previously determined provide a rough estimate of the subjects' most plausible sagittal facial profile, and the correct position and height of the chin (Fig. 6.10 (b)). More insights to the position and shape of the chin can be obtained considering the spatial relations between the maxilla and the mandible defined by the Angle's classification and the Ballard's conversion. In neutrocclusion the mandible is 2 to 3 mm posterior to the maxilla (Fig. 6.9). In addition, according to the Ballard's conversion the lower incisor are commonly rotated relative to the mandibular plane about 88.5 degrees. The lower teeth should also be positioned with a teeth overjet between 2 to 4 mm from the upper incisor, and the vertical distance between the lower border of the maxillary incisors and the upper border of the lower incisor (overbite) should be approximately 2 to 3 mm (Mitchell, 2013). With these anatomical relationships, the relative orientation and position of the lower incisors can be determined (Fig. 6.10 (b)).

6.5 Microvascular Fibular Reconstruction

Microvascular flap reconstruction of the mandible has numerous advantages when compared with other reconstruction techniques. These vascularized bone grafts are preferred to non-vascularized grafts because avascular grafts are more prone to resorption (Söderholm et al., 1992). The success of bone grafting in mandibular reconstruction is highly dependent on the revascularization of the implanted bone and in the subsequent bone remodeling process (Goh et al., 2008). The induction of extensive bone remodelling in the total reconstruction of the symphysis in individuals subjected to microvascular fibular flaps mandibulectomy has been reported (Shen et al., 2012). Interestingly, it was also observed the absence of growth retardation in children's subjected to this technique (Ferri et al., 1997).

In addition to the aesthetic outcome, mandibular reconstruction aims to restore normal mastication. To guarantee the complete functional rehabilitation, the size of each mandibular segment should consider the need for a subsequent oral rehabilitation with a prosthetic device, and allow the restoration of the normal occlusion between the upper and lower teeth. The lower teeth arch was segmented from elsewhere and each individual tooth was positioned according to the Angle's Classification and the previous cephalometric analysis, (Fig. 6.11 (a) and (b)). The size of each individual tooth was adjusted considering the upper and lower teeth anatomical relationships reported by El-Zanaty et al. (2010). The process of tooth positioning and dimensioning followed in this work was performed in a general purpose CAD software the Delcam Powershape^{TM}. Single tooth positioning and resizing performed here is very similar to the workflow proposed by many commercially available dental software's (and a common practice in oral rehabilitation). The width of the chin segment was set slightly larger than the nasal cavity, at the level of the left and right cuspid teeth. From the facial profile and the estimated lower teeth arch, a fibular segment of approximately 96 mm is needed to completely restore the missing part of the mandibular body.

The surgical aid to guide the osteotomy of each individual fibular segment may be designed pre-operatively (Fig. 6.11 (c)). The surgical guide provides the 3D orientation of each individual cut along the fibula. Since it defines the shape of each osteotomy, this device may optimize bone harvesting and facilitate the assembly of all different segments.

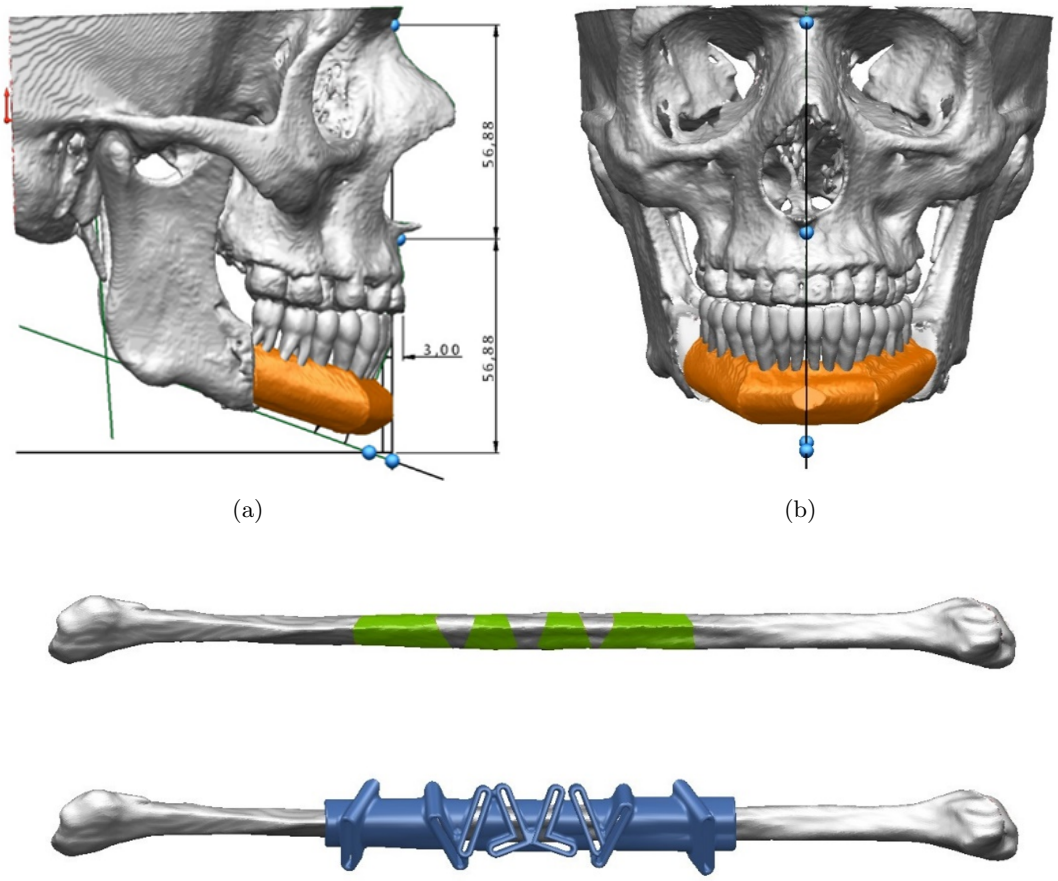

(a) (b)

(c)

Figure 6.11: In (a) and (b) the sagittal and coronal view of the mandibular reconstruction through fibular microvascular free flap, and in (c) the surgical guides to perform the 3D osteotomy of each fibular segment according to the proposed mandibular geometry

It may also enhance the aesthetic outcome of the surgery, by assuring the overall facial symmetry and contour. Facial symmetry is critical to restore chewing function after the surgical procedure (Singare et al., 2005). Fig. 6.11 (a) and (b) also show the main drawback of selecting the fibula as donor site: the height of this bone is not enough to accurately restore the mandibular body. It also fails to reproduce accurately the height of the facial lower third. Now that the sagittal profile of the face was determined an optimized solution may be designed. The development of titanium trays for bone grafting or mandibular endoprosthesis is straightforward, and will be addressed in the next section.

6.6 Mandibular Endoprosthesis Design

Mandibular endoprosthesis seems to be a recent and promising approach to mandibular reconstruction, to which customization is critical. The early loosening observed in some of the modular endoprosthesis implanted by Lee et al. (2008) were related with the loosening of the connecting screws. These preliminary results suggest that the screw connection between different modules in the modular mandibular implant is the major source of problems. Two main conclusions arise from section 6.1: that screwed connections are very prone to failure in mandibular reconstruction; and that modularity in the mandibular endoprosthesis should be avoided. In both cases, screwed connections make the implants more susceptible to fatigue fracture.

Similarly to the conventional mandibular reconstruction and other craniofacial trauma implants, mandibular endoprosthesis must be developed in a custom-made philosophy, in order to guarantee both the functional and the aesthetic outcome. Encouraged by these results and applying the concepts related with the mandibular endoprosthesis proposed by Tideman H. (2006) and Lee et al. (2008), a new custom-made mandibular geometry for the rehabilitation of a major human mandibular defect is here developed and proposed. Fig. 6.12 shows the mandibular endoprosthesis with some additional geometrical details, whereas Fig. 6.13 depicts the final geometry of the mandibular implant with and without a prosthetic device. The mandibular endoprosthesis takes into account the facial height, chin protrusion, and the oral rehabilitation after implantation. The weight of the solid implant is, for Ti-6Al-4V titanium alloy, of approximately 67 grams. The height of the implant body was defined as the distance between the mandibular plane and a plane lying approximately 15 mm below the tips of the lower teeth. The 15 mm gap takes into account the space for a full arch fixed implant restoration such as in Fig. 6.13 (a). The dental superstructure is placed directly over four standard dental implants, positioned according to the All-on-Four system (Fig. 6.13 (b)). In the All-on-Four technique, the two most anterior implants are typically placed immediately below the lateral or central incisors, and the two posterior implants emerge at the second pre-molar or second premolar/first molar region (Maló et al., 2003, 2005).

The mandibular implant has a stem geometry similar to the modular endoprosthesis proposed by Tideman H. (2006) and Lee et al. (2008), and aims to recover more accurately

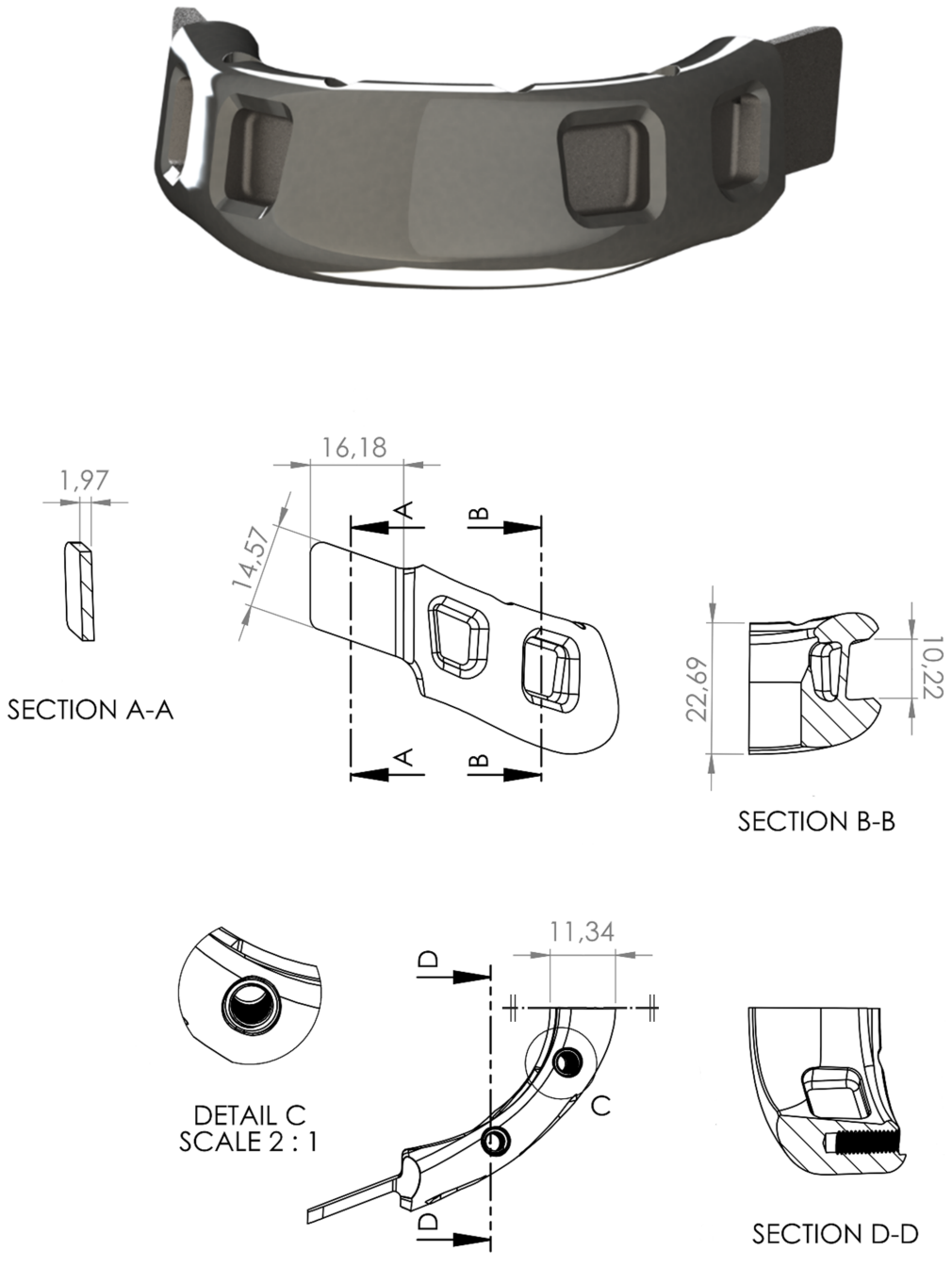

Figure 6.12: Rendering of the mandibular endoprosthesis, with additional geometrical details and cross-sections

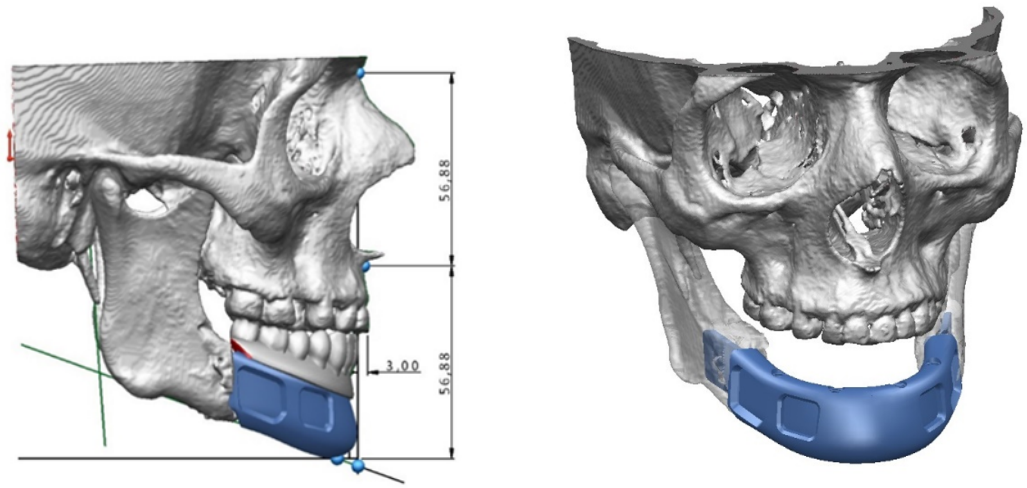

(a) (b)

Figure 6.13: (a) the mandibular endoprosthesis in the sagittal view, and (b) the mandibular endoprosthesis implant without the dental prosthesis

the facial profile, enhancing facial aesthetics, and functioning of the masticatory system. The mandibular endoprosthesis may recover more accurately the facial height and the correct position of the chin. It takes into account the oral rehabilitation through a full arch fixed prosthetic device in a second-stage (oral) surgery. It may also allow the precise restoration of the lower border of the mandible and, consequently, preserve the muscle tension along the mandibular bone stock, as well as the correct chewing biomechanics (Galoob, 2013). Mandibular endoprosthesis placement can be performed with a one-stage surgery, without the need for harvesting any tissue from the patient during reconstructive surgery. This may be important to reduce both surgery and recovery times, and risk of medical complications post-operatively (Nickels, 2012). In addition, it is known that there is a strong affinity between the titanium and the soft tissues, similarly to what has been observed with bone tissues (Albrektsson et al., 1981). The titanium oxide may bias a tight connection between the implant and the gingivae, minimizing the proliferation of micro-organisms at the implant-soft tissue interface, and providing attachment to the facial soft tissues.

A mandibular endoprothesis may be advantageous against other prosthetic solutions, mostly because it avoids the complications associated with reconstruction plates, such as the fracture and the detachment of the hardware, infection, bone resorption, and with microvascular flaps, such as the lack of bone volume to enable the placement of

osseointegrated implants for oral rehabilitation (Goh et al., 2008; Knoll et al., 2006; Wong et al., 2012b). Implants fixed with screws to the mandibular bone apply forces that are different from the physiological forces caused by mastication. These unfavourable forces cause bone resorption and are responsible for screw loosening over time, and the consequent loss of function observed in some temporomandibular replacements (Skedros et al., 1996; Spencer et al., 1999).

6.7 Mandibular Endoprosthesis Evaluation

To understand the mechanical behaviour of the proposed mandibular endoprosthesis, the implant was simulated under static clenching conditions. Simulations were carried according to the loading conditions defined in Korioth and Hannam (1994). In addition, in Korioth and Hannam (1994) the orthogonal directions, the muscle forces, and the scaling factors for different clenching tasks were also defined. Here, three mastication tasks are considered, namely, incisal clenching, unilateral molar clenching, and left group clenching, which involves the left canine, premolars and molar teeth.

6.7.1 Finite Element Model and Boundary Conditions

The forces along the teeth arch have a large variability, and biting forces of more than 2200 N have been reported in the literature (Misch, 2007). Besides, different bite forces have been reported for different teeth groups, however the bite force is commonly larger at the first molar region and reduces gradually towards the incisor teeth. For instance, Hellsing (1980) reported a variation of the incisal bite force that ranging between 110 and 200 N in eight healthy adult male subjects with a full dentition. Lyons and Baxendale (1990) investigated the maximum bite force, as well as muscle recruitment, in normal individuals and recorded forces between 120 to 340 N in the canine region. Waltimo et al. (1993) measured an average bite force of 237 N in the incisors and an average maximum bite force of 747 N in the molar region for male subjects, whereas for women an average maximum force of 204 N and 573 N were found along the frontal and molar teeth, respectively.

Paphangkorakit and Osborn (1997) argued that these variations may come from the differences in muscle sizes, shapes of the mandibles and the articulating joint tissues, in instrumentation used, and even volunteers' motivation. More recently, this was also

observed by Tortopidis et al. (1998), who recorder an average clenching force of 286 N in the incisors and canines, 428 N for unilateral and 579 N for bilateral clenching with the first and second molar teeth. For mandibular endoprosthesis validation, the bite forces for each individual clenching task were derived directly from single tooth measurements. The forces are based on the measurements of Ferrario et al. (2004), and the main values are listed in Table 6.1.

Table 6.1: Static single tooth clenching forces (in Newton) for young adults according to Ferrario et al. (2004)

Tooth	Women	Men
Central Incisor	93.88	146.17
Lateral Incisor	95.75	139.30
Canine	119.68	190.31
1^{st} Premolar	178.54	254.08
2^{nd} Premolar	206.01	291.36
1^{st} Molar	234.46	306.07
2^{nd} Molar	221.71	294.30

According to the muscular model proposed by Korioth and Hannam (1994), to simulate the different Human clenching movements, three major muscle groups must be considered, namely the Masseter muscles, the Temporalis muscles, and the Pterygoid muscles (Fig. 6.14). For different clenching tasks, muscle groups may be recruited differently, a set of scaling factors to model the relative importance of each muscle group were also proposed. Therefore, considering the single tooth forces in Table 6.1 for male subjects, muscular forces were scaled to produce the desired forces for each individual clenching task. By adding the individual tooth forces, the reaction forces along the teeth arch should be 570.90 N for incisal clenching, 600.40 N for right molar clenching, and 1336.10 N for the left side group clenching.

Since the non-pathologic anatomy of the mandible was unknown, predicting the muscle forces necessary to produce the desired teeth reaction forces was unfeasible. To estimate these forces, an intact mandible model was segmented from a DICOM dataset INCISIX, available at the public database[1]. The segmentation protocol for the intact mandible was similar to the pipeline proposed in section 6.3. The new muscular forces were applied to the implanted model to understand the stress and strain distributions along the right and

[1] *http://www.osirix-viewer.com/datasets/*

left mandibular segments after endoprosthesis implantation. Table 6.2 summarizes the muscle forces for each masticatory activity required to obtain the desired biting forces.

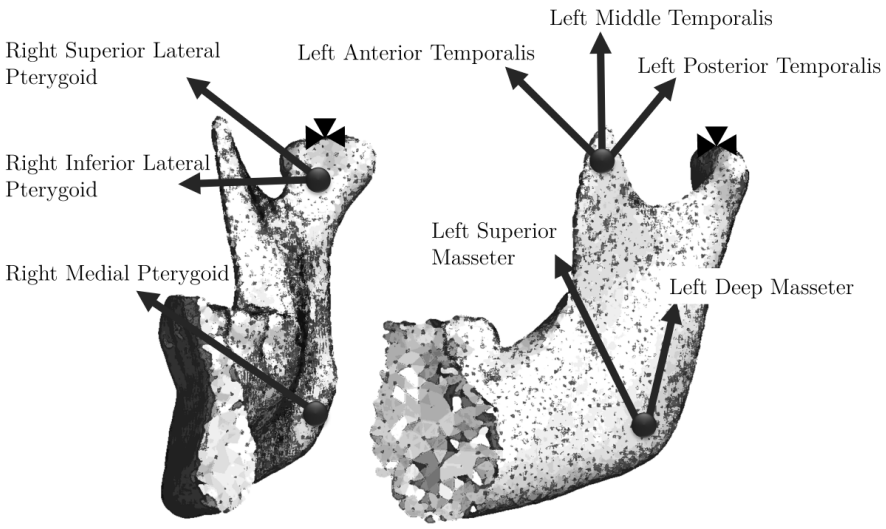

Figure 6.14: Schematic representation of the muscle model proposed by Korioth et al. (1994) for the simulation of Human clenching tasks (muscle insertions and direction are partly shown on the left and right mandible for simplicity)

Table 6.2: Muscle forces for different masticatory activities, namely incisor, right molar and left group clenching

	Incisal Clenching (N)			Right Molar Clenching (N)			Left Group Clenching (N)		
	x	y	z	x	y	z	x	y	z
Right Masseter	109.4	-123.0	375.4	47.4	-78.6	215.4	80.8	-128.9	356.9
Left Masseter	109.4	123.0	375.4	39.4	65.5	179.5	22.3	134.1	304.8
Right Temporalis	-22.0	-17.0	84.3	-84.0	-52.6	244.3	-36.3	-22.5	103.7
Left Temporalis	-22.0	17.0	84.3	-69.2	44.3	205.6	-383.2	225.4	1023.5
Right Lateral Pterygoid	203.5	183.8	-32.4	19.8	16.4	-4.5	49.7	44.3	-8.5
Left Lateral Pterygoid	203.5	-183.8	-32.4	42.8	-35.6	-9.8	194.8	-169.5	-37.3
Right Medial Pterygoid	228.9	298.2	485.3	71.2	92.8	151.0	287.4	374.5	609.5
Left Medial Pterygoid	228.9	-298.2	485.3	50.9	-66.3	107.8	26.5	-34.5	56.1

The Finite Element (FE) model of the intact mandible was generated with Simpleware $+FE$ Module (available with Simpleware ScanIP $v4.0$), with 4-node tetrahedral element with varying edge length between 0.50 mm and 2.0 mm. A Finite Element mesh with 27590 nodes and 108164 elements was obtained (Fig. 6.15 (a)). Next, the FE mesh was simplified using the software *Simptets*[2]. The target minimum number of elements was set to 50000 elements. Ultimately, the 4-node tetrahedral elements were converted

[2] *http://vcad-hpsv.riken.jp/en/release_software/Simptets/*

into 10-node tetrahedral elements by adding the intermediate nodes at edges. The final mesh of the intact mandible is depicted Fig. 6.15 (b), has 57253 10-node tetrahedral elements and 113417 nodes. Similarly to the intact mandible, a 4-node tetrahedral mesh of the implanted mandible was generated with Simpleware $+FE$ Module. The implanted mandible has 54642 nodes and 218888 elements. After mesh simplification and node addition, the final FE mesh of the implanted mandible has 139214 elements and 255489 nodes (Fig. 6.15 (c) and (d)).

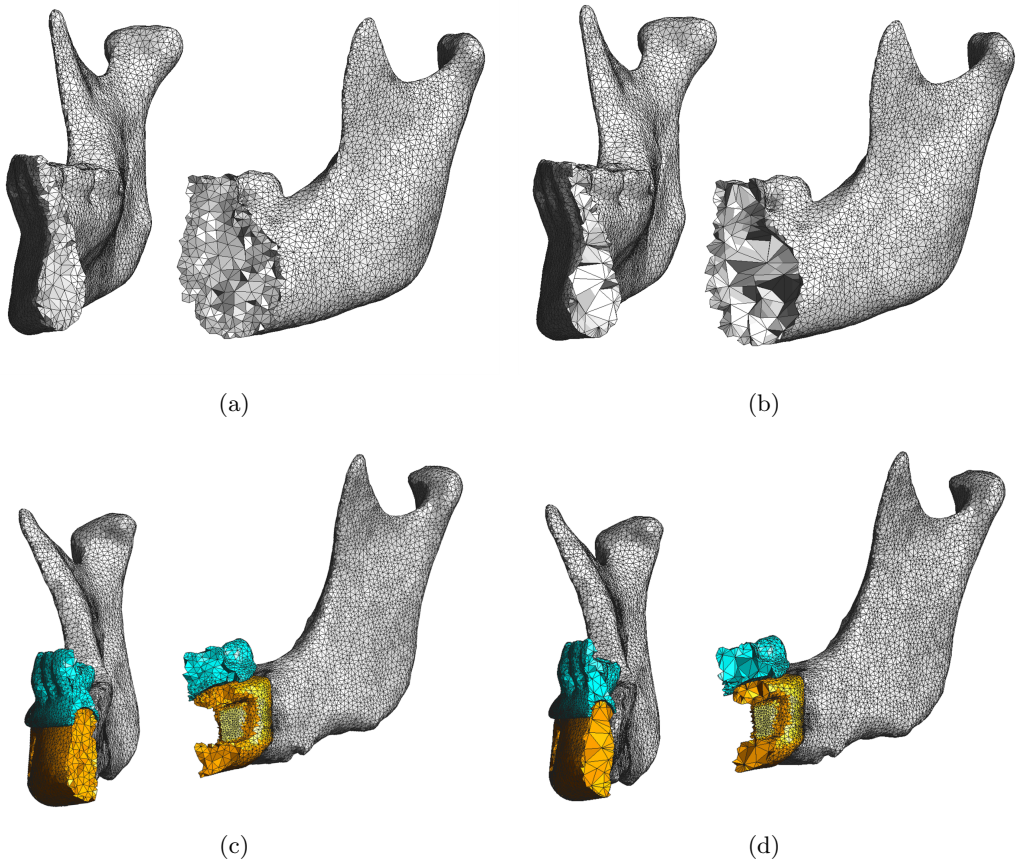

Figure 6.15: Intact model of the mandible was used to define the muscle forces to be applied to each loading case: (a) the Finite Element mesh generated with Simpleware +FE from the segmented data, and (b) the simplified model obtained by reducing the interior of the mesh and keeping the boundary unchanged; likewise (c) the FE mesh of the implanted mandible and (d) the final FE mesh of the implanted mandible after simplification

The displacement boundary conditions for the FE simulation as follows: the right and left temporomandibular joints were restrained in all three directions, and the teeth arch was also restrained vertically according to each simulated task, namely: during

incisal clenching, the four incisors were restrained from moving vertically; for right molar clenching, the first and second molars were restrained; for left-side group the canine, the first and second pre-molars, and the first and second molars were restrained vertically. The muscle forces were applied in a set of nodes at each muscle insertion site as shown schematically in Fig. 6.14. As mentioned in section 6.6, the mechanical properties of the Ti-6Al-4V alloy assigned to the mandibular endoprosthesis are: Young's modulus $E = 113800$ MPa and Poisson's Ratio of $\nu = 0.34$. The dental prosthesis was assigned with the mechanical properties of a cobalt-chrome alloy: $E = 240000$ MPa and $\nu = 0.30$. The mandible was modelled as being composed only by isotropic cortical bone, with an elastic modulus $E = 13700$ MPa and $\nu = 0.30$ (Welsch et al., 1993; Van Oosterwyck et al., 1998; Bozkaya et al., 2004; Baggi et al., 2008). All materials were modelled as isotropic linear elastic, perfectly homogeneous and the different components totally bounded.

6.7.2 Results

Surface nodal displacements were assessed along a transverse cut plane passing through the middle of the mandibular implant (Fig. 6.16 (a)). The nodal displacement fields of the implanted mandible along the y-axis for the three masticatory tasks are shown in Fig. 6.16 (b).

During incisal chewing the right and left muscle groups are recruited equally and therefore similar nodal displacements (in absolute value) were observed on both sides of the mandible. In the transverse plane, the posterior mandibular nodes are mainly displaced inward and the nodal displacement gradually decreases moving from the ascending ramus towards the chin. A slight displacement towards the right side was also observed in the anterior region of the implant (Fig. 6.16 (b)). In right molar clenching, the transverse nodal displacement along both sides of the mandible was minimal. Again, and similarly to incisal chewing, the implanted mandible is slightly displaced towards the right side at the chin. In contrast to right molar clenching, the largest nodal displacements were observed for left group clenching. The largest displacements were observed on the balancing side of the mandible when compared with the working side. This may be explained by the differences in muscle recruitment between the right and left medial Pterygoid during this particular task (see Table 6.2). The transverse nodal displacements (in y-axis direction)

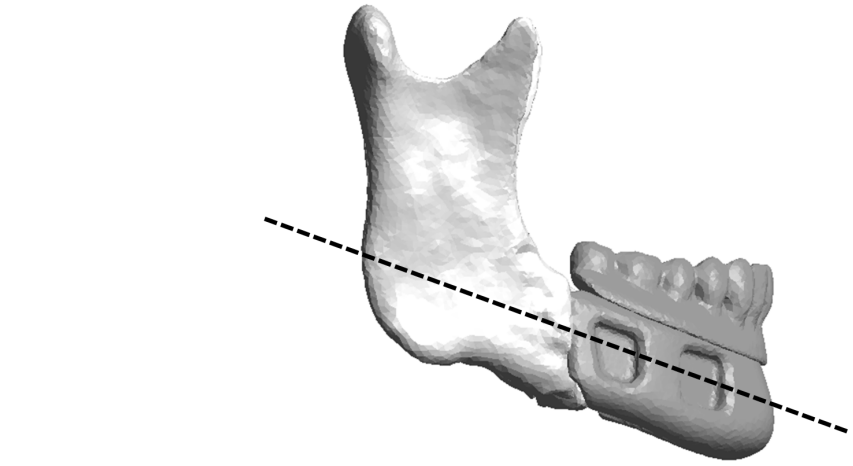

(a)

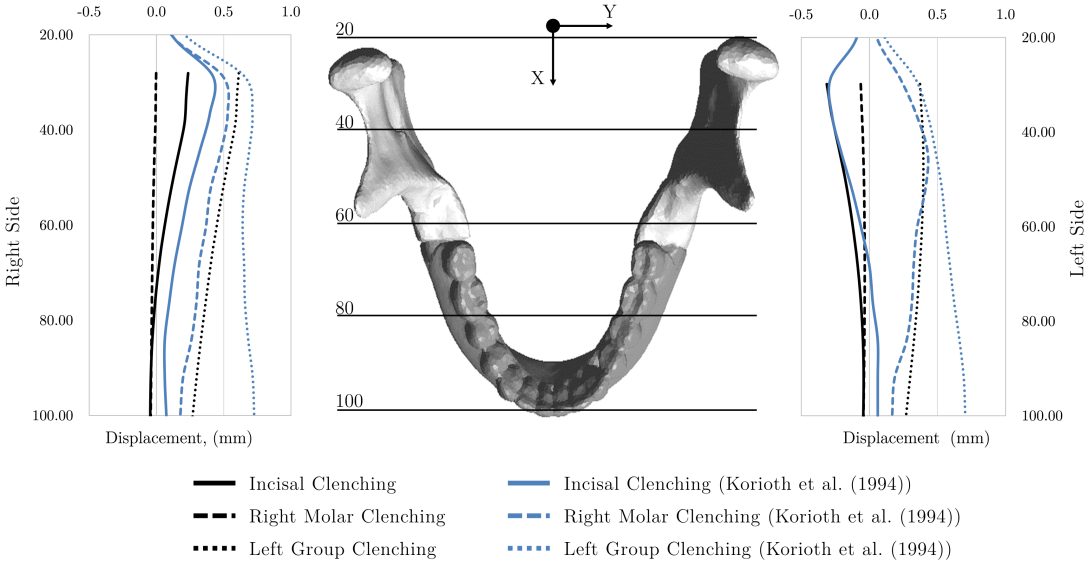

(b)

Figure 6.16: (a) transverse cut plane along the mandibular endoprosthesis; (b) transverse mandibular displacements (y-axis) during incisal clenching, right molar clenching and left group clenching

considerably decreases at the bone-implant interface (60 mm line in Fig. 6.16 (b)). This is particularly evident observing the transverse displacement field along the working side for left group clenching case.

Similarly to the transverse direction, Fig. 6.17 depicts the craniocaudal and antero-posterior displacement of the mandible for the three masticatory tasks. In all cases the mandible moves upward and forward. For incisal clenching, the vertical displacements

are almost symmetrical relatively to the facial sagittal plane, and decrease towards the chin. The anterior displacement is relatively constant along the whole mandible. During right mandibular function the proximal and anterior displacements are slightly larger on the left side of the mandible. Likewise, in left group clenching, the largest proximal displacements occur on the balancing side (right side), however, the greatest anterior displacements occur on the loaded side (left side). The displacement fields indicate that in both tasks the mandible is displaced forward, and rotates around the vertical restrains imposed along the teeth arch.

Fig. 6.18 shows the stress distribution along the implanted mandible and intact mandible during incisal chewing. The marked anatomical differences between the intact and the implanted mandibles make the quantitative comparison of the observed stresses and strains unfeasible. However, a qualitative comparison is still possible. In the intact mandible, high stress concentrations were observed along the distal temporal crest, posterior aspect ramus, and immediately below the condylar process (Fig. 6.18 (a)). Very similar stress fields were observed along the implanted model. High stress concentrations were observed along the distal temporal crest with a maximum equivalent stress of approximately 36 MPa, on the posterior aspect of the ascending ramus immediately below the condylar process (58 MPa), and around the mandibular notch (81 MPa) (Fig. 6.18 (b)). There is also a less pronounced stress concentration along the lower border of the body immediately anterior to the angle region, which was also observed in the implanted mandible.

The stress fields observed in both models during right molar and left group clenching are also quite similar. Interestingly, during unilateral clenching, high stress values were observed along the ipsilateral oblique line and temporal crest, when compared with contralateral side. Whereas in the posterior aspect of the ramus, the highest stress values were found along the contralateral ramus, when compared with the working side ramus. The highest stresses found along the ipsilateral may be a direct consequence of the differences between the ipsilateral and contralateral Temporal muscle forces. In right molar function, the right-side muscles have comparatively larger cranio-caudal components, however the stresses observed along the posterior border of the right ramus are smaller. The difference is caused mainly due to the increase in the third principal stress along the left side of the mandible, comparatively to the right side (working side). In the left

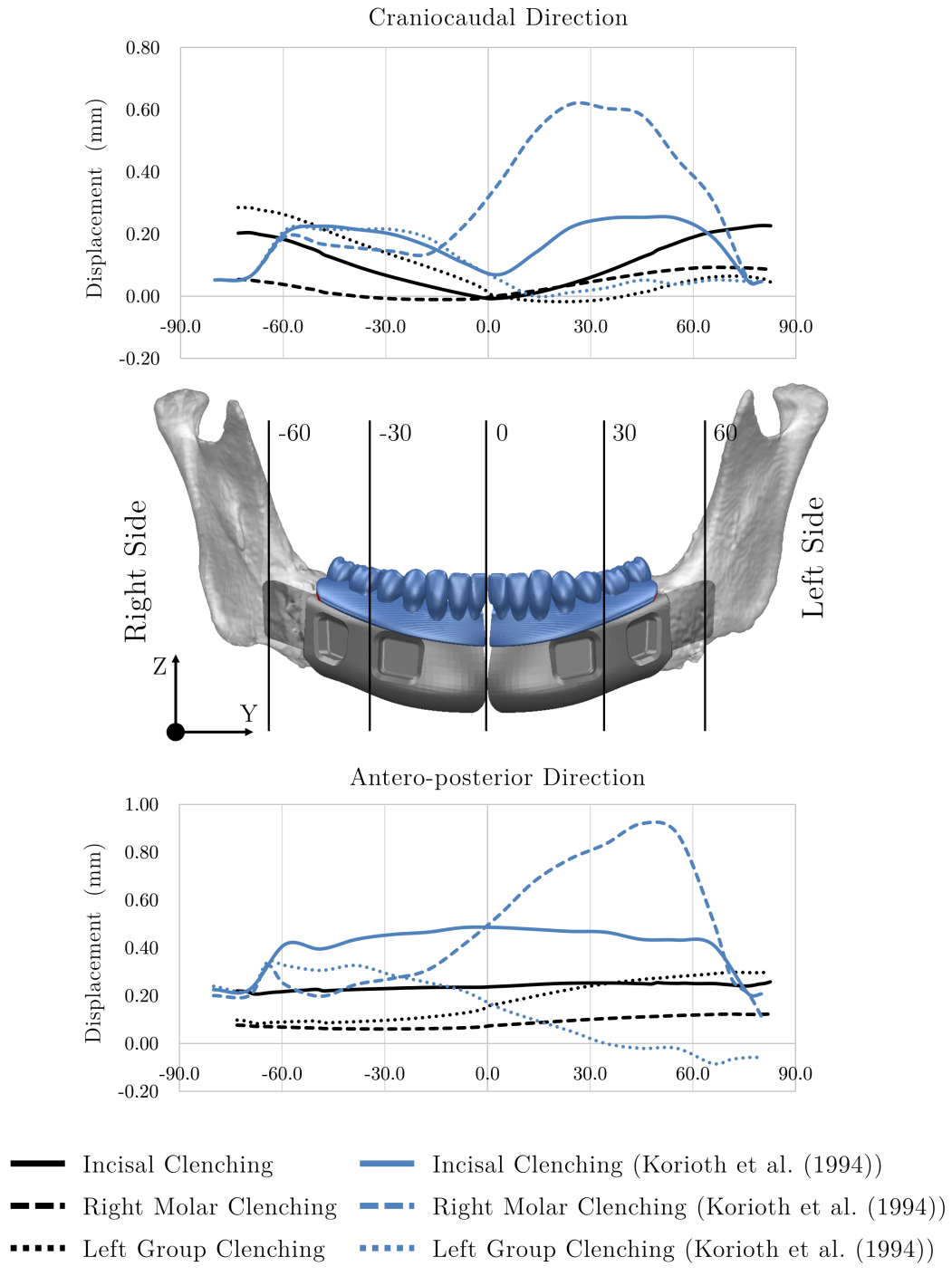

Figure 6.17: Cranio-caudal and antero-posterior mandibular displacement during incisal clenching, right molar clenching and left group clenching tasks

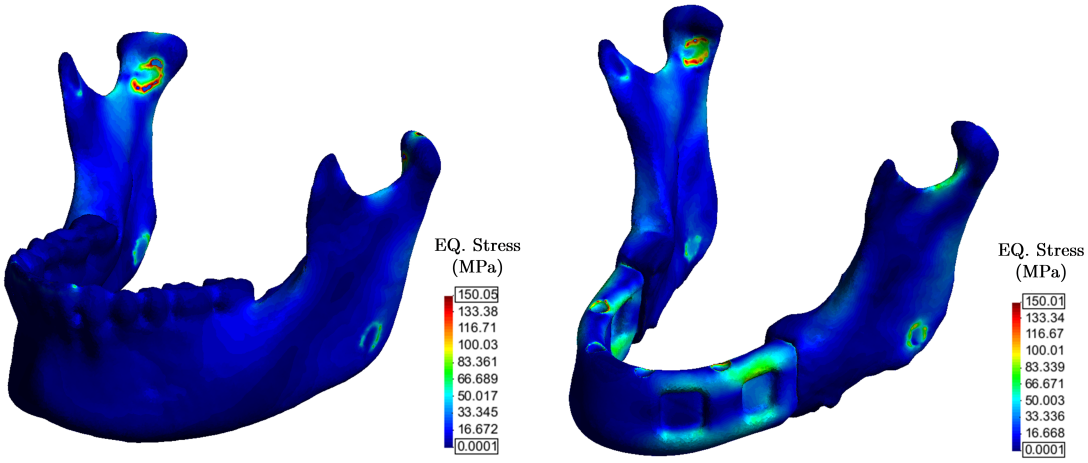

(a) (b)

Figure 6.18: Equivalent stress distribution along along the intact mandible in (a), and the implanted right and left mandibular segments in (b) for incisal clenching

group chewing, the Masseter and medial Pterygoid muscle forces are much larger on the balancing side (especially the right medial Pterygoid) than in the working side and this may contribute to the highest compressive stresses observed on the posterior surface of the right ramus.

Regarding the implant, the highest stress concentrations were observed at the implant-screw interface (between the implant and the dental prosthesis), namely 227.3 MPa for incisal chewing, 363.6 MPa for left group clenching, and 124.4 MPa for right molar chewing. However, these maximum stress values are below the fatigue limit for the Ti-6Al-4V alloy (510 MPa). The maximum stress values were found along the working side of the implant. In addition, the posterior aspect of the implant was more critically loaded than the anterior aspect, and the equivalent stresses decreased gradually towards the chin (Fig. 6.18). Excluding the implant-screw interface, the maximum stresses along the implant body for incisal, right molar, and left group chewing were 92.1 MPa on the buccal side, 40.3 MPa on the lingual aspect, and 96.5 MPa also on the lingual aspect of the implant, respectively.

The strain distribution along the bone-implant interface is thought to play a paramount role in the bone remodelling process, and consequently in the achievement of a rigid and durable fixation to the host bone (Simmons et al., 2001a,b; Jokstad, 2009). Fig. 6.19 shows the superficial von Mises equivalent strains along the bone-implant interface for the

three chewing tasks. High strain values were observed in the upper and lower border of the implant's stems.

During incisal clenching similar equivalent strain fields were observed on the left and right sides of the implant's surface. Equivalent strains were higher along either the outer upper border or the lower inner border of the bone-implant interface. Strain gradually decreased towards the centre of each stem, as seen in Fig. 6.19 (a). The superficial equivalent strains on the two implant stems ranged from 41.10 $\mu strains$ up to 3028.50 $\mu strains$. Equivalent strains higher than 200 $\mu strains$ (the threshold thought to trigger bone resorption) were observed on 63% of their surface area. For right molar clenching, the highest equivalent strains were found on the balancing side (Fig. 6.19 (b)). The equivalent strains observed along the bone-implant interface ranged from 3.4 $\mu strains$ to 849.6 $\mu strains$, but only 8% of them were above 200 $\mu strains$. Likewise, during left group chewing, the highest strains were observed on the right side of the stem (Fig. 6.19 (c)). Equivalent strains up to 3283.50 $\mu strains$ were observed, and 77% of the interfacial strains were above the 200 $\mu strains$. Further stem geometrical optimization may be necessary to enhance the mechanical behaviour of the implant, along the bone-implant interface.

6.7.3 Discussion

In this chapter a procedure for a custom mandibular reconstruction, whether with the standard free microvascular fibular flap or by a solid mandibular endoprosthesis, was proposed. The mandibular endoprosthesis was tested under three clenching tasks. Recently, several authors support the idea that mastication is carried by groups of teeth rather than independently by each tooth (Oosterhaven et al., 1988; Fontijn-Tekamp et al., 2000; Ichim et al., 2006), and therefore multiple teeth chewing was simulated.

Due to the absence of any prior geometrical information about the intact target mandible, an intact mandible obtained from a public DICOM images database was used to determine the muscle forces needed to produce the desired masticatory forces along the teeth arch. The use of different intact and implanted mandibular models restricts the analysis of the FE results. The mandibular shape and the localized variations of cortical thickness seem to influence the strain distribution along the mandible (Daegling and

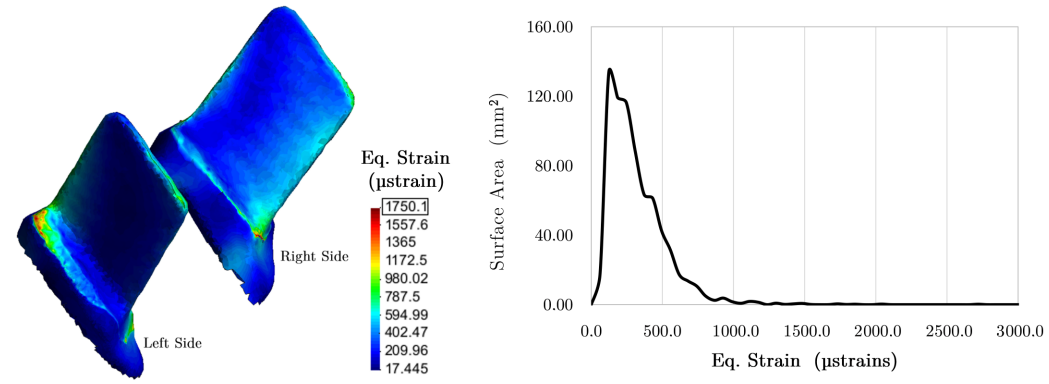

(a)

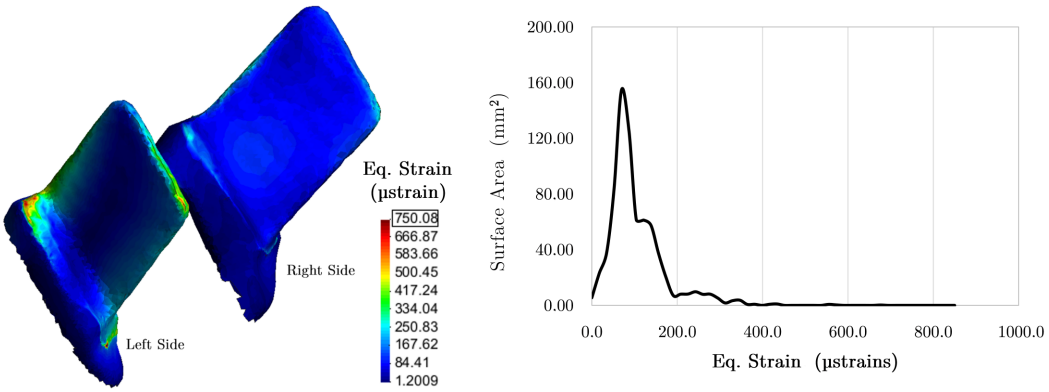

(b)

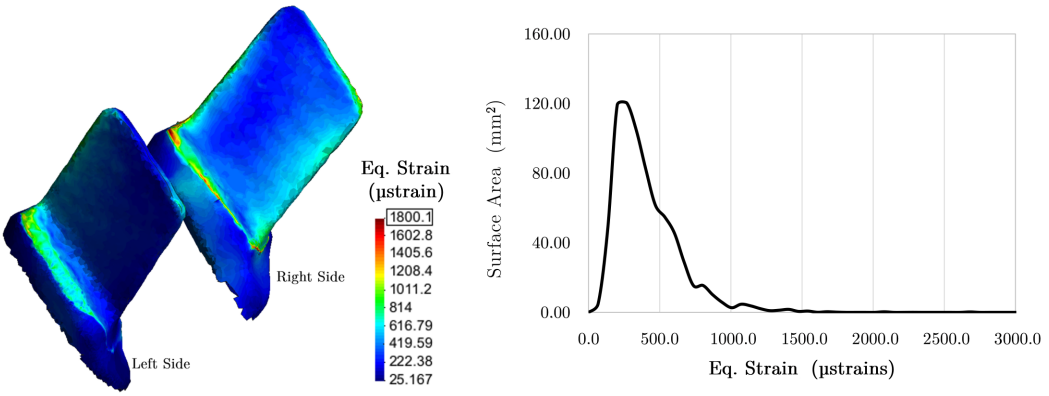

(c)

Figure 6.19: Equivalent strains along the bone-implant interface for incisal biting (a), right molar clenching (b), and left group biting (c)

Hylander, 1998; Van Eijden, 2000; Meyer et al., 2002). Therefore, the direct (quantitative) comparison of the stresses and strains observed along the intact and implanted mandibles may be unfeasible, due to their marked morphological differences (see Fig. 6.15).

Korioth and Hannam (1994) conducted an extensive analysis over the displacements of the intact Human mandible during different chewing tasks. For incisal clenching, it was observed a posterior compression of the mandible and a slight displacement towards the left side along the transverse plane. The nodal displacements obtained with the mandibular implant show that this behaviour can be recovered. Ideally, the equal recruitment of the different muscle fibres should produce a symmetrical (sagittal) displacement of the mandible. The slight asymmetrical displacement fields observed may be an evidence of the existence of an asymmetry in the reconstructed mandible, which may also contribute to a slight asymmetrical loading of the implant.

The anterior and vertical displacements after implantation also correlate well with the observations of Korioth and Hannam (1994). For right molar chewing, Korioth and Hannam (1994) observed a global displacement towards the balancing along the transverse plane of the mandible. The anterior and vertical displacements were more pronounced in the left (balancing) side when compared with the working side. In the intact mandible (used to generate the desired bite forces), the displacement fields are in agreement with these previous observations. However, with the mandibular endoprosthesis a residual transverse displacement towards the right side was observed on both sides of the implanted mandible, instead of a global displacement towards the balancing side (Fig. 6.16). The displacement fields of the implanted mandible in the antero-posterior and cranio-caudal direction were similar to the patterns found in the intact mandible, with the exception for the anterior displacement during left group clenching (Fig. 6.17). During left group chewing, the mandible was transversely displaced towards the working side, and the anterior displacement was higher on the working side. For left group chewing, Korioth and Hannam (1994) observed that higher anterior displacements along the balancing side. The results obtained are a consequence of the inward pull of the right medial Pterygoid, which causes the mandibular implant to rotate around itself towards the right side. Higher vertical displacements were observed on the right side of the mandible, which is in agreement with the observations of Korioth and Hannam (1994).

For incisal clenching, the nodal displacement fields show an inward rotation along the

antero-posterior direction (x-axis), where the teeth arch is mainly under compression. The mandible is also rotated forward (around the y-axis direction). In right molar clenching, the mandible is mainly rotated towards the right (around the x-axis), whereas in left group function the mandible is rotated towards the left side in the craniocaudal plane. The deformation fields observed along the implanted mandible show that it mainly rotates around the boundary conditions applied to the dental arch. These displacement fields are in agreement with the predictions of Hylander et al. (1987) and Korioth and Hannam (1994) for the intact mandible. Therefore, the proposed mandibular implant seems to restore (with the exception of the anterior displacements for left group chewing) the natural displacement fields along the intact mandible.

Similar stress fields were also observed for both intact and implanted mandibles (Fig. 6.18). This suggests that the proposed mandibular endoprosthesis allows the preservation of the normal stress distribution along the right and left mandibular segments. In addition, the proposed solid mandibular endoprosthesis showed no signs of mechanical failure, nor reduced stiffness as previously reported for other authors (Wong et al., 2012b). The results obtained show that stress distributions in the mandible are complex, and slightly different depending on the chewing task. In incisal clenching, stress concentrations were observed mainly along the distal temporal crest, the posterior aspect of the ascending ramus, the mandibular notch, and in the lower and lingual surface of the mandible immediately anterior to the mandible angle. These stress fields are consistent with the results obtained by Meyer et al. (2002) with photoelastic analysis.

For unilateral clenching, high stress concentrations were observed on the ipsilateral temporal crest and contralateral proximal posterior ramus. Stress concentrations along mandibular body of the working side and posterior mandibular ramus of the balancing side have been previously observed by Wang et al. (2010) for left unilateral chewing. The highest stresses along the mandibular implant were also observed at the implant-screw interface, nevertheless these stresses were always below the fatigue limit of the Ti-6Al-4V alloy considered for implant manufacturing. In addition, the mandibular endoprosthesis also avoids using screwed connections, usually associated with unfavourable stress concentrations along the mandibular bone, implant loosening and implant and screw fracture by several authors (Kim and Donoff, 1992; Spencer et al., 1999; Shibahara et al., 2002; Knoll et al., 2006; Ramos et al., 2011; Narra et al., 2014).

As mentioned in section 6.1 the endoprosthesis concept was successfully applied by Lee et al. (2008) and Goh et al. (2009a) for the reconstruction of the mandibular body and unilateral reconstruction of the ascending ramus. In a histological evaluation of a cemented modular mandibular endoprosthesis 6 months after implantation, Lee et al. (2009) found no signs of loosening and the radiological evaluation revealed a stable position of the implant. It was also observed an increase of woven bone volume around the implant stems, particularly along the inferior and lingual aspects of the implant stems. In addition, the histological evaluation of the endoprosthesis applied to the ramus 3 and 6 month after implantation showed an overall increase of the bone volume around the implant's stem (Goh et al., 2009b), and only a residual bone mass density loss of 1.8% to 5.8% were observed around the implant (Goh et al., 2010). Nearly complete bone union and bone in-growth were observed by Chanchareonsook et al. (2013) with an hydroxyapatite-coated custom modular endoprosthesis implanted in monkeys after 6 months follow-up.

High strain values were observed not only on the inferior and lingual regions of the stems, but also on the buccal and superior aspects, especially on the balancing side during unilateral chewing. In addition, the equivalent strains along the implant stems showed that 63% and 77% of the implant-bone interface experience strains are above 200 $\mu strains$ during incisal and left group clenching, what is thought to be the physiological threshold to trigger bone maintenance and remodelling. Nevertheless, a smaller and less stiff implant may be advantageous to reduced strain shielding around the implant-bone interface. For dental prosthesis-implant interface, a four dental implant system was considered. This system seems to be unsuitable for transmitting distal teeth chewing forces to the supporting bone. A different type of implant-dental prosthesis interface, such as a solid interface, or a screwed interface with more distal screws, should be considered in the future, to improve bone loading during right molar loading (Fig. 6.19).

The results obtained for the mandibular endoprosthesis are very encouraging. However, these results may be affected by the simplifications on the FE model. In this study, all materials in the FE model were assumed to be isotropic and homogeneous. Ichim et al. (2006) argued that modelling the Human mandible as an isotropic material was sufficient to obtain meaningful physiological strain variations during different chewing tasks. However, it is known that the Human mandible is more accurately modelled as an anisotropic (Ashman et al., 1984; Dechow et al., 1993), or a transversely isotropic material (Hart et al.,

1992; Van Eijden, 2000), and that it may be highly heterogeneous due to the variations of cortical thickness along the different anatomical regions (Daegling and Hylander, 1998). The muscle insertion areas in the FE model are also a simplification of the real insertion areas. For instance, the masseter muscles occupy almost all the lateral surface of the ascending ramus. The high stress concentrations at the muscle insertion sites and smaller stresses along the inner aspect of the ramus (in both intact and implanted mandibles) may be unrealistic.

The implant and the bone are also assumed to be perfectly bounded. Immediately after insertion there is always a certain amount of relative movement between the two bodies. The existence of micro-motions along the bone-implant interface at this early stage may compromise bone ingrowth into the implant, and in the long term lead to implant loosening, particularly in cementless designs such as the one proposed here. Interfacial micro-motions above 150 μm seems to inhibit bone ingrowth into the implant (Pilliar et al., 1986; Jasty et al., 1997). Hence, to predict more reliably the behaviour of the mandibular endoprosthesis in-vivo, a more realist model may be needed. The implant is also clearly over-dimensioned and the reduction of the implant's stiffness may be important to obtain a more natural deformation of the mandible and promote a more favourable environment for implant osseointegration. Reducing the implants cross-section to a simple titanium core capable to sustain the different chewing tasks, and the addition of other non-metallic features to obtain the desired mandibular shape defined in the cephalometric assessment, or the addition of other geometrical features, such as holes, may be a possible solutions.

6.8 Summary

In this chapter it was proposed a procedure for the development of both surgical cutting guides and a custom mandibular implant for the reconstruction of a mandible. The prior determination of the anatomical and relations of the skull is a paramount step towards the functional and aesthetic outcome of the mandibular reconstruction. For mandibular reconstruction, CT imaging should consider the acquisition of the entire skull, or at least the facial bones slightly above the N and below the Me anatomical points. Imaging the complete skull (or facial region) allows the complete cephalometric assessment of the Human face, and the correct development of custom mandibular surgical guides or

implants. In the cephalometric analysis, the Natural Head Position and the McNamara line were used to correctly define the head reference frame. The correct geometrical and anatomical relations between the maxilla and the mandible, as well as the lower arch teeth, should also be addressed in the project phase. It is important to guarantee correct teeth occlusion in order to facilitate the further prosthetic rehabilitation of the teeth in a second-stage surgery. The proposed mandibular endoprosthesis allows recovery of both displacement and stress fields along the two mandibular segments. It also produces strain values at the implant-bone interface that may promote bone preservation and ingrowth around the implant. Hence, this type of implants may be a reliable alternative to other prosthetic mandibular reconstruction approaches. The customization of the mandibular endoprosthesis is crucial to optimize both the functional and aesthetic outcomes after surgery.

Chapter 7

Custom Total Hip Replacement

In the present chapter the development of a tailor-made total hip replacement system is described. A customized modular acetabular component and femoral stem are proposed. The hip stem is validated through Finite Element Analysis. The hip stem is tested considering the boundary conditions described by ISO $7206-6$ *and ASTM F* $2996-13$ *standards, and a simplified muscular model of the hip.*

This page was intentionally left blank

7.1 Introduction to Total Hip replacement

Total hip replacement (THR) is considered the orthopaedic procedure of the 20th century, and it is the treatment of choice for severe cases of hip joint disorders or trauma. The attempts to correct hip disorders with replacement surgeries dates from the early 1800's, however most of the early techniques failed to produce successful results, whether due to an inadequate surgical procedure, poor implant design, or material failure (Learmonth et al., 2007). Probably the most important breakthrough in THR surgery date from the early 1960's. In 1962 *Sir John Charnley* proposed the concept of low friction torque arthroplasty by introducing a metal-on-plastic articulating couple, with a metal femoral head and a full polyethylene acetabular component. *Sir John Charnley* is now considered the father of the modern Total Hip Replacement, not only for the introduction of the concept of low friction torque arthroplasty, but also for the development of concepts about lubrication, materials, implant design and surgical procedure, some of which are still used today (Malhotra, 2011).

The hip joint may be affected by several age-related or congenital pathological conditions, that can cause pain and affect its normal biomechanics. The most common causes of adult hip joint disease are arthritis, osteoarthritis or rheumatoid arthritis, avascular necrosis, post-traumatic degenerative joint diseases, congenital hip diseases, and infection (Frontera et al., 2014). For instance, osteoarthritis is an age-related non-inflammatory and slowly progressive diarthrodial joint disease characterized by the deterioration and erosion of the articular cartilage. Osteoarthritis may be a natural consequence of aging, however it may also be correlated with metabolic, developmental, neurologic, or traumatic conditions (Schoen, 2000). Hip dysplasia is a congenital disorder related with the abnormal development of the hip joint. The disease has different degrees of severity, and may range from an unstable joint to a completely dislocated joint. Abnormalities in size, shape, and orientation of the femoral head, the acetabulum, or both, are often associated with this condition (Frazier and Drzymkowski, 2014). Different treatments may be used to reduce pain and avoid hip dislocation and post-pone the surgical treatment, however, in the long term THR may be unavoidable (Holzwarth and Cotogno, 2012).

Total hip arthroplasty is considered a successful, safe, and cost-effective medical intervention for restoring hip function, relieving pain and regaining pain-free mobility

(Holzwarth and Cotogno, 2012). The success of this treatment led to its wide spread in the management of hip disorders, and the number of patients undergoing THR has increased over the last decades. The average age for primary THR has also decreased, and the hip replacement systems are now expected to survive 20 or more years after the surgical procedure (Corten et al., 2011). Therefore, new challenges are addressed by engineers in order to obtain implant designs that meet the increased life expectancy and functional demand of younger and more active patients, including restoration of the full range-of-motion (ROM), complete and unrestrained return to physical activity, long-term bone-implant fixation, and a low rates of revision (Kim et al., 2004; McAuley et al., 2004).

Modern THR systems are modular endoprosthesis divided essentially in two main components, the femoral component and the acetabular component (Fig. 7.1). The femoral component is composed by the femoral head and the stem, which is responsible for attaching the head to the supporting bone in the proximal femur. The stem is also fundamental to efficiently transmit the loads generated from the upper body to the lower limbs. Regarding the acetabular component, it is often composed by an acetabular metallic shell that provides mechanical support to a polymeric liner. The liner provides the articulating surface between the acetabular shell and the femoral head. On the one hand, the femoral stem and the acetabular shell components should provide good bone integration and/or provide high resistance to static and dynamic loadings. These components are commonly made of titanium, titanium alloy, cobalt chrome alloys, or stainless steel. On the other hand, the main requirement for the articulating surfaces is a low wear rate. There are different combinations for the articulating pair, and the most common combinations are metal-on-metal, ceramic-on-ceramic, and metal-on-polymer (Holzwarth and Cotogno, 2012). Throughout the evolution of THR two types of fixations have also been proposed, namely the cemented fixation using an acrylic cement, and the cementless fixation obtained mainly by press-fitting a surface roughened implant against the host bone. Over the years these concepts have been applied to both acetabular and femoral components, with different rates of success.

The cemented acetabular components are thick polyethylene cups with horizontal and vertical grooves on the external surface to increase cement-bone interlocking. Implant stability is mainly dependent on a thick and homogeneous layer of cement mantle, in order to become mechanically attached to the underlying bone. The cemented fixation

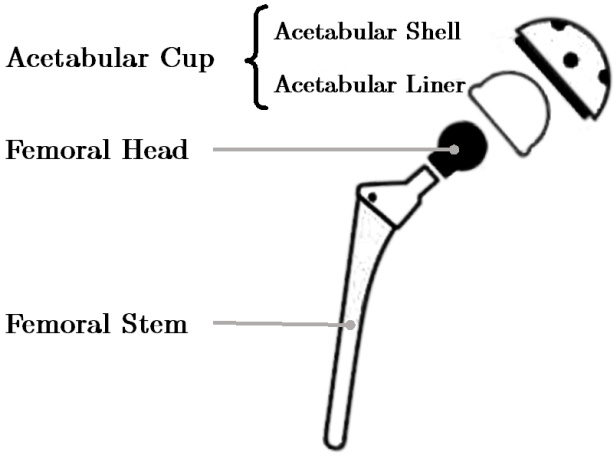

Figure 7.1: The modular Total Hip Replacement system is mainly composed by the femoral component with two independent parts (the femoral stem and the femoral head), and the acetabular component composed by a metallic acetabular shell and a polymeric liner (adapted from (Holzwarth and Cotogno, 2012))

is satisfactory and recommended for older, low-demanding patients, and is often used in revision surgeries (Malhotra, 2011). In spite of the technical improvements observed in cementing techniques, the shortcomings associated with this type of fixation are still correlated with the difficulty to obtain a uniform cement mantle. A non-homogeneous cement layer is thought to cause high local stress concentrations that can lead to cement fracture and implant loosening (Holzwarth and Cotogno, 2012). Cementless acetabular components were introduced to eliminate the shortcomings associated with cementing techniques. The cementless acetabular shells are mainly press-fitted cups that may have additional room for metal screws for supplementary fixation. Current acetabular shell designs are ingrowth cups, where the outer shell is porous coated to facilitate bone ingrowth. In cementless designs the acetabular liners may be made of metal, ceramic or polyethylene depending on the needs or the limitations imposed by the patient's anatomy (Malhotra, 2011).

Cemented femoral stems have the longest follow-up studies available in the literature, in particular the cemented hip replacement system proposed by *Charnley* (Wroblewski et al., 2006). Callaghan et al. (2009) reported a 78% survival rate after a 35 years follow-up for patients that received their *Charnley* total hip prosthesis in 1962. Some patients exceeded 40 years with their primary hip replacement system. Other reports have demonstrated

high success rates ranging from 92% to 97% for cemented femoral stems in a 10 to 15 years follow-up period (Sinha, 2002; Williams et al., 2002). The Charnley's cemented technique remains the gold standard for THR and, until now, other systems have only achieved similar results. Modern cemented stems are produced with high strength alloys such as cobalt chrome. The high elastic modulus of these alloys may reduce the amount of stress transmitted to the proximal cement mantle, diminishing the incidence of fractures in the bone-cement interface (Malhotra, 2011). For cemented fixation, polished stems are preferred against textured stems, since they mainly produce compressive stresses along the cement mantle (Fig. 7.2).

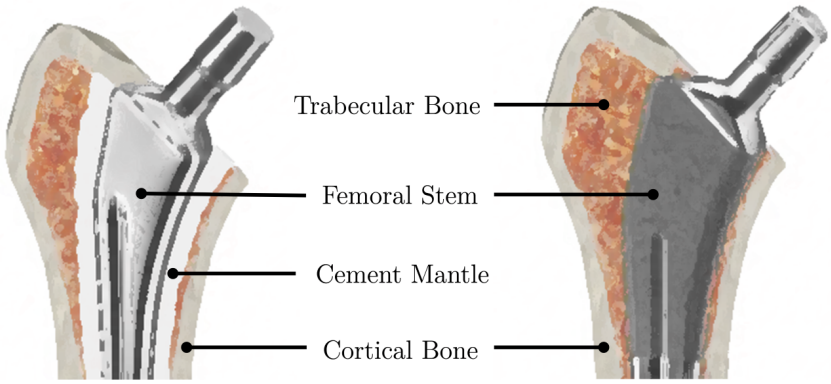

Figure 7.2: The differences between cemented and cementless Total Hip Replacement: in cemented THR the stem is polished and the cement mantle interfaces with the bone and the implant; in cementless THR a roughened stem is placed in direct contact with the host bone

Cementless femoral stems were proposed as an alternative to cemented stems, potentially without the shortcomings associated with the use of bone cement for implant fixation. Non-cemented fixation is achieved by osteointegration (Fig. 7.2). Excellent results were also reported with this type of fixation. Dorr et al. (1993) obtained a 95% survival of cementless anatomic stems, and 99.5% survival of cementless tapered stems at more than 10 years follow-up. To allow bone ingrowth, the femoral stem must promote adequate contact and fixation between the implant and the host bone, in order to avoid micro-motions along the bone-implant interface. Modern cementless stems are press-fit devices, either on the metaphyseal or diaphyseal region of the implant. Metaphyseal fit tapered femoral stems are preferred since it is the proximal end of the femur that must support the vertical loads applied to the lower limbs, and produce a more constant stress

along their length (Malhotra, 2011). One common drawback pointed to cementless femoral stems is the higher incidence of thigh pain after THR. Nevertheless, in randomized clinical trials comparing cemented and cementless THR, it was found that thigh pain prevalence was only 3% for both tapered cementless and cemented femoral components (Rorabeck et al., 1994).

There is a plethora of THR systems in the market with different sizes, shapes, and surface treatments. Morphological studies performed over a large number of femurs have tried to summarize the anatomical variability of the proximal femur (Noble et al., 1988; Rubin et al., 1992). Based on those studies, companies have developed designs that try to cover the great majority of the proximal femoral anatomical variation. Nevertheless, the accurate reproduction of all anatomical relations, as well as the optimal fit-and-fill of the metaphysis are difficult to achieve with commercially available prostheses, even considering the variety of the commercially available designs and sizes (Wettstein et al., 2005). Primary stability necessary for proper osseointegration may be difficult to achieve with standard stems (Berry, 1999; Osagie et al., 2012). In addition, most femoral deformities due to post-traumatic OA, dysplasia, congenital hip dislocation, or other congenital deformities, are found in young patients. The treatment of such deformities in an early stage of life make the choice of the implant even more critical. An implant geometry that optimizes bone-implant contact, primary stability, and promotes a more physiological load transfer to the proximal femur may minimize implant stress shielding and reduce the loss of supporting bone in the long term. Customized implants that fit the individual needs of each patient are seen as a reliable alternative against standard and modular hip replacement systems.

Tailor-made THR systems have been successfully applied in the treatment of several anatomical deformities. Koulouvaris et al. (2008) reported the development of custom femoral stems for the treatment of severely distorted femurs in young patients. After a 6 year follow-up, no thigh pain or signs of implant loosening were observed. Akbar et al. (2009) reported an 100% survival rate for a series of uncemented femoral stems inserted in young patients with femoral deformities. There were no signs of stem dislocation, and 86% of survival rate for the acetabular cup were observed with a minimum follow-up of 14 years. Custom-made cementless implants were also successfully applied in the treatment of dysplastic hips in patients with an average age at time of surgery of 60 years. After an average follow-up of 7 years, bone-ingrown fixation was observed in all stems, 9% of

the patients had post-operative thigh pain, and stress shielding was observed in 20% of the patients. The inadequate metaphyseal fit of the femoral canal was reported as the main cause for proximal stress shielding (Kawate et al., 2009). In a retrospective study of 212 patient treated with custom hip stems with less than 50 years, (Flecher et al., 2010) concluded that 172 patients had no pain, 187 had full activity recovery, 206 had full ROM, and the average leg length discrepancy was of 2.30 mm. The survivorship at 10 years was 96.7%, and 87% for a 15 years follow-up.

The treatment of femoral deformities with custom hip replacement systems have been associated with less post-operative thigh pain. Early studies in custom hip replacement systems showed that thigh pain is less frequent with custom fit-and-fill stems, when compared with conventional stems (Bargar, 1989; Stulberg et al., 1989; Flecher et al., 2010). Custom femoral stems are thought to provide a reliable alternative to standard designs, particularly in patients with severe anatomical deformities. The main drawback associated with these designs seems to be the highest manufacturing costs when compared with standard stems (Akbar et al., 2009; Wettstein et al., 2005). In this chapter, a custom implant is designed from medical image data. The necessary steps to evaluate the target anatomy and the main concepts related with both the acetabular and the femoral components are further investigated and applied to the development of a fully customized THR system. The remainder of this chapter is organized as follows: in section 7.2 the main anatomical and biomechanical concepts of the human hip joint are reviewed; the conventional THR pre-operative planning is described in section 7.3; in section 7.4 the protocol used for the segmentation of the pelvis, the femur and the tibia is described; in section 7.5 the necessary procedures for custom implant planning are presented; section 7.6 and 7.7 describe the concepts considered in the project of the acetabular component and the custom femoral stem; in section 7.8 the geometry of femoral stem is validated through the Finite Element Method; and, ultimately, section 7.9 the main conclusions of this chapter are summarized.

7.2 Anatomy and Biomechanics of the Hip

The lower limbs are specialized structures that evolved over time to efficiently sustain the body weight and allow the upright locomotion. The Human lower limbs are constituted

by the pelvic girdle, the femur, the tibia and fibula, and the foot (Dalley and Moore, 2001). The pelvic girdle is a bony ring composed by four bones, namely the two hip bones (iliac bones), the sacrum and the coccyx, providing the mechanical support to the vertebral column and the upper body. The iliac bone consists of three anatomical parts, the ilium, the ischium and the pubis, that meet in a large hemispherical articular cavity, the acetabulum (Fig. 7.3). The acetabulum is located in the lateral surface of the iliac bone and articulates with the femoral head (Gray and Lewis, 1918). The main functions of the pelvis are weight transmission to the lower body, locomotion, provide muscle attachment, and protect the pelvic viscera. The weight of the upper body and the axial skeleton is transmitted from the vertebrae to the base of the sacrum, and then to the left and right sacroiliac joint, and to the femoral head through the sacroiliac line (Halim, 2008).

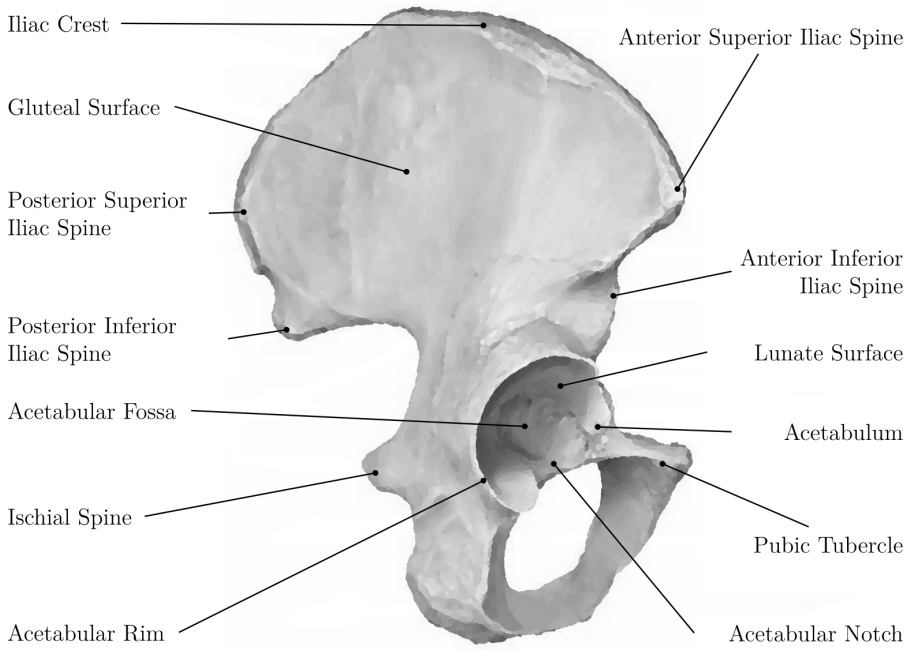

Figure 7.3: Anatomy of the Human right iliac bone: acetabulum is located in the lateral surface of the iliac bone and articulates with the femoral head (adapted from (Schuenke and Schulte, 2011))

The femur is the longest and strongest bone of the Human body, and is responsible for transmitting the body weight from the pelvis to the tibia in an upright position (Fig. 7.4). It can be anatomically divided into the body and two articular extremities. The upper femur consists of the femoral head, the neck, and the lesser and greater trochanters (Dalley

and Moore, 2001). The femoral head has a hemispherical shape and articulates with the acetabular cavity, being partially covered by articular cartilage. The femoral neck is a pyramidal process connecting the head to the body, and it projected upward, medialward and forward relative to the body of the femur. The greater trochanter is a large, irregular eminence located at the junction between the femoral neck and the upper part of the femoral body, whereas the lesser trochanter is a conical protuberance that projects from the lower back part of the base of the neck. Both trochanters provide attachment to the muscles of the thigh (Gray and Lewis, 1918). The upper extremity of the femur fuses with the femoral body along the intertrochanteric line, which runs downward and medialward and connects the lesser and the greater trochanter (Dalley and Moore, 2001).

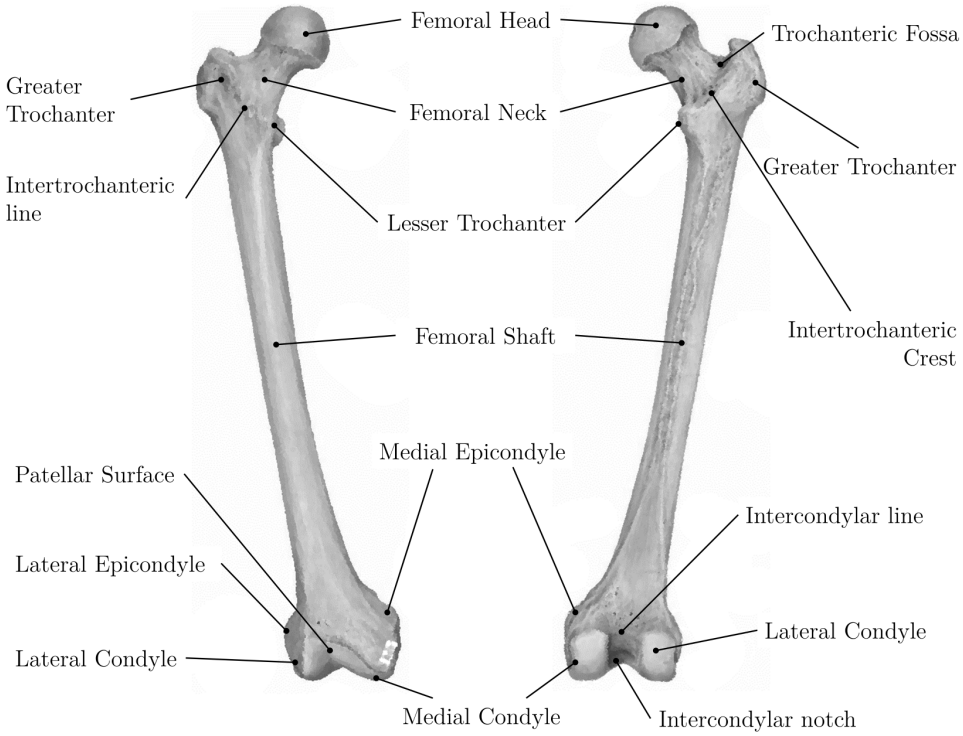

Figure 7.4: The anterior and posterior view of the human right femur (adapted from (Schuenke and Schulte, 2011))

The femoral body is almost cylindrical in shape and slightly bowed anteriorly. The body becomes wider as it approaches the lower extremity, which contains two eminences known as the condyles. The condyles project more posteriorly than anteriorly, and are separated by a deep notch, the intercondyloid fossa (Gray and Lewis, 1918). Anteriorly,

the condyles merge to form the patellar surface, where the patella articulates. The femoral condyles articulate with the tibial condyles to form the knee joint. The lateral epicondyle possesses a lateral prominence, the lateral epicondyle, whereas the medial face has the medial epicondyle that provides attachment to muscles and ligaments. The tibia and the fibular articulate with the femur. The tibia sustains the body weight, whereas the fibula only provides attachment to the muscles and additional stability to the ankle (Gray and Lewis, 1918).

There are several landmarks and anatomical axis important for the assessment of the femoral anatomy. The femoral neck axis is the line connecting the base of the greater trochanter to the apex of the femoral head (Center et al., 1998). The transepicondylar axis is the line connecting the lateral epicondylar prominence and the most prominent point of the medial epicondyles (Catani and Zaffagnini, 2013). By superimposing these two axes, it is possible to measure the angle of torsion between the femoral shaft and the femoral neck, or anteversion angle. Another important measure is the Caput-collum-diaphyseal angle (CCD) that quantifies the angle between the anatomical axis of the shaft of the femur, defined as the line connecting the piriformis fossa and that intersects the knee joint line approximately 10 mm medial to the knee joint centre, and the femoral neck axis (Thienpont, 2012). In a normal femur, the angle between the axis of the femoral neck and the axis of the proximal femur is approximately 126 degrees in adults, whereas the angle between the transepicondylar axis of the knee and the femoral neck axis is approximately 12 degrees (Schuenke and Schulte, 2011).

The hip joint is crucial for weight transmission and locomotion, and the iliac bone and femur provide attachment to a multitude of muscles that allow Human upright locomotion, such as the abductor muscles, gluteal muscles, the iliotibial tract, the tensor fasciae latae, the adductor muscles, and the extensor muscles (Schuenke and Schulte, 2011). According to Heller et al. (2005), the most relevant muscles for Human locomotion are the gluteal muscles, the iliotibial tract, the tensor fasciae latae and the quadriceps muscles, more particularly the vastus medialis and the vastus lateralis. Fig. 7.5 depicts a schematic representation of the anatomical location of each muscle group, as well as their origins and insertion sites. The gluteal muscle group is composed by the gluteus maximus, medius, and minumus. This group of muscles origins at the dorsal surface if the sacrum and posterior surface of the ilium, right beneath the iliac crest, and insert at the posterior surface of

the proximal femur at the lateral and antero-lateral surface of the greater trochanter. The tensor fasciae latae origins at the anterior superior iliac spine and inserts at the iliotibial tract, as well some of the upper muscle fibres of the gluteus maximus (Fig. 7.5). The iliotibial tract flips back and forth across the greater trochanter, and inserts at the level of the proximal end of the fibula in the leg. The vastus medialis muscle origins at the medial lip of the linea aspera and distal part of the intertrochanteric line, and inserts at the tibial tuberosity, whether the vastus lateralis origins at the lateral lip of the linea aspera and lateral surface of the greater trochanter, and also inserts at the tibial tuberosity (Schuenke and Schulte, 2011).

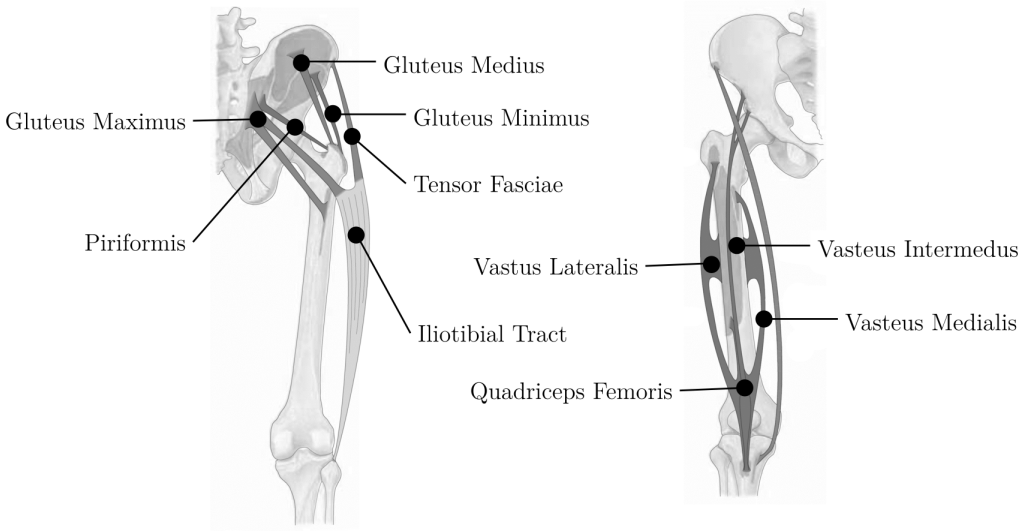

Figure 7.5: Schematic representation of the muscle insertion at the hip joint level: gluteal muscles, tensor fascia latae, and iliotibial tract, and the quadriceps muscles, especially the vastus medialis and the vastus lateralis (adapted from (Schuenke and Schulte, 2011))

According to the shape of the articulating surfaces, the hip possesses ball-and-socket configuration, and hence provide a wide range of motion. It permits movements in all three anatomical planes (Fig. 7.6), as well as rotational movements around a central axis (Shier et al., 2011). To increase joint stability, the acetabulum is deepened by a rim of fibrocartilage, the acetabular labrum, which provides more femoral head coverage. Due to the acetabular labrum, more than one half of the femoral head is placed within the acetabulum (Dalley and Moore, 2001). The movements of the hip are very extensive, and consists of flexion, extension, adduction, abduction, and rotation (Gray and Lewis, 1918).

The rotation around the transverse axis allows a range of motion of 140 degrees of flexion, and 20 degrees of extension from the neutral position. In the sagittal plane the hip allows 50 degrees of abduction and 30 degrees of adduction movements in an upright position, and 80 degrees of abduction and 20 degrees of adduction with a 90 degrees flexion. The ROM along the longitudinal axis consists of 40 degrees of internal rotation and 50 degrees of external rotation (Schuenke and Schulte, 2011).

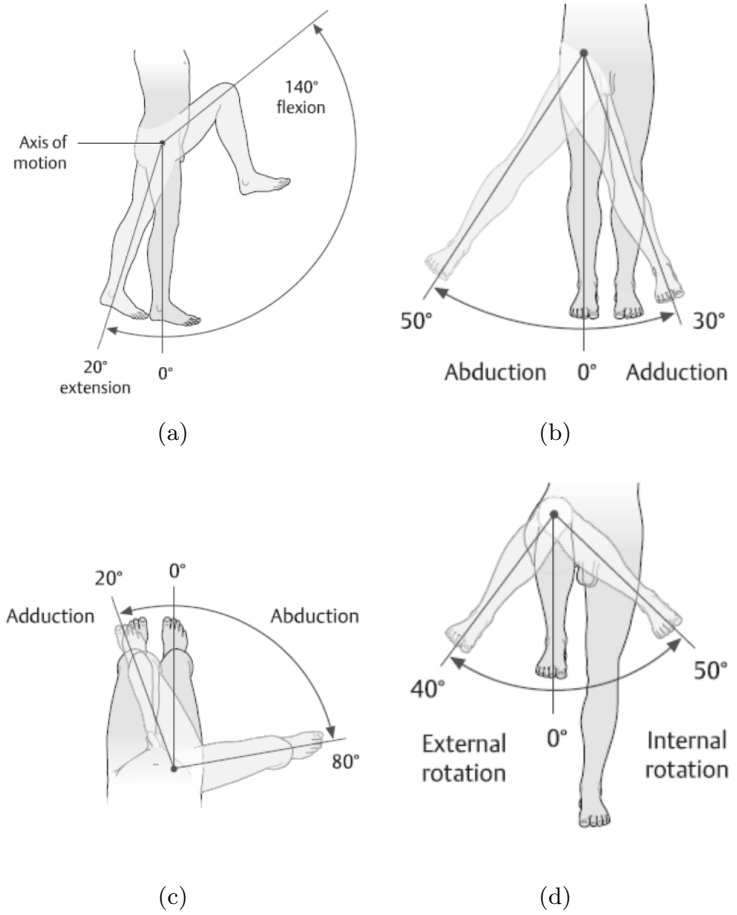

Figure 7.6: Hip joint range of motion: (a) flexion and extension movements around the transverse axis; (b) and (c) abduction and adduction in the upright position and with 90 degrees of leg flexion, respectively; and (d) the limits of internal and external rotation (adapted from (Schuenke and Schulte, 2011))

7.3 Surgical Preoperative Planning

THR provides excellent results in the relief of pain and in the restoration of hip function. The success is dependent on the ability of the surgeon to provide an implant that allows

the immediate stabilization and correct restoration of the biomechanics of the hip. The pre-operative planning is of paramount importance to account for anatomical variability of each patient, to evaluate bone quality, to reduce the time and avoid unexpected problems during surgery (Sinha, 2002). The restoration of the hip biomechanics is achieved by the accurate determination of the centre of rotation, the neck-shaft offset and desired limb length. These three aspects are the main guidelines for the selection of the correct size of the implant to be placed, as well as the correct neck osteotomy level (Malhotra, 2011).

Commonly, the pre-operative planning is performed recurring to 2D radiographs. Two different views are used for pre-operative planning, namely an antero-posterior (AP) view, which often includes the proximal third of the femur, and a lateral view, with the patient positioned in a 45 degrees lateral position. The AP allows the assessment of the neck shaft angle, the lateral offset and the comparison with the opposite unaffected side, whereas the lateral view allows the assessment of the femoral neck anteversion and the extent of bow in the shaft of the femur (Sinha, 2002). Fig. 7.7 depicts the anatomical and mechanical landmarks used for pre-operative planning.

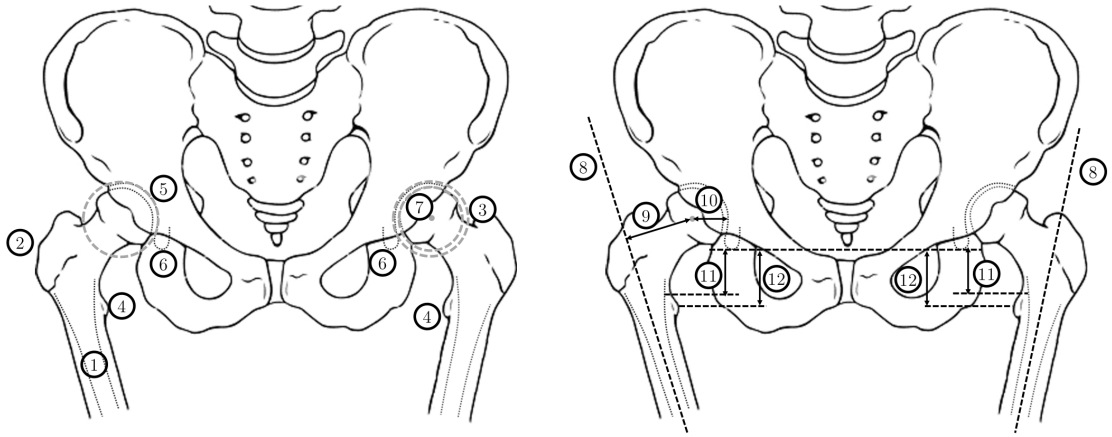

(a) (b)

Figure 7.7: The anatomical and mechanical landmarks used in pre-operative planning: in (a) the anteroposterior pelvic view with the anatomical landmarks: 1 - Femoral shaft inner contour; 2 - Greater trochanter; 3 - Saddle Point between the greater trochanter and femoral neck; 4 - Lesser trochanter; 5 - Acetabular roof; 6 - Right and left teardrops; and in (b) the mechanical landmarks: 7 - Hip centre of rotation; 8 - Longitudinal axis of the proximal femur; 9 - Femoral neck-shaft offset; 10 - Acetabular offset; 11 - Hip length; 12 - Leg length discrepancy is calculated as the difference between the right and left leg (adapted from (Scheerlinck, 2010))

The first step in standard THR pre-operative planning is the identification of the bilateral acetabular teardrops, and define the inter-teardrop line (Fig. 7.7 (a)). This line is used, in conjunction with the proximal edge or the tip of the lesser trochanter, to determine the leg length discrepancy (Fig. 7.7 (b)) (Malhotra, 2011). Hip deformities and trauma are commonly related with the proximal femur, therefore the centre of rotation of the joint is usually determined by templating the acetabular component to the acetabular roof. The size of the acetabular component is chosen in order to fit the acetabular cavity with minimal subchondral bone removal (Fig. 7.7 (b)). The template is placed laterally to the acetabular teardrop, with an inclination of 40 to 45 degrees between the longest axis of the cup and with the medial border of the cup near the lateral border of the ipsilateral teardrop (Sinha, 2002; Malhotra, 2011)

Next, the femoral implant is templated to the proximal femur in order to maximize the fit to the medullary canal, and preserve the centre of rotation obtained with the acetabular component. The longitudinal axis of the implant is positioned parallel to the longitudinal axis of the femur, which in this case is defined as the line connecting the midpoints of the femoral canal measured at two different levels along the proximal femur (Fig. 7.7 (b)) (Scheerlinck, 2010). The position of the femoral component is optimized to place the femoral head at the level of the centre of rotation, and the size is determined by adjusting its medial aspect to the medial wall of the medullary canal (Eggli et al., 1998). The definition of the correct neck length is fundamental to restore both leg length and femoral offset, to define both the approximate insertion depth and the level of osteotomy (Scheerlinck, 2010).

The lateral radiograph is used to evaluate the femoral neck anteverion, to guarantee that the selected size can be safely placed into the medullary canal without impingement, and to ensure a neutral or slightly valgus alignment of the femoral stem (McGrory et al., 1995; Sinha, 2002; Charles et al., 2004). In the case of unilateral hip disease, it is common to use the contralateral side to define the correct implant size and position, and then mirror the result to the affected side. Moreover, when both the acetabulum and the femoral head are intact, the acetabulum and the femoral head are concentric and both points project onto the hip rotation centre (Poitout, 2004; Scheerlinck, 2010; Miashiro et al., 2014).

In conventional THR planning, handling with image magnification is particularly important and the accuracy of the pre-operative planning is highly dependent on the

experience of surgeon (Scheerlinck, 2010). Eggli et al. (1998) reported an agreement between the planned and implanted component size of 92% on the femoral component and 90% for the acetabular component. Miashiro et al. (2014) reported an accuracy of 78.6% and 82.2% for the acetabular component and femoral component, respectively. The femoral offset was also determined with a deviation up to 1.0 mm in 87.5% of the cases. Kalteis et al. (2006) concluded that CT-based surgical planning is the method of choice for accurate acetabular component placement when compared with conventional X-ray radiographs. Custom implant design and pre-operative planning using CT imaging was advocated by several authors as a means to optimize the stem size to the femoral cavity (Sugano et al., 1998; Viceconti et al., 2003; Akbar et al., 2009; Flecher et al., 2010).

7.4 Segmentation of the Lower Limbs

For custom THR, the DICOM data was download from an online database[1]. Similarly to the segmentation of the Human tibia, the Otsu volume thresholding and the Boolean RG starting from high attenuation voxels were used to completely separate the foreground from the background in a relatively automatic way (Fig. 7.8 (a) and (b)).

A four clusters FCM was applied to segment the tissues contained in the foreground (Fig. 7.8 (c)). The target bone for THR is the right femur, hence from section 7.3 one can identify different needs regarding the segmentation for each region. On the one hand, for the pelvic griddle and left femur the segmentation of the bone's outer shell is enough. On the other hand, for the right femur, an accurate description of both the endosteal and periosteal surfaces are needed for proper planning. Thus, the right femur mask was isolated from the remaining data and a second FCM with four clusters was applied solely to the right femur (Fig. 7.8 (d)). In Fig. 7.8 (e) it is possible to observe the tissue classification after the second FCM step. An important observation from image clustering is that the average grayscale value inside the medullary canal is closer to the soft tissue average attenuation than to any other cluster centroid. Locally, the foreground and the background seem to have well defined average values. Finally, the segmentation refinement protocol proposed in Chapter 4 was used to enhance the outer surface of the pelvic bones and left femur, as well as the outer and inner surfaces of the right femur (Fig. 7.8 (f)).

[1] http://www.osirix-viewer.com/datasets/

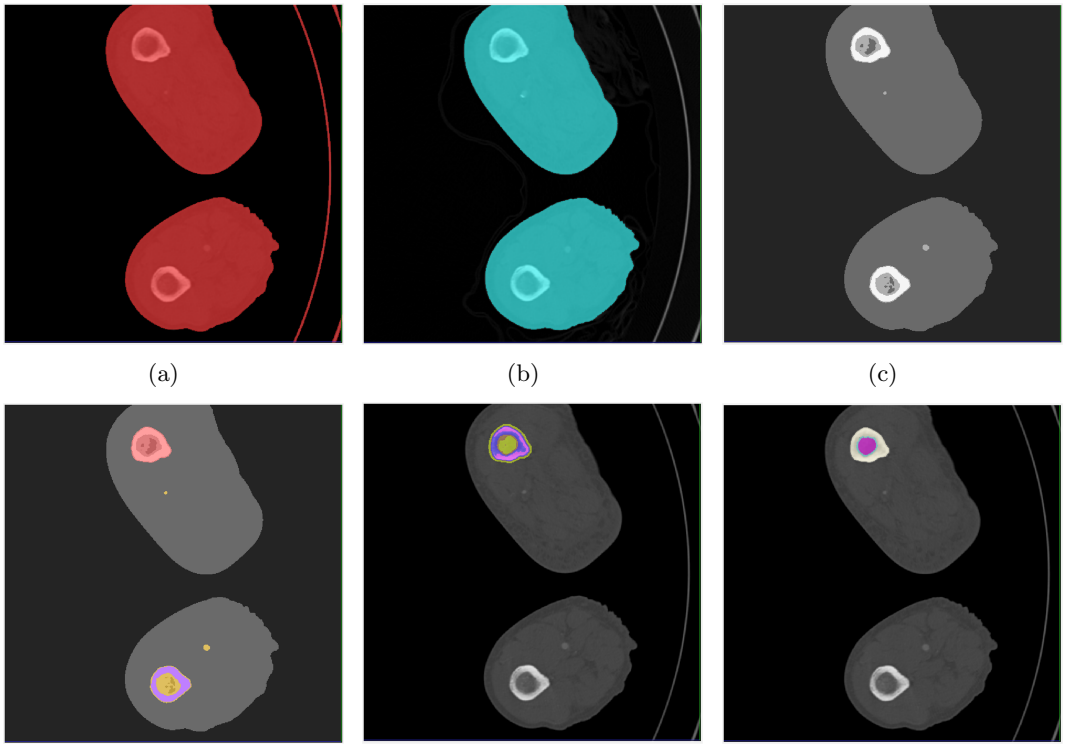

(a) (b) (c)

(d) (e) (f)

Figure 7.8: Image segmentation and refinement of the Human lower limbs: in (a) volume foreground-background segmentation; in (b) Boolean RG from high attenuation voxels to separate the biological tissue from the CT table; in image (c) FCM clustering inside the volume obtained in RG; in (d) definition of the right femur mask from the clustered data; in (e) the second-stage four-classes clustering of the right femur; and in (f) segmentation refinement as proposed in Chapter 4

7.5 Custom Total Hip Replacement Planning

In THR it is recommended to perform a controlled radiographic pre-operative planning, not only to guarantee a reproducible positioning of the patient, but also to guarantee an accurate definition of both femoral and acetabular components. In the radiographic pre-operative planning the patient is positioned in relatively standard and reproducible position, in order to minimize radiographic magnification and to obtain accurate coronal measurements (Thienpont, 2012). To facilitate implant templating, the lower limbs need to be initially positioned into a standardized position to ensure that all anatomical measurements are correctly performed. A common standard position to evaluate the lower limbs is the so-called anatomical position. This anatomical reference positioning of the lower body creates a common ground for the description of the body motion, position,

and movements (McGinnis, 2013). Therefore, the first step towards implant design should be the recovering (if necessary) of the anatomical position of the lower limbs.

7.5.1 Standard Position of the Lower Limbs

A global anatomical reference frame needs to be defined prior to the positioning of the lower body in its natural upright position. The global anatomical reference frame aims to define a coordinate system that is solely dependent on the subject's skeletal anatomy, and it is totally independent from the image acquisition process. Cappozzo et al. (1995) proposed several reference frames for the pelvis, femur, tibia and fibula and feet to describe the position and orientation of the lower limbs during motion. Most of these coordinate systems are currently recommended by the ISB as the standard coordinate systems for the lower limbs (Wu et al., 2002, 2005). Following the guidelines of Cappozzo et al. (1995) and Wu et al. (2002), the anatomical (global) frame was defined, identifying four anatomical landmarks on the pelvis, namely the left and right anterior superior iliac spine, and the left and right posterior superior iliac spine.

The whole body is in its natural anatomical position when it is standing erect, facing forward, with the feet aligned parallel to each other, toes forward, and harms and hands hanging straight bellow the shoulders at the sides (McGinnis, 2013). In an upright stance the lower limbs have all the major joints laying on a straight line with the feet are slightly apart, defining the mechanical longitudinal axis of the leg (Fig. 7.9) (Schuenke and Schulte, 2011). In this position the femoral shaft axis and the femoral anatomical axis (collinear with the mechanical longitudinal axis of the leg) should diverge approximately 6 degrees (Scuderi and Tria, 2006; Stojkovic et al., 2009; Schuenke and Schulte, 2011; Thienpont, 2012). The tibial long axis can be considered as being collinear with the longitudinal mechanical axis of the leg, and the long axis of the foot (defined between the heel and the second metatarsal bone) is parallel to the global frame (Schuenke and Schulte, 2011). Since the centres of all three joints lie in the same vertical line, it is possible to recover the anatomical position of the lower limbs. Additional reference frames for the femur and the tibia were defined. However, unlike the pelvic anatomical landmarks, which were determined manually, the anatomical landmarks and axes of the right femur were determined with a specialized procedure. The anatomical frame of the tibia is defined as described in section 5.5.

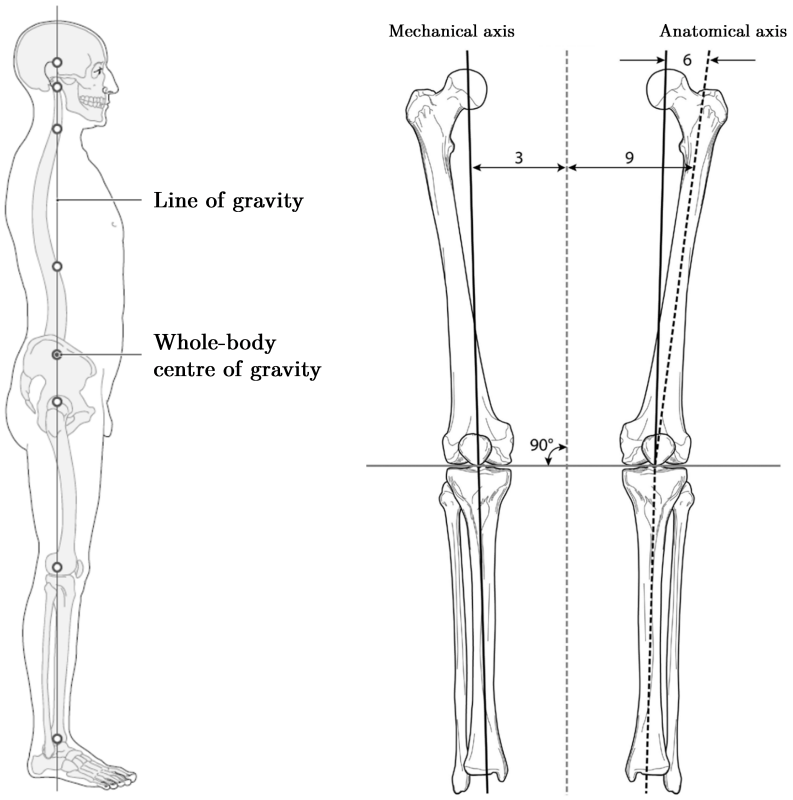

(a) (b)

Figure 7.9: (a) the normal anatomical position relative to the line of gravity, in humans in the upright position, the hip, the knee and the ankle joints lie in the same vertical line; (b) upright stance with feet together: the femoral shaft axis and the femoral mechanical axis diverge in approximately 6 degrees (adapted from (Schuenke and Schulte, 2011) and Pickering and Armstrong (2012))

7.5.2 Reference Frame of the Femur

The femoral reference frame is defined by three landmarks, the lateral and medial epicondyles and the centre of the femoral head. The boundary between the femoral head and neck may be ambiguous, and the inaccurate separation of both anatomical regions can be detrimental for the correct estimation of the femoral head centre and femoral neck axis. In addition, the femoral head centre is crucial for custom hip implant design, and therefore special care must be taken in the determination of this anatomical reference.

Casciaro and Craiem (2014) proposed a procedure to identify both femoral head and neck regions from the proximal femur. The proposed procedure is based on a so-called *Unfolding Transformation*, where all proximal femur surface mesh points are mapped

from the Euclidean space (x, y, z) into another space (λ,d,α), where λ is the projection of an arbitrary point onto the femoral neck centreline, d is the orthogonal distance of each point to the centreline, and α is the unfolding angle. To perform the unfolding transformation, an initial estimate of both femoral head centre and femoral neck axis were manual determined. The initial estimate of the femoral head was obtained manually by fitting a sphere to the femoral head, whereas femoral neck axis was defined as a line passing through the femoral head centre and the base of the greater trochanter (Gregory and Aspden, 2008). The assumption of the femoral head as a sphere is widely used in the literature, both in standard pre-operative planning, in custom hip implant design, in femoral neck bone mineral density assessment, and in femoral geometrical assessment (Mahaisavariya et al., 2002; Kang et al., 2005; Stojkovic et al., 2009; Victor et al., 2009; Scheerlinck, 2010; Jun and Choi, 2010).

The unfolding transform allows the representation of the information contained in the 3D mesh in a more amenable way, such as a 2D image, where the $x - y$ position is defined by the unfolding angle and the projection of each point onto the femoral neck centreline. The image grayscale is proportional to the orthogonal distance to the manually determined femoral axis (Fig. 7.10 (a)). The femoral head and neck can be determined by simply finding the zero-crossings in each side of the image's centreline (Fig. 7.10 (b)). Fig. 7.10 (c) and (d) depict the proximal femur with the initial guess for the femoral head and neck regions, and the final regions obtained with the described algorithm, respectively. The new estimates of the femoral head centre and diameter were determined by non-linear least-squares fit of a sphere $S_{fit}(a, b, c, r)$ to the newly defined set of points:

$$S_{fit}(a, b, c, r) = \sum_{i=1}^{n} \left(r - \sqrt{(x_i - a)^2 + (y_i - b)^2 + (z_i - c)^2} \right)^2 \tag{7.1}$$

where parameters (a, b, c) define the sphere centre, and r is the sphere radius.

The lateral epicondyle is the most prominent anterior and distal point on the lateral aspect of the distal femur, whereas the medial epicondyle is the most anterior and distal prominence on the medial surface of the distal femur Cappozzo et al. (1995); Stojkovic et al. (2009); Victor et al. (2009). The same unfolding procedure can be applied to the distal femur to determine both the lateral and medial epicondyles of the femur, and the centre of the knee joint. In Total Knee Replacement the centre of the knee joint lies in

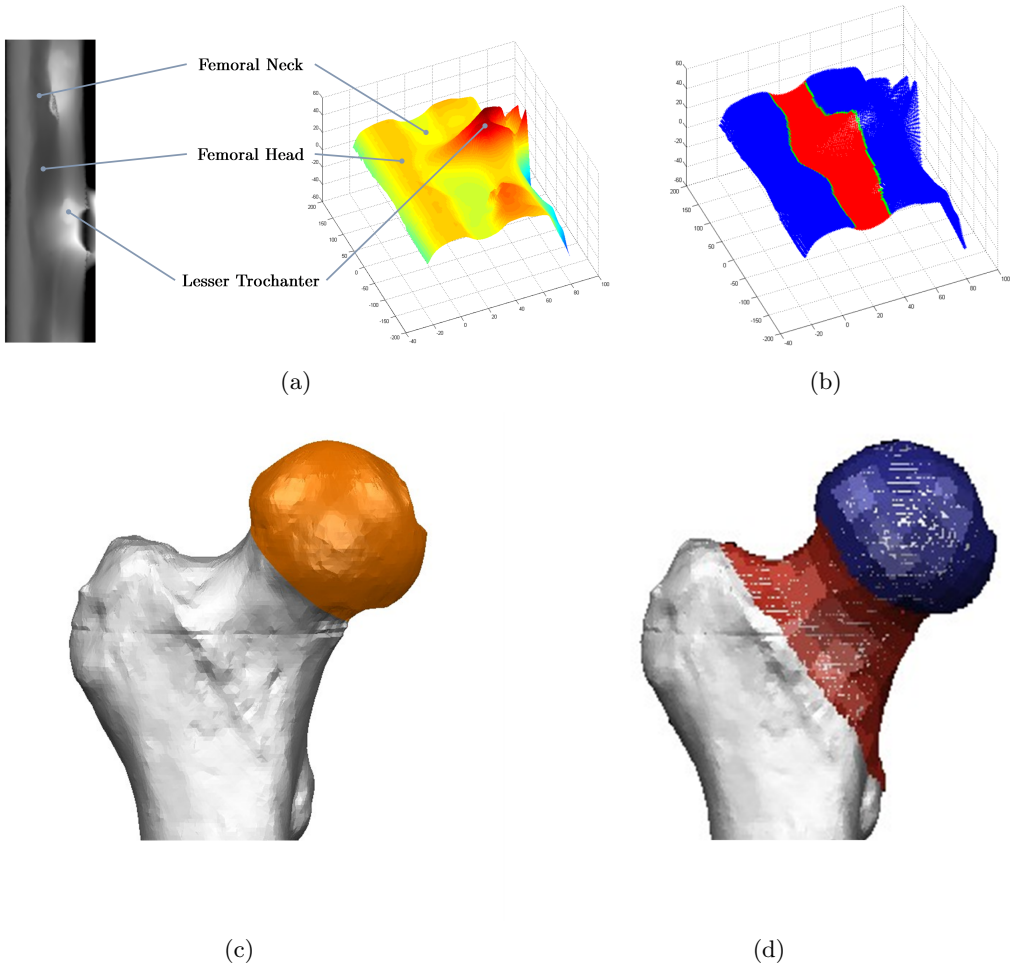

Figure 7.10: In the unfolding transform of the proximal femur the 3D mesh points are encoded into a 2D image matrix where the x-y positions are the angular position and the projection onto the femoral neck centreline in (a); the femoral head and neck are determined by finding the zero-crossings starting from the image centreline (b); visual depiction of the final femoral head and neck regions after unfolding the domain (c)

the middle of the intercondylar notch, and can be defined by finding the intersection point of the transepicondylar axis and the Whiteside's line. Where the Whiteside's line runs through the deepest part of the intertrochlear groove and the top of the intercondylar notch, and is perpendicular to the transepicondylar axis (Stiehl et al., 2007).

Surface unfolding can be applied to estimate the anteroposterior axis of the knee or the Whiteside's line. In the unfolded surface, the Whiteside's line lies between the two epicondyles and can be determined by moving the centreline points in the intercondylar region in the negative gradient direction ($-\nabla I(x, y)$) of the resulting 2D map (similar to Fig. 7.10 (a)). The folded points determined in such a way enable the definition of a

3D representation of the 2D Whiteside's line, which one will call the *Whiteside's plane*. The Whiteside's frame associated with the Whitesid's plane was determined by computing the eigenvectors of the folded points through the Principal Component Analysis (PCA). Since the Whiteside's line and transepicondylar axis are, by definition perpendicular, the medial and lateral epicondyles can be determined as the points located more medially and more laterally relative to the Whiteside's plane. With the femoral head centre, the medial and lateral epicondyles, one can define the Femoral Coronal plane. The knee joint is just the intersection point between the surface mesh, the Whiteside's plane and the Femoral Coronal plane. Given the Whiteside's frame, the definition of the medial and lateral posterior condylar apexes and the posterior condylar axis is also straightforward. Fig. 7.11 depicts the definition of the Whiteside's plane, the lateral and medial epicondyles, as well as the posterior medial and lateral condyle points and the centre of the knee joint.

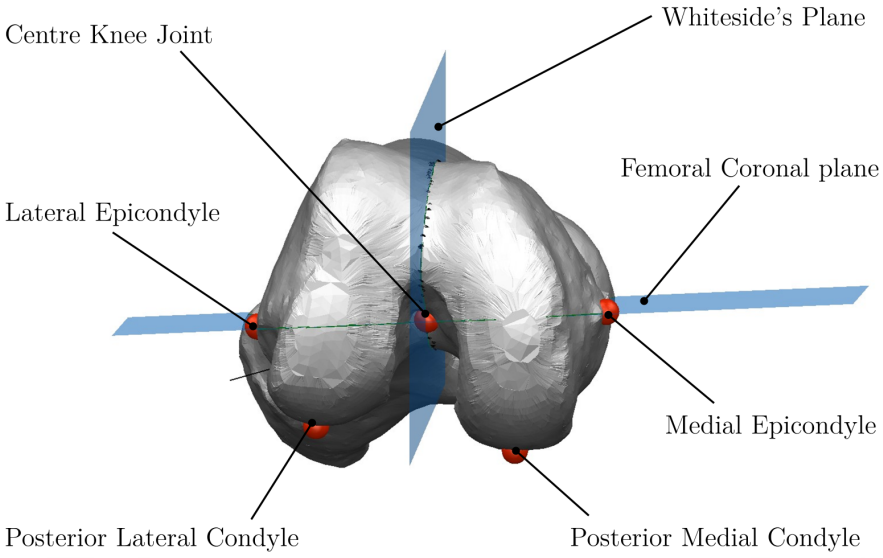

Figure 7.11: Definition of the reference landmarks and planes of the distal femur: the centre of the knee joint is defined by the intersection between the Transepicondylar plane and the Whiteside's plane; the medial and lateral epicondyles are defined as the most medial and lateral points of the medial and lateral condyles, and the posterior condylar axis is defined as the line connecting the posterior points in both the medial and lateral condyles

After defining the geometrical centre of both the hip and knee joint, the natural anatomical position of the femur can be recovered. In a similar fashion, the anatomical position of the tibia and fibula can also be recovered, considering that the long axis of

the tibia lies vertically and parallel to the axis of the contralateral tibia. In Fig. 7.12 is shown the position of the lower limbs according to the aforementioned procedure against, the standard upright position as defined in (Schuenke and Schulte, 2011).

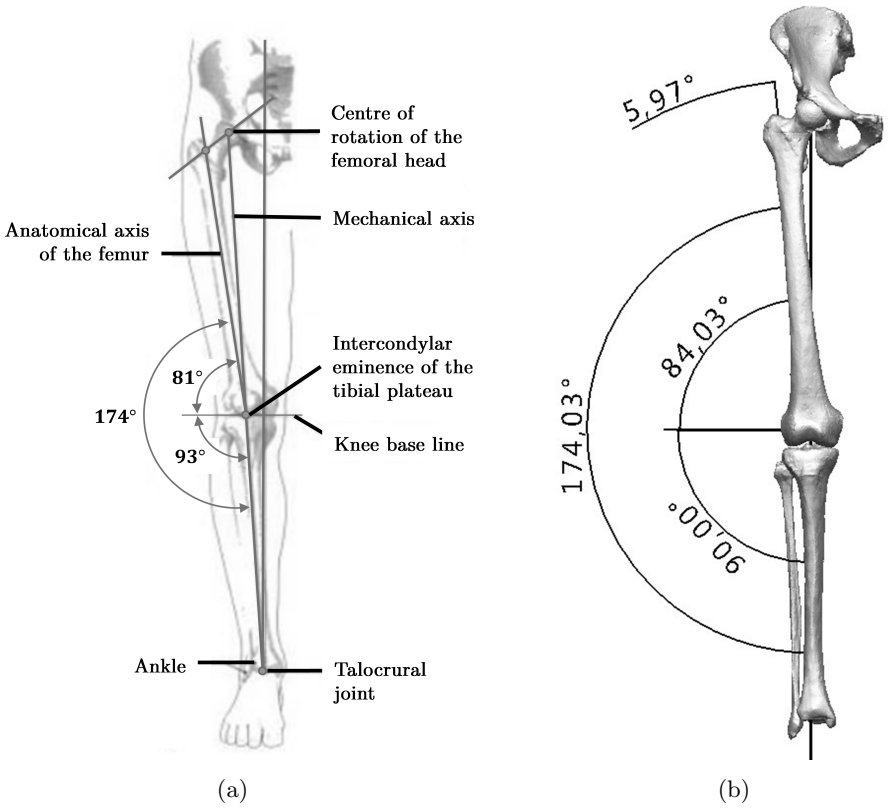

(a) (b)

Figure 7.12: Recovering the standard anatomical position of the lower limbs: in (a) the coronal view of the mechanical axis of the leg in the anatomical position with the correspondent angular position between the different bones, and in (b) the recovery of the anatomical position of the lower limbs according to the determination of the proposed hip and knee centre

7.5.3 Custom Implant Planning

As mentioned in section 7.3, the advantages of CT-based THR planning cannot be ignored in custom implant development, where a perfect fit between the femur and the implant is crucial. CT implant planning has already proved to be a very valuable tool in previous studies, and in the future may become the *de facto* standard procedure in clinical practice. In the previous section several important landmarks and anatomical planes were defined in order to recover the natural position of the lower limbs. Since the images were collected from an online database, the previous procedure was needed to ensure consistency and

reliability in the anatomical analysis of the acetabulum and proximal femur.

Several other important anatomical landmarks and frames were determined in section 7.5.2, namely the femoral anatomical frame, the transepicondylar axis, the posterior condylar axis, and the femoral head centre. Since both the acetabulum and the femoral head are in good condition, the femoral head centre defines the centre of rotation of the hip (Scheerlinck, 2010). Furthermore, with the Unfolding Transformation, the femoral neck can be separated from the femoral head and the remaining proximal femur (Fig. 7.10). The femoral neck axis can be determined by fitting a cylinder ($C_{fit}(a, b, c, r)$) to the femoral neck points and the femoral head centre determined previously:

$$C_{fit}(a, b, c, r) = \sum_{i=1}^{n} w_i (R(i) - r)^2 \tag{7.2}$$

where $R(i)$ is the orthogonal distance of i^{th} point to the cylinder centreline defined by the direction cosines (a, b, c):

$$R(i) = \sqrt{(cy_i - bz_i)^2 + (az_i - cx_i)^2 + (bx_i - ay_i)^2} \tag{7.3}$$

where (x_i, y_i, z_i) are the coordinates of the i^{th} point, the weights $w_i \in [0, 1]$ and $w_i \propto 1/z_i$, and r the radius of the cylinder (Muralikrishnan and Raja, 2008). Here, all femoral neck mesh points were folded back to the original domain, and a penalty was added to the projection of each point onto the femoral neck. The fitting process is, hence, biased to privilege error minimization near the femoral head centre instead of minimizing it along the whole extent of the femoral neck.

Similarly to the tibia in Chapter 5, the axis of the proximal femur was determined by fitting 2D circles to a series of equally spaced cross-sections of the intramedullary canal, between the lower border of the lesser trochanter and 150.0 mm bellow the femoral head centre (Fig. 7.13). The proximal femur axis is the 3D line that best-fits the centres of all cross sections. A similar approach to determine the femur axis was used by Mahaisavariya et al. (2002) to study the $3D$ morphology of the proximal femur, and by Jun and Choi (2010) for the design of a custom hip replacement from $3D$ image data.

In standard pre-operative planning, the acetabular component is defined prior to the femoral component. However, in this case the two steps are interchangeable. The acetabular component should restore the femoral head centre and should lie in close contact

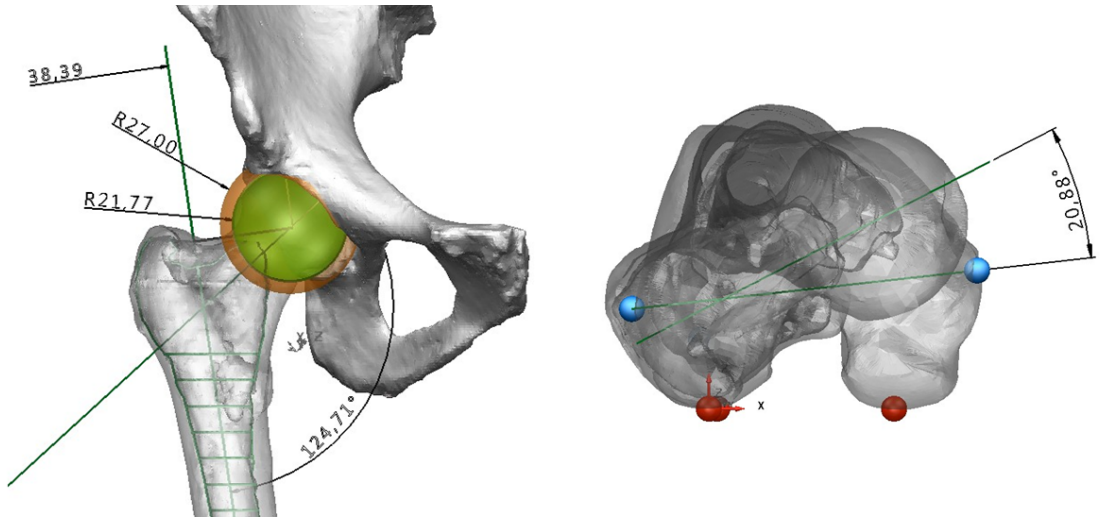

(a) (b)

Figure 7.13: (a) the implant planning, with the determination of the 3D orientation proximal femoral axis and femoral neck axis, determination of the neck-shaft angle (CCD), definition of the acetabular component size, size of the femoral head, and measurement of femoral offset, and (b) the determination of femoral anteversion angle considering the transepicondylar axis and the femoral neck axis (all linear measurements in mm)

with the acetabular surface. To determine the outer diameter of the acetabular shell, sphere centred at the hip joint centre was fitted to the acetabular roof. An outer diameter of 54.0 mm provides a compromise between the complete removal of the acetabular fossa and the lunate surface at the level of the transverse acetabular ligament, and the preservation of the most part of the subchondral supporting bone of the acetabulum (Fig. 7.13 (a)).

Next, the femoral neck-shaft angle and the femoral anteversion angle were quantified, according to the previous estimates of both the proximal femur axis, femoral neck axis and transepicondylar axis. With the proposed methodology, the estimates for both the femoral neck-shaft angle and femoral anteversion angle are 124.71 degrees and 20.88 degrees, respectively (Fig. 7.13 (a) and (b)). Both values fall within the normal range for adult subjects presented by other references. The average anteversion angle may vary between the interval of 12 to 25 degrees, whereas the femoral neck-shaft angle is usually between 120 to 135 degrees in adult subjects (Anderson and Trinkaus, 1998; Hammer, 2007). The femoral offset is defined as the shortest distance between the femoral rotation centre and the longitudinal axis of the proximal femur, and according to the proposed methodology

is approximately 38.39 mm (Fig. 7.13 (a)). The leg length discrepancy of 2.5 mm was obtained by levelling the medial condyles of the right and left femur along the global frame defined by the pelvis. The femoral neck resection/osteotomy level was defined along the intertrochanteric region 10 mm above the lesser trochanter, and with 45 degrees of inclination (Pfeil and Siebert, 2010).

7.6 Acetabular Component Design

Cementless acetabular components are the current gold standard for acetabular replacement in THR. Cementless acetabular fixation showed better long-term results when compared with cemented acetabular fixation (Gaffey et al., 2004). Modern cementless acetabular components are hemispherical or modified hemispherical designs, and are made of cobalt chrome, commercially pure titanium, or other titanium alloys. The outer shell of these implants is porous coated to stimulate bone ingrowth into their porous metal surface and achieve durable long-term stability. However, bone ingrowth may be compromised by implant micro-motions along the implant-bone interface. Initial stability may be provided by an in-built interface press-fit, and can be enhanced with other design features such as screws, pegs, spikes, and fins (Kraay et al., 2012).

Acetabular components are available in various sizes in order to cover most anatomical needs, and the liner may be of metal, polyethylene or ceramic. The thickness of the liner varies according to the inner diameter of the acetabular shell and the size of the femoral head used in THR (Malhotra, 2011). There are some design features that influence the risk of implant dislocation and liner rim-neck impingement, such as the head-neck ratio, and the height and shape of the elevated rim that extends beyond the metal shell. The safe ROM of an implant can be optimized by reducing or even eliminating liner rim elevation from the design, at the cost of losing some implant stability. Kraay et al. (2012) recommended the use of a hemispherical titanium porous-coated acetabular component, with a cluster-hole configuration for supplemental screw fixation in the acetabular dome, with a 1.0 mm under-reaming to minimize insertion forces and reduce the risk of pelvic fracture. In addition, Furmanski et al. (2009) also found that the existence of sharp edges in the liner rim and in the metallic shell appear to provide the means for cracks initiation and propagation into the bulk of the component. Therefore, sharp features at

the mechanical coupling between the liner and the metallic shell should be avoided.

In the project of a modular acetabular component, several other aspects come into play, namely: the femoral head size and the achievable ROM; and the materials used in the mechanical coupling (acetabular shell and liner). The achievable ROM after hip joint surgery is very important. The achievable ROM is affected by the position of the acetabular component, and size of the femoral head diameter. Larger femoral head sizes are commonly associated with increased joint stability and larger ROM, because the size of such femoral heads corresponds geometrically better to the anatomy of the natural hip joint. Larger femoral heads are desirable because they have a lower risk of dislocation (Berry et al., 2005), but their use was recently discouraged due to the high amount of polyethylene wear debris produced (Wang et al., 2001). Burroughs et al. (2005) concluded that head sizes larger than 32 mm essentially eliminate component-to-component impingement, and that an increase in the ROM is only produced with femoral-head sizes between 28 to 38 mm. Therefore, the optimum head size lies between these two values, and a femoral head of 28 mm was suggested as the ideal diameter providing the right balance between liner size and volumetric wear (Malhotra, 2011). Regarding the articulating pairs, recently, metal-on-metal couplings have regained some popularity due to the possibility to using larger femoral heads. Nevertheless, recent findings have correlated larger head sizes (above 36 mm) with significantly increased rates of revision surgery for conventional THR using metal-on-metal prosthesis (Smith et al., 2001, 2012).

Orthopaedic surgeons are forced to find a compromise between anatomical limitations, achievable ROM, and release of wear debris to the surrounding soft tissues and blood stream. Following the above mentioned guidelines, as well as the individual needs of the target acetabulum, a cementless hemispherical press-fit acetabular component with 54.0 mm of outer diameter was designed (Fig. 7.14 (a), (b) and (c)). Both acetabular shell and liner were designed to avoid sharp features in the shell-liner interlocking system.

The articulating couple considered in the design of the custom THR system was a ceramic-on-polymer. Ceramic femoral heads possess better wear properties when compared with metal heads. Ceramic femoral heads also feature the highest achievable surface smoothness, which results in the lowest friction coefficients and less production of wear debris (Cigada et al., 2010). Recent findings showed that polyethylene wear

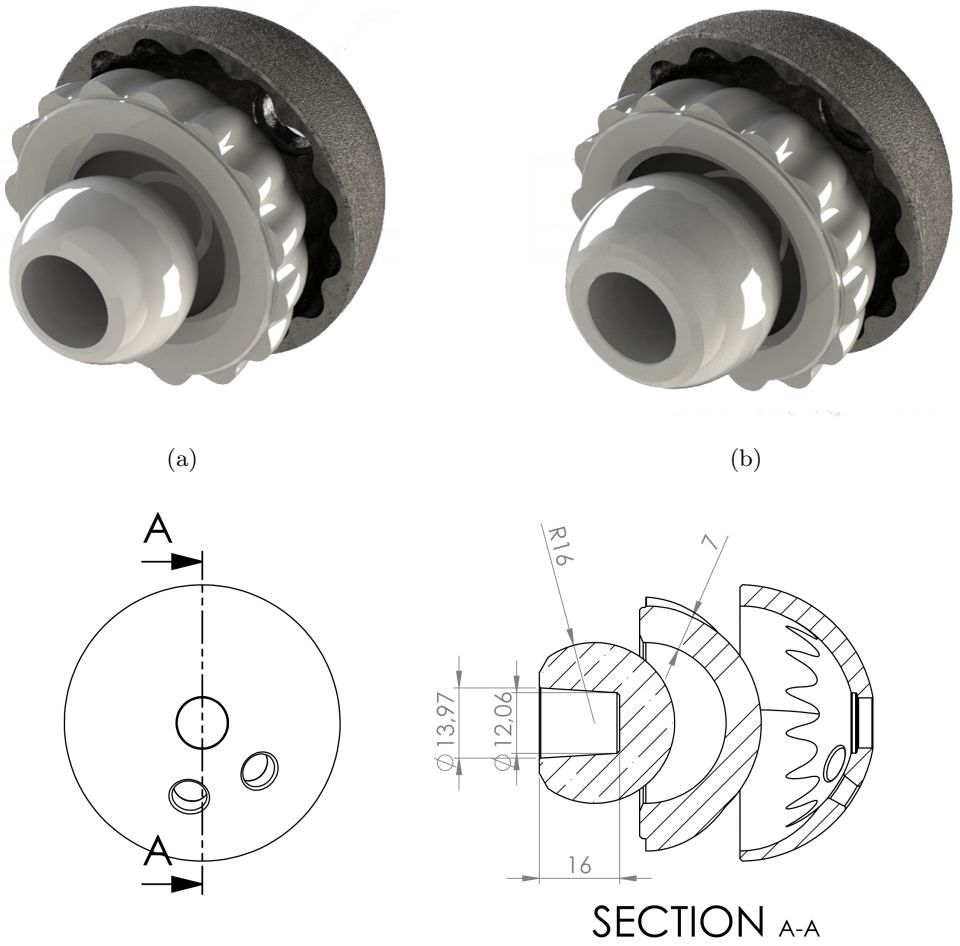

Figure 7.14: Modular acetabular component with hemispherical shell with 54.0 mm of outer diameter (a) with a femoral head with a diameter of 28.0 mm and liner thickness of 9.0 mm, (b) with a femoral head with a diameter of 32.0 mm and a liner thickness of 7.0 mm liner, and (c) section of the acetabular component construct in (b)

properties can be enhanced, and that the reduction in wear was independent of head size within the range of 22 to 46 mm in diameter (Muratoglu et al., 2001a,b). These findings support the idea that Ultra High Molecular Weight Polyethylene (UHMWPE) liners can be used with larger femoral heads. In comparison with metallic and ceramic liners, polyethylene liners do not release metal ions to the surrounding tissues, and are less prone to brittle fracture as the ceramic liners.

The femoral head size cannot be increased indefinitely and larger femoral heads are not necessarily better. Two femoral head sizes were considered, namely: a femoral head with a diameter of 28.0 mm (Fig. 7.14 (a)); and a femoral head with a diameter

of 32.0 mm (Fig. 7.14 (b)); in order to maximize the liner thickness and to provide some inter-operative flexibility to the surgeon (Fig. 7.14). The 28.0 mm and 32.0 mm diameter heads are a compromise between the limitations imposed by the outer shell of the acetabular component (54.0 mm) and the theoretical achievable ROM. In the liner design, a small elevation of 1.25 mm was also considered in order to increase femoral head coverage. Rim elevation was optimized to avoid component-to-component impingement between the liner and the femoral neck during simulated static hip motion. For the current femoral head diameters and acetabular shell-liner coupling the minimum liner thickness must be between 6.0 to 8.0 mm, to guarantee the mechanical integrity of the component after THR (Callaghan et al., 2007). The outer dimension of the acetabulum (54.0 mm), the most appropriate femoral head diameters (28.0 or 32.0 mm), and the minimum liner thickness, bound the maximum thickness of the acetabular shell to 4.0 mm (Fig. 7.14).

7.7 Custom Femoral Stem Design

The choice between cemented or non-cemented implant is multifactorial, and depends on the patient's age and lifestyle, the health condition and the existence of other health-related problems, the quality of bone stock available, among others factors. The cementless femoral stems have been recurrently recommended for younger and more active patients, whereas for older and less demanding patients, cemented femoral stems are commonly seen as the treatment of choice (Sinha, 2002). In the Swedish Hip Arthroplasty Registry cementless femoral stem fixation proved to be superior to cemented fixation in patients with less than 60 years of age (Hailer et al., 2010). The cementless femoral stems are designed to fit-and-fill the metaphyseal region of the femur, in order to ensure a more physiological loading of the proximal femur, and to purchase the necessary primary stability for secondary bone osteointegration. The geometry of the femoral stem must establish an intimate contact between the stem and the anatomy of the proximal femur (Zenz et al., 1994).

Numerous stem designs have been proposed over the years. However, tapered femoral components seems to be more appropriate. The Ti-alloy tapered designs have shown to have excellent 20-year survivorship, with only one stem revision for periprosthetic fracture. The tapered femoral stems have also a survivorship at least comparable or even better than

other cementless and cemented designs (Corten et al., 2011). These outcomes seem to be correlated with the wedged nature of the stem, which allows a proximal and uniform load transmission to the supporting bone. The cementless tapered designs are also associated with the successful treatment of osteoarthritis and rheumatoid arthritis. Excellent results after a 12-year follow-up period were also obtained by Carl et al. (2011) in patients with rheumatoid arthritis. The low incidence of thigh pain with these designs, when compared with other cementless femoral stem geometries, is thought to be related with their ability to distribute better the stress along the proximal femur. Custom tapered stems adapted to the proximal femur were also thought to prevent implant subsidence and reduce femoral bone osteolysis after surgery (Flecher et al., 2010).

Tapered stems may possess a collar at the base of the neck. The collar is thought to provide initial fixation to uncemented stems, to promote the load transfer to the calcar bone, and avoid initial implant subsidence (Demey et al., 2011). The use of collared femoral stems is also associated with a decreased ROM after surgery, an increased risk of component impingement, and implant dislocation. Currently, the use of collared stems is discouraged. No benefits were found in using collared stems regarding subsidence or load transmission when compared with collarless stems (Malhotra, 2011). For custom stem design, Akbar et al. (2009) stressed that the femoral component should also avoid distal fixation by reducing the diameter of the distal end of the stem, and that the length of the stem should range from 140 to 160 mm to enhance fixation and stability.

A cementless straight double-tapered collarless was chosen as the femoral component (Fig. 7.15). The femoral stem aims to optimize the medio-lateral fit-an-fill of the proximal medullary canal between the level of the femoral osteotomy and the lesser trochanter (Fig. 7.16 (a) and (b)). It has a slight offset from the segmented medullary canal, in order to promote the intramedullary fit with cancellous bone contact instead of cortical bone contact as proposed by Flecher et al. (2010). To maximize the stem fit to the proximal femoral region, a slight lateral flare was added to the stem above the lesser trochanter. The purpose of lateral flare is to maximize the proximal implant-bone contact along the lateral aspects of the medullary canal (Fig. 7.16 (b)).

The implant cross-section is rectangular in the proximal aspect of the stem and gradually converges to a circular cross-section at the distal end of the stem. It was shown clinically that rectangular cross-sections possess better rotational stability (Aldinger

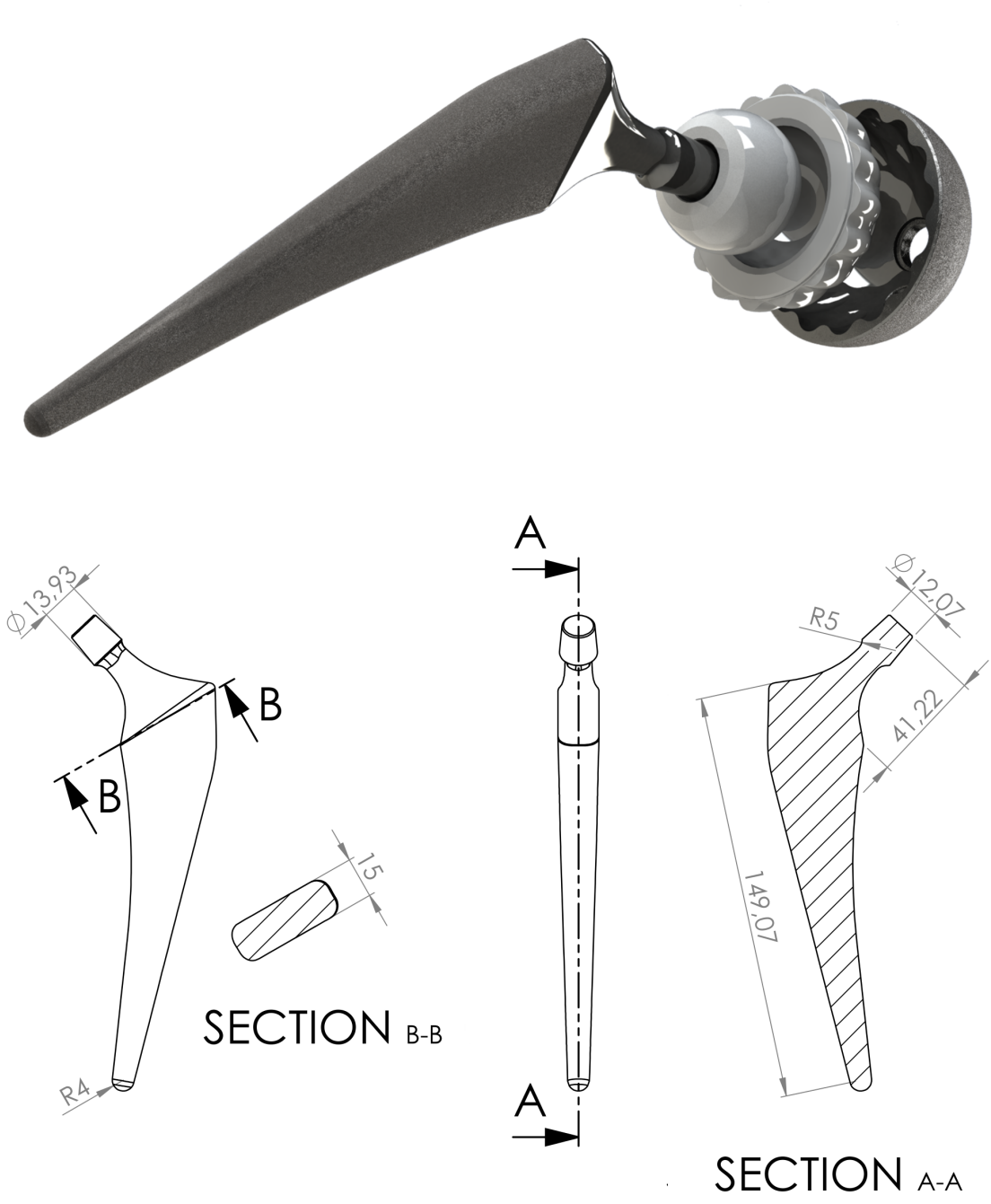

Figure 7.15: Total Hip Replacement system proposed: double tapered femoral stem; femoral head with a diameter of 32.0 mm; UHMWPE liner with a thickness of 7.0 mm, cementless hemispherical press-fit acetabular shell with 4.0 mm of thickness; and some additional geometrical details of the femoral stem

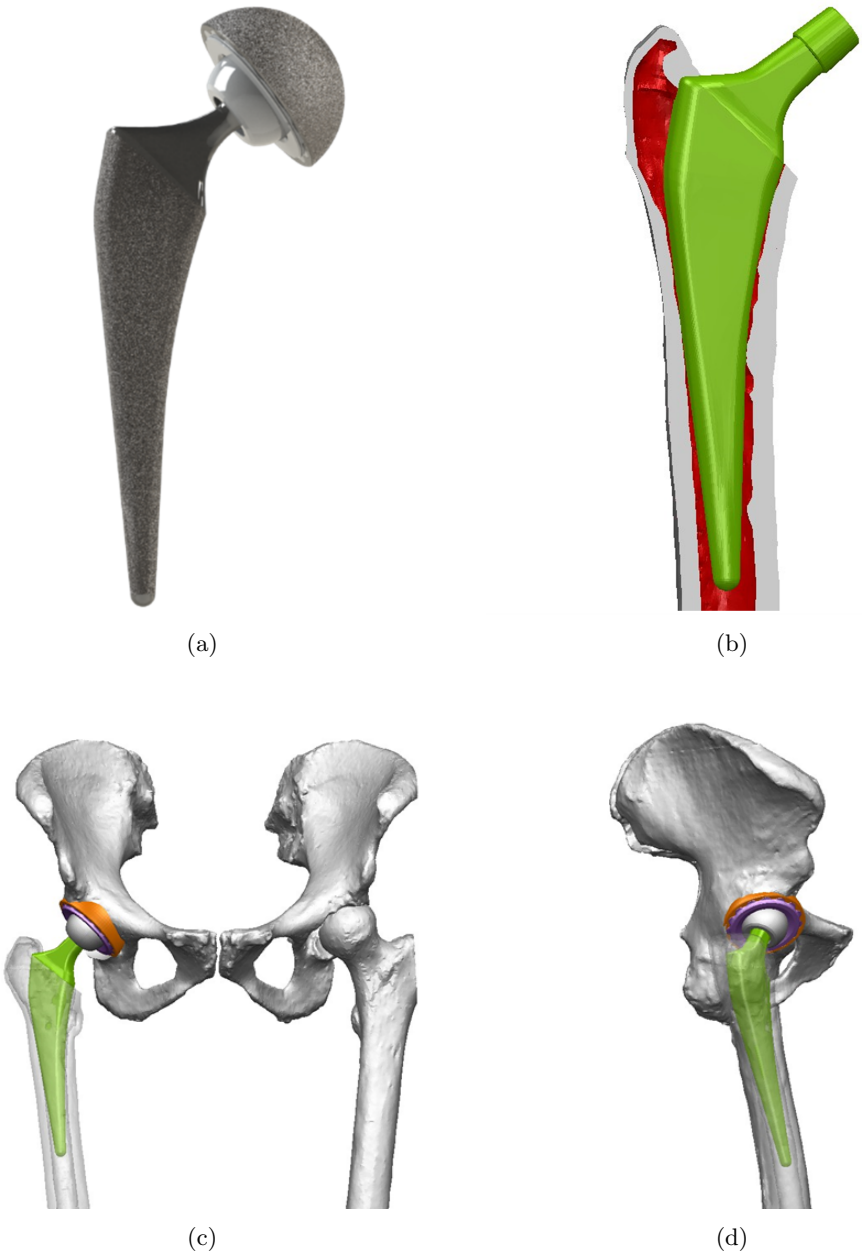

Figure 7.16: (a) coronal view of the double-tapered collarless femoral stem, along with the femoral head and acetabular component; (b) proximal fit-and-fill of the proximal femoral cavity; (c) the coronal view of the custom implant positioned within the femoral cavity alongside with the contralateral femur for comparison; and (d) sagittal view of the custom hip replacement placed along the femoral canal in a neutral position

et al., 1983; Abdul-Kadir et al., 2008). In addition, Ramos et al. (2011) concluded that different cross-sections promote different stress concentrations at different levels of the femoral stem, and that at the distal end a circular cross-section promoted the

most suitable stress distribution for cemented components. Femoral stems with proximal rectangular cross-sections, which gradually converge to a circular cross-section distally, are also associated with excellent survival rates at 10 to 15 years (Sochart and Hardinge, 1998; Vidalain, 2011). To compensate for both leg length discrepancy and the neck-shaft angle of the left femur, the CCD angle of the femoral stem was changed from the originally measured 124.71 degrees to 127.0 degrees (see Fig. 7.13 (a)). The stem length was set to 163.0 mm in order to maximize femoral stem length and avoid the distal contact between the tip of the femoral stem and the cortical bone (Fig. 7.16 (d)). The existence of distal impingement between the femoral stem tip and the cortical bone is often associated with thigh pain after THR.

Regarding the femoral neck cross-section, the ratio between the femoral head size and the neck diameter is another important factor influencing the post-operative ROM and the risk of implant dislocation. The position of the acetabular component is also relevant in the achievable ROM without component-to-component impingement. The positioning of the acetabular component with 45 degrees lateral abduction and with 15 to 30 degrees of anteversion is thought to result in an appropriate ROM and dislocation stability (Kluess et al., 2007). After position the acetabular component with 45.0 degrees of inclination and with 20.0 degrees of anteversion, the achievable passive range of motion of the custom THR system for a 32.0 mm femoral head diameter and several femoral neck geometries was analysed (ranging from 8.0 to 13.0 mm of diameter). Limitations to the full ROM were observed for a leg flexion angle above 120.0 degrees for different neck diameters. With a femoral head-neck ratio of 3.55 (9.0 mm), a full 140.0 degrees of flexion could be performed without component-to-component impingement. Therefore, a femoral neck diameter of 9.0 mm will be considered in the following validation steps. It is also worth noting that no bone-implant impingement was observed for all femoral neck geometries tested.

7.8 Femoral Stem Design Validation

For optimization purposes, a THR system with a 32.0 mm femoral head and 9.0 mm of femoral neck diameter was considered. The design allows the restoration of the full passive ROM without component-to-component or component-to-bone impingement. First, the

fatigue endurance of the femoral neck design was validated according to the requirements of ASTM F 2996-13 - Standard Practice for Finite Element Analysis (FEA) of Non-Modular Metallic Orthopaedic Hip Femoral Stems. Second, stem implantation into the target femur was simulated and evaluated considering the muscle forces along the hip joint during walking and stair climbing as proposed by Heller et al. (2005).

In the FEA, the mechanical properties considered for the Ti-6Al-4V, the cortical bone, the trabecular bone and the ceramic femoral head are summarized in Table 7.1.

Table 7.1: Mechanical Properties of the femoral stem and femur for implant optimization (Reilly and Burstein, 1975; Welsch et al., 1993; Cowin, 2001; Kutz et al., 2003; Misch, 2007)

	Ti-6Al-4V	Cortical Bone	Trabecular Bone	Ceramic
Modulus of Elasticity (MPa)	113800	17900	1500	372000
Yield Stress (MPa)	880.0	180.0	15.0	--
Poisson Ratio	0.34	0.30	0.32	0.20
Fatigue Strength 1.0×10^7 cycles (MPa)	510.0	--	--	--
Shear Strength (MPa)	550.0	65.0	--	--
Ultimate Strength (MPa)	950.0	205.0	131.0	550.00

7.8.1 ASTM F 2996-13 Validation of the Femoral Stem Geometry

The achievable passive ROM and fatigue strength of the femoral neck are concurrent requirements. On the one hand, a large femoral neck increases the fatigue resistance of the stem, but may reduce the achievable ROM after THR. On the other hand, a large femoral head-neck ratio is also desirable since it allow a greater ROM. Since the size of the acetabular shell and liner are limited by the anatomy of the patient, a larger femoral head-neck ratio is often achieved by reducing the diameter of the femoral neck. However, the neck geometry must not compromise the behaviour of the hip stem in the long term. The femoral neck geometry must guarantee the mechanical resistance of the implant against high peak stresses and fatigue. The optimization of the stem design against fatigue failure followed the guidelines of the ISO 7206 - Implants for surgery - Partial and total hip joint prosthesis, which was transposed to FE testing by the ASTM F 2996-13. The ISO 7206-6 defines the orientations and loading conditions for determining the endurance properties of the femoral stem, and the ASTM F 2996-13 defines the loading conditions, boundary conditions, and mesh convergence criteria to replicate the ISO testing with FEA.

The ISO 7206-6 defines the orientation of the implant in both sagittal and coronal planes (ISO 7206-6). For a stem length of 163.0 mm of length, the ASTM F 2996-13 specifies an implant loading of 2300.0 N (ASTM F2996-13). In addition, the femoral stem should be restrained in all three directions at 90.0 mm below the centre of the femoral head. Fig. 7.17 depicts the boundary and loading conditions defined in the ASTM F 2996-13 standard. The stress distribution should be evaluated at the femoral neck region and at the femoral stem at a distance D from the femoral head centre (termed as potting level (Fig. 7.17)). To evaluate the femoral stem, a quadratic tetrahedral element mesh was generated and the boundary conditions applied as define by the standard. In addition, in the ASTM F 2996-13 it is recommended a model convergence within each region of interest to be $\leq 5\%$. For FE mesh convergence, both the nodal displacement and von Mises equivalent stresses were analysed along the femoral neck and potting level. Model convergence was achieved for a FE mesh with approximately 190000 nodes and 119000 elements, generated with a surface element size of 1.0 mm. Fig. 7.18 shows the equivalent stress distribution obtained with this FE mesh at the neck and potting levels.

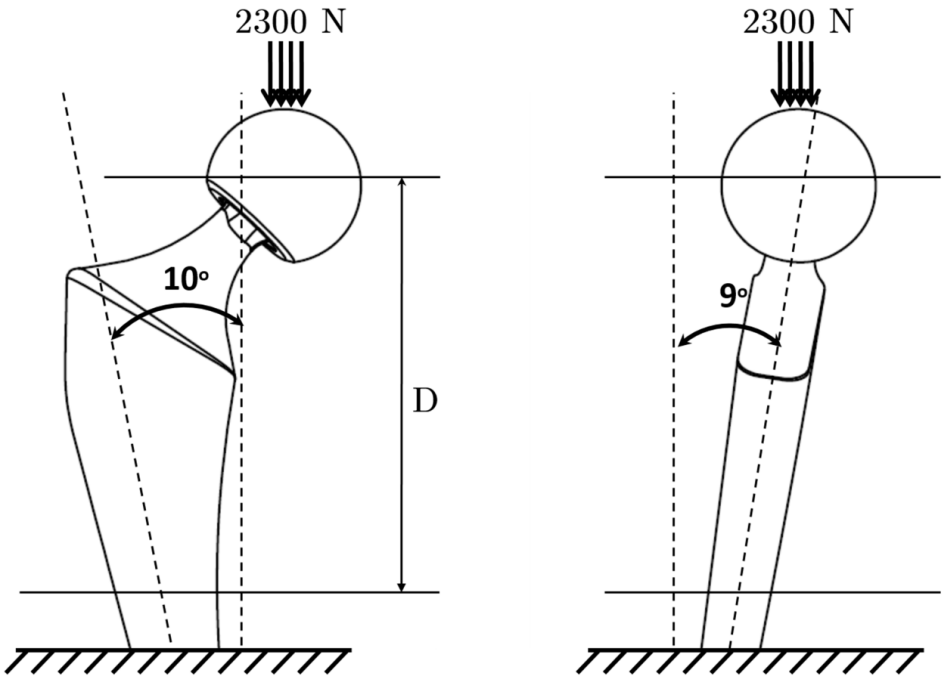

Figure 7.17: Implant 3D orientation and boundary conditions, according to the ASTM F 2996-13 standard for the validation of the femoral neck geometry

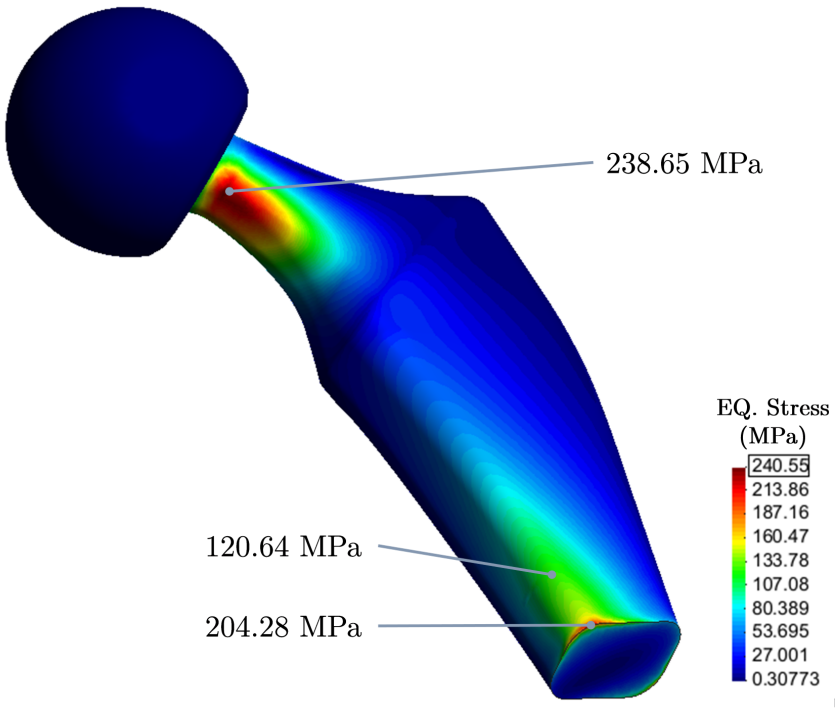

Figure 7.18: The von Mises equivalent stress distribution for the 3.55 femoral neck-head ratio model under the simulation setup defined by the ASTM F 2996-13 standard at the neck and potting levels for a stem of 163.0 mm of length

The maximum equivalent stresses are registered at the femoral neck, near the femoral head-stem interface, whereas at the potting level the maximum stress is only 120.64 MPa (Fig. 7.18). The maximum equivalent stress of 238.65 MPa registered in the present design is below the 510 MPa of fatigue stress for Ti-6Al-4V (Table 7.1). For a femoral head-neck ratio of 3.55, the stem design has a safety factor of approximately 2.14. A safety factor superior to 2.0 is desirable since the femoral stem may be subjected to physiological loads that can exceed the loading conditions defined by the ISO and ASTM standards. The femoral stem is further validated with more physiologically plausible loading conditions, in order to guarantee that the stem is correctly dimensioned.

7.8.2 Femoral Stem Validation under Physiological Loading Conditions

As mentioned in the previous section, the loading conditions defined by the ISO and ASTM standards may not correspond to the critical conditions found during Human locomotion (Bergmann et al., 2010). In this section, this possibility is further investigated. One also

aims to compare the stress distributions observed on the intact femur and on the implanted femur, in order to assess the amount of strain shielding in the proximal femur caused by the implant.

Boundary Conditions

The loads at the hip joint may reach several times the subject's body weight (BW). To evaluate the performance of the implant under more physiologically plausible conditions. Heller et al. (2005) proposed a simplified muscle model for a THR *typical patient* for the simulation of both walking and stair climbing activities. The hip contact forces using this simplified model differed from the in-vivo model by approximately 7.0% during walking and 10% during stair climbing. Fig. 7.19 depicts the muscle model composed by the abductor muscles, the iliotibial tract, the tensor fasciae latae, the vastus medialis, the vastus lateralis and the intersegmental resultant.

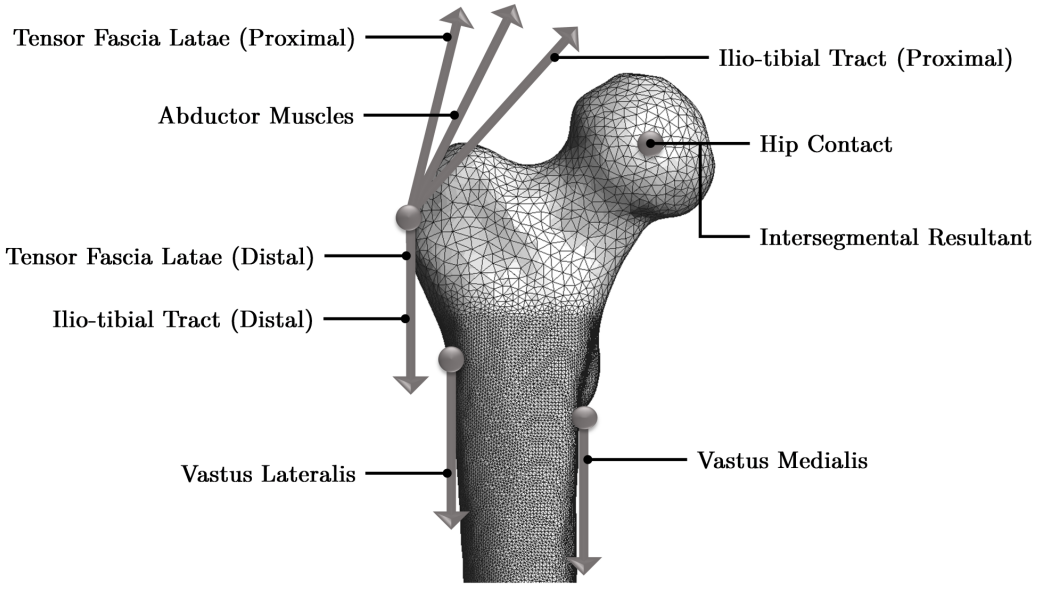

Figure 7.19: The simplified muscle model proposed by Heller et al. (2005) to simulate Human walking and stair climbing

The simplified muscle model takes into consideration both the reaction forces and the muscle forces applied to the Human hip (Fig. 7.19). The intersegmental resultant force applied at the hip joint centre represents the load applied to the hip by the weight of the upper body. The simplified model is used to predict the behaviour of the implant after

THR. The relations between the muscle forces and the subject's BW, derived by Heller et al. (2005), are also used to compute the muscle forces for an theoretical patient with 80 Kg (784.8 N). The loading conditions, for both walking and stair climbing are summarized in Table 7.2 and Table 7.3. The FE simulation is carried considering the whole femur, since the simulation of the proximal femur instead of the whole femur was recently correlated with inaccurate estimates of both stresses and strains along the femur (Speirs et al., 2007a). The femoral head, hip stem, cortical bone, trabecular bone and ceramic femoral head were modelled as linear elastic, isotropic and homogeneous materials. All model parts were considered perfectly bounded. Fixed boundary conditions were also applied to the centre of the knee, as well as to the medial and lateral condyles, in order to avoid translations and rotations of the model.

Table 7.2: Loading conditons under Walking

	Walking, vector forces (N)		
	x	y	z
Hip Contact	423.8	-257.4	-1798.8
Intersegmental Resultant	63.6	-100.5	-613.7
Abductor Muscles	-455.2	33.7	678.9
Tensor Fascia Latae (Proximal)	-56.5	91.0	103.6
Tensor Fascia Latae (Distal)	3.9	-5.5	-149.1
Vastus Lateralis	7.1	145.2	-729.1

Table 7.3: Loading conditons under Stair Climbing

	Stair Climbing, vector forces (N)		
	x	y	z
Hip Contact	465.4	-475.6	-1854.5
Intersegmental Resultant	102.0	-219.7	-550.1
Abductor Muscles	-550.1	226.0	666.3
Ilio-tibial Tract (Proximal)	-82.4	23.5	100.5
Ilio-tibial Tract (Distal)	3.9	-6.3	-131.8
Tensor Fascia Latae (Proximal)	-24.3	38.5	22.8
Tensor Fascia Latae (Distal)	1.6	-2.4	-51.0
Vastus Lateralis	17.3	175.8	-1060.3
Vastus Medialis	69.1	310.8	-2096.2

Finite Element Model and Mechanical Properties

In THR the adequate loading of the proximal femur is critical. The existence of bone stress/strain shielding after THR commonly causes the reduction of the bone density around the femoral stem, especially on the proximal medial region (calcar region)

(Karachalios et al., 2004). Inadequate bone loading may induce massive bone resorption around the femoral stem, and thus cause implant instability and, ultimately, lead to implant loosening. To study the impact of implantation in the stress distribution along the proximal region, a mesh refinement between the lesser trochanter and level slightly below the femoral stem tip level was applied to the intact and implanted femurs. Since the neck is the critical region of the implant, a mesh refinement was also added in this region. Considering the convergence analysis performed in section 7.8.1, the element size in both mesh refinement regions was set to 1.0 mm in the refinement region.

Similarly to Chapters 5 and 6 the CAD model was discretized with a voxel size of 0.5 mm and a 10-nodes tetrahedral FE mesh was generated with Simpleware ScanIP $+FE$ module. The software produces large non-optimized meshes at the mesh refinement region, where the inner mesh edge size is basically kept constant throughout the entire refinement volume. To overcome this limitation linear tetrahedral meshes were generated instead, and the mesh simplification algorithm *Simptets* was used to reduce the mesh size. With emphSimptets the inner mesh was simplified and the surface mesh was left unchanged. After simplification, the quadratic nodes were added. For instance, for the intact femur, the initial linear mesh was composed by 73728 modes and 365052 elements. With FE mesh simplification, the FE mesh was reduced to 42417 nodes and 175875 elements. Likewise, the initial mesh implanted femur comprised 98051 nodes and 494399 linear tetrahedral elements, and after simplification, the number of nodes and elements was reduced to 50961 nodes and 229086 elements, respectively. The final meshes of intact femur is composed by 282461 nodes and 175857 elements, whereas the final mesh of the implanted femur has 353110 nodes and 229086 elements (Fig. 7.20 (a) and (b)).

Results

In section 7.8.1 a safety factor of approximately 2.14 was determined to the femoral neck region, according to the standard ASTM F 2996-13. Similarly to the ASTM, the critical region of the femoral stem was the neck, near the Morse taper between the femoral stem and femoral head (Fig. 7.21). However, under more physiological loading conditions, the von Mises equivalent stresses at this critical region were higher than in the ASTM setup. For walking, the maximum equivalent stress was approximately 400 MPa, whereas for stair climbing a maximum equivalent stress above the fatigue limit of the Ti-6Al-4V (533

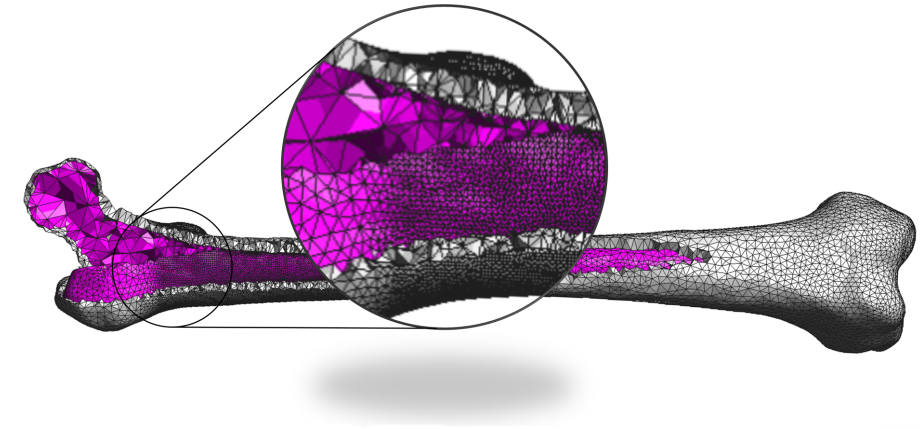

(a)

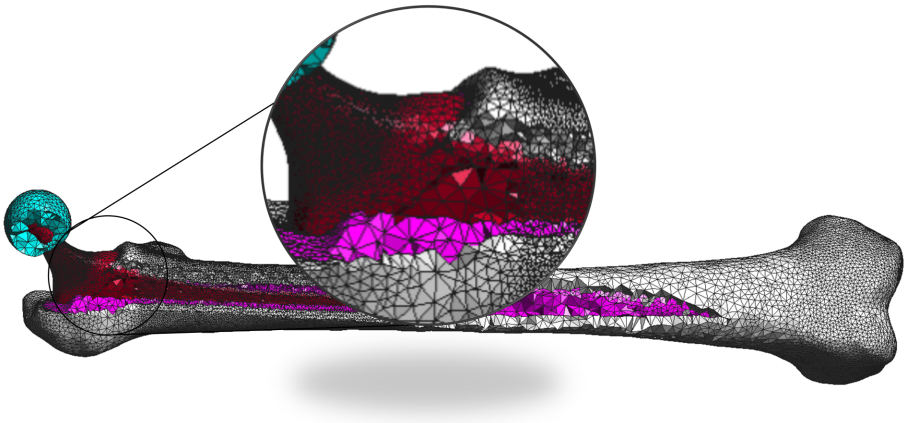

(b)

Figure 7.20: Finite Element Meshes of the intact bone in (a) and of the implanted femur in (b)

MPa) was observed. Therefore, the validation of the femoral stem regarding the boundary conditions defined by the ASTM F 2996-13 may not be sufficient to guarantee the safety of the femoral stem after implantation. From the results obtained, the stem should be optimized considering the patient's BW and the expected loading at the hip joint under stair climbing.

Regarding intact femur, Fig. 7.22 shows that under walking it is observed that the medial side of the bone is mainly under compression, and the lateral side under tension (solid lines). The maximum principal strains on the lateral side reached 1390 $\mu strains$, whereas the minimum principal strain on the medial side were approximately -2050 $\mu strains$. After stem insertion, a reduction on the strain deformation on both medial and lateral sides is observed. The strain fields in the intact and implanted femur are similar, but

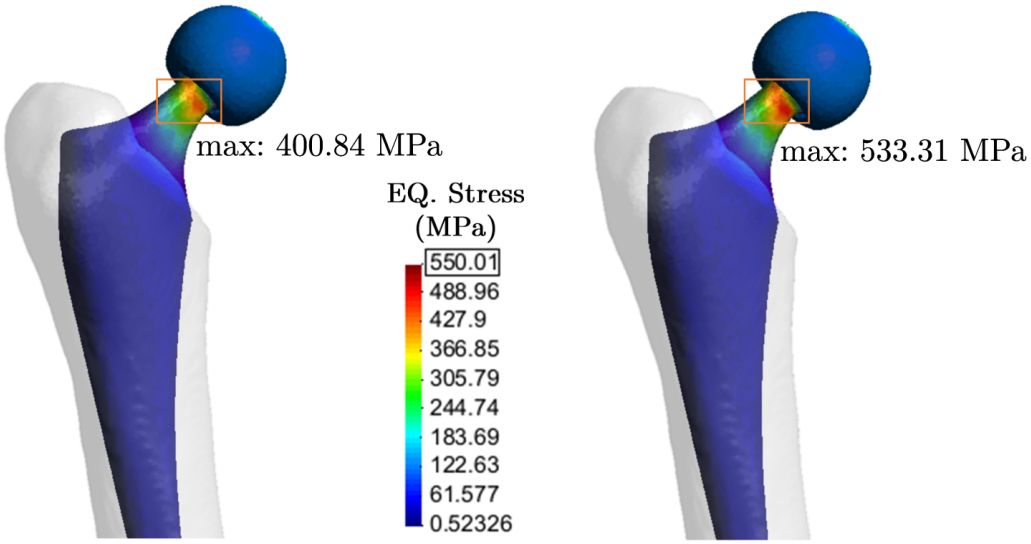

Figure 7.21: Equivalent stress concentration at the femoral stem under walking (on the left) and stair climbing (on the right) loading conditions

the maximum and minimum principal strains are approximately one-fourth and one-half of the values observed for the intact femur, respectively. The implant strain shielding propagates along the diaphysis of the femur, both medially and laterally. The maximum first principal strain on the lateral side is reduced to approximately 380 $\mu strains$, whereas the peak third principal strain is only -852 $\mu strains$ on the medial side (Fig. 7.22). Considering only the strain distribution along the implanted region (between the 250 mm to 350 mm), the maximum principal strain was reduced (in average) to about 22%, and the minimum principal strain to approximately 27% of the values observed for the intact femur.

In the antero-posterior direction, the femur is mainly bended posteriorly. Contrarily to the observations for the medio-lateral direction, strain shielding was more visible on the proximal anterior and proximal aspects of the implanted femur (Fig. 7.23). In the sagittal plane, the proximal anterior aspect of the femur is mainly loaded in compression, and the proximal posterior aspect in tension. For the proximal aspect the maximum principal strain on the posterior surface of the femur was 676 $\mu strains$, and the minimum principal strain at the anterior surface of the femur was approximately -1128 $\mu strains$. Below the lesser trochanter there is an inversion on this loading pattern, and the anterior

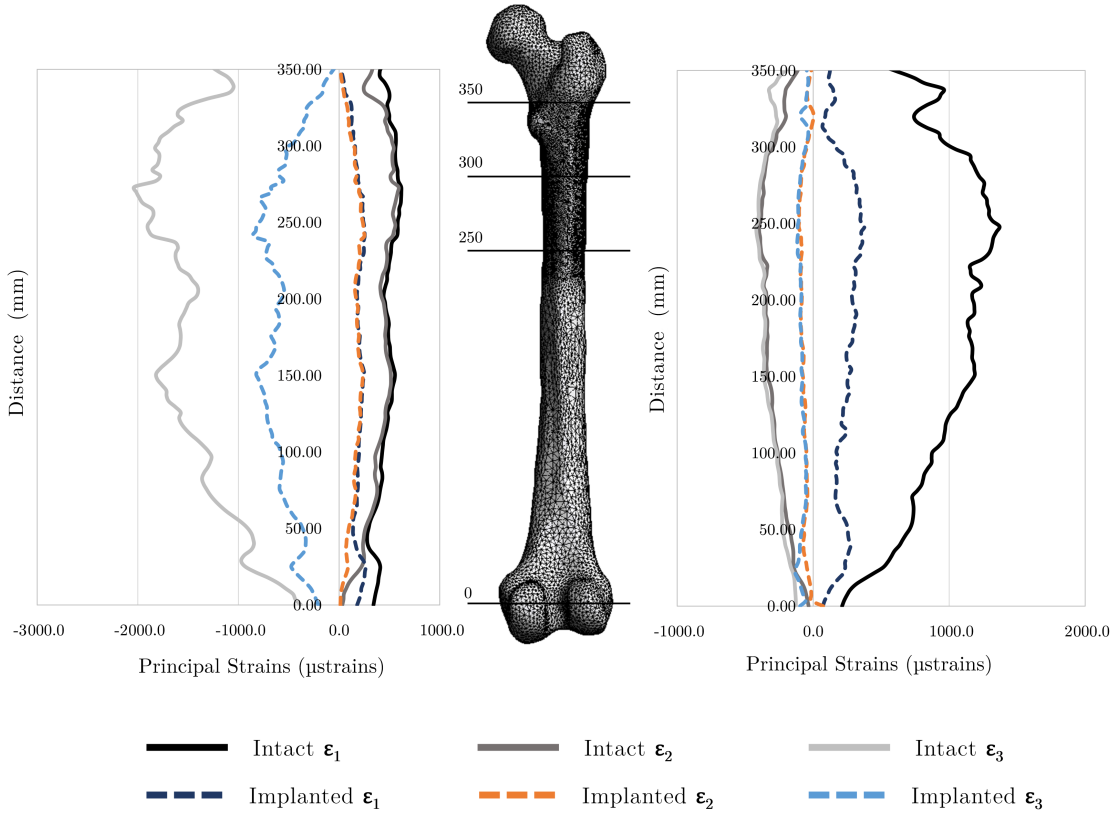

Figure 7.22: Principal lateral and medial strains under walking for the intact (solid lines) and implanted (dashed lines) femurs

aspect of the femur becomes loaded mainly in tension, while the posterior aspect of the femur is in compression. For the diaphyseal region of the femur, the minimum principal strains reach approximately -1251 $\mu strains$ on the posterior region of the intact femur, whereas the maximum anterior principal strain along the femur diaphysis surface was only 388 $\mu strains$. In the implanted femur, the proximal maximum first and third principal strains were reduced to 264 $\mu strains$ (posterior) and to -405 $\mu strains$ (anterior), whereas in the distal femur the maximum third and first principal strains were -1209 $\mu strains$ (posterior) and 383 $\mu strains$ (anterior), respectively. Comparing the intact and implanted proximal femurs, the average maximum and minimum principal strains on the posterior and anterior aspects were reduced to approximately 52% (posterior first principal strain) and 35% (anterior third principal strain) of their original values, respectively.

Under stair climbing the maximum and minimum principal strains along the intact femur were larger when compared with the strain profiles during walking. On the lateral

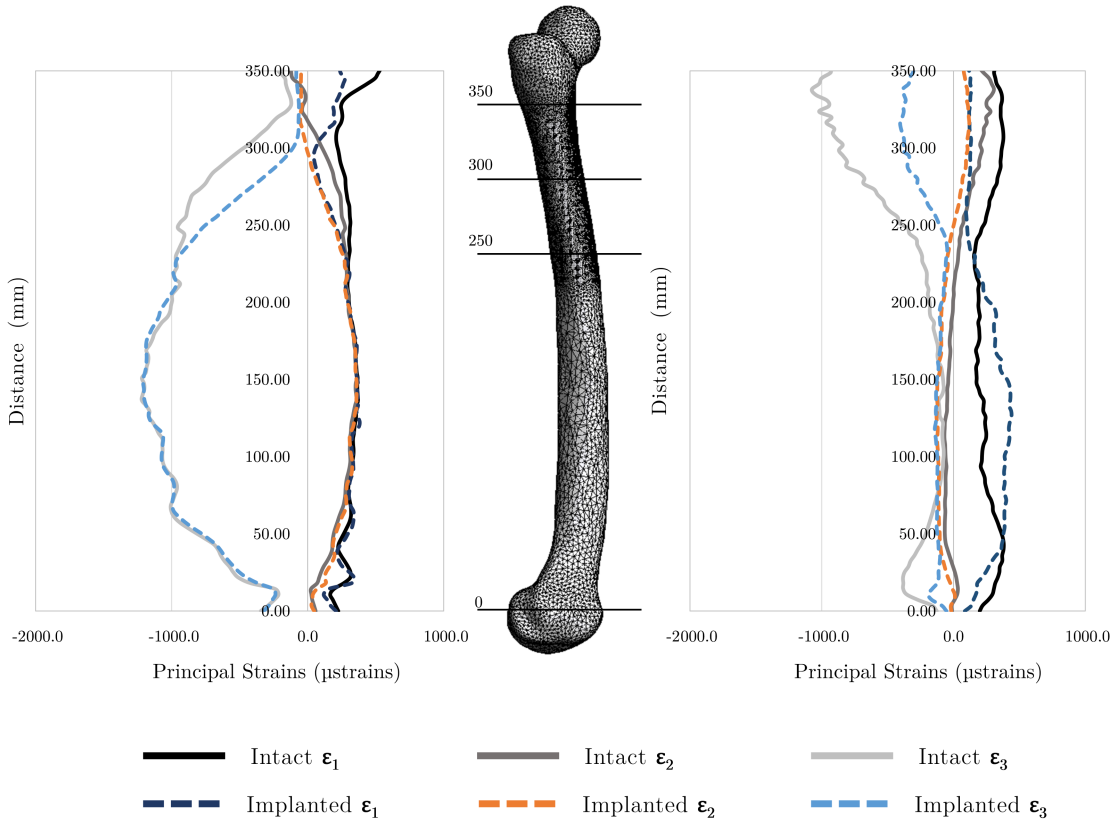

Figure 7.23: Anterior and posterior principal strains during walking for the intact and implanted femurs

side the maximum principal strains reached 1408 $\mu strains$ on the lateral side, whereas the third principal strain was about -2921 $\mu strains$ on the medial side (Fig. 7.24). In the antero-posterior direction, the maximum principal strain in the anterior aspect of the intact femur was 638 $\mu strains$, and the minimum principal strain along the posterior aspect of the femur was -2255 $\mu strains$ (Fig. 7.25). By adding the vastus medialis, the bending tendency of the intact femur along the coronal and sagittal planes is more pronounced. In agreement with the observations for walking, implant insertion causes a generalized reduction of the strain magnitude along the medio-lateral aspect of the femur (Fig. 7.24). The peak of the first principal strains was reduced to 463 $\mu strains$ and 536 $\mu strains$ on the lateral and anterior aspects, and the minimum principal strains to -2255 $\mu strains$ and -2054 $\mu strains$ on the medial and posterior aspects of the femur, respectively. For stair climbing, the average value of the first principal strain along the lateral side was only 22% of the strain value observed for the intact femur. On the medial

side, the average value of the third principal strain was also reduced to 33% of its original value. Along the anterior and posterior profiles, the first principal strain was reduced in average about 57% on the anterior side, and the third principal strain in 54% on the posterior aspect of the proximal implanted femur.

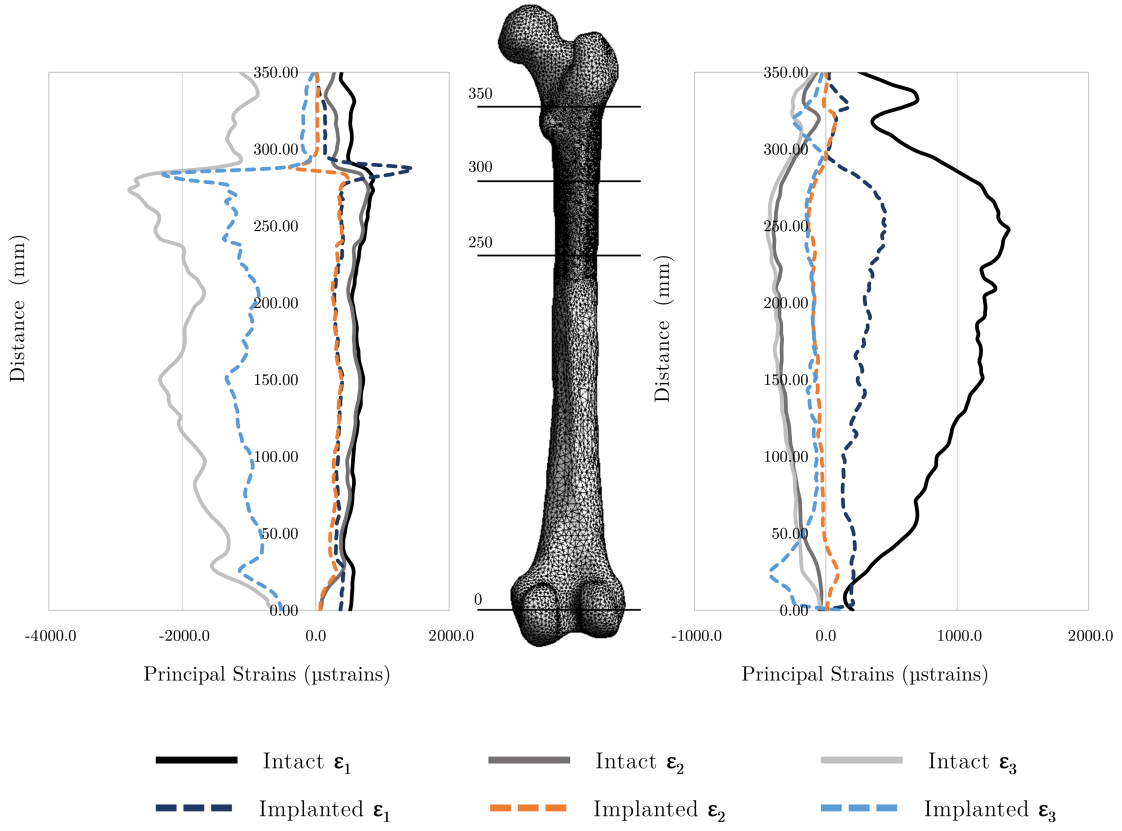

Figure 7.24: Principal lateral and medial strains along the femur during stair climbing in the intact and implanted femurs

In an attempt to optimize the load transfer to the proximal femur, several changes to the initial geometry were analysed, namely, increasing the diameter of the femoral neck, reduction of the antero-posterior thickness of the stem, and lateral flare reduction (reduction of the medio-lateral cross-section above the lesser trochanter).

Under static loading conditions, increasing the diameter of the femoral neck increases the mechanical safety of the implant after THR. For a neck diameter of 11.0 mm, the maximum equivalent von Mises stress for walking is 323.14 MPa, and 448.60 MPa for stair climbing, rather than the 533.31 MPa observed for the 9.0 mm; whereas for a femoral neck of 12.0 mm the maximum equivalent stress drops to 259.60 MPa for walking and to

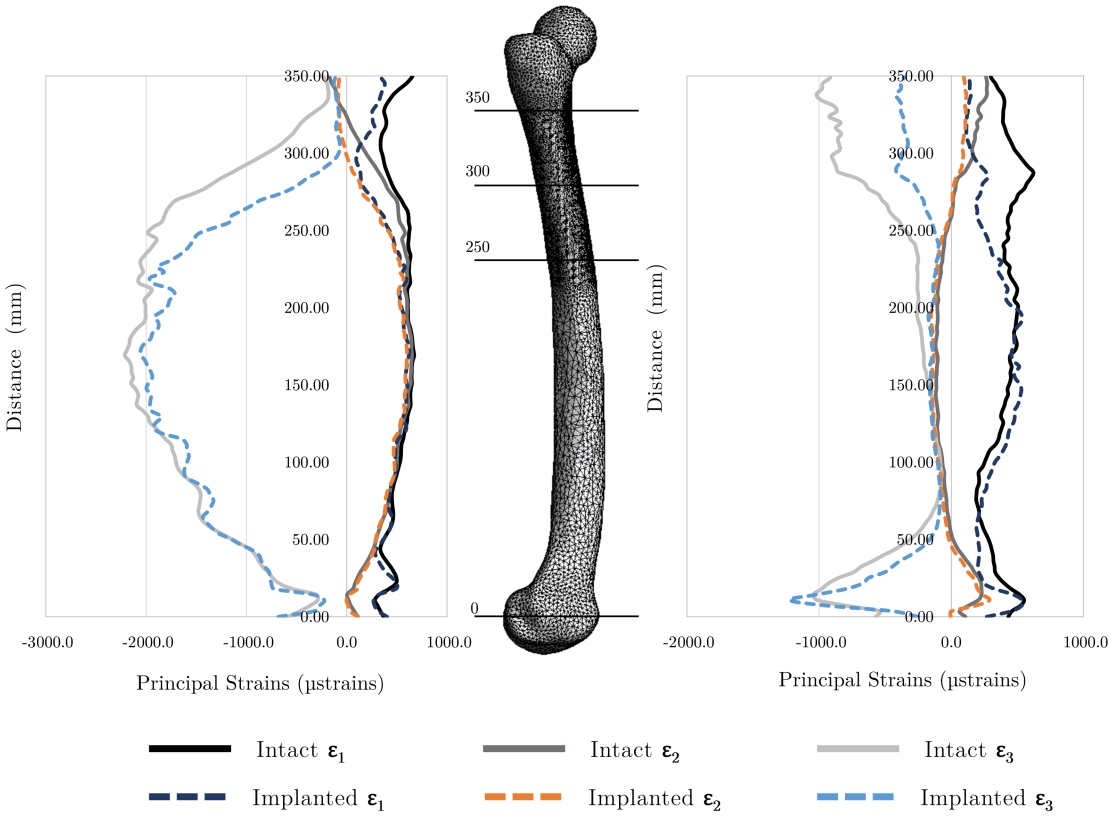

Figure 7.25: Principal anterior and posterior strains during stair climbing in the intact and implanted femurs

376.32 MPa for stair climbing, respectively. Regarding the strain fields along the proximal femur, increasing the neck diameter causes an overall reduction of the strain shielding effect between 2% and 5% along the lateral, medial, anterior, and posterior profiles (considering both walking and stair climbing). Similar changes on the average strain values were obtained varying both the the antero-posterior thickness of the stem, and the medio-lateral cross-section above the lesser trochanter. A femoral stem with a smaller medio-lateral flare, a neck with a diameter of 12.0 mm, and with 15.0 mm of proximal antero-posterior thickness produced the most interesting results. For walking, this stem produced a 4% increase on the average first and third principal strain values along the proximal medial and lateral directions, respectively. A 6% increase was observed on the first principal strain along anterior aspect of the proximal femur, and a 2% increase was observed along the posterior aspect of the femur. For stair climbing, an overall (average) decrease of 6% on the proximal strain shielding along all four directions was observed.

Discussion

In this section the mechanical behaviour of the hip stem design proposed in section 7.7 is evaluated through FEA according to the ASTM F 2996-13, and physiologically more plausible loading conditions, as proposed by Heller et al. (2005). The simplified muscle model is mainly composed by the hip reaction force, the abductor muscles, the iliotibial tract, the tensor fasciae latae, the vastus medialis, the vastus lateralis, and the intersegmental resultant that represents the loading on the hip caused by the weight of the upper body. The simplified muscle model aims to reflect more accurately the loading conditions that the hip stem may experience during function, and in conjunction with the ASTM F 2996-13 standard may provide an additional criterion for the validation of the implant geometry.

The simulation of the femoral stem under physiological loading conditions showed that the implant may fail due to fatigue during stair climbing. The results show that the boundary conditions defined by the ASTM F 2996-13 standard may not represent the most extreme loading conditions that the hip stem can experience after THR. These findings are in agreement with Bergmann et al. (2010), that proposed a new and simplified set of boundary conditions validation of the femoral stem geometry.

The equivalent stresses observed at the proximal neck during walking are almost twice when compared with the equivalent stresses caused by the 2300N defined in the ASTM F 2996-13 standard (Fig. 7.18 and 7.21). According to these results, stair climbing is more critical than walking, and the implant will more likely to fail in the neck region. Similar observations were reported by Stolk et al. (2002) and Kassi et al. (2005), which also concluded that stair climbing is more critical to the femoral stem than walking. During the design phase, these loading conditions may provide more insights about the real loads that are applied to the femoral stem, aiding in the development of more safe solutions. In this work, the behaviour of the femoral stem was evaluated only under static loading conditions. However, the behaviour of the implant under dynamic loading conditions should not be neglected. Senalp et al. (2007) concluded that the safety factors may differ under static and dynamic loading conditions; it was observed a reduction in the stem safety factor under dynamic loading, and that stem shapes that are safer against fatigue under static conditions may fail under dynamic loading conditions. Therefore, after THR,

the peak loads applied to the hip stem may be even greater than the loads considered during stair climbing.

Under physiological boundary conditions, the full femur was simulated instead of simulating only the proximal part of the femur. The simulation of the proximal femur was recently associated with unrealistic stress distributions by several authors (Taylor et al., 1996; Duda et al., 1998; Speirs et al., 2007a). In a FE study, Taylor et al. (1996) obtained a medial displacement of the femoral head between 13.0 mm to 15.3 mm, whereas the vertical displacement varied between 5.0 mm to 5.4 mm (absolute values). However, in a radiological study, the average medial deflection of the femoral head was only 1.25 mm and the average vertical deflection was about 1.50 mm; despite the FE results, it was concluded that the femur is loaded primarily under compression rather than in flexion. In this work, a vertical displacement of 1.69 mm and a medial displacement of 6.78 mm were observed for walking, and a vertical deflection of 1.96 mm and a medial displacement of 7.63 mm were observed for stair climbing. This indicates that the femur is mainly bended along the coronal plane rather than compressed vertically.

The larger coronal and sagittal bending observed may be a consequence of leaving the femoral head unconstrained. Physiologically, the femoral head is restrained posteriorly and medially by the acetabulum, hence the boundary conditions applied may be a simplification of the reality. Speirs et al. (2007a) found that, under such simplified boundary conditionse large posterior and medial deflections of the hip joint centre are expected; to avoid this, the restriction of the movement of the femoral head along a line connection the centre of the femoral head and the centre of the knee was proposed. These boundary conditions may be more approximate to describe the physiological restrictions imposed on the movement of the femoral head.

Nevertheless, despite these simplifications, the results obtained correlate well with other studies found in the literature. During both walking and stair climbing, the medial side of the femur is mainly under compression, whereas the lateral side is mainly loaded in tension. The compressive strains on the medial side were higher than the tensile strains observed on the lateral side. Similar observations were described by other authors (Cristofolini et al., 1995; Taylor et al., 1996; Duda et al., 1998; Speirs et al., 2007a). In an ex-vivo study, Cristofolini et al. (1995) analysed the strain pattern along the femur considering ten muscle groups from the proximal and distal femur. In the proximal

diaphyseal region of the femur, a first principal strain of approximately 1000 $\mu strains$ and a third principal strain of approximately -1500 $\mu strains$ were observed on the lateral and medial aspects of the femur, respectively. In addition, Duda et al. (1998) observed, in the proximal femur, tensile strains slightly above the 1000 $\mu strains$ for the lateral side, and compressive strains below -2000 $\mu strains$ for the medial side of the femur under physiological loading conditions.

In the anterior aspect of the femur, an inversion from compression to tension around the 250 mm was observed (Fig. 7.23 and Fig. 7.25). The same inversion was also previously observed by Cristofolini et al. (1995), nevertheless the tensile strains at the mid-shaft were approximately 1500 $\mu strains$, whereas in the proposed model the tensile strains were no more than 500 $\mu strains$. In the FE study conducted by Taylor et al. (1996) anterior strains of approximately 500 $\mu strains$ were obtained, which correlate well with our observations. The posterior proximal intact and implanted femurs are mainly under tension rather than compression. Similar observations were obtained by Aamodt et al. (2001) in an ex-vivo study aiming the characterization of the strain changes in the proximal femur due to the insertion of an uncemented femoral stem. In the diaphyseal region, compressive posterior strains reached -1209 $\mu strains$ and -2255 $\mu strains$ for both walking and stair climbing (Fig. 7.23 and Fig. 7.25); for the same region Cristofolini et al. (1995) obtained approximately -1700 $\mu strains$. The strain fields obtained for the intact femur also correlate well with the results obtained by Speirs et al. (2007a) for both walking and stair climbing. According to the later authors, large posterior and medial deflections of the hip joint centre are expected under simplified boundary conditions.

In both walking and stair climbing there was a marked reduction on the strain fields mainly along the proximal femur. The reduction of the strain deformation along the proximal femur after THR is widely documented in the literature. In a cadaveric study conducted by Finlay et al. (1991), it was observed that the strain levels at the proximal medial surface of the femur correspond only to approximately 40% of the strain values observed in the intact femur after the implantation of an uncemented femoral stem. In an ex-vivo study, Aamodt et al. (2001) compared the strain fields across the proximal femur for both anatomical and customized stems. It was observed a reduction of 90% on principal compressive strain for anatomical stems and a reduction of 67% for customized stems; it was concluded that customized femoral stems produce more physiological load

transfer when compared with standard femoral stems. With similar loading conditions to this work, Speirs et al. (2007b) analysed the influence of short-stemmed hip implants in strain distributions along the proximal femur. It was observed a 95% reduction on the third principal strain on the medial side, and a 36% reduction in the first principal strain on the lateral side of the implanted femur for both walking and stair climbing. More recently, the proximal strain shielding ranging from 52% to 66% on the medial side and between 59% to 72% for the lateral side was reported for commercially available femoral stems (Bieger et al., 2012).

The strain shielding produced by the proposed femoral stem along the proximal femur ranged from 48% and 78%. On the medial side, strain shielding was 73% and 67%, whereas on the lateral side, strain shielding was 78% for walking and stair climbing, respectively. The stress shielding seems to be more pronounced in the medio-lateral direction. Lengsfeld et al. (2005) combined subject-specific FE models and in-vivo CT bone density data to predict bone remodelling after THR; it was found that the largest remodelling stimulus were found in in Gruen zones I, V and VII. Significant strain density energy reductions of 43% for Gruen zone VII (proximal medial femur) and of 32% in Gruen zone I (proximal lateral femur) were expected after implantation. In a clinical and radiological analysis of 27 patients with rheumatoid arthritis treated with cementless stems, Carl et al. (2011) observed the presence of stress shielding and bone resorption in Gruen zones I and VII in 96% of the femoral stems. The largest strain differences between the intact and implanted femurs were observed on the lateral side. Pettersen et al. (2009) concluded that the FE models significantly overestimate the stress shielding on the lateral side of the femur when compared with strains determined experimentally.

In the anterior and posterior aspects of the femur, strain shielding is mainly observed at the metaphyseal region of the femur, and strain values tend to their original values as we move distally. The same was not observed on the medial and lateral sides, where the strain shielding propagate along the whole femur, and both principal tensile and compressive strains are globally reduced. The return of the strain fields to more physiological levels in the diaphyseal and distal regions of the femur was observed by several authors for both medio-lateral and antero-posterior regions (Aamodt et al., 2001; Speirs et al., 2007a). The proposed customized stem failed to restore the cortical strains closer to the physiological levels along the proximal femur as previously observed (Aamodt et al., 2001). The results

obtained show the need to reduce the stiffness of the implant's stem, particularly along its medio-lateral direction.

Several changes to the initial geometry of the stem were tested, in order to reduce the strain shielding along the proximal femur. The most interesting results were obtained with a femoral stem with a neck diameter of 12.0 mm, 15.0 mm of proximal antero-posterior thickness, and with a small lateral flare. The increase of the average strain levels along the proximal femur varied between 2% and 6% for walking, and in 6% for stair climbing. The neck diameter of 12.0 mm allows a maximum leg flexion angle of approximately 130 degrees, without component-to-component impingement. Larger neck diameters effectively reduce the achievable ROM after THR. However, this reduction may not be significant in practice, given that the amount of leg flexion needed for performing daily routine does not exceed 125 degrees (Magee, 2014). Therefore, the femoral neck diameter may be increased even further to guarantee implant safety in both static and dynamic loading conditions, without compromising the achievable ROM after THR.

Regarding the stem geometry, the proposed femoral stem design has a varying rectangular cross-section with a medio-lateral length defined by the size of the medullary canal. The stem was designed to enhance the medio-lateral fit, and fill of the medullary canal. Improving the proximal loading, especially along the proximal medial region of the femur, is important, since this is the region were the most extensive bone loss is expected to occur due to implant stress shielding (Kerner et al., 1999). A lateral flare was added to the stem, both to maximize the stem fit to the proximal femoral region and to maximize lateral load transfer. The results obtained failed to justify the usefulness of this geometrical feature, as a way to improve lateral load transfer. The lateral extension of the stem is thought to provide additional stability to the implant after THR. Implants with wider medio-lateral cross-section are known to provide better torsional stability to the femoral stem. However, this increase in implant stability seems to be accompanied with a concomitant increase in stem stiffness. Reducing the medio-lateral length of the stem may reduce implant stiffness, at a cost of compromising the fit to the target intramedullary canal. The results show that a balance between implant fit and the amount of proximal stress shielding must be obtained.

7.9 Summary

In this chapter the necessary procedures for the design of a new Total Hip Replacement system are described. Recovering the standard anatomical position is important to guarantee the consistency on the determination of the relevant planes, axes and landmarks for Total Hip Replacement planning. In this work, a modular replacement system was considered. A modular hemispherical acetabular component that avoids all sharp features in the interlocking system was designed to replace the acetabulum. The sharp features in the interlocking system is seen as the main cause for liner breakage during function. On the femoral side, a hip stem that optimizes the medio-lateral fill of the medullary canal was designed. The stem geometry was validated through the ASTM F 2996-13, which defines the loading and boundary conditions, and mesh convergence criteria to replicate the ISO 7206-Implants for surgery-Partial and total hip joint prosthesis testing with FEA. It was found that the loading conditions specified by the standards may not reflect the critical loading that the implant may experience in practice. The implant was also validated using the simplified model proposed by Heller et al. (2005) regarding the level of strain shielding produced along the proximal femur. The initial geometry fails to produce more physiological strain fields along the proximal femur, when compared to commercially available stems. In an attempt to optimize the load transfer to the proximal femur, several variations to the initial geometry of the stem were tested. Residual improvement to the overall performance of the implant were obtained. Therefore, the femoral stem needs to be further optimized, in order to guarantee a more physiological strain distribution along the implanted femur.

This page was intentionally left blank

Chapter 8

Conclusions and Future Work

In this chapter the main conclusions of the present thesis are summarized, as well as some proposals for future developments.

This page was intentionally left blank

8.1 Conclusions

A new pipeline for accurate musculo-skeletal model extraction from medical image data was proposed, and its usage exemplified on the development of several custom-made implants from medical image data. Moreover, the accurate bone segmentation of bone from CT imaging, together with the most advanced CAD-CAM-CAE technologies, may allow the development of fully optimized implants to the specificities of the target patient. Highly customized implants may optimize the overall fit of the implant to the target anatomy, when compared with standard implants, especially in people that deviate from the anatomical standards. In custom implant modelling from medical image data, several steps can be identified, namely:

- Medical Image Processing and Artifact Removal;
- Accurate Image Segmentation and 3D Surface Model Generation;
- Geometrical Customization based on CAD and CAE techniques;
- FEA Optimization of the Implant Geometry;
- Manufacturing using CAD-CAM Technologies.

In this pipeline, multiple potential sources of domain inaccuracies can be identified. Geometrical inaccuracies may emerge during the image acquisition, image processing, image segmentation and surface meshing processes. The techniques applied in each step must be chosen in order to avoid the deterioration of the underlying information. Medical imaging techniques are extremely important in modern medicine, not only as a complementary tool for diagnosis, but also in the development of accurate biomechanical models from living tissues. Computed Tomography is probably the most successful medical imaging technique existing today, and is particularly suitable for imaging high density structures such as the Human skeleton. The major limitations associated with this technique are the image artifacts, which may compromise the perceivable image quality, and the system's spatial resolution that can be modelled by the system's MTF. The accuracy of the final model may be also affected by the image processing, image segmentation and surface meshing techniques used to produce a 3D representation of the target ROI.

In **Chapter 4** the limitations imposed by the image acquisition process, image processing and segmentation variability were addressed. A new two-step segmentation pipeline was proposed. In the (first) pre-segmentation step the user must provide a good approximation to the target ROI, applying any suitable segmentation technique(s). In a second step, a standardized and fully automatic set of steps are applied to refine the pre-segmentation. The refinement steps encompasses image deconvolution, cropping, interpolation, and level-set segmentation. The proposed methodology produces highly accurate estimates of the target geometry with a maximum average deviation of 0.159 mm for noise-free images and 0.178 mm for images corrupted with AWGN.

The results show that the surface meshes extracted directly from a high-resolution 3D point cloud derived directly from the interpolated data produce more accurate estimates of the target ROI. For these meshes, the model accuracy is mostly affected by the image acquisition and reconstruction, rather than by the image segmentation and surface meshing processes. This workflow also reduces the number of processing steps towards a volumetric representation of the target domain, when compared with the standard workflow that produces surface meshes from the voxelized data. In addition, the results obtained also show that the limiting spatial resolution of the CT machine can be accurately determined using simple objects that can be imaged simultaneously with the patient. From the three phantom objects, the brass alloy wire phantom with 0.10 mm of diameter produced the most accurate estimates of the PSF when compared with the CATPHAN 528. Hence, the direct measures provide slightly more accurate estimates of the system's Point Spread Function, when compared with indirect measures based on the Edge Spread Function.

The accurate 3D representation of the target geometry is crucial to guarantee the overall fit of the custom implant to the target anatomy. The geometrical modelling of the custom implants must consider the specific anatomical features of each patient, and the best practices and project guidelines found in the literature. The proposed segmentation pipeline was employed in the development of three customized implants that cover both trauma, cranio-maxillofacial, and orthopaedic applications. The guidelines for modelling custom tibial trauma nailing systems, custom mandibular reconstructions, and THR systems were developed in the subsequent chapters.

In **Chapter 5** a customized tibial nailing system was developed. The results obtained for the tibial nailing system corroborate the hypothesis that smaller diameter nails in

conjunction with larger diameter interlocking screws may have an enhanced fatigue strength. No signs of implant failure on the tibial nail and interlocking system were observed for both proximal, medial, and distal fractures. The proximal interlocking system composed by two oblique screws and two medio-lateral screws may avoid the breakage of proximal oblique screws, as often observed in commercially available implants. It can be concluded that two distal screws placed in the medio-lateral and antero-posterior direction are less prone to fatigue fracture than the antero-posterior and medio-lateral configuration.

In **Chapter 6** the reconstruction of a major mandibular fragment was addressed. In this chapter a customized surgical guide to optimize bone harvesting at the donor site and a tailor-made mandibular endoprosthesis were proposed. The oral rehabilitation in a second stage surgery should be considered during the implant modelling phase, in order to guarantee the proper chewing function after implantation. It was concluded that the mandibular endoprosthesis allows the recovery of the displacement and stress patterns along the two mandibular segments; as commonly observed in intact mandibles. In addition, the strain levels observed at the bone-implant interface may be compatible with bone ingrowth and implant osseointegration. Therefore, a mandibular endoprosthesis may be a reliable alternative to other prosthetic mandibular reconstruction approaches.

In **Chapter 7** a custom-made Total Hip Replacement system was designed. A modular hemispherical acetabular component that avoids all sharp features along the interlocking system was designed to replace the acetabulum. On the femoral side, a hip stem that optimizes the medio-lateral fill of the medullary canal was designed. Regarding implant validation and optimization, it can be concluded that boundary conditions imposed by the ASTM F 2996-13 and ISO 7206 standards may not reflect the critical loadings that the implant may experience in practice. Other criteria may be necessary to guarantee the proper functioning of the implant after implantation. Under more physiological loading conditions, the initial geometry fails to produce enhanced strain patterns along the proximal femur, when compared to commercially available stems.

The three case studies presented encompass three distinct medical fields, namely trauma and fracture management, cranio-maxillo-facial reconstruction, and orthopaedics. This shows both the potential and flexibility of the proposed customization pipeline. Many other implants may be developed following the guidelines proposed in this thesis. The new segmentation pipeline may be applied in the accurate segmentation of other structures,

such as muscles, to construct highly accurate biomechanical models from medical image data. In addition, any of the customization protocols proposed in thesis may be used, only in implant development, but also as a standard procedure pre-operative planning, replacing the traditional pre-operative planning methods.

8.2 Future Work

In this section one presents some proposals for future developments of the current work.

The segmentation pipeline described in **Chapter 4** was implemented in an image-based (2D) approach. The extension of the segmentation refinement step to the third dimension may improve the geometrical detail of the Point Cloud model near the extremities of bones. According to the results, the segmentation pipeline shows some dependency on image contrast. One possible solution for this problem is the inclusion of the information about the HU attenuation profile normal to the level-set curve into the equation governing curve evolution. This information may contribute not only to the overall accuracy of the segmentation refinement, especially for lower resolution Datasets, but also to reduce the dependency on segmentation initialization (especially in the presence of object under-segmentation).

Regarding the tibial nailing system proposed in **Chapter 5**, the FE results show that the implant is safe even under very critical loading conditions. Nevertheless, the full system should be machined and the prototype should be mechanically tested to further validate the results obtained with FEA.

In **Chapter 6** the mandibular endoprosthesis showed promising results regarding the stress and strain patterns along the two mandibular segments. However, there are some issues related with the geometry that should be addressed. The first is the optimization of the implant's weight. A lighter implant will mimic more accurately the missing mandibular body, possibly reducing the passive muscle force after implantation. Implant manufacturing with a functionally graded material, with an optimized metallic core with a polymeric of ceramic shell, may be an interesting solution to guarantee both the functional and aesthetic outcomes. The results obtained at the bone-implant interface should be further investigated. A more realistic FE model considering the anisotropy or transverse isotropy of the Human mandible and implant micro-motions should be implemented to

understand better the strain patterns along bone-implant interface. Additional changes in the implant may be needed to improve strain patterns along the bone-implant interface and bias osseointegration.

Finally, in **Chapter 7** a customization protocol and a THR system were proposed. The results obtained failed to validate the hypothesis that customized THR systems produce improved strain patterns along the proximal femur, when compared with standard stems. Several changes to the initial geometry were tested, however none of them produced significant improvements in the strain distributions along the proximal femur. The addition of other geometrical features to the stem, as well as other stem cross-sections, should be investigated. If all geometrical changes fail to produce more favourable strain patterns, the customization process must be revised. It would be also interesting to do mechanical testing with the proposed prototype, and compare the obtained results with commercially available stems. Mechanical tests can also be valuable to validate the results obtained with FEA, and identify possible changes to the design.

In brief, the necessary procedures for designing customizable implants are proposed and discussed throughout this thesis. New guidelines for the characterization of the image acquisition process, image processing, and image segmentation are proposed. This new image processing pipeline is then validated in the development of three examples of customized implants, for different medical applications and that satisfy specific anatomical needs. The extension of the proposed methodology to the design of other customizable implants is straightforward.

This page was intentionally left blank

References

A. Aamodt, J. Lund-Larsen, J. Eine, E. Andersen, P. Benum, and O. S. Husby, "Changes in proximal femoral strain after insertion of uncemented standard and customised femoral stems an experimental study in human femora," *Journal of Bone & Joint Surgery, British Volume*, vol. 83, no. 6, pp. 921–929, 2001.

A. Aamodt, K. A. Kvistad, E. Andersen, J. Lund-Larsen, J. Eine, P. Benum, and O. S. Husby, "Determination of the hounsfield value for ct-based design of custom femoral stems," *Journal of Bone & Joint Surgery, British Volume*, vol. 81, no. 1, pp. 143–147, 1999.

M. R. Abdul-Kadir, U. Hansen, R. Klabunde, D. Lucas, and A. Amis, "Finite element modelling of primary hip stem stability: the effect of interference fit," *Journal of biomechanics*, vol. 41, no. 3, pp. 587–594, 2008.

R. Adams and L. Bischof, "Seeded region growing," *Pattern Analysis and Machine Intelligence, IEEE Transactions on*, vol. 16, no. 6, pp. 641–647, 1994.

M. N. Ahmed, S. M. Yamany, N. Mohamed, A. A. Farag, and T. Moriarty, "A modified fuzzy c-means algorithm for bias field estimation and segmentation of mri data," *Medical Imaging, IEEE Transactions on*, vol. 21, no. 3, pp. 193–199, 2002.

M. Akbar, G. Aldinger, K. Krahmer, T. Bruckner, and P. R. Aldinger, "Custom stems for femoral deformity in patients less than 40 years of age: 70 hips followed for an average of 14 years," *Acta orthopaedica*, vol. 80, no. 4, pp. 420–425, 2009.

A. Akhondi-Asl and S. K. Warfield, "A tutorial introduction to staple," 2004.

T. Albrektsson, P.-I. Brånemark, H.-A. Hansson, and J. Lindström, "Osseointegrated titanium implants: requirements for ensuring a long-lasting, direct bone-to-implant anchorage in man," *Acta Orthopaedica*, vol. 52, no. 2, pp. 155–170, 1981.

G. Aldinger, A. Fischer, and B. Kurtz, "Computer assisted production of individual anatomic endoprostheses," *Zeitschrift fur Orthopadie und ihre Grenzgebiete*, vol. 122, no. 5, pp. 733–736, 1983.

A. Alho, J. G. Benterud, H. E. Høgevold, A. Ekeland, and K. Strømsøe, "Comparison of functional bracing and locked intramedullary nailing in the treatment of displaced tibial shaft fractures," *Clinical orthopaedics and related research*, vol. 277, pp. 243–250, 1992.

J. Y. Anderson and E. Trinkaus, "Patterns of sexual, bilateral and interpopulational variation in human femoral neck-shaft angles," *Journal of anatomy*, vol. 192, no. 02, pp. 279–285, 1998.

X. Artaechevarria, A. Munoz-Barrutia, and C. Ortiz-de Solorzano, "Combination strategies in multi-atlas image segmentation: Application to brain mr data," *Medical Imaging, IEEE Transactions on*, vol. 28, no. 8, pp. 1266–1277, 2009.

R. Ashman, S. Cowin, W. Van Buskirk, and J. Rice, "A continuous wave technique for the measurement of the elastic properties of cortical bone," *Journal of biomechanics*, vol. 17, no. 5, pp. 349–361, 1984.

Standard Practice for Finite Element Analysis (FEA) of Non-Modular Metallic Orthopaedic Hip Femoral Stems, ASTM - American Society for Testing and Materials Standard, 2013.

A. E. Athanasiou, *Orthodontic Cephalometry*. Mosby-Wolfe, 1995.

A. Au, A. Aiyangar, P. Anderson, and H. Ploeg, "Replicating interbody device subsidence with lumbar vertebrae surrogates," *Proceedings of the Institution of Mechanical Engineers, Part H: Journal of Engineering in Medicine*, vol. 225, no. 10, pp. 972–985, 2011.

P. Augat, J. Burger, S. Schorlemmer, T. Henke, M. Peraus, and L. Claes, "Shear movement at the fracture site delays healing in a diaphyseal fracture model," *Journal of orthopaedic research*, vol. 21, no. 6, pp. 1011–1017, 2003.

G. Ayers and J. C. Dainty, "Iterative blind deconvolution method and its applications," *Optics letters*, vol. 13, no. 7, pp. 547–549, 1988.

R. Bade, J. Haase, and B. Preim, "Comparison of fundamental mesh smoothing algorithms for medical surface models." in *SimVis*, vol. 6. Citeseer, 2006, pp. 289–304.

L. Baggi, I. Cappelloni, M. Di Girolamo, F. Maceri, and G. Vairo, "The influence of implant diameter and length on stress distribution of osseointegrated implants related to crestal bone geometry: a three-dimensional finite element analysis," *The Journal of prosthetic dentistry*, vol. 100, no. 6, pp. 422–431, 2008.

M. Bak, A. S. Jacobson, D. Buchbinder, and M. L. Urken, "Contemporary reconstruction of the mandible," *Oral oncology*, vol. 46, no. 2, pp. 71–76, 2010.

I. Bankman, *Handbook of Medical Image Processing and Analysis*, ser. Academic Press series in biomedical engineering. Elsevier Science, 2008.

W. L. Bargar, "Shape the implant to the patient: a rationale for the use of custom-fit cementless total hip implants," *Clinical orthopaedics and related research*, vol. 249, pp. 73–78, 1989.

G. Bergmann, G. Deuretzbacher, M. Heller, F. Graichen, A. Rohlmann, J. Strauss, and G. Duda, "Hip contact forces and gait patterns from routine activities," *Journal of biomechanics*, vol. 34, no. 7, pp. 859–871, 2001.

G. Bergmann, F. Graichen, A. Rohlmann, A. Bender, B. Heinlein, G. Duda, M. Heller, and M. Morlock, "Realistic loads for testing hip implants," *Bio-medical materials and engineering*, vol. 20, no. 2, pp. 65–75, 2010.

O. Bernard, D. Friboulet, P. Thévenaz, and M. Unser, "Variational b-spline level-set: a linear filtering approach for fast deformable model evolution," *Image Processing, IEEE Transactions on*, vol. 18, no. 6, pp. 1179–1191, 2009.

D. J. Berry, "Total hip arthroplasty in patients with proximal femoral deformity," *Clinical orthopaedics and related research*, vol. 369, pp. 262–272, 1999.

D. J. Berry, M. Von Knoch, C. D. Schleck, and W. S. Harmsen, "Effect of femoral head diameter and operative approach on risk of dislocation after primary total hip arthroplasty," *The Journal of Bone & Joint Surgery*, vol. 87, no. 11, pp. 2456–2463, 2005.

J. Beutel, H. Kundel, and R. Van Metter, *Handbook of Medical Imaging: Physics and psychophysics*, ser. Handbook of Medical Imaging. SPIE Press, 2000.

J. C. Bezdek, *Pattern recognition with fuzzy objective function algorithms.* Kluwer Academic Publishers, 1981.

M. Bhandari, P. Tornetta, S. Sprague, S. Najibi, B. Petrisor, L. Griffith, G. H. Guyatt *et al.*, "Predictors of reoperation following operative management of fractures of the tibial shaft," *Journal of orthopaedic trauma*, vol. 17, no. 5, pp. 353–361, 2003.

H. K. Bhatt, "Finite element optimization of hip implant geometrical parameters to determine safe zones and resist dislocation," Ph.D. dissertation, Wright State University, 2008.

R. Bieger, A. Ignatius, R. Decking, L. Claes, H. Reichel, and L. Dürselen, "Primary stability and strain distribution of cementless hip stems as a function of implant design," *Clinical Biomechanics*, vol. 27, no. 2, pp. 158–164, 2012.

W. Birkfellner, *Applied Medical Image Processing: A Basic Course.* Taylor & Francis, 2011.

M. R. Bong, K. J. Koval, and K. A. Egol, "The history of intramedullary nailing," *BULLETIN-HOSPITAL FOR JOINT DISEASES NEW YORK*, vol. 64, no. 3/4, p. 94, 2006.

I. B. Botser, A. Herman, R. Nathaniel, D. Rappaport, and A. Chechik, "Digital image enhancement improves diagnosis of nondisplaced proximal femur fractures," *Clinical orthopaedics and related research*, vol. 467, no. 1, pp. 246–253, 2009.

H. Bouma, A. Vilanova, L. J. Van Vliet, and F. A. Gerritsen, "Correction for the dislocation of curved surfaces caused by the psf in 2d and 3d ct images," *IEEE transactions on pattern analysis and machine intelligence*, vol. 27, no. 9, pp. 1501–1507, 2005.

K. Bowyer and P. J. Phillips, *Empirical evaluation techniques in computer vision.* IEEE Computer Society Press, 1998.

Y. Boykov and G. Funka-Lea, "Graph cuts and efficient nd image segmentation," *International Journal of Computer Vision*, vol. 70, no. 2, pp. 109–131, 2006.

Y. Boykov and V. Kolmogorov, "An experimental comparison of min-cut/max-flow algorithms for energy minimization in vision," *Pattern Analysis and Machine Intelligence, IEEE Transactions on*, vol. 26, no. 9, pp. 1124–1137, 2004.

Y. Boykov, O. Veksler, and R. Zabih, "Fast approximate energy minimization via graph cuts," *Pattern Analysis and Machine Intelligence, IEEE Transactions on*, vol. 23, no. 11, pp. 1222–1239, 2001.

D. Bozkaya, S. Muftu, and A. Muftu, "Evaluation of load transfer characteristics of five different implants in compact bone at different load levels by finite elements analysis," *The Journal of prosthetic dentistry*, vol. 92, no. 6, pp. 523–530, 2004.

M. Brinker, *Review of Orthopaedic Trauma*. Wolters Kluwer Health, 2013.

B. R. Burroughs, B. Hallstrom, G. J. Golladay, D. Hoeffel, and W. H. Harris, "Range of motion and stability in total hip arthroplasty with 28-, 32-, 38-, and 44-mm femoral head sizes: an in vitro study," *The Journal of arthroplasty*, vol. 20, no. 1, pp. 11–19, 2005.

J. Bushberg, *The Essential Physics of Medical Imaging*. Lippincott Williams & Wilkins, 2002.

T. Buzug, *Computed Tomography: From Photon Statistics to Modern Cone-Beam CT*. Springer, 2008.

J. Callaghan, A. Rosenberg, and H. Rubash, *The Adult Hip*, ser. The Adult Hip. Lippincott Williams & Wilkins, 2007, no. vol. 1.

J. J. Callaghan, P. Bracha, S. S. Liu, S. Piyaworakhun, D. D. Goetz, and R. C. Johnston, "Survivorship of a charnley total hip arthroplasty a concise follow-up, at a minimum of thirty-five years, of previous reports*," *The Journal of Bone & Joint Surgery*, vol. 91, no. 11, pp. 2617–2621, 2009.

P. Campisi and K. Egiazarian, *Blind image deconvolution: theory and applications*. CRC press, 2007.

A. Cappozzo, F. Catani, U. Della Croce, and A. Leardini, "Position and orientation in space of bones during movement: anatomical frame definition and determination," *Clinical biomechanics*, vol. 10, no. 4, pp. 171–178, 1995.

M. J. Cardoso, G. Winston, M. Modat, S. Keihaninejad, J. Duncan, and S. Ourselin, "Geodesic shape-based averaging," in *Medical Image Computing and Computer-Assisted Intervention–MICCAI 2012*. Springer, 2012, pp. 26–33.

H. D. Carl, J. Ploetzner, B. Swoboda, G. Weseloh, and L. A. Mueller, "Cementless total hip arthroplasty in patients with rheumatoid arthritis using a tapered designed titanium hip stem minimum: 10-year results," *Rheumatology international*, vol. 31, no. 3, pp. 353–359, 2011.

L. Carlsson, T. Röstlund, B. Albrektsson, and T. Albrektsson, "Implant fixation improved by close fit cylindrical implant-bone interface studied in rabbits," *Acta Orthopaedica*, vol. 59, no. 3, pp. 272–275, 1988.

B. C. Carr and T. Goswami, "Knee implants–review of models and biomechanics," *Materials & Design*, vol. 30, no. 2, pp. 398–413, 2009.

M. E. Casciaro and D. Craiem, "Towards automatic measurement of anteversion and neck–shaft angles in human femurs using ct images," *Computer methods in biomechanics and biomedical engineering*, vol. 17, no. 2, pp. 128–136, 2014.

V. Caselles, R. Kimmel, and G. Sapiro, "Geodesic active contours," *International journal of computer vision*, vol. 22, no. 1, pp. 61–79, 1997.

F. Catani and S. Zaffagnini, *Knee Surgery using Computer Assisted Surgery and Robotics*. Springer, 2013.

J. Center, T. Nguyen, N. Pocock, K. Noakes, P. Kelly, J. Eisman, and P. Sambrook, "Femoral neck axis length, height loss and risk of hip fracture in males and females," *Osteoporosis international*, vol. 8, no. 1, pp. 75–81, 1998.

T. F. Chan and L. A. Vese, "Active contours without edges," *Image processing, IEEE transactions on*, vol. 10, no. 2, pp. 266–277, 2001.

N. Chanchareonsook, H. Tideman, S. E. Feinberg, L. Jongpaiboonkit, S. Lee, C. Flanagan, G. Krishnaswamy, and J. Jansen, "Segmental mandibular bone reconstruction with a carbonate-substituted hydroxyapatite-coated modular endoprosthetic poly (ε-caprolactone) scaffold in macaca fascicularis," *Journal of Biomedical Materials Research Part B: Applied Biomaterials*, 2013.

P. B. Chang, B. H. Robie, and D. L. Bartel, "Preclinical cost analysis of orthopaedic implants: a custom versus standard cementless femoral component for revision total hip arthroplasty," *Journal of biomechanics*, vol. 32, no. 12, pp. 1309–1318, 1999.

M. N. Charles, R. B. Bourne, J. R. Davey, A. S. Greenwald, B. F. Morrey, and C. H. Rorabeck, "Soft-tissue balancing of the hipthe role of femoral offset restoration," *The Journal of Bone & Joint Surgery*, vol. 86, no. 5, pp. 1078–1088, 2004.

V. Chu and G. Hamarneh, "Matlab-itk interface for medical image filtering, segmentation, and registration," in *Proc. SPIE*, vol. 6144, 2006, pp. 61 443T–1.

K.-S. Chuang, H.-L. Tzeng, S. Chen, J. Wu, and T.-J. Chen, "Fuzzy c-means clustering with spatial information for image segmentation," *computerized medical imaging and graphics*, vol. 30, no. 1, pp. 9–15, 2006.

A. Cigada, G. Cotogno, and R. Chiesa, "The ceramic-on-metal coupling in total hip replacements for young patients: a review study." *Journal of applied biomaterials & biomechanics: JABB*, vol. 9, no. 1, pp. 2–10, 2010.

M. C. Clark, L. O. Hall, D. B. Goldgof, R. Velthuizen, F. R. Murtagh, and M. S. Silbiger, "Automatic tumor segmentation using knowledge-based techniques," *Medical Imaging, IEEE Transactions on*, vol. 17, no. 2, pp. 187–201, 1998.

J. Cobb, H. Dixon, W. Dandachli, and F. Iranpour, "The anatomical tibial axis reliable rotational orientation in knee replacement," *Journal of Bone & Joint Surgery, British Volume*, vol. 90, no. 8, pp. 1032–1038, 2008.

M. Cobourne and A. DiBiase, *Handbook of Orthodontics*. Elsevier Health Sciences UK, 2010.

D. Comaniciu and P. Meer, "Mean shift: A robust approach toward feature space analysis," *Pattern Analysis and Machine Intelligence, IEEE Transactions on*, vol. 24, no. 5, pp. 603–619, 2002.

O. Commowick, A. Akhondi-Asl, and S. K. Warfield, "Estimating a reference standard segmentation with spatially varying performance parameters: Local map staple," *Medical Imaging, IEEE Transactions on*, vol. 31, no. 8, pp. 1593–1606, 2012.

A. Completo, F. Fonseca, and J. Simoes, "Finite element and experimental cortex strains of the intact and implanted tibia," *Journal of biomechanical engineering*, vol. 129, no. 5, pp. 791–797, 2007.

L. P. Cordella, P. Foggia, C. Sansone, F. Tortorella, and M. Vento, "Reliability parameters to improve combination strategies in multi-expert systems," *Pattern Analysis & Applications*, vol. 2, no. 3, pp. 205–214, 1999.

K. Corten, R. B. Bourne, K. D. Charron, K. Au, and C. H. Rorabeck, "What works best, a cemented or cementless primary total hip arthroplasty?: minimum 17-year followup of a randomized controlled trial," *Clinical Orthopaedics and Related Research®*, vol. 469, no. 1, pp. 209–217, 2011.

S. Cortez, J. Claro, and J. Alves, "3d reconstruction of a spinal motion segment from 2d medical images: Objective quantification of the geometric accuracy of the fe mesh generation procedure," in *Bioengineering (ENBENG), 2013 IEEE 3rd Portuguese Meeting in*. IEEE, 2013, pp. 1–6.

T. Cour, S. Yu, and J. Shi, "Normalized cut segmentation code. copyright 2004 university of pennsylvania," *Computer and Information Science Department*, 2004.

S. Cowin, *Bone Mechanics Handbook, Second Edition*. Taylor & Francis, 2001.

D. Cremers, M. Rousson, and R. Deriche, "A review of statistical approaches to level set segmentation: integrating color, texture, motion and shape," *International journal of computer vision*, vol. 72, no. 2, pp. 195–215, 2007.

L. Cristofolini, M. Viceconti, A. Toni, and A. Giunti, "Influence of thigh muscles on the axial strains in a proximal femur during early stance in gait," *Journal of biomechanics*, vol. 28, no. 5, pp. 617–624, 1995.

L. Cristofolini, M. Viceconti, A. Cappello, and A. Toni, "Mechanical validation of whole bone composite femur models," *Journal of biomechanics*, vol. 29, no. 4, pp. 525–535, 1996.

I. Cunningham and A. Fenster, "A method for modulation transfer function determination from edge profiles with correction for finite-element differentiation," *Medical physics*, vol. 14, no. 4, pp. 533–537, 1987.

I. Cunningham and B. Reid, "Signal and noise in modulation transfer function determinations using the slit, wire, and edge techniques," *Medical physics*, vol. 19, no. 4, pp. 1037–1044, 1992.

D. J. Daegling and W. L. Hylander, "Biomechanics of torsion in the human mandible," *American Journal of Physical Anthropology*, vol. 105, no. 1, pp. 73–88, 1998.

M. Dalkiz, B. Beydemir, and Y. Günaydin, "Treatment of a microvascular reconstructed mandible using an implant-supported fixed partial denture: case report," *Implant dentistry*, vol. 10, no. 2, pp. 121–125, 2001.

A. Dalley and K. Moore, *Anatomia orientada para a clínica, 4. ª edição.* Guanabara Koogan, Rio de Janeiro, Brasil, 2001.

J. Damstra, Z. Fourie, J. J. Huddleston Slater, and Y. Ren, "Accuracy of linear measurements from cone-beam computed tomography-derived surface models of different voxel sizes," *American Journal of Orthodontics and Dentofacial Orthopedics*, vol. 137, no. 1, pp. 16–e1, 2010.

W. Dauber, *Pocket Atlas of Human Anatomy: Founded by Heinz Feneis*, ser. Thieme e-book library. Thieme, 2011.

P. Dechow, G. Nail, C. Schwartz-Dabney, and R. Ashman, "Elastic properties of human supraorbital and mandibular bone," *American Journal of Physical Anthropology*, vol. 90, no. 3, pp. 291–306, 1993.

G. Demey, C. Fary, S. Lustig, P. Neyret *et al.*, "Does a collar improve the immediate stability of uncemented femoral hip stems in total hip arthroplasty? a bilateral comparative cadaver study," *The Journal of arthroplasty*, vol. 26, no. 8, pp. 1549–1555, 2011.

Ö. Demirkaya, M. Asyali, and P. Sahoo, *Image Processing With MATLAB: Applications in Medicine And Biology*, ser. MATLAB examples. Taylor & Francis, 2009.

A. Dervieux and F. Thomasset, "Multifluid incompressible flows by a finite element method," in *Seventh International Conference on Numerical Methods in Fluid Dynamics.* Springer, 1981, pp. 158–163.

A. Dervieux and F. Thomasset, "A finite element method for the simulation of a rayleigh-taylor instability," in *Approximation methods for Navier-Stokes problems.* Springer, 1980, pp. 145–158.

L. R. Dice, "Measures of the amount of ecologic association between species," *Ecology*, vol. 26, no. 3, pp. 297–302, 1945.

H. Digabel and C. Lantuéjoul, "Iterative algorithms," in *Proc. 2nd European Symp. Quantitative Analysis of Microstructures in Material Science, Biology and Medicine*, vol. 19, no. 7. Stuttgart, West Germany: Riederer Verlag, 1978, p. 8.

J. J. Disa and P. G. Cordeiro, "Mandible reconstruction with microvascular surgery," in *Seminars in surgical oncology*, vol. 19, no. 3. Wiley Online Library, 2000, pp. 226–234.

K. Doi, "Computer-aided diagnosis in medical imaging: historical review, current status and future potential," *Computerized medical imaging and graphics*, vol. 31, no. 4-5, pp. 198–211, 2007.

D. L. Donoho, "De-noising by soft-thresholding," *Information Theory, IEEE Transactions on*, vol. 41, no. 3, pp. 613–627, 1995.

D. L. Donoho and I. M. Johnstone, "Adapting to unknown smoothness via wavelet shrinkage," *Journal of the american statistical association*, vol. 90, no. 432, pp. 1200–1224, 1995.

S. Dore and Y. Goussard, "Experimental determination of ct point spread function anisotropy and shift-variance," in *Engineering in Medicine and Biology Society, 1997. Proceedings of the 19th Annual International Conference of the IEEE*, vol. 2. IEEE, 1997, pp. 788–791.

L. D. Dorr, M.-C. Faugere, A. M. Mackel, T. A. Gruen, B. Bognar, and H. H. Malluche, "Structural and cellular assessment of bone quality of proximal femur," *Bone*, vol. 14, no. 3, pp. 231–242, 1993.

G. Dougherty, *Digital Image Processing for Medical Applications*. Cambridge University Press, 2009.

P. Drapikowski, "Surface modelinguncertainty estimation and visualization," *Computerized Medical Imaging and Graphics*, vol. 32, no. 2, pp. 134–139, 2008.

G. N. Duda, M. Heller, J. Albinger, O. Schulz, E. Schneider, and L. Claes, "Influence of muscle forces on femoral strain distribution," *Journal of biomechanics*, vol. 31, no. 9, pp. 841–846, 1998.

G. N. Duda, F. Mandruzzato, M. Heller, J. Goldhahn, R. Moser, M. Hehli, L. Claes, and N. P. Haas, "Mechanical boundary conditions of fracture healing: borderline indications in the treatment of unreamed tibial nailing," *Journal of biomechanics*, vol. 34, no. 5, pp. 639–650, 2001.

J. C. Dunn, "A fuzzy relative of the isodata process and its use in detecting compact well-separated clusters," *Journal of Cybernetics*, vol. Vol. 3, no. No. 3., pp. pp. 32–57, 1973.

R. L. Easton Jr, *Fourier methods in imaging*. John Wiley & Sons, 2010.

S. Eggli, M. Pisan, and M. Müller, "The value of preoperative planning for total hip arthroplasty," *Journal of Bone & Joint Surgery, British Volume*, vol. 80, no. 3, pp. 382–390, 1998.

H. M. El-Zanaty, A. R. El-Beialy, A. M. Abou El-Ezz, K. H. Attia, A. R. El-Bialy, and Y. A. Mostafa, "Three-dimensional dental measurements: An alternative to plaster models," *American Journal of Orthodontics and Dentofacial Orthopedics*, vol. 137, no. 2, pp. 259–265, 2010.

C. A. Engh and J. D. Bobyn, *Biological fixation in total hip arthroplasty*. Slack Thorofare (NJ), 1985.

Ç. E. Erdem, B. Sankur, and A. M. Tekalp, "Performance measures for video object segmentation and tracking," *Image Processing, IEEE Transactions on*, vol. 13, no. 7, pp. 937–951, 2004.

P. F. Felzenszwalb and D. P. Huttenlocher, "Efficient graph-based image segmentation," *International Journal of Computer Vision*, vol. 59, no. 2, pp. 167–181, 2004.

V. Ferrario, C. Sforza, G. Serrao, C. Dellavia, and G. Tartaglia, "Single tooth bite forces in healthy young adults," *Journal of oral rehabilitation*, vol. 31, no. 1, pp. 18–22, 2004.

J. Ferri, B. Piot, B. Ruhin, and J. Mercier, "Advantages and limitations of the fibula free flap in mandibular reconstruction," *Journal of oral and maxillofacial surgery*, vol. 55, no. 5, pp. 440–448, 1997.

C. G. Finkemeier, A. H. Schmidt, R. F. Kyle, D. C. Templeman, and T. F. Varecka, "A prospective, randomized study of intramedullary nails inserted with and without reaming for the treatment of open and closed fractures of the tibial shaft," *Journal of orthopaedic trauma*, vol. 14, no. 3, pp. 187–193, 2000.

J. B. Finlay, D. G. Chess, W. R. Hardie, C. H. Rorabeck, and R. B. Bourne, "An evaluation of three loading configurations for the in vitro testing of femoral strains in total hip arthroplasty," *Journal of orthopaedic research*, vol. 9, no. 5, pp. 749–759, 1991.

X. Flecher, O. Pearce, S. Parratte, J.-M. Aubaniac, and J.-N. Argenson, "Custom cementless stem improves hip function in young patients at 15-year followup," *Clinical Orthopaedics and Related Research®*, vol. 468, no. 3, pp. 747–755, 2010.

L. Flint, *Trauma: Contemporary Principles and Therapy*, ser. M - Medicine Series. Wolters Kluwer Health/Lippincott Williams & Wilkins, 2008.

P. Flint, B. Haughey, J. Niparko, M. Richardson, V. Lund, K. Robbins, M. Lesperance, and J. Thomas, *Cummings Otolaryngology - Head and Neck Surgery: Head and Neck Surgery, 3-Volume Set.* Elsevier Health Sciences, 2010, no. vol. 1.

F. Fontijn-Tekamp, A. Slagter, A. Van Der Bilt, M. V. Hof, D. Witter, W. Kalk, and J. Jansen, "Biting and chewing in overdentures, full dentures, and natural dentitions," *Journal of Dental Research*, vol. 79, no. 7, pp. 1519–1524, 2000.

D. Forsyth and J. Ponce, *Computer Vision: A Modern Approach*, ser. Always learning. Pearson, 2012.

E. Frank, B. Long, and B. Smith, *Merrill's Atlas of Radiographic Positioning and Procedures.* Elsevier Health Sciences, 2013, no. vol. 3.

J. Franklin, R. Winquist, S. Benirschke, and S. Hansen, "Broken intramedullary nails," *The Journal of Bone & Joint Surgery*, vol. 70, no. 10, pp. 1463–1471, 1988.

M. Frazier and J. Drzymkowski, *Essentials of Human Diseases and Conditions.* Elsevier Health Sciences, 2014.

P. Frey and P. George, *Mesh Generation*, ser. ISTE. Wiley, 2013.

J. L. Frodel, G. F. Funk, D. T. Capper, K. L. Fridrich, J. R. Blumer, J. R. Haller, and H. T. Hoffman, "Osseointegrated implants: a comparative study of bone thickness in four vascularized bone flaps." *Plastic and reconstructive surgery*, vol. 92, no. 3, pp. 456–458, 1993.

W. Frontera, J. Silver, and T. Rizzo, *Essentials of Physical Medicine and Rehabilitation*. Elsevier Health Sciences, 2014.

J. Furmanski, M. Anderson, S. Bal, A. S. Greenwald, D. Halley, B. Penenberg, M. Ries, and L. Pruitt, "Clinical fracture of cross-linked uhmwpe acetabular liners," *Biomaterials*, vol. 30, no. 29, pp. 5572–5582, 2009.

C. Gaebler, S. Stanzl-Tschegg, G. Heinze, B. Holper, T. Milne, G. Berger, and V. Vecsei, "Fatigue strength of locking screws and prototypes used in small-diameter tibial nails: a biomechanical study," *Journal of Trauma-Injury, Infection, and Critical Care*, vol. 47, no. 2, pp. 379–384, 1999.

J. L. Gaffey, J. J. Callaghan, D. R. Pedersen, D. D. Goetz, P. M. Sullivan, and R. C. Johnston, "Cementless acetabular fixation at fifteen yearsa comparison with the same surgeon's results following acetabular fixation with cement," *The Journal of Bone & Joint Surgery*, vol. 86, no. 2, pp. 257–261, 2004.

H. Galoob, "Reconstruction of the head and neck: A defect-oriented approach," *American Journal of Cosmetic Surgery*, vol. 30, no. 1, pp. 44–45, 2013.

M. Garcia, *NonInvasive Cardiovascular Imaging: A Multimodality Approach*. Wolters Kluwer Health, 2012.

A. Garg, J. Deland, and P. Walker, "Design of intramedullary femoral stems using computer graphics," *Engineering in medicine*, vol. 14, no. 2, pp. 89–93, 1985.

G. Gerig, M. Jomier, and M. Chakos, "Valmet: A new validation tool for assessing and improving 3d object segmentation," in *Medical Image Computing and Computer-Assisted Intervention–MICCAI 2001*. Springer, 2001, pp. 516–523.

P. Giannoudis and H. Pape, *Practical Procedures in Orthopaedic Trauma Surgery*, ser. Cambridge medicine. Cambridge University Press, 2014.

B. T. Goh, S. Lee, H. Tideman, and P. J. Stoelinga, "Mandibular reconstruction in adults: a review," *International journal of oral and maxillofacial surgery*, vol. 37, no. 7, pp. 597–605, 2008.

B. T. Goh, S. Lee, H. Tideman, J. A. Jansen, and P. J. Stoelinga, "Replacement of the condyle and ascending ramus by a modular endoprosthesis in macaca fascicularis - part 2: Microcomputed tomographic and histologic evaluation of the ramus and stem," *Journal of Oral and Maxillofacial Surgery*, vol. 67, no. 12, pp. 2617–2626, 2009.

B. T. Goh, S. Lee, H. Tideman, and P. J. Stoelinga, "Replacement of the condyle and ascending ramus by a modular endoprosthesis in macaca fascicularis - part 1: A clinical and radiographic study," *Journal of Oral and Maxillofacial Surgery*, vol. 67, no. 7, pp. 1392–1400, 2009.

B. T. Goh, S. Lee, H. Tideman, P. J. Stoelinga, and J. A. Jansen, "Replacement of the condyle and ascending ramus by a modular endoprosthesis in macaca fascicularis - part 3: Evaluation of peri-implant bone remodeling," *Journal of Oral and Maxillofacial Surgery*, vol. 68, no. 8, pp. 1776–1782, 2010.

L. W. Goldman, "Principles of ct and ct technology," *Journal of nuclear medicine technology*, vol. 35, no. 3, pp. 115–128, 2007.

L. W. Goldman, "Principles of ct: radiation dose and image quality," *Journal of nuclear medicine technology*, vol. 35, no. 4, pp. 213–225, 2007.

L. W. Goldman, "Principles of ct: multislice ct," *Journal of nuclear medicine technology*, vol. 36, no. 2, pp. 57–68, 2008.

R. C. Gonzalez and R. E. Woods, *Digital image processing.* Addison-Wesley, 1992.

T. K. Goto, S. Nishida, Y. Nakamura, K. Tokumori, Y. Nakamura, K. Kobayashi, Y. Yoshida, and K. Yoshiura, "The accuracy of 3-dimensional magnetic resonance 3d vibe images of the mandible: an in vitro comparison of magnetic resonance imaging and computed tomography," *Oral Surgery, Oral Medicine, Oral Pathology, Oral Radiology, and Endodontology*, vol. 103, no. 4, pp. 550–559, 2007.

H. Gray and W. Lewis, *Anatomy of the Human Body.* Lea & Febiger, 1918.

J. S. Gregory and R. M. Aspden, "Femoral geometry as a risk factor for osteoporotic hip fracture in men and women," *Medical engineering & physics*, vol. 30, no. 10, pp. 1275–1286, 2008.

W. E. L. Grimson, G. Ettinger, T. Kapur, M. E. Leventon, W. M. Wells III, and R. Kikinis, "Utilizing segmented mri data in image-guided surgery," *International Journal of Pattern Recognition and Artificial Intelligence*, vol. 11, no. 08, pp. 1367–1397, 1997.

A. Grosse, I. Kempf, and D. Lafforgue, "Treatment of fragments, loss of bony substance and pseudarthrosis of femur and tibia using screw fixation (40 cases)," *Revue de chirurgie orthopédique et réparatrice de l'appareil moteur*, vol. 64, p. 33, 1978.

R. Gunderman, *Essential Radiology: Clinical Presentation, Pathophysiology, Imaging*, ser. Thieme ElectronicBook Library. Thieme, 2006.

G. C. Gurtner and G. R. Evans, "Advances in head and neck reconstruction," *Plastic and reconstructive surgery*, vol. 106, no. 3, pp. 672–682, 2000.

H. K. Hahn and H.-O. Peitgen, "Iwt-interactive watershed transform: a hierarchical method for efficient interactive and automated segmentation of multidimensional gray-scale images," in *Medical Imaging 2003.* International Society for Optics and Photonics, 2003, pp. 643–653.

N. P. Hailer, G. Garellick, and J. Kärrholm, "Uncemented and cemented primary total hip arthroplasty in the swedish hip arthroplasty register: evaluation of 170,413 operations," *Acta orthopaedica*, vol. 81, no. 1, pp. 34–41, 2010.

P. Hajek, H. Bicknell, W. Bronson, J. Albright, and S. Saha, "The use of one compared with two distal screws in the treatment of femoral shaft fractures with interlocking intramedullary nailing. a clinical and biomechanical analysis," *The Journal of Bone & Joint Surgery*, vol. 75, no. 4, pp. 519–525, 1993.

A. Halim, *Human Anatomy:Volume II Abdomen And Lower Limb.* I.K. International Publishing House Pvt. Limited, 2008.

W. Hammer, *Functional Soft-tissue Examination and Treatment by Manual Methods*. Jones and Bartlett, 2007.

T. N. Hangartner and V. Gilsanz, "Evaluation of cortical bone by computed tomography," *Journal of Bone and Mineral Research*, vol. 11, no. 10, pp. 1518–1525, 1996.

R. M. Haralick and L. G. Shapiro, "Image segmentation techniques," *Computer vision, graphics, and image processing*, vol. 29, no. 1, pp. 100–132, 1985.

I. Harrington, "A bioengineering analysis of force actions at the knee in normal and pathological gait." *Biomedical engineering*, vol. 11, no. 5, pp. 167–172, 1976.

O. L. Harrysson, Y. A. Hosni, and J. F. Nayfeh, "Custom-designed orthopedic implants evaluated using finite element analysis of patient-specific computed tomography data: femoral-component case study," *BMC Musculoskeletal Disorders*, vol. 8, no. 1, p. 91, 2007.

R. T. Hart, V. V. Hennebel, N. Thongpreda, W. C. Van Buskirk, and R. C. Anderson, "Modeling the biomechanics of the mandible: a three-dimensional finite element study," *Journal of biomechanics*, vol. 25, no. 3, pp. 261–286, 1992.

B. H. Haughey, J. M. Fredrickson, A. J. Lerrick, A. Sclaroff, and W. D. Gay, "Fibular and iliac crest osteomuscular free flap reconstruction of the oral cavity," *The Laryngoscope*, vol. 104, no. 11, pp. 1305–1313, 1994.

J. He, D. Li, B. Lu, Z. Wang, and T. Zhang, "Custom fabrication of a composite hemi-knee joint based on rapid prototyping," *Rapid Prototyping Journal*, vol. 12, no. 4, pp. 198–205, 2006.

E. Heissler, F.-S. Fischer, S. Boiouri, T. Lehrnann, W. Mathar, A. Gebhardt, W. Lanksch, and J. Bler, "Custom-made cast titanium implants produced with cad/cam for the reconstruction of cranium defects," *International journal of oral and maxillofacial surgery*, vol. 27, no. 5, pp. 334–338, 1998.

M. Heller, G. Bergmann, J.-P. Kassi, L. Claes, N. Haas, and G. Duda, "Determination of muscle loading at the hip joint for use in pre-clinical testing," *Journal of biomechanics*, vol. 38, no. 5, pp. 1155–1163, 2005.

G. Hellsing, "On the regulation of interincisor bite force in man," *Journal of oral rehabilitation*, vol. 7, no. 5, pp. 403–411, 1980.

M. Henley, J. Chapman, J. Agel, E. Harvey, A. Whorton, and M. Swiontkowski, "Treatment of type ii, iiia, and iiib open fractures of the tibial shaft: a prospective comparison of unreamed interlocking intramedullary nails and half-pin external fixators," *Journal of orthopaedic trauma*, vol. 12, no. 1, pp. 1–7, 1998.

K. Herzog, "Die technik der geschlossenen marknagelung frischer tibiafrakturen mit dem rohrschlitznage," *Chirurg*, vol. 29, pp. 501–506, 1958.

D. A. Hidalgo, "Fibula free flap: a new method of mandible reconstruction," *Plastic and reconstructive surgery*, vol. 84, no. 1, pp. 71–79, 1989.

C. F. Hildebolt, M. W. Vannier, and R. H. Knapp, "Validation study of skull three-dimensional computerized tomography measurements," *American journal of physical anthropology*, vol. 82, no. 3, pp. 283–294, 1990.

M. L. Hilgers, W. C. Scarfe, J. P. Scheetz, and A. G. Farman, "Accuracy of linear temporomandibular joint measurements with cone beam computed tomography and digital cephalometric radiography," *American journal of orthodontics and dentofacial orthopedics*, vol. 128, no. 6, pp. 803–811, 2005.

T. K. Ho, J. J. Hull, and S. N. Srihari, "Decision combination in multiple classifier systems," *Pattern Analysis and Machine Intelligence, IEEE Transactions on*, vol. 16, no. 1, pp. 66–75, 1994.

C. Hoad and A. Martel, "Segmentation of mr images for computer-assisted surgery of the lumbar spine," *Physics in medicine and biology*, vol. 47, no. 19, p. 3503, 2002.

U. Holzwarth and G. Cotogno, *Total Hip Arthroplasty: State of the Art, Challenges and Prospects*. Publications Office, 2012.

G. J. Hooper, R. G. Keddell, and I. D. Penny, "Conservative management or closed nailing for tibial shaft fractures. a randomised prospective trial," *Journal of Bone & Joint Surgery, British Volume*, vol. 73, no. 1, pp. 83–85, 1991.

G. Horne, J. Iceton, J. Twist, and R. Malony, "Disability following fractures of the tibial shaft." *Orthopedics*, vol. 13, no. 4, pp. 423–426, 1990.

G. N. Hounsfield, "Computerized transverse axial scanning (tomography): Part 1. description of system," *British Journal of Radiology*, vol. 46, pp. 1016–1022, 1973.

C.-C. Hsiao, W.-H. Hsu, P.-Q. Chen, and S.-J. Lin, "Optimal alignment of the distal screws in the tibial nailing," *Journal of the Chinese Institute of Engineers*, vol. 26, no. 2, pp. 165–172, 2003.

J. Hsieh, *Computed Tomography: Principles, Design, Artifacts, and Recent Advances*, ser. SPIE PM. SPIE, 2009.

J. Hsu and K. Dickson, "Advances in tibial nailing," in *Practice of Intramedullary Locked Nails*. Springer, 2006, pp. 99–107.

H. Hu, "Multi-slice helical ct: scan and reconstruction," *Medical physics*, vol. 26, no. 1, pp. 5–18, 1999.

S. Hu, E. A. Hoffman, and J. M. Reinhardt, "Automatic lung segmentation for accurate quantitation of volumetric x-ray ct images," *Medical Imaging, IEEE Transactions on*, vol. 20, no. 6, pp. 490–498, 2001.

J. J. Hutson, G. A. Zych, J. D. Cole, K. D. Johnson, P. Ostermann, E. L. Milne, and L. Latta, "Mechanical failures of intramedullary tibial nails applied without reaming," *Clinical orthopaedics and related research*, vol. 315, pp. 129–137, 1995.

W. L. Hylander, K. R. Johnson, and A. Crompton, "Loading patterns and jaw movements during mastication in macaca fascicularis: A bone-strain, electromyographic, and cineradiographic analysis," *American Journal of Physical Anthropology*, vol. 72, no. 3, pp. 287–314, 1987.

L. Ibanez, W. Schroeder, L. Ng, and J. Cates, "The itk software guide," 2003.

I. Ichim, M. Swain, and J. Kieser, "Mandibular biomechanics and development of the human chin," *Journal of dental research*, vol. 85, no. 7, pp. 638–642, 2006.

K. Iniewski, *Medical Imaging: Principles, Detectors, and Electronics.* Wiley, 2009.

A. International and J. R. Davis, *Handbook of materials for medical devices.* ASM international, 2003.

Implants for surgery - Partial and total hip joint prostheses - Part 6: Endurance properties testing and performance requirements of neck region of stemmed femoral components, ISO - International Organization for Standardization Standard, 2012.

P. Jaccard, "The distribution of the flora in the alpine zone. 1," *New phytologist*, vol. 11, no. 2, pp. 37–50, 1912.

J. Jackson, *A User's Guide to Principal Components*, ser. Wiley Series in Probability and Statistics. Wiley, 2005.

A. K. Jain and R. C. Dubes, *Algorithms for clustering data.* Prentice-Hall, Inc., 1988.

R. Jain, R. Kasturi, and B. G. Schunck, *Machine vision.* McGraw-Hill New York, 1995, vol. 5.

M. Jasty, C. Bragdon, D. Burke, D. O'CONNOR, J. Lowenstein, and W. H. Harris, "In vivo skeletal responses to porous-surfaced implants subjected to small induced motions*," *The Journal of Bone & Joint Surgery*, vol. 79, no. 5, pp. 707–14, 1997.

H. Jiankang, L. Dichen, L. Bingheng, W. Zhen, and Z. Tao, "Custom fabrication of composite tibial hemi-knee joint combining cad/cae/cam techniques," *Proceedings of the Institution of Mechanical Engineers, Part H: Journal of Engineering in Medicine*, vol. 220, no. 8, pp. 823–830, 2006.

A. Jokstad, *Osseointegration and dental implants.* John Wiley & Sons, 2009.

N. Joshi, R. Szeliski, and D. Kriegman, "Psf estimation using sharp edge prediction," in *Computer Vision and Pattern Recognition, 2008. CVPR 2008. IEEE Conference on.* IEEE, 2008, pp. 1–8.

Y. Jun, "Morphological analysis of the human knee joint for creating custom-made implant models," *The International Journal of Advanced Manufacturing Technology*, vol. 52, no. 9-12, pp. 841–853, 2011.

Y. Jun and K. Choi, "Design of patient-specific hip implants based on the 3d geometry of the human femur," *Advances in Engineering Software*, vol. 41, no. 4, pp. 537–547, 2010.

W. A. Kalender, W. Seissler, E. Klotz, and P. Vock, "Spiral volumetric ct with single-breath-hold technique, continuous transport, and continuous scanner rotation," *Radiology*, vol. 176, no. 1, pp. 181–183, 1990.

T. Kalteis, M. Handel, T. Herold, L. Perlick, C. Paetzel, and J. Grifka, "Position of the acetabular cupaccuracy of radiographic calculation compared to ct-based measurement," *European journal of radiology*, vol. 58, no. 2, pp. 294–300, 2006.

Y. Kang, K. Engelke, and W. A. Kalender, "A new accurate and precise 3-d segmentation method for skeletal structures in volumetric ct data," *Medical Imaging, IEEE Transactions on*, vol. 22, no. 5, pp. 586–598, 2003.

Y. Kang, K. Engelke, C. Fuchs, and W. A. Kalender, "An anatomic coordinate system of the femoral neck for highly reproducible bmd measurements using 3d qct," *Computerized Medical Imaging and Graphics*, vol. 29, no. 7, pp. 533–541, 2005.

T. Karachalios, C. Tsatsaronis, G. Efraimis, P. Papadelis, G. Lyritis, and G. Diakoumopoulos, "The long-term clinical relevance of calcar atrophy caused by stress shielding in total hip arthroplasty: A 10-year, prospective, randomized study1 1no benefits or funds were received in support of this study." *The Journal of arthroplasty*, vol. 19, no. 4, pp. 469–475, 2004.

M. Kass, A. Witkin, and D. Terzopoulos, "Snakes: Active contour models," *International journal of computer vision*, vol. 1, no. 4, pp. 321–331, 1988.

J.-P. Kassi, M. O. Heller, U. Stoeckle, C. Perka, and G. N. Duda, "Stair climbing is more critical than walking in pre-clinical assessment of primary stability in cementless tha in vitro," *Journal of biomechanics*, vol. 38, no. 5, pp. 1143–1154, 2005.

S. Kawashima, T. Peltomäki, H. Sakata, K. Mori, R.-P. Happonen, and O. Rönning, "Craniofacial morphology in preschool children with sleep-related breathing disorder and hypertrophy of tonsils," *Acta paediatrica*, vol. 91, no. 1, pp. 71–77, 2002.

K. Kawate, Y. Ohneda, T. Ohmura, H. Yajima, K. Sugimoto, and Y. Takakura, "Computed tomography–based custom-made stem for dysplastic hips in japanese patients," *The Journal of arthroplasty*, vol. 24, no. 1, pp. 65–70, 2009.

P. J. Keall, S. Joshi, S. S. Vedam, J. V. Siebers, V. R. Kini, and R. Mohan, "Four-dimensional radiotherapy planning for dmlc-based respiratory motion tracking," *Medical physics*, vol. 32, no. 4, pp. 942–951, 2005.

I. Kempf, A. Grosse, and G. Beck, "Closed locked intramedullary nailing," *J Bone Joint Surg Am*, vol. 67, no. 5, pp. 709–20, 1985.

R. Kenedi, "Strength of biological materials," *Journal of anatomy*, vol. 108, no. Pt 3, p. 582, 1971.

E. Keppel, "Approximating complex surfaces by triangulation of contour lines," *IBM Journal of Research and Development*, vol. 19, no. 1, pp. 2–11, 1975.

J. Kerner, R. Huiskes, G. Van Lenthe, H. Weinans, B. Van Rietbergen, C. Engh, and A. Amis, "Correlation between pre-operative periprosthetic bone density and post-operative bone loss in tha can be explained by strain-adaptive remodelling," *Journal of biomechanics*, vol. 32, no. 7, pp. 695–703, 1999.

M.-R. Kim and R. B. Donoff, "Critical analysis of mandibular reconstruction using ao reconstruction plates," *Journal of oral and maxillofacial surgery*, vol. 50, no. 11, pp. 1152–1157, 1992.

S.-Y. Kim, H.-S. Kyung, J.-C. Ihn, M.-R. Cho, K.-H. Koo, and C.-Y. Kim, "Cementless metasul metal-on-metal total hip arthroplasty in patients less than fifty years old," *The Journal of Bone & Joint Surgery*, vol. 86, no. 11, pp. 2475–2481, 2004.

D. Kluess, H. Martin, W. Mittelmeier, K.-P. Schmitz, and R. Bader, "Influence of femoral head size on impingement, dislocation and stress distribution in total hip replacement," *Medical engineering & physics*, vol. 29, no. 4, pp. 465–471, 2007.

T. Kneifel and R. Buckley, "A comparison of one versus two distal locking screws in tibial fractures treated with unreamed tibial nails: a prospective randomized clinical trial," *Injury*, vol. 27, no. 4, pp. 271–273, 1996.

W.-D. Knoll, A. Gaida, and P. Maurer, "Analysis of mechanical stress in reconstruction plates for bridging mandibular angle defects," *Journal of Cranio-Maxillofacial Surgery*, vol. 34, no. 4, pp. 201–209, 2006.

V. Kolmogorov and R. Zabin, "What energy functions can be minimized via graph cuts?" *Pattern Analysis and Machine Intelligence, IEEE Transactions on*, vol. 26, no. 2, pp. 147–159, 2004.

G. Konrath, B. R. Moed, J. T. Watson, S. Kaneshiro, D. E. Karges, and K. E. Cramer, "Intramedullary nailing of unstable diaphyseal fractures of the tibia with distal intraarticular involvement," *Journal of orthopaedic trauma*, vol. 11, no. 3, pp. 200–205, 1997.

T. Korioth and A. Hannam, "Deformation of the human mandible during simulated tooth clenching," *Journal of Dental Research*, vol. 73, no. 1, pp. 56–66, 1994.

P. Koulouvaris, K. Stafylas, T. Sculco, and T. Xenakis, "Custom-design implants for severe distorted proximal anatomy of the femur in young adults followed for 4-8 years," *Acta orthopaedica*, vol. 79, no. 2, pp. 203–210, 2008.

M. J. Kraay, J. S. Rowbottom, and M. G. Razek, "The acetabular component in primary total hip arthroplasty," in *Seminars in Arthroplasty*, vol. 23, no. 3. Elsevier, 2012, pp. 163–166.

K. Krissian, G. Malandain, N. Ayache, R. Vaillant, and Y. Trousset, "Model-based detection of tubular structures in 3d images," *Computer vision and image understanding*, vol. 80, no. 2, pp. 130–171, 2000.

S. Kuhn, M. Hansen, and P. Rommers, "Extending the indications of intramedullary nailing with the expert tibial nail®," *Acta chirurgiae orthopaedicae et traumatologiae Cechoslovaca*, vol. 75, no. 2, p. 77, 2008.

S. Kuhn, M. Hansen, and P. M. Rommens, "Extending the indication of intramedullary nailing of tibial fractures," *European Journal of Trauma and Emergency Surgery*, vol. 33, no. 2, pp. 159–169, 2007.

G. Küntscher, "Die marknalung von knochenbrüchen," *Langenbecks Arch Klin Chir*, vol. 200, pp. 443–455, 1940.

G. Küntscher and H. Rinne, *Practice of intramedullary nailing*. CC Thomas, 1967.

M. Kutz, R. S. Adrezin, R. E. Barr, C. Batich, R. V. Bellamkonda, A. J. Brammer, T. S. Buchanan, A. M. Cook, J. M. Currie, A. M. Dolan *et al.*, *Standard handbook of biomedical engineering and design*. McGraw-Hill New York, NY, USA, 2003.

G. Laflamme, D. Heimlich, D. Stephen, H. Kreder, and C. Whyne, "Proximal tibial fracture stability with intramedullary nail fixation using oblique interlocking screws," *Journal of orthopaedic trauma*, vol. 17, no. 7, pp. 496–502, 2003.

M. O. Lagravère, L. Hansen, W. Harzer, and P. W. Major, "Plane orientation for standardization in 3-dimensional cephalometric analysis with computerized tomography imaging," *American journal of orthodontics and dentofacial orthopedics*, vol. 129, no. 5, pp. 601–604, 2006.

S. Lakare and A. Kaufman, "3d segmentation techniques for medical volumes," *Center for Visual Computing, Department of Computer Science, State University of New York*, 2000.

B. A. Landman, J. A. Bogovic, and J. L. Prince, "Simultaneous truth and performance level estimation with incomplete, over-complete, and ancillary data," in *SPIE Medical Imaging*. International Society for Optics and Photonics, 2010, pp. 76 231N–76 231N.

T. R. Langerak, U. A. van der Heide, A. N. Kotte, M. A. Viergever, M. van Vulpen, and J. P. Pluim, "Label fusion in atlas-based segmentation using a selective and iterative method for performance level estimation (simple)," *Medical Imaging, IEEE Transactions on*, vol. 29, no. 12, pp. 2000–2008, 2010.

S. Lankton and A. Tannenbaum, "Localizing region-based active contours," *Image Processing, IEEE Transactions on*, vol. 17, no. 11, pp. 2029–2039, 2008.

S. M. Lawrie and S. S. Abukmeil, "Brain abnormality in schizophrenia. a systematic and quantitative review of volumetric magnetic resonance imaging studies." *The British Journal of Psychiatry*, vol. 172, no. 2, pp. 110–120, 1998.

I. D. Learmonth, C. Young, and C. Rorabeck, "The operation of the century: total hip replacement," *The Lancet*, vol. 370, no. 9597, pp. 1508–1519, 2007.

M.-Y. Lee, C.-C. Chang, C.-C. Lin, L.-J. Lo, and Y.-R. Chen, "Custom implant design for patients with cranial defects," *Engineering in Medicine and Biology Magazine, IEEE*, vol. 21, no. 2, pp. 38–44, 2002.

S. Lee, B. Goh, H. Tideman, and P. Stoelinga, "Modular endoprosthesis for mandibular reconstruction: A preliminary animal study," *International journal of oral and maxillofacial surgery*, vol. 37, no. 10, pp. 935–942, 2008.

S. Lee, B. Goh, H. Tideman, P. Stoelinga, and J. Jansen, "Modular endoprosthesis for mandibular body reconstruction: a clinical, micro-ct and histologic evaluation in eight macaca fascicularis," *International journal of oral and maxillofacial surgery*, vol. 38, no. 1, pp. 40–47, 2009.

M. Lengsfeld, R. Burchard, D. Günther, T. Pressel, J. Schmitt, R. Leppek, and P. Griss, "Femoral strain changes after total hip arthroplastypatient-specific finite element analyses 12 years after operation," *Medical engineering & physics*, vol. 27, no. 8, pp. 649–654, 2005.

B. R. Leon, F. J. O. Carrillo, H. M. Gonzalez, and J. L. B. Franco, "Mandibular reconstruction with the free vascularized fibular flap: Utility of three-dimensional computerized tomography," *Journal of reconstructive microsurgery*, vol. 15, no. 02, pp. 91–97, 1999.

K.-S. Leung, V. Alt, I. Kempf, H. Haarman, G. Taglang, R. Schnettler, and H. Seidel, *Practice of intramedullary locked nails: New developments in techniques and applications.* Springer, 2006, vol. 3.

D. Levine, P. D. Barnes, J. R. Madsen, J. Abbott, T. Mehta, and R. R. Edelman, "Central nervous system abnormalities assessed with prenatal magnetic resonance imaging," *Obstetrics & Gynecology*, vol. 94, no. 6, pp. 1011–1019, 1999.

M. Levoy, "Display of surfaces from volume data," *Computer Graphics and Applications, IEEE*, vol. 8, no. 3, pp. 29–37, 1988.

C. Li, C. Xu, C. Gui, and M. D. Fox, "Distance regularized level set evolution and its application to image segmentation," *Image Processing, IEEE Transactions on*, vol. 19, no. 12, pp. 3243–3254, 2010.

P. Li, L. Shen, J. Li, R. Liang, W. Tian, and W. Tang, "Optimal design of an individual endoprosthesis for the reconstruction of extensive mandibular defects with finite element analysis," *Journal of Cranio-Maxillofacial Surgery*, vol. 42, no. 1, pp. 73–78, 2014.

X. Liang, I. Lambrichts, Y. Sun, K. Denis, B. Hassan, L. Li, R. Pauwels, and R. Jacobs, "A comparative evaluation of cone beam computed tomography (cbct) and multi-slice ct (msct). part ii: On 3d model accuracy," *European journal of radiology*, vol. 75, no. 2, pp. 270–274, 2010.

Y.-P. Lin, C.-T. Wang, and K.-R. Dai, "Reverse engineering in cad model reconstruction of customized artificial joint," *Medical Engineering & Physics*, vol. 27, no. 2, pp. 189–193, 2005.

J. Lindon, G. Tranter, and D. Koppenaal, *ONLINE Encyclopedia of Spectroscopy and Spectrometry, 2nd Edition: 3 volume set.* Elsevier Science, 2010.

W. E. Lorensen and H. E. Cline, "Marching cubes: A high resolution 3d surface construction algorithm," in *ACM siggraph computer graphics*, vol. 21, no. 4. ACM, 1987, pp. 163–169.

L. Luccheseyz and S. Mitray, "Color image segmentation: A state-of-the-art survey," *Image Processing, Vision, and Pattern Recognition*, vol. 67, no. 2, pp. 207–221, 2001.

M. Lyons and R. Baxendale, "A preliminary electromyographic study of bite force and jaw-closing muscle fatigue in human subjects with advanced tooth wear," *Journal of Oral Rehabilitation*, vol. 17, no. 4, pp. 311–318, 1990.

Z. Ma, J. M. R. Tavares, R. N. Jorge, and T. Mascarenhas, "A review of algorithms for medical image segmentation and their applications to the female pelvic cavity," *Computer Methods in Biomechanics and Biomedical Engineering*, vol. 13, no. 2, pp. 235–246, 2010.

J. MacQueen *et al.*, "Some methods for classification and analysis of multivariate observations," in *Proceedings of the fifth Berkeley symposium on mathematical statistics and probability*, vol. 1, no. 281-297. California, USA, 1967, p. 14.

S. Mader and P. Galliart, *Understanding Human Anatomy and Physiology*. McGraw-Hill Higher Education, 2005.

D. P. Madsen, W. J. Sampson, and G. C. Townsend, "Craniofacial reference plane variation and natural head position," *The European Journal of Orthodontics*, vol. 30, no. 5, pp. 532–540, 2008.

D. Magee, *Orthopedic Physical Assessment*. Elsevier Health Sciences, 2014.

B. Mahaisavariya, K. Sitthiseripratip, T. Tongdee, E. L. Bohez, J. Vander Sloten, and P. Oris, "Morphological study of the proximal femur: a new method of geometrical assessment using 3-dimensional reverse engineering," *Medical engineering & physics*, vol. 24, no. 9, pp. 617–622, 2002.

M. Mahesh, *MDCT Physics: The Basics - Technology, Image Quality and Radiation Dose*. Lippincott Williams & Wilkins, 2009.

R. M. S. Malhotra, *Total Hip Arthroplasty*, ser. Mastering Orthopedic Techniques. Jaypee Brothers, Medical Publishers, 2011.

S. G. Mallat, "A theory for multiresolution signal decomposition: the wavelet representation," *Pattern Analysis and Machine Intelligence, IEEE Transactions on*, vol. 11, no. 7, pp. 674–693, 1989.

S. G. Mallat and S. Zhong, *Complete signal representation with multiscale edges*. New York University, Courant Institute of Mathematical Sciences, Computer Science Division, 1989.

P. Maló, B. Rangert, and M. Nobre, ""all-on-four" immediate-function concept with brånemark system® implants for completely edentulous mandibles: A retrospective clinical study," *Clinical implant dentistry and related research*, vol. 5, no. s1, pp. 2–9, 2003.

P. Maló, B. Rangert, and M. Nobre, "All-on-4 immediate-function concept with brånemark system® implants for completely edentulous maxillae: A 1-year retrospective clinical study," *Clinical implant dentistry and related research*, vol. 7, no. s1, pp. s88–s94, 2005.

A. Maloul, J. Fialkov, and C. Whyne, "The impact of voxel size-based inaccuracies on the mechanical behavior of thin bone structures," *Annals of biomedical engineering*, vol. 39, no. 3, pp. 1092–1100, 2011.

J. A. Mandell, D. R. Carter, S. B. Goodman, D. J. Schurman, and G. S. Beaupré, "A conical-collared intramedullary stem can improve stress transfer and limit micromotion," *Clinical Biomechanics*, vol. 19, no. 7, pp. 695–703, 2004.

J. P. McAuley, E. S. Szuszczewicz, A. Young, and C. A. Engh Sr, "Total hip arthroplasty in patients 50 years and younger," *Clinical orthopaedics and related research*, vol. 418, pp. 119–125, 2004.

P. McGinnis, *Biomechanics of Sport and Exercise*. Human Kinetics, 2013.

B. McGrory, B. Morrey, T. Cahalan, K. An, and M. Cabanela, "Effect of femoral offset on range of motion and abductor muscle strength after total hip arthroplasty," *Journal of Bone & Joint Surgery, British Volume*, vol. 77, no. 6, pp. 865–869, 1995.

G. Melcher, B. Claudi, U. Schlegel, S. Perren, G. Printzen, and J. Munzinger, "Influence of type of medullary nail on the development of local infection. an experimental study of solid and slotted nails in rabbits," *Journal of Bone & Joint Surgery, British Volume*, vol. 76, no. 6, pp. 955–959, 1994.

G. A. Melcher, A. Metzdorf, U. Schlegel, W. J. Ziegler, S. M. Perren, and G. Printzen, "Influence of reaming versus nonreaming in intramedullary nailing on local infection rate: experimental investigation in rabbits," *Journal of Trauma-Injury, Infection, and Critical Care*, vol. 39, no. 6, pp. 1123–1128, 1995.

P. R. Mendonça, D. Padfield, J. Miller, and M. Turek, "Bias in the localization of curved edges," in *Computer Vision-ECCV 2004*. Springer, 2004, pp. 554–565.

F. Meneghini and P. Biondi, *Clinical Facial Analysis: Elements, Principles, and Techniques*. Springer Berlin Heidelberg, 2012.

M. I. Meurer, K. P. Souza, A. von Wangenheim, D. D. Abdala, L. F. de Souza Nobre, E. Meurer, and J. V. L. da Silva, "Influence of tomographic slice thickness and field of view variation on the reproduction of thin bone structures for rapid prototyping purposesan in vitro study," *Open Journal of Radiology*, vol. 3, p. 12, 2013.

C. Meyer, J.-L. Kahn, P. Boutemi, and A. Wilk, "Photoelastic analysis of bone deformation in the region of the mandibular condyle during mastication," *Journal of Cranio-Maxillofacial Surgery*, vol. 30, no. 3, pp. 160–169, 2002.

F. Meyer and S. Beucher, "Morphological segmentation," *Journal of visual communication and image representation*, vol. 1, no. 1, pp. 21–46, 1990.

E. H. Miashiro, E. N. Fujikib, E. N. Yamaguchi, T. Chikude, L. H. S. Rodrigues, G. M. Fontes, and F. B. Rosa, "Preoperative planning of primary total hip arthroplasty using conventional radiographs," *Revista Brasileira de Ortopedia*, vol. 49, no. 2, pp. 140–148, 2014.

M. Miloro, G. Ghali, P. Larsen, and P. Waite, *Peterson's Principles of Oral and Maxillofacial Surgery*, ser. Peterson's Principles of Oral and Maxillofacial Surgery. B C Decker, 2004, no. vol. 1.

C. E. Misch, *Contemporary implant dentistry*. Elsevier Health Sciences, 2007.

L. Mitchell, *An Introduction to Orthodontics*. OUP Oxford, 2013.

B. Modayur, J. Prothero, G. Ojemann, K. Maravilla, and J. Brinkley, "Visualization-based mapping of language function in the brain," *Neuroimage*, vol. 6, no. 4, pp. 245–258, 1997.

C. F. Moorrees and M. R. Kean, "Natural head position, a basic consideration in the interpretation of cephalometric radiographs," *American Journal of Physical Anthropology*, vol. 16, no. 2, pp. 213–234, 1958.

M. Morandi, T. Banka, G. P. Gaiarsa, S. T. Guthrie, J. Khalil, J. Hoegler, and B. Lindeque, "Intramedullary nailing of tibial fractures: review of surgical techniques and description of a percutaneous lateral suprapatellar approach," *Orthopedics*, vol. 33, no. 3, pp. 172–179, 2010.

I. Mori and Y. Machida, "Deriving the modulation transfer function of ct from extremely noisy edge profiles," *Radiological physics and technology*, vol. 2, no. 1, pp. 22–32, 2009.

J. Morrison, "The mechanics of the knee joint in relation to normal walking," *Journal of biomechanics*, vol. 3, no. 1, pp. 51–61, 1970.

J. F. Moscoso, J. Keller, E. Genden, H. Weinberg, H. F. Biller, D. Buchbinder, and M. L. Urken, "Vascularized bone flaps in oromandibular reconstruction: a comparative anatomic study of bone stock from various donor sites to assess suitability for enosseous dental implants," *Archives of Otolaryngology–Head & Neck Surgery*, vol. 120, no. 1, pp. 36–43, 1994.

K. Mudry, R. Plonsey, and J. Bronzino, *Biomedical Imaging*, ser. Principles and Applications in Engineering. Taylor & Francis, 2003.

M. Müller, S. Perren, M. Allgöwer, and A. für Osteosynthesefragen, *Manual of Internal Fixation: Techniques Recommended by the AO-ASIF Group*. Springer-Verlag, 1991.

D. Mumford and J. Shah, "Optimal approximations by piecewise smooth functions and associated variational problems," *Communications on pure and applied mathematics*, vol. 42, no. 5, pp. 577–685, 1989.

B. Muralikrishnan and J. Raja, *Computational surface and roundness metrology*. Springer Science & Business Media, 2008.

O. K. Muratoglu, C. R. Bragdon, D. O'Connor, R. S. Perinchief, D. M. Estok II, M. Jasty, and W. H. Harris, "Larger diameter femoral heads used in conjunction with a highly cross-linked ultra–high molecular weight polyethylene: a new concept," *The Journal of arthroplasty*, vol. 16, no. 8, pp. 24–30, 2001.

O. K. Muratoglu, C. R. Bragdon, D. O. O'Connor, M. Jasty, and W. H. Harris, "A novel method of cross-linking ultra-high-molecular-weight polyethylene to improve wear, reduce oxidation, and retain mechanical properties: recipient of the 1999 hap paul award," *The Journal of arthroplasty*, vol. 16, no. 2, pp. 149–160, 2001.

K. Nagy, L. Borbely, A. Kovacs, A. Fazekas, I. Vajdovich, and A. Mari, "Implant-prosthetic rehabilitation after segmental mandibulectomy and bone grafting." *Journal of long-term effects of medical implants*, vol. 9, no. 3, pp. 185–191, 1998.

N. Narra, J. Valášek, M. Hannula, P. Marcián, G. K. Sándor, J. Hyttinen, and J. Wolff, "Finite element analysis of customized reconstruction plates for mandibular continuity defect therapy," *Journal of biomechanics*, vol. 47, no. 1, pp. 264–268, 2014.

A. Natali, *Dental Biomechanics*. Taylor & Francis, 2003.

D. T. Nicholson, C. Chalk, W. R. J. Funnell, and S. J. Daniel, "Can virtual reality improve anatomy education? a randomised controlled study of a computer-generated three-dimensional anatomical ear model," *Medical Education*, vol. 40, no. 11, pp. 1081–1087, 2006.

L. Nickels, "World's first patient-specific jaw implant," *Metal Powder Report*, vol. 67, no. 2, pp. 12–14, 2012.

E. L. Nickoloff and R. Riley, "A simplified approach for modulation transfer function determinations in computed tomography," *Medical physics*, vol. 12, no. 4, pp. 437–442, 1985.

J. Nilsson and A. Thorstensson, "Ground reaction forces at different speeds of human walking and running," *Acta Physiologica Scandinavica*, vol. 136, no. 2, pp. 217–227, 1989.

T. Nishioka, T. Shiga, H. Shirato, E. Tsukamoto, K. Tsuchiya MD, T. Kato, K. Ohmori, A. Yamazaki, H. Aoyama, S. Hashimoto *et al.*, "Image fusion between¡ sup¿ 18¡/sup¿ fdg-pet and mri/ct for radiotherapy planning of oropharyngeal and nasopharyngeal carcinomas," *International Journal of Radiation Oncology* Biology* Physics*, vol. 53, no. 4, pp. 1051–1057, 2002.

P. C. Noble, J. W. Alexander, L. J. Lindahl, D. T. Yew, W. M. Granberry, and H. S. Tullos, "The anatomic basis of femoral component design," *Clinical orthopaedics and related research*, vol. 235, pp. 148–165, 1988.

S. E. Nork, A. K. Schwartz, J. Agel, S. K. Holt, J. L. Schrick, and R. A. Winquist, "Intramedullary nailing of distal metaphyseal tibial fractures," *The Journal of Bone & Joint Surgery*, vol. 87, no. 6, pp. 1213–1221, 2005.

T. F. Novacheck, "The biomechanics of running," *Gait & posture*, vol. 7, no. 1, pp. 77–95, 1998.

D. O'Connor, D. Burke, and W. Harris, "Bone-implant micromotion in titanium ingrowth hip stems," *Trans Orthop Res Soc*, vol. 33, p. 97, 1987.

M. Ohkubo, S. Wada, M. Kunii, T. Matsumoto, and K. Nishizawa, "Imaging of small spherical structures in ct: simulation study using measured point spread function," *Medical & biological engineering & computing*, vol. 46, no. 3, pp. 273–282, 2008.

K. Oka, T. Murase, H. Moritomo, A. Goto, K. Sugamoto, and H. Yoshikawa, "Accuracy analysis of three-dimensional bone surface models of the forearm constructed from multidetector computed tomography data," *The International Journal of Medical Robotics and Computer Assisted Surgery*, vol. 5, no. 4, pp. 452–457, 2009.

M. Oliveira, J. Alves, and L. Menezes, "Algorithms and strategies for treatment of large deformation frictional contact in the numerical simulation of deep drawing process," *Archives of Computational Methods in Engineering*, vol. 15, no. 2, pp. 113–162, 2008.

S. P. Oosterhaven, G. P. Westert, R. M. Schaub, and A. Bilt, "Social and psychologic implications of missing teeth for chewing ability," *Community dentistry and oral epidemiology*, vol. 16, no. 2, pp. 79–82, 1988.

L. Osagie, M. Figgie, and M. Bostrom, "Custom total hip arthroplasty in skeletal dysplasia," *International orthopaedics*, vol. 36, no. 3, pp. 527–531, 2012.

S. Osher and R. Fedkiw, *Level Set Methods and Dynamic Implicit Surfaces*, ser. Applied Mathematical Sciences. Springer, 2003.

S. Osher and J. A. Sethian, "Fronts propagating with curvature-dependent speed: algorithms based on hamilton-jacobi formulations," *Journal of computational physics*, vol. 79, no. 1, pp. 12–49, 1988.

L. T. Östrup and J. M. Fredrickson, "Reconstruction of mandibular defects after radiation, using a free, living bone graft transferred by microvascular anastomoses: An experimental study." *Plastic and reconstructive surgery*, vol. 55, no. 5, pp. 563–572, 1975.

N. Otsu, "A threshold selection method from gray-level histograms," *Automatica*, vol. 11, no. 285-296, pp. 23–27, 1975.

S. J. Owen, "A survey of unstructured mesh generation technology." in *IMR*, 1998, pp. 239–267.

A. Pakdel, N. Robert, J. Fialkov, A. Maloul, and C. Whyne, "Generalized method for computation of true thickness and x-ray intensity information in highly blurred sub-millimeter bone features in clinical ct images," *Physics in medicine and biology*, vol. 57, no. 23, p. 8099, 2012.

N. R. Pal and S. K. Pal, "A review on image segmentation techniques," *Pattern recognition*, vol. 26, no. 9, pp. 1277–1294, 1993.

E. Pantin, J.-L. Starck, and F. Murtagh, "Deconvolution and blind deconvolution in astronomy," *Blind image deconvolution: theory and applications*, pp. 100–138, 2007.

J. Paphangkorakit and J. Osborn, "The effect of pressure on a maximum incisal bite force in man," *Archives of Oral Biology*, vol. 42, no. 1, pp. 11–17, 1997.

N. Paragios, O. Mellina-Gottardo, and V. Ramesh, "Gradient vector flow fast geodesic active contours," in *Computer Vision, 2001. ICCV 2001. Proceedings. Eighth IEEE International Conference on*, vol. 1. IEEE, 2001, pp. 67–73.

H. A. Paul, W. L. Bargar, B. Mittlestadt, B. Musits, R. H. Taylor, P. Kazanzides, J. Zuhars, B. Williamson, and W. Hanson, "Development of a surgical robot for cementless total hip arthroplasty," *Clinical Orthopaedics and related research*, vol. 285, pp. 57–66, 1992.

J. Pawley, *Handbook of Biological Confocal Microscopy*. Springer, 2010.

U. Pazzaglia, F. Brossa, G. Zatti, R. Chiesa, and L. Andrini, "The relevance of hydroxyapatite and spongious titanium coatings in fixation of cementless stems," *Archives of orthopaedic and trauma surgery*, vol. 117, no. 4-5, pp. 279–285, 1998.

N. Peckitt, "Stereoscopic lithography: customized titanium implants in orofacial reconstruction," *British Journal of Oral and Maxillofacial Surgery*, vol. 37, no. 5, pp. 353–369, 1999.

M. Peled, I. A. El-Naaj, Y. Lipin, and L. Ardekian, "The use of free fibular flap for functional mandibular reconstruction," *Journal of oral and maxillofacial surgery*, vol. 63, no. 2, pp. 220–224, 2005.

R. Penzkofer, M. Maier, A. Nolte, G. von Oldenburg, K. Püschel, V. Bühren, and P. Augat, "Influence of intramedullary nail diameter and locking mode on the stability of tibial shaft fracture fixation," *Archives of orthopaedic and trauma surgery*, vol. 129, no. 4, pp. 525–531, 2009.

P. Perona and J. Malik, "Scale-space and edge detection using anisotropic diffusion," *Pattern Analysis and Machine Intelligence, IEEE Transactions on*, vol. 12, no. 7, pp. 629–639, 1990.

S. H. Pettersen, T. S. Wik, and B. Skallerud, "Subject specific finite element analysis of stress shielding around a cementless femoral stem," *Clinical Biomechanics*, vol. 24, no. 2, pp. 196–202, 2009.

J. Pfeil and W. Siebert, *Minimally Invasive Surgery in Total Hip Arthroplasty.* Springer, 2010.

D. L. Pham, C. Xu, and J. L. Prince, "Current methods in medical image segmentation 1," *Annual review of biomedical engineering*, vol. 2, no. 1, pp. 315–337, 2000.

S. Pickering and D. Armstrong, "Focus on alignment in total knee replacement," *J Bone Joint Surg*, pp. 1–3, 2012.

R. Pilliar, J. Lee, and C. Maniatopoulos, "Observations on the effect of movement on bone ingrowth into porous-surfaced implants." *Clinical Orthopaedics and Related Research*, vol. 208, pp. 108–113, 1986.

M. Pogrel, S. Podlesh, J. P. Anthony, and J. Alexander, "A comparison of vascularized and nonvascularized bone grafts for reconstruction of mandibular continuity defects," *Journal of oral and maxillofacial surgery*, vol. 55, no. 11, pp. 1200–1206, 1997.

R. Pohle and K. D. Toennies, "Segmentation of medical images using adaptive region growing," in *Medical Imaging 2001.* International Society for Optics and Photonics, 2001, pp. 1337–1346.

D. Poitout, *Biomechanics and Biomaterials in Orthopedics.* Springer, 2004.

A. Popovic, M. de la Fuente, M. Engelhardt, and K. Radermacher, "Statistical validation metric for accuracy assessment in medical image segmentation," *International Journal of Computer Assisted Radiology and Surgery*, vol. 2, no. 3-4, pp. 169–181, 2007.

A. Praemer, S. Furner, D. Rice, and A. A. of Orthopaedic Surgeons, *Musculoskeletal Conditions in the United States.* American Academy of Orthopaedic Surgeons, 1999.

M. Prastawa, E. Bullitt, S. Ho, and G. Gerig, "A brain tumor segmentation framework based on outlier detection," *Medical Image Analysis*, vol. 8, no. 3, pp. 275–283, 2004.

B. Preim and D. Bartz, *Visualization in Medicine: Theory, Algorithms, and Applications*, ser. The Morgan Kaufmann Series in Computer Graphics. Elsevier Science, 2007.

S. Prevrhal, K. Engelke, and W. A. Kalender, "Accuracy limits for the determination of cortical width and density: the influence of object size and ct imaging parameters," *Physics in medicine and biology*, vol. 44, no. 3, p. 751, 1999.

W. Proffit, H. Fields, and D. Sarver, *Contemporary Orthodontics*. Elsevier Health Sciences, 2006.

M. Prokop and M. Galanski, *Spiral and Multislice Computed Tomography of the Body*. Thieme, 2011.

J. Radon, "Über die bestimmung von funktionen durch ihre integralwerte längs gewisser mannigfaltigkeiten," *Classic papers in modern diagnostic radiology*, p. 5, 2005.

A. Ramos, A. Completo, C. Relvas, M. Mesnard, and J. Simões, "Straight, semi-anatomic and anatomic tmj implants: the influence of condylar geometry and bone fixation screws," *Journal of Cranio-Maxillofacial Surgery*, vol. 39, no. 5, pp. 343–350, 2011.

K. Rathnayaka, T. Sahama, M. A. Schuetz, and B. Schmutz, "Effects of ct image segmentation methods on the accuracy of long bone 3d reconstructions," *Medical engineering & physics*, vol. 33, no. 2, pp. 226–233, 2011.

D. T. Reilly and A. H. Burstein, "The elastic and ultimate properties of compact bone tissue," *Journal of biomechanics*, vol. 8, no. 6, pp. 393–405, 1975.

C. Revol-Muller, F. Peyrin, Y. Carrillon, and C. Odet, "Automated 3d region growing algorithm based on an assessment function," *Pattern Recognition Letters*, vol. 23, no. 1, pp. 137–150, 2002.

W. H. Richardson, "Bayesian-based iterative method of image restoration," *JOSA*, vol. 62, no. 1, pp. 55–59, 1972.

N. Robitaille and S. Duchesne, "Label fusion strategy selection," *International journal of biomedical imaging*, vol. 2012, 2012.

C. Rockwood, R. Bucholz, D. Green, C. Court-Brown, J. Heckman, and P. Tornetta, *Rockwood and Green's Fractures in Adults*, ser. Fractures in Adults. Wolters Kluwer Health/Lippincott Williams & Wilkins, 2010, no. vol. 1.

J. B. Roerdink and A. Meijster, "The watershed transform: Definitions, algorithms and parallelization strategies," *Fundamenta Informaticae*, vol. 41, no. 1, pp. 187–228, 2000.

T. Rohlfing and C. R. Maurer Jr, "Shape-based averaging," *Image Processing, IEEE Transactions on*, vol. 16, no. 1, pp. 153–161, 2007.

C. H. Rorabeck, R. B. Bourne, A. Laupacis, D. Feeny, C. Wong, P. Tugwell, K. Leslie, and R. Bullas, "A double-blind study of 250 cases comparing cemented with cementless total hip arthroplasty: cost-effectiveness and its impact on health-related quality of life," *Clinical orthopaedics and related research*, vol. 298, pp. 156–164, 1994.

J.-L. Rose, C. Revol-Muller, M. Almajdub, E. Chereul, and C. Odet, "Shape prior integrated in an automated 3d region growing method," in *Image Processing, 2007. ICIP 2007. IEEE International Conference on*, vol. 1. IEEE, 2007, pp. I–53.

P. Rothuizen, L. Van Erning, and R. Huiskes, "The accuracy of criteria for automatic 3-d graphics reconstruction of bone from computer tomography," in *Biomechanics: basic and applied research*. Springer, 1987, pp. 109–114.

P. Rubin, P. Leyvraz, J. Aubaniac, J. Argenson, P. Esteve, and B. De Roguin, "The morphology of the proximal femur. a three-dimensional radiographic analysis," *Journal of Bone & Joint Surgery, British Volume*, vol. 74, no. 1, pp. 28–32, 1992.

T. Rüedi, R. Buckley, and C. Moran, *AO Principles of Fracture Management: Principles*, ser. AO Principles of Fracture Management. Thieme, 2007.

A. Ruiz, W. Kealey, and G. McCoy, "Implant failure in tibial nailing," *Injury*, vol. 31, no. 5, pp. 359–362, 2000.

T. V. S. Jayaraman, S. Esakkirajam, *Digital Image Processing*. McGraw-Hill Education (India) Pvt Limited, 2011.

M. R. Sabuncu, B. T. Yeo, K. Van Leemput, B. Fischl, and P. Golland, "A generative model for image segmentation based on label fusion," *Medical Imaging, IEEE Transactions on*, vol. 29, no. 10, pp. 1714–1729, 2010.

E. Samei, M. J. Flynn, and D. A. Reimann, "A method for measuring the presampled mtf of digital radiographic systems using an edge test device," *Medical Physics*, vol. 25, no. 1, pp. 102–113, 1998.

N. Samman, W. Luck, L. Cheung, H. Tideman, and R. Clark, "Custom-made titanium mandibular reconstruction tray," *Australian dental journal*, vol. 44, no. 3, pp. 195–199, 1999.

R. Sanders, I. Jersinovich, J. Anglen, T. DiPasquale, and D. Herscovici Jr, "The treatment of open tibial shaft fractures using an interlocked intramedullary nail without reaming." *Journal of orthopaedic trauma*, vol. 8, no. 6, pp. 504–510, 1994.

E. Santamaria, F.-C. Wei, and H.-C. Chen, "Fibula osteoseptocutaneous flap for reconstruction of osteoradionecrosis of the mandible." *Plastic and reconstructive surgery*, vol. 101, no. 4, pp. 921–929, 1998.

S. Sathasivam, P. S. Walker, I. M. Pinder, S. R. Cannon, and T. W. Briggs, "Custom constrained condylar total knees using cad-cam," *The Knee*, vol. 6, no. 1, pp. 49–53, 1999.

K. Sato, T. Shirakawa, H. Sakata, and S. Asanuma, "Effectiveness of the analysis of craniofacial morphology and pharyngeal airway morphology in the treatment of children with obstructive sleep apnoea syndrome," *Dento-Maxillo-Facial Radiology*, 2014.

Y. Sato, H. Tanaka, T. Nishii, K. Nakanishi, N. Sugano, T. Kubota, H. Nakamura, H. Yoshikawa, T. Ochi, and S. Tamura, "Limits on the accuracy of 3-d thickness measurement in magnetic resonance images-effects of voxel anisotropy," *Medical Imaging, IEEE Transactions on*, vol. 22, no. 9, pp. 1076–1088, 2003.

P. Schandelmaier, C. Krettek, and H. Tscherne, "Biomechanical study of nine different tibia locking nails," *Journal of orthopaedic trauma*, vol. 10, no. 1, pp. 37–44, 1996.

P. Schandelmaier, C. Krettek, J. Rudolf, A. Kohl, B. E. Katz, and H. Tscherne, "Superior results of tibial rodding versus external fixation in grade 3b fractures," *Clinical orthopaedics and related research*, vol. 342, pp. 164–172, 1997.

T. Scheerlinck, "Primary hip arthroplasty templating on standard radiographs: a stepwise approach," *Acta Orthop Belg*, vol. 76, no. 4, pp. 432–442, 2010.

H. Schell, D. Epari, J. Kassi, H. Bragulla, H. Bail, and G. Duda, "The course of bone healing is influenced by the initial shear fixation stability," *Journal of orthopaedic research*, vol. 23, no. 5, pp. 1022–1028, 2005.

A. H. Schmidt, C. G. Finkemeier, and P. TornettaIII, "Treatment of closed tibial fractures," *The Journal of Bone & Joint Surgery*, vol. 85, no. 2, pp. 352–368, 2003.

B. Schmutz, K. Rathnayaka, M. Wullschleger, J. Meek, and M. Schuetz, "Quantitative fit assessment of tibial nail designs using 3d computer modelling," *Injury*, vol. 41, no. 2, pp. 216–219, 2010.

B. Schmutz, M. E. Wullschleger, H. Noser, M. Barry, J. Meek, and M. A. Schütz, "Fit optimisation of a distal medial tibia plate," *Computer methods in biomechanics and biomedical engineering*, vol. 14, no. 04, pp. 359–364, 2011.

D. Schoen, *Adult Orthopaedic Nursing*. Lippincott, 2000.

M. Schuenke and E. Schulte, *General Anatomy and Musculoskeletal System (THIEME Atlas of Anatomy)*, ser. THIEME Atlas of Anatomy Series. Thieme, 2011.

G. Scuderi and A. Tria, *Knee Arthroplasty Handbook: Techniques in Total Knee and Revision Arthroplasty*, ser. Medicine (Springer-11650; ZDB-2-SME). Springer, 2006.

A. Z. Senalp, O. Kayabasi, and H. Kurtaran, "Static, dynamic and fatigue behavior of newly designed stem shapes for hip prosthesis using finite element analysis," *Materials & design*, vol. 28, no. 5, pp. 1577–1583, 2007.

N. Senthilkumaran and R. Rajesh, "Image segmentation-a survey of soft computing approaches," in *Advances in Recent Technologies in Communication and Computing, 2009. ARTCom'09. International Conference on.* IEEE, 2009, pp. 844–846.

J. A. Sethian, *Level set methods and fast marching methods: evolving interfaces in computational geometry, fluid mechanics, computer vision, and materials science*. Cambridge university press, 1999, vol. 3.

M. Sezgin *et al.*, "Survey over image thresholding techniques and quantitative performance evaluation," *Journal of Electronic imaging*, vol. 13, no. 1, pp. 146–168, 2004.

D. W. Shattuck, S. R. Sandor-Leahy, K. A. Schaper, D. A. Rottenberg, and R. M. Leahy, "Magnetic resonance image tissue classification using a partial volume model," *NeuroImage*, vol. 13, no. 5, pp. 856–876, 2001.

Y. Shen, J. Sun, J. Li, J. Shi, and A. Ow, "Long-term results of partial double-barrel vascularized fibula graft in symphysis for extensive mandibular reconstruction," *Journal of Oral and Maxillofacial Surgery*, vol. 70, no. 4, pp. 983–991, 2012.

L. A. Shepp and B. F. Logan, "The fourier reconstruction of a head section," *Nuclear Science, IEEE Transactions on*, vol. 21, no. 3, pp. 21–43, 1974.

J. Shi and J. Malik, "Normalized cuts and image segmentation," *Pattern Analysis and Machine Intelligence, IEEE Transactions on*, vol. 22, no. 8, pp. 888–905, 2000.

T. Shibahara, H. Noma, Y. Furuya, and R. Takaki, "Fracture of mandibular reconstruction plates used after tumor resection," *Journal of oral and maxillofacial surgery*, vol. 60, no. 2, pp. 182–185, 2002.

D. Shier, J. Butler, and R. Lewis, *Hole's Essentials of Human Anatomy & Physiology*. McGraw-Hill Education, 2011.

Z. Shuxian, Z. Wanhua, and L. Bingheng, "3d reconstruction of the structure of a residual limb for customising the design of a prosthetic socket," *Medical engineering & physics*, vol. 27, no. 1, pp. 67–74, 2005.

C. A. Simmons, S. A. Meguid, and R. M. Pilliar, "Differences in osseointegration rate due to implant surface geometry can be explained by local tissue strains," *Journal of Orthopaedic Research*, vol. 19, no. 2, pp. 187–194, 2001.

C. A. Simmons, S. A. Meguid, and R. M. Pilliar, "Mechanical regulation of localized and appositional bone formation around bone-interfacing implants," *Journal of biomedical materials research*, vol. 55, no. 1, pp. 63–71, 2001.

Simpleware, *ScanIP +FE +CAD Reference Guide*, Exeter, United Kingdom, 2011.

S. Singare, L. Dichen, L. Bingheng, L. Yanpu, G. Zhenyu, and L. Yaxiong, "Design and fabrication of custom mandible titanium tray based on rapid prototyping," *Medical engineering & physics*, vol. 26, no. 8, pp. 671–676, 2004.

S. Singare, L. Dichen, L. Bingheng, L. Yanpu, G. Zhenyu, and L. Yaxiong, "Design and fabrication of custom mandible titanium tray based on rapid prototyping," *Medical engineering & physics*, vol. 26, no. 8, pp. 671–676, 2004.

S. Singare, L. Dichen, L. Bingheng, G. Zhenyu, and L. Yaxiong, "Customized design and manufacturing of chin implant based on rapid prototyping," *Rapid Prototyping Journal*, vol. 11, no. 2, pp. 113–118, 2005.

G. Singh, *Textbook of Orthodontics*, ser. G - Reference,Information and Interdisciplinary Subjects Series. Jaypee Brothers, Medical Publishers, 2008.

R. Sinha, *Hip Replacement: Current Trends and Controversies*. Taylor & Francis, 2002.

J. Skedros, M. Mason, M. Nelson, and R. Bloebaum, "Evidence of structural and material adaptation to specific strain features in cortical bone," *The Anatomical Record*, vol. 246, no. 1, pp. 47–63, 1996.

J. D. Slover, H. E. Rubash, H. Malchau, and J. A. Bosco, "Cost-effectiveness analysis of custom total knee cutting blocks," *The Journal of arthroplasty*, vol. 27, no. 2, pp. 180–185, 2012.

A. J. Smith, P. Dieppe, K. Vernon, M. Porter, and A. W. Blom, "Failure rates of stemmed metal-on-metal hip replacements: analysis of data from the national joint registry of england and wales," *The Lancet*, vol. 379, no. 9822, pp. 1199–1204, 2012.

S. Smith, D. Dowson, and A. Goldsmith, "The effect of femoral head diameter upon lubrication and wear of metal-on-metal total hip replacements," *Proceedings of the Institution of Mechanical Engineers, Part H: Journal of Engineering in Medicine*, vol. 215, no. 2, pp. 161–170, 2001.

S. Smith, *The Scientist and Engineer's Guide to Digital Signal Processing*. California Technical Pub., 1997.

D. H. Sochart and K. Hardinge, "Comparison of the wrightington fc hip with the charnley low-friction arthroplasty 10-to 15-year results and survival analysis," *Journal of Bone & Joint Surgery, British Volume*, vol. 80, no. 4, pp. 577–584, 1998.

A.-L. Söderholm, D. Hallikainen, and C. Lindqvist, "Radiologic follow-up of bone transplants to bridge mandibular continuity defects," *Oral surgery, oral medicine, oral pathology*, vol. 73, no. 3, pp. 253–261, 1992.

P. Soille and L. M. Vincent, "Determining watersheds in digital pictures via flooding simulations," in *Lausanne-DL tentative*. International Society for Optics and Photonics, 1990, pp. 240–250.

C. Solomon and T. Breckon, *Fundamentals of Digital Image Processing: A Practical Approach with Examples in Matlab*. Wiley, 2011.

A. D. Speirs, M. O. Heller, G. N. Duda, and W. R. Taylor, "Physiologically based boundary conditions in finite element modelling," *Journal of biomechanics*, vol. 40, no. 10, pp. 2318–2323, 2007.

A. D. Speirs, M. O. Heller, W. R. Taylor, G. N. Duda, and C. Perka, "Influence of changes in stem positioning on femoral loading after thr using a short-stemmed hip implant," *Clinical biomechanics*, vol. 22, no. 4, pp. 431–439, 2007.

K. Spencer, A. Sizeland, G. Taylor, and D. Wiesenfeld, "The use of titanium mandibular reconstruction plates in patients with oral cancer," *International journal of oral and maxillofacial surgery*, vol. 28, no. 4, pp. 288–290, 1999.

B. Starly, Z. Fang, W. Sun, A. Shokoufandeh, and W. Regli, "Three-dimensional reconstruction for medical-cad modeling," *Computer-Aided Design and Applications*, vol. 2, no. 1-4, pp. 431–438, 2005.

J. Stiehl, W. Konermann, R. Haaker, and A. DiGioia, *Navigation and MIS in Orthopedic Surgery*. Springer, 2007.

M. Stojkovic, M. Trajanovic, N. Vitkovic, J. Milovanovic, S. Arsic, and M. Mitkovic, "Referential geometrical entities for reverse modeling of geometry of femur," in *Proceedings of VIPIMAGE2009 - second thematic conference on computational vision and medical image processing, Porto, Portugal*, 2009, pp. 189–194.

J. Stolk, N. Verdonschot, and R. Huiskes, "Stair climbing is more detrimental to the cement in hip replacement than walking." *Clinical orthopaedics and related research*, vol. 405, pp. 294–305, 2002.

S. D. Stulberg, B. N. Stulberg, and R. L. Wixson, "The rationale, design characteristics, and preliminary results of a primary custom total hip prosthesis," *Clinical orthopaedics and related research*, vol. 249, pp. 79–96, 1989.

T. Su and R. Fernandes, "Microvascular reconstruction of the mandible: An argument for the fibula osteocutaneous free flap," *Revista Española de Cirugía Oral y Maxilofacial*, vol. 36, no. 1, pp. 1–8, 2014.

P. Suetens, *Fundamentals of Medical Imaging*, ser. Cambridge medicine. Cambridge University Press, 2009.

N. Sugano, K. Ohzono, T. Nishii, K. Haraguchi, T. Sakai, and T. Ochi, "Computed-tomography-based computer preoperative planning for total hip arthroplasty," *Computer aided surgery*, vol. 3, no. 6, pp. 320–324, 1998.

J. M. Sullivan, Z. Wu, and A. Kulkarni, "3d volume mesh generation of human organs using surface geometries created from the visible human data set," in *In Proceedings of the 3rd Visible Human Project Conference, NIH*, 2000, pp. 5–6.

M. Sussman, P. Smereka, and S. Osher, "A level set approach for computing solutions to incompressible two-phase flow," *Journal of Computational physics*, vol. 114, no. 1, pp. 146–159, 1994.

G. Swennen, F. Schutyser, and J. Hausamen, *Three-Dimensional Cephalometry: A Color Atlas and Manual*. Springer, 2005.

Synthes, "Expert tn tibial nail. surgical technique," Synthes GmbH, Tech. Rep., 2006.

L. Szilagyi, Z. Benyo, S. M. Szilágyi, and H. Adam, "Mr brain image segmentation using an enhanced fuzzy c-means algorithm," in *Engineering in Medicine and Biology Society, 2003. Proceedings of the 25th Annual International Conference of the IEEE*, vol. 1. IEEE, 2003, pp. 724–726.

D. Tanna, *Interlocking Nailing*, ser. G - Reference,Information and Interdisciplinary Subjects Series. Jaypee Brothers, Medical Publishers, 2010.

W. Tao, H. Jin, and Y. Zhang, "Color image segmentation based on mean shift and normalized cuts," *Systems, Man, and Cybernetics, Part B: Cybernetics, IEEE Transactions on*, vol. 37, no. 5, pp. 1382–1389, 2007.

G. I. Taylor, "Reconstruction of the mandible with free composite iliac bone grafts," *Annals of plastic surgery*, vol. 9, no. 5, pp. 361–376, 1982.

M. Taylor, K. Tanner, M. Freeman, and A. Yettram, "Stress and strain distribution within the intact femur: compression or bending?" *Medical engineering & physics*, vol. 18, no. 2, pp. 122–131, 1996.

P. Taylor, "Computer aids for decision-making in diagnostic radiology - a literature review," *Computer*, vol. 68, no. 813, 1995.

R. Texhammar, C. Colton, and F. Séquin, *AO/ASIF instruments and implants: a technical manual*. Springer-Verlag, 1994.

P. Thévenaz, T. Blu, and M. Unser, "Interpolation revisited [medical images application]," *Medical Imaging, IEEE Transactions on*, vol. 19, no. 7, pp. 739–758, 2000.

E. Thienpont, *Improving Accuracy in Knee Arthroplasty*, ser. G - Reference,Information and Interdisciplinary Subjects Series. Jaypee Brothers, Medical Publishers, 2012.

L. S. Tideman H., "The tl endoprosthesis for mandibular reconstruction - a metallic yet biological approach," *Asian Journal of Oral and Maxillofacial Surgery*, vol. 18, no. 5, 2006.

Y. Toki, "Principles of helical scanning," *Basic Principles and Clinical Applications of Helical Scan: Application of Continuous-Rotation CT*, pp. 110–20, 1993.

D. Tortopidis, M. Lyons, R. Baxendale, and W. Gilmour, "The variability of bite force measurement between sessions, in different positions within the dental arch," *Journal of oral rehabilitation*, vol. 25, no. 9, pp. 681–686, 1998.

C. Townsend, R. Beauchamp, B. Evers, and K. Mattox, *Sabiston Textbook of Surgery: Expert Consult Premium Edition: Enhanced Online Features*, ser. MD Consult. Elsevier Health Sciences, 2012.

W. E. Tracy, B. S. Savara, and J. W. Brant, "Relation of height, width and depth of the mandible*," *The Angle Orthodontist*, vol. 35, no. 4, pp. 269–277, 1965.

G. M. Treece, A. H. Gee, P. Mayhew, and K. Poole, "High resolution cortical bone thickness measurement from clinical ct data," *Medical image analysis*, vol. 14, no. 3, pp. 276–290, 2010.

P. T. Truc, T.-S. Kim, S. Lee, and Y.-K. Lee, "A study on the feasibility of active contours on automatic ct bone segmentation," *Journal of digital imaging*, vol. 23, no. 6, pp. 793–805, 2010.

J. K. Udupa, V. R. Leblanc, Y. Zhuge, C. Imielinska, H. Schmidt, L. M. Currie, B. E. Hirsch, and J. Woodburn, "A framework for evaluating image segmentation algorithms," *Computerized Medical Imaging and Graphics*, vol. 30, no. 2, pp. 75–87, 2006.

B. Uhlin and R. Hammer, "Attempted unreamed nailing in tibial fractures: a prospective consecutive series of 55 patients," *Acta Orthopaedica*, vol. 69, no. 3, pp. 301–305, 1998.

T. Van Eijden, "Biomechanics of the mandible," *Critical reviews in oral biology & medicine*, vol. 11, no. 1, pp. 123–136, 2000.

H. Van Oosterwyck, J. Duyck, J. Vander Sloten, G. Van der Perre, M. De Coomans, S. Lieven, R. Puers *et al.*, "The influence of bone mechanical properties and implant fixation upon bone loading around oral implants," *Clinical oral implants research*, vol. 9, no. 6, pp. 407–418, 1998.

P. W. Verbeek and L. J. Van Vliet, "On the location error of curved edges in low-pass filtered 2-d and 3-d images," *Pattern Analysis and Machine Intelligence, IEEE Transactions on*, vol. 16, no. 7, pp. 726–733, 1994.

B. Verbist, R. Joemai, W. Teeuwisse, W. Veldkamp, J. Geleijns, and J. Frijns, "Evaluation of 4 multisection ct systems in postoperative imaging of a cochlear implant: a human cadaver and phantom study," *American Journal of Neuroradiology*, vol. 29, no. 7, pp. 1382–1388, 2008.

M. Viceconti, R. Lattanzi, B. Antonietti, S. Paderni, R. Olmi, A. Sudanese, and A. Toni, "Ct-based surgical planning software improves the accuracy of total hip replacement preoperative planning," *Medical engineering & physics*, vol. 25, no. 5, pp. 371–377, 2003.

J. Victor, D. Van Doninck, L. Labey, B. Innocenti, P. Parizel, and J. Bellemans, "How precise can bony landmarks be determined on a ct scan of the knee?" *The Knee*, vol. 16, no. 5, pp. 358–365, 2009.

J.-P. Vidalain, "Twenty-year results of the cementless corail stem," *International orthopaedics*, vol. 35, no. 2, pp. 189–194, 2011.

P. S. Walker and D. D. Robertson, "Design and fabrication of cementless hip stems," *Clinical orthopaedics and related research*, vol. 235, pp. 25–34, 1988.

P. Walker, D. Schneeweis, S. Murphy, and P. Nelson, "Strains and micromotions of press-fit femoral stem prostheses," *Journal of biomechanics*, vol. 20, no. 7, pp. 693–702, 1987.

A. Waltimo, P. Kemppainen, and M. Könönen, "Maximal contraction force and endurance of human jaw-closing muscles in isometric clenching," *European Journal of Oral Sciences*, vol. 101, no. 6, pp. 416–421, 1993.

A. Wang, A. Essner, and R. Klein, "Effect of contact stress on friction and wear of ultra-high molecular weight polyethylene in total hip replacement," *Proceedings of the Institution of Mechanical Engineers, Part H: Journal of Engineering in Medicine*, vol. 215, no. 2, pp. 133–139, 2001.

H. Wang, B. Ji, W. Jiang, L. Liu, P. Zhang, W. Tang, W. Tian, and Y. Fan, "Three-dimensional finite element analysis of mechanical stress in symphyseal fractured human mandible reduced with miniplates during mastication," *Journal of Oral and Maxillofacial Surgery*, vol. 68, no. 7, pp. 1585–1592, 2010.

H. Wang and P. A. Yushkevich, "Spatial bias in multi-atlas based segmentation," in *Computer Vision and Pattern Recognition (CVPR), 2012 IEEE Conference on.* IEEE, 2012, pp. 909–916.

J. Wang, M. Ye, Z. Liu, and C. Wang, "Precision of cortical bone reconstruction based on 3d ct scans," *Computerized Medical Imaging and Graphics*, vol. 33, no. 3, pp. 235–241, 2009.

S. K. Warfield, K. H. Zou, and W. M. Wells, "Validation of image segmentation and expert quality with an expectation-maximization algorithm," in *Medical Image Computing and Computer-Assisted InterventionMICCAI 2002.* Springer, 2002, pp. 298–306.

S. K. Warfield, K. H. Zou, and W. M. Wells, "Simultaneous truth and performance level estimation (staple): an algorithm for the validation of image segmentation," *Medical Imaging, IEEE Transactions on*, vol. 23, no. 7, pp. 903–921, 2004.

T. Wehner, L. Claes, and U. Simon, "Internal loads in the human tibia during gait," *Clinical Biomechanics*, vol. 24, no. 3, pp. 299–302, 2009.

G. Welsch, R. Boyer, and E. Collings, *Materials properties handbook: titanium alloys*. ASM international, 1993.

P. Weninger, M. Schueller, M. Jamek, S. Stanzl-Tschegg, H. Redl, and E. K. Tschegg, "Factors influencing interlocking screw failure in unreamed small diameter nails–a biomechanical study using a distal tibia fracture model," *Clinical Biomechanics*, vol. 24, no. 4, pp. 379–384, 2009.

M. Wettstein, E. Mouhsine, J.-N. Argenson, P. J. Rubin, J.-M. Aubaniac, and P.-F. Leyvraz, "Three-dimensional computed cementless custom femoral stems in young patients: midterm followup," *Clinical orthopaedics and related research*, vol. 437, pp. 169–175, 2005.

A. P. Whittle, W. Wester, and T. A. Russell, "Fatigue failure in small diameter tibial nails," *Clinical orthopaedics and related research*, vol. 315, pp. 119–128, 1995.

H. Williams, G. Browne, G. Gie, R. Ling, A. Timperley, and N. Wendover, "The exeter universal cemented femoral component at 8 to 12 years a study of the first 325 hips," *Journal of Bone & Joint Surgery, British Volume*, vol. 84, no. 3, pp. 324–334, 2002.

D. Windridge and J. Kittler, "A morphologically optimal strategy for classifier combination: Multiple expert fusion as a tomographic process," *Pattern Analysis and Machine Intelligence, IEEE Transactions on*, vol. 25, no. 3, pp. 343–353, 2003.

O. Wirjadi, *Survey of 3d image segmentation methods*. Fraunhofer-Institut für Techno-und Wirtschaftsmathematik, Fraunhofer (ITWM), 2007.

R. C. Wong, H. Tideman, M. A. Merkx, J. Jansen, and S. M. Goh, "The modular endoprosthesis for mandibular body replacement. part 1: Mechanical testing of the reconstruction," *Journal of Cranio-Maxillofacial Surgery*, vol. 40, no. 8, pp. e479–e486, 2012.

R. C. Wong, H. Tideman, M. A. Merkx, J. Jansen, and S. M. Goh, "The modular endoprosthesis for mandibular body replacement. part 2: Finite element analysis of endoprosthesis reconstruction of the mandible," *Journal of Cranio-Maxillofacial Surgery*, vol. 40, no. 8, pp. e487–e497, 2012.

R. Wong, H. Tideman, L. Kin, and M. Merkx, "Biomechanics of mandibular reconstruction: a review," *International journal of oral and maxillofacial surgery*, vol. 39, no. 4, pp. 313–319, 2010.

B. Wroblewski, P. Siney, and P. Fleming, "The charnley hip replacement–43 years of clinical success," *Infection*, vol. 22, pp. 1–53, 2006.

G. Wu, S. Siegler, P. Allard, C. Kirtley, A. Leardini, D. Rosenbaum, M. Whittle, D. D. DĹima, L. Cristofolini, H. Witte *et al.*, "Isb recommendation on definitions of joint coordinate system of various joints for the reporting of human joint motion - part i: ankle, hip, and spine," *Journal of biomechanics*, vol. 35, no. 4, pp. 543–548, 2002.

G. Wu, F. C. Van Der Helm, H. Veeger, M. Makhsous, P. Van Roy, C. Anglin, J. Nagels, A. R. Karduna, K. McQuade, X. Wang *et al.*, "Isb recommendation on definitions of joint coordinate systems of various joints for the reporting of human joint motion - part ii: shoulder, elbow, wrist and hand," *Journal of biomechanics*, vol. 38, no. 5, pp. 981–992, 2005.

J. Xia, H. H. Ip, N. Samman, D. Wang, C. S. Kot, R. W. Yeung, and H. Tideman, "Computer-assisted three-dimensional surgical planning and simulation: 3d virtual osteotomy," *International journal of oral and maxillofacial surgery*, vol. 29, no. 1, pp. 11–17, 2000.

C. Xu and J. L. Prince, "Snakes, shapes, and gradient vector flow," *Image Processing, IEEE Transactions on*, vol. 7, no. 3, pp. 359–369, 1998.

C. Xu, A. Yezzi Jr, and J. L. Prince, "On the relationship between parametric and geometric active contours," in *Signals, Systems and Computers, 2000. Conference Record of the Thirty-Fourth Asilomar Conference on*, vol. 1. IEEE, 2000, pp. 483–489.

R. M. Yáñez-Vico, A. Iglesias-Linares, D. Torres-Lagares, J. L. Gutiérrez-Pérez, and E. Solano-Reina, "Three-dimensional evaluation of craniofacial asymmetry: an analysis using computed tomography," *Clinical oral investigations*, vol. 15, no. 5, pp. 729–736, 2011.

W. Yao, P. Abolmaesumi, M. Greenspan, and R. E. Ellis, "An estimation/correction algorithm for detecting bone edges in ct images," *Medical Imaging, IEEE Transactions on*, vol. 24, no. 8, pp. 997–1010, 2005.

T. Yoo, *Insight Into Images: Principles and Practice for Segmentation, Registration, and Image Analysis*, ser. Ak Peters Series. Taylor & Francis, 2004.

P. Young, T. Beresford-West, S. Coward, B. Notarberardino, B. Walker, and A. Abdul-Aziz, "An efficient approach to converting three-dimensional image data into highly accurate computational models," *Philosophical Transactions of the Royal Society A: Mathematical, Physical and Engineering Sciences*, vol. 366, no. 1878, pp. 3155–3173, 2008.

L. A. Zadeh, "Fuzzy sets," *Information and control*, vol. 8, no. 3, pp. 338–353, 1965.

H. Zaidi *et al.*, *Quantitative analysis in nuclear medicine imaging*. Springer, 2006.

G. Zeng, *Medical Image Reconstruction: A Conceptual Tutorial*. Higher Education Press, 2010.

P. Zenz, C. Pospisil, W. Fertschak, and W. Schwägerl, "10 years of cementless implantation of total hip endoprosthesis using zweymuller's stem," *Zeitschrift fur Orthopadie und ihre Grenzgebiete*, vol. 133, no. 6, pp. 558–561, 1994.

H. Zhang, J. E. Fritts, and S. A. Goldman, "Image segmentation evaluation: A survey of unsupervised methods," *computer vision and image understanding*, vol. 110, no. 2, pp. 260–280, 2008.

Y. J. Zhang, "A survey on evaluation methods for image segmentation," *Pattern recognition*, vol. 29, no. 8, pp. 1335–1346, 1996.

B. H. Ziran, M. Darowish, B. Klatt, J. Agudelo, and W. Smith, "Intramedullary nailing in open tibia fractures: a comparison of two techniques," *International orthopaedics*, vol. 28, no. 4, pp. 235–238, 2004.